Micromechanical Methods of Measuring Interfacial Adhesion in Solid-State Batteries



Shatha Almarri
Trinity College
University of Oxford

A thesis submitted for the degree of
Doctor of Philosophy
Trinity 2024

ABSTRACT

Characterization of the electrolyte-electrode interface is critical for the development of solid-state batteries. Despite its importance, this area remains under-explored, with limited research available on quantifying delamination energy at the electrolyte-electrode interface through mechanical testing methods. In this work, nanoindentation and nanoscratch techniques are utilized to characterize ceramic and polymer electrolyte thin film interfaces.

In Chapter 3, nanoindentation and nanoscratch techniques are developed on reference tungsten on silicon films to quantify their delamination energies. These films were selected due to their brittle behaviour, which simplifies the assessment of failure, and because the delamination energies of tungsten-silicon systems are well-documented in literature. Comparisons between the delamination energies obtained from both methods were conducted, alongside investigations into the influence of testing parameters. Delamination energy values obtained from nanoindentation were found to be independent of testing parameters, while nanoscratch results exhibited a high dependence on testing parameters, making it a semi-quantitative test. Delamination energy values agreeing with literature were found, confirming the reliability of the developed methods.

In Chapter 4 two battery polymers, a novel tri-block copolymer (P1) and polyethylene oxide (PEO) on silicon wafers were tested. The ductile nature of polymers led to failure behaviors which were different than those observed in tungsten. P1 was found to avoid delamination through plastic deformation, while PEO displayed delamination at the interface, with a nanoindentation delamination energy of 1.17 J/m^2 and a nanoscratch delamination energy of 2.3 J/m^2. Finite element modelling (FEM) was employed to understand the effect of the electrolyte mechanical properties and interfacial strength, on the observed failure mode (plastic deformation or delamination). A failure mode map was created, to facilitate future

predictions of failure modes based on electrolyte properties. Through FEM, electrolytes with lower yield strength and lower modulus were found to avoid delamination through plastic deformation, agreeing with the observed experimental results.

The interfacial energy between LLZO and NMC is a crucial parameter in solid-state battery design; however, no prior studies have experimentally determined this value. In Chapter 5, the interfacial behavior of LLZO was assessed on silicon and NMC substrates. The effect of film thickness and annealing on the delamination energy was investigated through both techniques. The thinner LLZO on silicon film exhibited higher interfacial energy in both nanoindentation and nanoscratch tests compared to the thicker film. The relative displacement (h_{max}/t_{film}) at which nanoindentation delamination was first observed was highest for LLZO on NMC, which gives a qualitative indication that the interfacial strength in this sample was higher than LLZO on silicon. Finite element models of an electrolyte coated cathode particle with 5% volume contraction were developed to assess the minimum interfacial energy needed to avoid delamination for different electrolyte materials. Target interfacial energy for compliant electrolytes such as polymers was found to be 1 J/m^2, while for brittle electrolytes such as ceramics, a target of 10 –30 J/m^2 was found.

PUBLICATIONS

"Quantifying delamination energy in tungsten-silicon thin films through nanoindentation and nanoscratch" Shatha Almarri, Matthew Lloyd, Ed Darnbrough, David Armstrong, 2024. *Materials and Design. 2025;253:113873.* *https://doi.org/10.1016/j.matdes.2025.113873*

"Evaluation of interfacial strength in polymer thin films through nanoindentation and finite element modelling" Shatha Almarri, Holly Yeo, Ed Darnbrough, David Armstrong, 2024. (In preparation)

CONFERENCES

Faraday Institution Conference 2023 "Mechanical Properties of Interfacial Adhesion in Solid State Batteries" – Poster Presentation

Nanobrücken Nanomechanical Testing Conference 2023 "Measuring interface adhesion through nanoindentation and nanoscratching" – Oral Presentation

Nanobrücken Nanomechanical Testing Conference 2022 "Mechanical Properties of Interfacial Adhesion in Solid State Batteries" – Poster Presentation

ACKNOWLEDGEMENTS

I would like to express my deepest gratitude to my supervisor, Professor David Armstrong, for his continuous guidance, support, and encouragement throughout my PhD journey. I would also like to extend my sincere thanks to my co-supervisor, Dr. Ed Darnbrough, for his invaluable advice, thoughtful discussions, and constructive criticism that have greatly contributed to the quality of this work. I am sincerely thankful to my collaborators, Holly Yeo and Georgina Gregory for providing the polymer samples, Matthew Lloyd for providing the tungsten samples, and Stephen Turrell for providing the ceramic samples used in this work. Thank you to Mahmut Erol for assisting me with the XRD work in this thesis. I would also like to acknowledge the financial support provided by the UAE Ministry of Education, without which this research would not have been possible. I am eternally grateful for everything my country has provided for me; I hope to repay the favour and provide meaningful scientific contributions to the UAE in the future.

To my friends that I met during my time here, thank you for being an invaluable source of support throughout this journey, and for offering much needed distractions during the most stressful periods of my PhD. Thank you for reminding me that there is life beyond the lab.

Finally, to my siblings, Wajd, Ahmed and Saif, thank you for your unconditional love and support. To my parents – Hazzaa Almarri and Maryam Aljarman, your constant support has been my greatest motivation throughout this long and challenging process. The values of hard work, perseverance, and resilience that you instilled in me have been the foundation of everything I've achieved, and I owe it all to you and your unwavering belief in me. I promise now I am done with education and will finally get a job.

CONTENTS

1. Introduction 9

1.1. Context 9

1.2. Lithium-Ion Batteries 10

1.2.1. Liquid lithium-ion battery 10
1.2.2. Solid-State Batteries 12
1.2.3. Importance of interfacial characterization 15

1.3. Nanoindentation 17

1.3.1. Introduction to Nanoindentation 17
1.3.2. Sources of Error in the Oliver-Pharr Method 21
1.3.3. Nanoindentation Adhesion Testing 29

1.4. Nanoscratch Adhesion Testing 35

1.4.1. Nanoscratch Model 36
1.4.2. Influence of Parameters 37
1.4.3. Nanoscratch Failure Modes 39

1.5. Introduction to Cohesive Zone Modelling 41

1.5.1. Cohesive Properties Selection Guidelines 44

1.6. Review of Reported Delamination Energies 45

1.7. Outline of thesis 47

2. Methods 49

2.1. Characterization Techniques 49

2.1.1. Scanning Electron Microscopy (SEM) 49
2.1.2. Focused Ion Beam (FIB) 51
2.1.3. X-ray Diffraction (XRD) 53

2.2. Thin Film Fabrication Techniques 53

2.2.1. Physical Vapor Deposition (PVD) 53
2.2.2. Solvent Casting 54

2.3. Mechanical Testing Techniques 55

2.3.1. Nanoindentation 55
2.3.2. Nanoscratch 56

2.4. Adhesion Testing 58

2.4.1. Nanoindentation Adhesion 58
2.4.2. Nanoscratch Adhesion 62

2.5. Finite Element Modelling *63*

3. Method Development on Tungsten Films **65**

3.1. Aim *65*

3.2. Materials and Methods *66*

3.2.1. Thin Film Fabrication 66
3.2.2. Nanoindentation Methodology 67
3.2.3. Nanoscratch Methodology 67
3.2.4. Silicon Substrate and Tungsten Film Characterization 68
3.2.5. Finite Element Modelling 70

3.3. Results and Discussion *72*

3.3.1. Hardness and elastic modulus of tungsten thin films 72
3.3.2. Nanoindentation Adhesion 75
3.3.3. Nanoscratch Adhesion 86

3.4. Comparison and Discussion *94*

3.5. Conclusions *95*

4. Polymer Thin Films **98**

4.1. Aim *98*

4.2. Materials and Methods *99*

4.2.1. Thin Film Fabrication 99
4.2.2. Nanoindentation Methodology 100
4.2.3. Nanoscratch Methodology 101
4.2.4. Thin Film Characterization 102
4.2.5. Finite Element Modelling 108

4.3. Results and Discussion *111*

4.3.1. Creep, Elastic Modulus and Hardness Measurements 111
4.3.2. Nanoindentation Adhesion 123
4.3.3. Nanoscratch Adhesion 134
4.3.4. Nanoindentation FEM Parametric Study 142

4.4. Conclusions *151*

5. LLZO Thin Films **154**

5.1. Aim *154*

5.2. Materials and Methods *155*

5.2.1. Thin film fabrication 155
5.2.2. Nanoindentation Methodology 156

5.2.3. Nanoscratch Methodology 156
5.2.4. Film Characterization 157
5.2.5. Finite Element Modelling 164

5.3. Results and Discussion 166

5.3.1. Elastic Modulus and Hardness Measurements 166
5.3.2. Nanoindentation Adhesion Experiments 170
5.3.3. Nanoscratch Adhesion Experiments 187
5.3.4. Comparison of nanoindentation and nanoscratch results 200
5.3.5. Cathode Volume Change Modelling 202

5.4. Conclusions 204

6. Conclusions 207

7. References 211

Appendix 229

Appendix 1: Mesh Convergence (1/6th model) 229

Appendix 2: Load-displacement curve (FEM vs Experimental) tungsten on silicon 230

Appendix 3: Mesh Convergence (Cohesive model) 231

Appendix 4: LLZO Films Sputtering Conditions 231

Appendix 5: XRD results with silicon substrate 233

Appendix 6: XRD Air exposure 234

1. INTRODUCTION

1.1. Context

The transport sector is the largest contributor to CO_2 emissions in the United Kingdom, responsible for an estimated 113 million tonnes of CO_2 annually[1]. Therefore, the electrification of transport vehicles is essential to achieving net zero carbon emissions by 2030. Currently, electric vehicles (EVs) constitute only 3% of the cars in the UK[2]. Range anxiety has frequently been cited by consumers as the most significant barrier preventing their transition from internal combustion engine (ICE) vehicles to electric vehicles (EVs). Although state-of-the-art luxury electric vehicles, such as those produced by Tesla, can compete with ICE vehicles in terms of range[2], widespread electrification requires the integration of high-range capabilities into more affordable vehicles. The development of high-performance batteries with better range, cost and safety is essential in encouraging consumers to adopt electric vehicles and to reduce transport emissions. Lithium-ion batteries, which currently dominate the EV battery market are approaching their theoretical performance limits and as a consequence, effort has been directed into researching alternative battery chemistries to meet the demand for longer-range and safer electric vehicles.

This chapter aims to give an introduction on the current state of the art batteries and highlights the most promising alternative battery architecture, the solid-state battery. The challenges facing solid-state batteries, particularly interfacial characterization and its importance, are highlighted. An introduction is given on the mechanical testing techniques used in this thesis to assess the interface, along with the models used to quantify the adhesion energy.

1.2. Lithium-Ion Batteries

1.2.1. Liquid lithium-ion battery

Lithium ion-batteries (LIBs) have emerged as a crucial technology to meet the escalating demands for sustainable energy storage solutions. Since their initial commercialization in the 1990s by Sony, LIBs have been integral in a wide range of applications from electric vehicles to portable electronics, due to their high energy density (260 Wh/kg^3), lifetime and recyclability.

A typical lithium battery shown in Figure 1 consists of three main components: cathode (positive electrode), anode (negative electrode) and a liquid electrolyte. The right side represents the porous cathode, typically a transition metal oxide such as $LiCoO_2$ (LCO) or $LiNiMnCoO_2$ (NMC). On the left side is the porous anode, typically made out of graphite due to its low cost, abundance and high performance. The liquid electrolyte infiltrates the entire cell to transport lithium-ions between the two electrodes. The separator prevents electrons from passing through the electrolyte, forcing them to flow through an external wire. During discharging (de-intercalation), positive lithium ions move from the anode to the cathode through the liquid electrolyte. In order to maintain charge neutrality, for each lithium ion, one electron is released to the external circuit. The opposite reaction occurs during charging (intercalation).

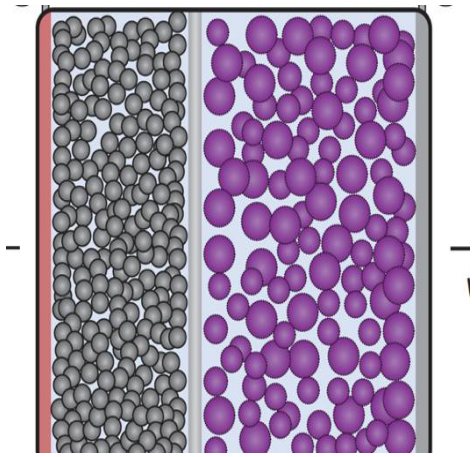


Figure 1: Liquid lithium-ion battery (taken from Janek, 2016[3])

An important metric to describe a battery's performance is energy density, which is the total energy stored per unit of weight, given in units of Wh/kg. Power density refers to how fast the energy in a battery can be delivered, given in units of W/kg. The theoretical capacity (Q) of an electrode material can be calculated using as:

$$Q = \frac{nF}{3600\ M_W} \quad (1)$$

Where n: number of electrons transferred, F: Faraday constant and M_W: molar weight. The exact calculated values of theoretical limits depend on the manufacturing conditions, however for graphite anodes, this theoretical limit is calculated to be 372 (mAh/g)[4]. Today's state of the art LIBs are nearing this limit, so alternative battery chemistries are being considered. The goal of battery engineering is to move from graphite anodes to alternative anodes such as lithium or silicon due to their high theoretical capacities of 3,860 (mAh/g)[5] and 4,200 (mAh/g)[6] respectively. Replacement of the graphite anode in liquid LIBs with either of those anode materials is not currently possible due to several issues. The liquid electrolyte is highly reactive with lithium, leading to the growth of lithium dendrites on the anode, that increase in size and ultimately pierce the separator leading to a short circuit[5]. Additionally,

silicon anodes are not currently utilized due to their large volumetric expansion (up to 300%) when cycled, which leads to low reversibility[6].

For electric vehicles to compete with internal combustion engine vehicles, the energy density of LIBs needs to increase fivefold to achieve similar driving ranges. Given the safety issues of liquid LIBs and their approach to the theoretical limit, alternative chemistries and architectures must be explored.

1.2.2. Solid-State Batteries

One of the most promising improvements to the conventional LIB is the replacement of the liquid electrolyte with a solid electrolyte (SE). A typical solid-state battery (SSB) architecture is shown in Figure 2. The SE is infiltrated into both electrodes and between them. Using a solid electrolyte opens up the possibility of using lithium anodes that can lead to a volumetric energy density improvement of 70%[3]. This is possible due to the SE forming a stable interface with lithium, and its mechanical rigidity able to further supress any dendrite growth, both of which were not previously possible with liquid electrolytes. Bulk polarization is also reduced within SEs since only lithium ions can pass through, leading to higher current densities and faster charging also leading to less dendrite growth[3].

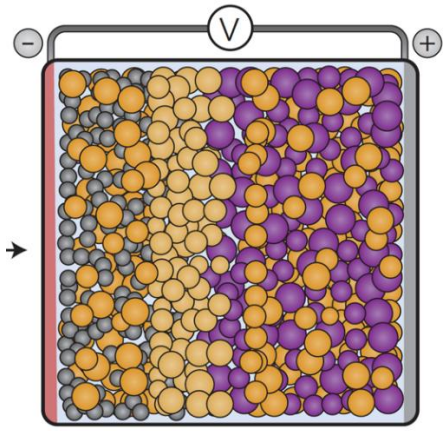


Figure 2: Solid-state battery (taken from Janek, 2016[3])

Even though SSBs offer many advantages, there are still some challenges facing their widespread adoption. Firstly, using a high-capacity anode like lithium leads to large volumetric changes. The introduction of new solid-solid interfaces means that these volume changes can induce high levels of stress in the materials, which can lead to material fracture and loss of interfacial contact. Furthermore, a careful balance is needed in selecting solid electrolyte materials to maximize both mechanical properties and ionic conductivity.

Solid electrolytes are primarily polymers, ceramics, or composites, each with their own advantages and drawbacks, which will be discussed in detail in the next section. In terms of mechanical performance, polymers have the clear advantage over ceramics since they are flexible enough to accommodate large stresses without fracture. In terms of electrochemical performance, ceramics display much higher ionic conductivities compared to polymers. For this reason, composite cathodes are typically used to combine the advantages of both. Other requirements for SEs are good thermal stability, low electronic conductivity, and anode interface stability.

Solid State Battery Electrolytes

Polymers are excellent solid electrolyte candidates due to their low cost and ease of processing. Above the polymer's glass transition temperature, ions are able to freely move in the polymer matrix in a liquid-like fashion. Additionally, the polymer's flexibility can accommodate large volume changes, and their excellent adhesive properties ensure a good interface with the electrodes. A further advantage is the suppression of dendrite formation, that has been observed when the shear modulus of the polymer is double that of the lithium anode[5]. Poly(ethylene oxide) (PEO) is one of the most frequently studied electrolyte candidates due to its good thermal stability, mechanical properties and compatibility with lithium salts. However, PEO displays low ionic conductivity at room temperature (10^{-8} –10^{-4} S/cm)[7], which is below

the required minimum conductivity for battery operation. To circumvent this, polymer-polymer hybrids have been developed. Polymer mixing morphologies include single-ion polymers, cross-linked polymers, and block copolymers as shown in Figure 3. Block copolymers offer a unique way to separate electrochemical and mechanical properties, allowing the optimization both properties. Polymer A acts as the ionic conductor block while polymer B provides mechanical strength. This approach has been extensively used to improve the properties of PEO with the addition of polystyrene (PS) blocks and the ionic conductivity was improved to 2.3 x 10^{-4} S/cm[8,9]. Improvements to PEO mechanical properties were also achieved through the use copolymers which were 1-4 orders of magnitude higher than pure PEO[10].

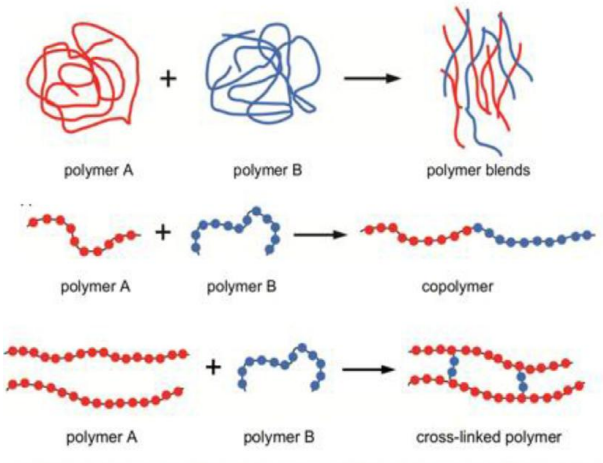


Figure 3: Different polymer mixing morphologies (taken from Wu, 2020[11])

Garnet type ceramics such as $Li_7La_3Zr_2O_{12}$ (LLZO) have been widely studied as solid electrolyte candidates due to their excellent stability with lithium anode and high ionic conductivities. These ceramics are usually doped with either aluminium, gallium or tantalum to stabilize the cubic phase. Out of all of these dopants, Ta doped LLZO has been reported with the highest ionic conductivity of 10^{-3} S/cm at room temperature[12,13]. The main drawback with the use of ceramics is their inability to accommodate volume changes due to their brittle nature.

The advantages offered by both polymers and ceramics has led to the development of hybrid composites to maximize the benefits of both. Improvements to the polymer solid

electrolyte ionic conductivity can be achieved by the addition of inorganic ceramic fillers such as Al_2O_3[14], SiO_2[15], LLZO[16–18], or LLTO[19]. The ion transport mechanism varies in the case of active (Li containing) and passive fillers. In terms of ionic conductivity improvements, active fillers have been shown to improve ionic conductivity more effectively due to the faster lithium-ion transport paths[17]. The mechanical properties improvement due to the addition of ceramic fillers remains unclear as some paper report a degradation[18] or no change in mechanical properties[20] after the addition of fillers. Further benefits introduced by the use of composite electrolytes include enhanced interfacial stability[15,20], high electrochemical stability window[18] and good cycling stability[16].

1.2.3. Importance of interfacial characterization

In traditional liquid electrolyte cells, lithium-ions can easily diffuse across the interface with minimal resistance, since the liquid electrolyte can entirely infiltrate the electrode. Due to the introduction of solid-solid interface in solid-state batteries, discontinuous physical contact between the electrolyte and electrode can lead to lithium-ions being unable to transport through the voids. During cathode volume contraction, large tensile forces are generated at the interface which can lead to delamination[21]. This delamination has adverse effects on the battery cycling performance and lifetime[21–26]. The extent of delamination has been shown to be dependent on the electrode-electrolyte adhesive strength[26], electrolyte mechanical properties[21,24–26], electrode mechanical properties[21] and particle size[21,22].

Bucci et al.[26] used analytical models to create a plot of electrolyte Poisson's ratio versus the ratio of yield stress to fracture strength (i.e.: adhesive strength), showing which combination leads to plastic flow and delamination, shown in Figure 4. Under a yield strength to fracture strength of 0.5, no delamination takes place and plastic deformation dominates.

These results indicate that ductile electrolytes are better at avoiding delamination compared to brittle electrolytes.

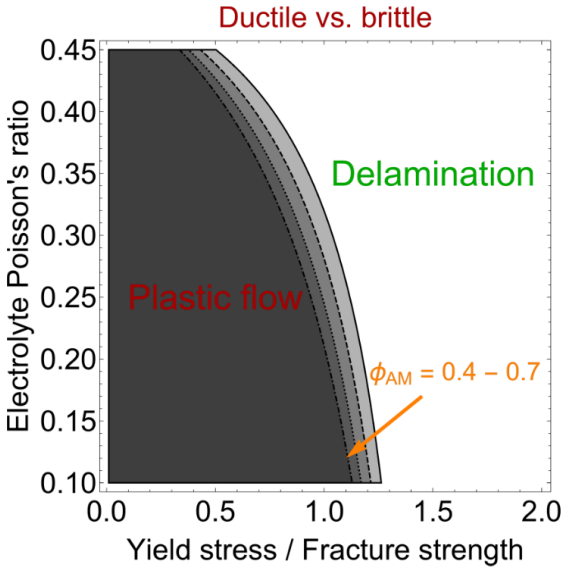


Figure 4: Ductile vs brittle deformation based on mechanical properties (taken from Bucci, 2018[26])

Barai et al.[24] investigated the effect of delamination at the LLZO-NMC interface through mathematical modelling. The cycling curves comparing a delaminated and undelaminated interface are shown in Figure 5. As the NMC is charging, volume contraction occurs and at the end of the charge cycle, delamination first occurs. During discharge, volume expansion occurs with no additional delamination, however the already delaminated regions reduce the available regions for charge transfer. This effect leads to lower achievable voltage and a capacity fade denoted by ΔQ_{NMC} on the figure. Their model also concluded that in order to avoid delamination, electrolytes with smaller grains and low Young's modulus is preferred. Similar results of the advantage of using a low Young's modulus were shown by Hao[21]. Additionally, it was shown that smaller cathode particles are better at avoiding delamination due to the lower levels of stress. This is contrary to the results of Bucci[26] which explained that delamination initiation is independent of particle size.

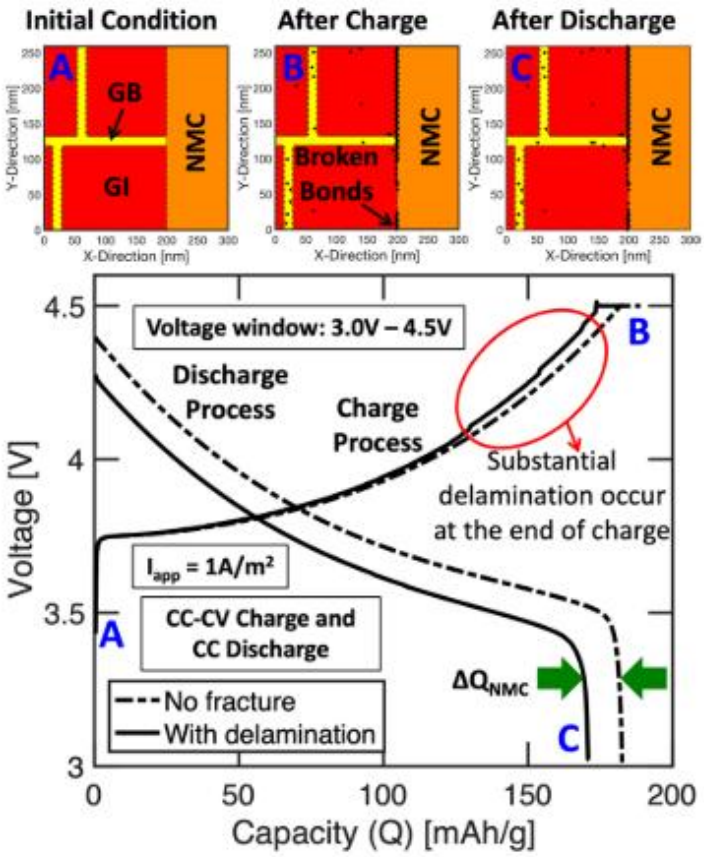


Figure 5: Effect of delamination on charge process in LLZO-NMC (taken from Barai, 2021[24])

1.3. Nanoindentation

1.3.1. Introduction to Nanoindentation

Nanoindentation offers a simple and quick way of measuring a material's elastic modulus and hardness. The main difference between nanoindentation and conventional hardness methods is that visual measurements of the contact area are not needed and is instead calculated from the indentation depth which is usually in the ranges of 100 nm – 5,000 nm. This test is advantageous since it is non-destructive, and no material preparation is needed. Nanoindentation testing is extremely fast, with a single indent taking seconds or minutes to perform depending on the load profile. In addition, this technique enables multiple indents to

be performed across different areas of the sample, creating a map of its mechanical properties and illustrating how these properties vary throughout the sample.

The test involves driving a tip with a well-defined shape into a sample either by defining the maximum load (load control) or maximum displacement (displacement control). As the tip is driven into the sample, the response (either load or displacement values) is continuously recorded, and the result is a load-displacement curve as shown schematically in Figure 6. One of the most commonly used tips is the Berkovich tip, which consists of a three-sided pyramid with a face angle of 65.27°. Other tip geometries, such as spherical or cube-corner tips, are also used depending on the application. The choice of indenter geometry significantly affects the stress distribution beneath the tip. For instance, sharp tips like cube-corner produce higher stress concentrations and are more likely to initiate fracture, whereas spherical tips create broader, more uniform stress fields, which are better suited for elastic–plastic characterization. Additionally, tip radius plays a critical role in determining the contact area and resulting stress field, especially at shallow depths where curvature dominates the response. These considerations are important when interpreting results, particularly for thin films and heterogeneous materials.

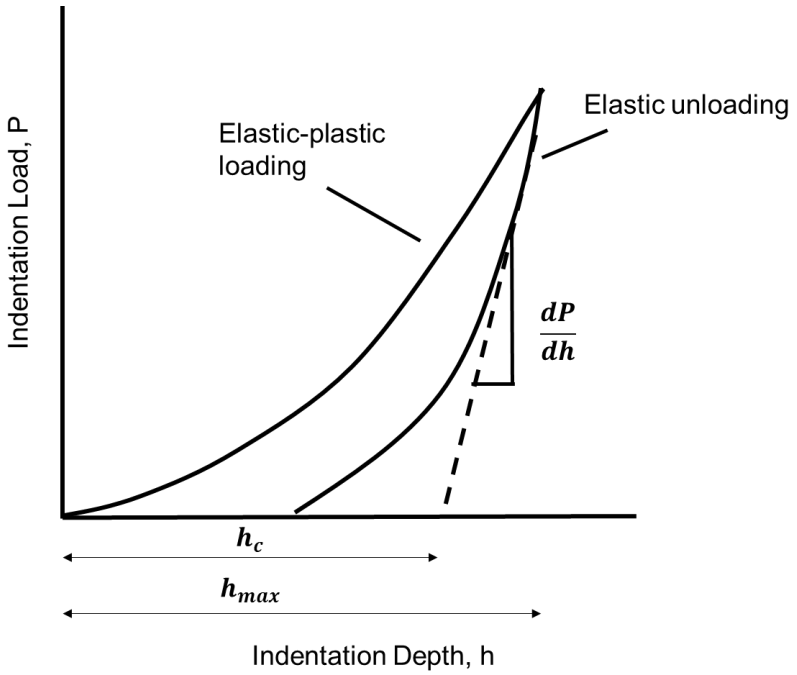


Figure 6: Schematic of typical load-displacement curve

The analysis developed for spherical indenters based on Hertzian contact mechanics[88] can be extended to sharp indenters to extract the sample elastic modulus and hardness from the shape of the load-displacement curve. For a Berkovich indenter, the projected contact area (A_c) is given as:

$$A_c = 3\sqrt{3}h_c^2 \tan^2\theta \quad (2)$$

Where h_c is the contact depth (seen in Figure 6) and θ is the tip semi-angle (θ=65.27° for a Berkovich tip). Equation (2) can be simplified as:

$$A_c = 24.5h_c^2 \quad (3)$$

The contact depth h_c is calculated as:

$$h_c = h_{max} - \epsilon\frac{P_{max}}{S} \quad (4)$$

$$S = \frac{dP}{dh}$$

(5)

Where h_{max} is the maximum depth, P_{max} is the maximum load, ϵ is a constant depending on indenter geometry (ϵ = 0.75 for Berkovich tip), and S is the contact stiffness. The stiffness describes the material's resistance to applied force and is the slope of the upper portion of the unloading curve (Figure 6).

The Oliver-Pharr method[27] is the standard model used to analyse the indentation curve to extract mechanical properties of the sample. The model assumes that the loading portion of the curve consists of both elastic and plastic recovery, whereas the initial portion of the unloading curve is fully elastic. Early models by Doerner and Nix[89] used a linear relationship to fit the initial portion of the unloading curve; however, Oliver and Pharr have found that the following power law more accurately models the material behaviour:

$$P = \alpha\left(h - h_f\right)^m$$

(6)

A least-squares fitting procedure is used to determine h_f (final residual indent depth), α and m (fitting law constants). The sample reduced modulus (E_r) and hardness (H) is then be calculated as:

$$H = \frac{P}{24.5h_c^2}$$

(7)

$$E_r = \frac{\sqrt{\pi}}{2}\frac{S}{\sqrt{A_c}}$$

(8)

Where E_r is the combined response of the indenter tip (i) and sample (s) Young's modulus as follows:

$$\frac{1}{\mathrm{E_r}} = \frac{(1-\nu_s^2)}{E_s} + \frac{(1-\nu_i^2)}{E_i} \quad (9)$$

Here ν_i, ν_s are the indenter and sample Poisson ratio respectively.

To investigate the change in mechanical properties with depth in a single indent, continuous stiffness measurement (CSM)[27] indents can be carried out. CSM is conducted by applying an oscillating load on top of the primary increasing load that allows for the measurement of the sample stiffness at various depths along the loading curve in a single indent. This type of dynamic testing is referred to as nanoDMA by Bruker.

In the context of this work, characterizing thin film mechanical properties is crucial since the behaviour can differ drastically from bulk properties. Mechanical properties of solid-state battery materials such as lithium[28], solid electrolyte polymers[29] and ceramics[30,31] have been investigated in literature. Nanoindentation studies have revealed a strong size dependence in lithium, showing different mechanical properties compared to bulk lithium[28]. Therefore, characterizing the mechanical properties of the battery materials in thin film form is essential to understand their size dependence in practical applications.

1.3.2. Sources of Error in the Oliver-Pharr Method

Pile-up and sink-in

As the sample experiences plastic deformation, the plastic flow of the material can be displaced either around the indenter as pile-up, or downwards as sink-in. These two phenomena are shown schematically in Figure 7.

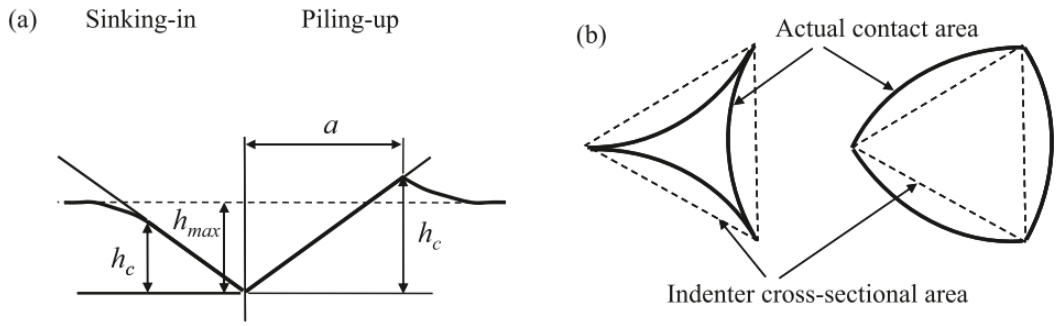


Figure 7: Pile-up and sink-in shown schematically a) cross-sectional and b) top views (taken from Fischer-Cripps, 2004[32])

During pile-up formation, plastic flow causes the material to be pushed outward and upward as the indenter penetrates the surface, leading to an accumulation of material around the indentation perimeter. Pile-up is most commonly observed in non-strain hardened materials with a high elastic modulus to yield strength ratio (E/σ_y)[32,90]. Pile-up is also a notable feature in ductile coatings on hard substrates, as the film deformation is constrained by the substrate. Pile-up leads to overestimated mechanical properties due to the real contact area being larger than the calculated contact area measured from contact depth. Pile-up characterization is mostly performed by SPM or AFM, where the degree of pileup can be assessed and subsequently corrected for.

Pileup in the polymer films was corrected for through the method described by Kese and Bergman[91]. Here the pile-up area is assumed to be a perfect ellipse as shown schematically in Figure 8, where a_i is the pile-up contact width measured from SPM/AFM. This method assumes that the pile-up around each side of the indenter is not equal, so the process is repeated three times for each side of the indenter i = 1,2,3.

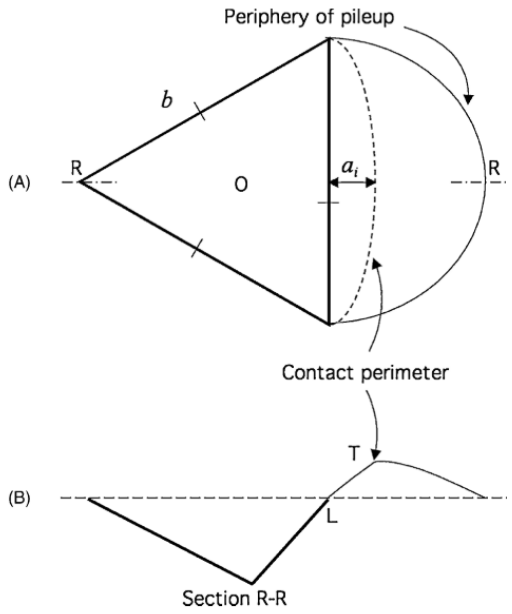


Figure 8: Pile-up correction method (taken from Kese, 2005 [91])

From the measured pile-up contact widths (a_i), the total pile-up area (A_{PU}) is calculated as:

$$A_{PU} = 5.915 * h_c * \sum a_i \quad (10)$$

The true contact area (A_C) of the indenter with the sample is the summation of the Oliver-Pharr contact area (A_{OP}) calculated directly from the contact depth, and the pile-up area (A_{PU}). The calculated true contact area (A_C) is then used in the Oliver-Pharr method to obtain the corrected values of elastic modulus and hardness.

$$A_C = A_{OP} + A_{PU} \quad (11)$$

Sink-in is typically observed in non-strain- hardened materials with low E/σ_y ratios and strain-hardened materials[32]. As the indenter is withdrawn, the surrounding material tends to elastically recover more than the material directly under the indenter, leading to a concave deformation profile. Similar to pile-up, sink-in also causes incorrect calculations of the mechanical properties from the Oliver-Pharr method. In this case, the true contact area is

smaller than that measured from the contact depths, leading to underestimated mechanical properties.

Nanoindentation Creep

Nanoindentation creep is observed as a change in indentation depth under constant load and is a time-dependent deformation behaviour. Creep is typically categorized into two types: 1) viscoelastic creep, which is elastic and time-dependent, commonly observed in polymers and 2) viscoplastic creep, which is plastic and time-dependent, commonly observed in metals or ceramics. Other mechanisms contributing to creep include dislocation movement, which occurs due to stress concentrations under the indenter, and diffusional creep, related to the movement of atoms or molecules through the material. Creep behaviour is typically divided into three stages: primary, secondary, and tertiary creep. During nanoindentation, only the primary and secondary stages are usually observed due to the short time scales involved. Primary creep is characterized by a high initial creep rate that decreases over time as strain hardening occurs. In the secondary stage, the creep rate stabilizes, often modelled as a steady-state creep rate, which is a key indicator of the material's long-term time-dependent behaviour. Creep can significantly affect nanoindentation results, sometimes leading to the formation of a steep, bowed unloading curve, as shown in Figure 9. This occurs because the material continues to deform even during the unloading segment, which distorts the shape of the curve, leading to overestimated and sometimes negative stiffness values. Creep can cause up to 50% overestimation of mechanical properties compared to bulk properties[92]. To minimize the effects of creep during nanoindentation, it is common to either add a long hold period at constant load before unloading or to use a fast unloading rate. The hold period allows creep deformation to reach the secondary stage and stabilize, reducing its impact on the unloading curve, while a fast unloading rate minimizes the time available for creep to influence the measurements.

Typically, a combination of both is required to minimize creep effects and ensure more accurate measurement of the material's mechanical properties.

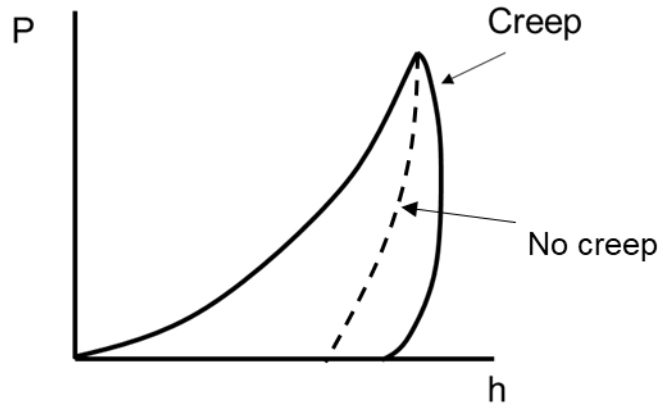


Figure 9: Bowed unloading curve due to creep

Feng and Ngan[93] devised an equation to correct for creep and thermal drift, enabling the calculation of the corrected sample stiffness (S) as:

$$\frac{1}{S} = \frac{1}{S_u} + \frac{\dot{h}_h}{|\dot{P}|}$$

(12)

Where S_u is the apparent stiffness measured from the nanoindentation test, $\dot{h}_h$ is the indenter displacement rate at the end of the hold segment, and $\dot{P}$ is the unloading rate. The indenter displacement rate ($\dot{h}_h$) is a combination of creep ($\dot{h}_c$) and thermal drift ($\dot{h}_t$) as:

$$\dot{h}_h = \dot{h}_c + \dot{h}_t$$

(13)

The corrected stiffness found from equation (12) corrects for both creep and thermal drift, and can be used in the Oliver-Pharr model (equation (8)) in place of the apparent stiffness, to obtain the corrected reduced modulus. The authors also define a creep factor, C as:

$$C = \frac{\dot{h_c} S}{\dot{P}}$$

(14)

It can be seen from equation (14) that a very large unloading rate will minimize the creep factor. The authors explain that if C is minimized to less than 0.1, the effect of creep on the mechanical properties can be considered negligible.

Substrate Effects

Indentation is commonly used to extract the mechanical properties of thin films; however, complications arise due to the substrate's influence on the indentation response. Significant substrate effects result in the Oliver-Pharr method producing a combined response from both the film and substrate, with these effects typically increasing at greater depths. This effect is especially prominent when a large mechanical property mismatch exists between the film and substrate. A simple procedure for obtaining the film elastic modulus involves indenting the film at various depths and plotting the obtained elastic modulus as a function of the ratio of indentation depth to thickness[32]. By fitting the curve, the extrapolated elastic modulus at ratio equal to zero can be found which represents the film only elastic modulus. Errors in this method mainly can be introduced during the fitting procedure, however this method presents a simple and fast way to obtain estimated values of film only modulus.

Saha and Nix[33] found that for hardness measurements, substrate effects were negligible in the case of soft films on a hard substrate. The plastic deformation in this case is contained in the film as long as the indentation depth is less than the film thickness. Contact areas calculated by Oliver-Pharr without pile-up corrections lead to high substrate effects and overestimated film properties, making it important to account for pile-up. The film only elastic modulus is more difficult to measure as compared to hardness because the elastic field cannot easily be contained within the film. A schematic by Bull[34], illustrating the size of elastic and plastic zones, is shown in Figure 10. Saha and Nix state that the elastic modulus of the film can be determined by using indentation depths less than 10% of the film thickness. This 10%

condition has been extensively used in literature as a rule; however its validity has been questioned. Some studies of soft films on hard substrates support the validity of the 10% rule in both hardness and elastic modulus measurements[35,36]. However, correcting for pile-up and accurately determining the true contact areas is essential for the method's effectiveness. Zak et al.[37] have shown using FEM that confinement within the film is possible for the plastic zone, but difficult in the elastic zone since it is much larger and easily extends into the substrate even at 10% indentation depths. Similarly, experimental results of TiN coatings on steel also found that the 10% rule was valid for hardness but not for elastic modulus measurements, which were only valid at 1% indentation depths [34].

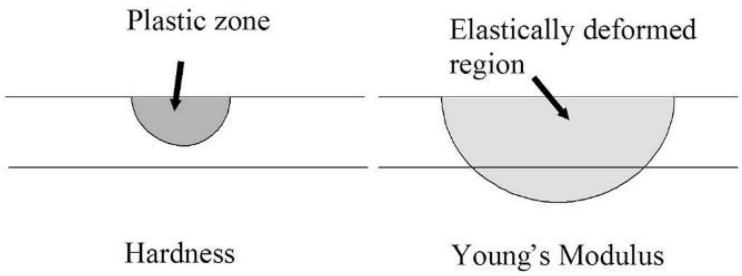


Figure 10: Elastic and plastic zones created through indentation (illustrative, taken from Bull, 2019 [34])

Some analytical models have been developed to correct for substrate effects in hardness measurements. Early studies by Jonsson and Hogmark[38] incorporated law of mixtures to express the combined hardness response of the film and substrate (H_{eff}) as:

$$H_{eff} = \frac{H_f A_f}{A} + \frac{H_s A_S}{A} \tag{15}$$

In this expression A is the total contact area, and A_f and A_s represent the relative contact areas carried by the film and substrate respectively. H_f and H_s are the hardness values

of the film and substrate respectively. This model has been since improved and simplified by Korsunsky et al.[39] using an energy model as:

$$H_{eff} = H_s + \frac{H_f - H_s}{1 + \frac{t}{\alpha}\left(\frac{h}{t}\right)^2}$$

(16)

Where α is a constant, t is the film thickness and h is the indentation depth.

Despite the increased complexities in measurements of film only elastic modulus as compared to hardness, several models have been developed. King[40] modified the empirical expression formulated by Doerner and Nix[41] using integral equation analysis for a flat punch indenter. The combined response of the film, substrate and indenter (E_{eff}) is described as:

$$\frac{1}{E_{eff}} = \frac{(1-\nu_f^2)}{E_f}\left(1 - e^{-\frac{\alpha t}{\sqrt{A}}}\right) + \frac{(1-\nu_s^2)}{E_s}\left(e^{-\frac{\alpha t}{\sqrt{A}}}\right) + \frac{(1-\nu_i^2)}{E_i}$$

(17)

The subscripts f, s, i represent the film, substrate and indenter respectively. King provided values for the empirical constant α for different ratios of a/t where a is the square root of the contact area and t is the film thickness. Saha and Nix[33] modified King's analysis for a Berkovich tip and arrived at the following expression:

$$\frac{1}{E_r} = \frac{1-\nu_i^2}{E_i} + \frac{1-\nu_f^2}{E_f}\left(1 - e^{-\frac{\alpha(t-h_{max})}{a}}\right) + \frac{1-\nu_s^2}{E_s}\left(e^{-\frac{\alpha(t-h_{max})}{a}}\right)$$

(18)

Where h_{max} is the maximum indenter displacement.

The models summarized above were developed on elastic or elastic-plastic materials, and no experimental or analytical models could be found for viscoelastic films. Therefore, it is unclear how well these models and rules translate to polymer thin films. Geng et al. have shown

that the 10% rule works well for polymers to determine the elastic modulus of the film[36]. Whereas Humood et al. have shown that even at 10% indentation depth, both modulus and hardness are overestimated[42]. Another challenge for thin coatings (thickness 200 nm – 2 μm) arises from indenting within the 10% range (20 nm – 200 nm) which is not practical due to the surface effects that arise in these indentation ranges (tip artefacts, surface roughness).

1.3.3. Nanoindentation Adhesion Testing

With the development of nanoindentation, effort has been directed into using this test to assess the delamination energy of thin films. Generally, if delamination takes place during indentation, a sudden deviation in the curve is observed. However, in thin films displaying delamination during unloading, or gradual loading delamination, this is not observed, and delamination can be inferred from visual assessment of the indent.

Linear Fracture Based Methods

Marshall and Evans [43] pioneered the use of indentation to measure the delamination energy of thin films by modelling the delaminated thin film as a clamped elastic plate. Their analysis assumes that the indentation volume remains within the film, therefore a main assumption is that no substrate deformation or film pile-up occurs. This is important to accurately determine the indentation volume (V_o) needed in equation (20) . The delamination energy G is given by equations (19) - (22) as follows:

$$G = \frac{h\left(1-\nu_f\right)}{E_f}\left[(1-\alpha)\sigma_R^2 + \frac{\sigma_1^2(1+\nu_f)}{2} - (1-\alpha)(\sigma_1-\sigma_B)^2\right] \tag{19}$$

$$\sigma_1 = \frac{V_o E_f}{2\pi h a^2(1-\nu_f)} \tag{20}$$

$$V_o = \frac{\pi}{3} h_p^3 tan\varphi^2$$

(21)

$$\sigma_B = \frac{\mu^2 h^2 E_f}{12a^2(1-\nu_f)}$$

(22)

Where $\sigma_R, \sigma_1, \sigma_B$ are the residual, indentation and Euler buckling stresses respectively. h_p is the plastic depth after indentation and φ is the indenter semi-angle. μ is a constant dependant on boundary conditions, and α is equal to 1 in the case of no film buckling. If no buckling delamination takes place, then the delamination is only driven by the indentation stress without any contribution of residual stresses.

This model has been applied extensively to quantify delamination in various brittle films[44–47], including tungsten on silicon films which yielded delamination energies of (G = 5 - 15 J/m^2)[44,83,103]. The application of this method has largely been complicated due to the overestimation of indentation volume, as this cannot be measured directly. Additionally, the use of this model has been limited to brittle films as the assumption of confined plastic deformation does not hold true for ductile films, so alternative methods need to be investigated.

Energy Based Methods

Omiya et. al[48] proposed a method to evaluate the delamination energy of a polymer film on a silicon substrate through an energy dissipation model, which is more applicable to ductile films. FEM results showed that the load displacement curve of thin films deviate from the perfectly bonded case when delamination occurs. Figure 11 shows a schematic of the load-displacement curve for a delaminated film. Points A and B represent the points just before and after delamination respectively.

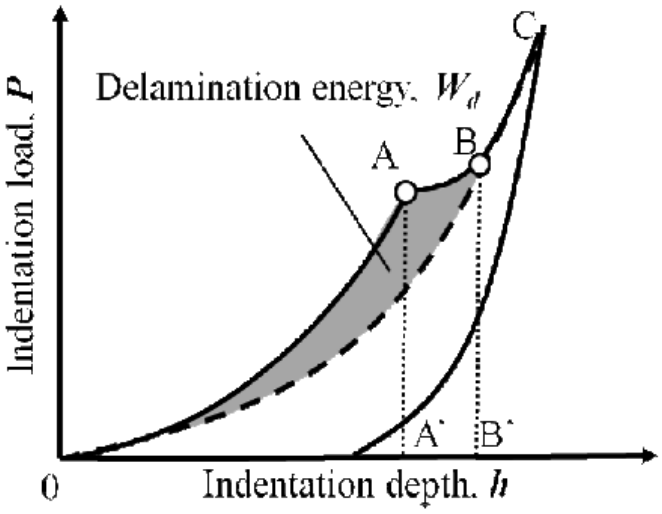


Figure 11: Schematic of determination of delamination work from load-displacement curve (taken from Kozuki, 2010 [49])

A theoretical no-delamination curve is constructed by extrapolating the loading data from points B to C back to the origin through the following power law relationship:

$$P = ah^b + c \tag{23}$$

Where P is the indentation load, h is the indentation depth and a, b, c are fitting constants. The difference in the areas between the two curves is the work of delamination W_d. The delamination energy is then calculated as:

$$G = \frac{W_d}{A_d} \tag{24}$$

Where A_d is the delamination area. One key assumption in the power law method, which uses data after delamination for curve extrapolation, is that the system's properties remain constant following delamination. In brittle films, it was found that this assumption does not hold true and changes in mechanical properties were observed after the onset of delamination[50]. This indicates that the data after delamination may not be representative of the film's true properties.

Li[51] studied weakly bonded thin film systems to determine their interfacial strength through cohesive zone modelling. Three cases were compared through FEM modelling: a perfectly bonded, strong, and a weak interface. Results showed that in the case of the weakly bonded film, buckling occurs at the maximum indentation depth however, no visible deviation in the load displacement curve occurs. Whereas the strongly bonded interface displayed a clear deviation in the load displacement. The power law method has been applied to polymer thin films displaying a clear curve deviation[49,52,53]. In brittle film systems, a similar method has been applied to determine the film's fracture toughness[54], however no studies have been found for the power law method application to determine delamination energy of brittle films.

Energy-based methods for analysing brittle film delamination include the approach described by Malzbender[50], which utilizes the total irreversible work done by the indenter. The total irreversible work is the area enclosed by the load-displacement curve. The three stages of deformation include plastic deformation (stage I), delamination (stage II) and fragmentation (stage III). The total irreversible work in each stage is calculated as:

$$Stage\ I: W_{irr} = W_p \tag{25}$$

$$Stage\ II: W_{irr} = W_p + W_d \tag{26}$$

$$Stage\ III: W_{irr} = W_p + W_d + W_f \tag{27}$$

This method assumes that other dissipation mechanisms such as buckling, and substrate deformation are assumed to be negligible. Linear extrapolation of plastic work and delamination work allows for the determination of the delamination work and fragmentation work respectively as shown in Figure 12. This method has been implemented in several papers to investigate the adhesive energies of thin films[55–57]. However, the validity of the plastic work

linear extrapolation has been questioned, and FEM studies have found it to overestimate the delamination energy[46].

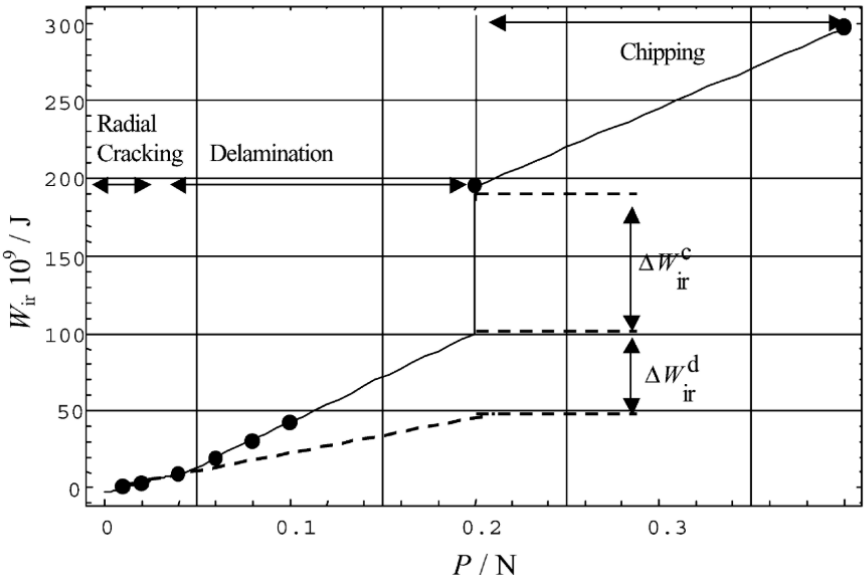


Figure 12: Irreversible work plot (taken from Malzbender, 2000 [50])

Overall, energy-based methods offer a simpler approach to analysing load-displacement curves compared to linear fracture methods. However, caution must be exercised to avoid overestimating delamination energy due to secondary events such as substrate cracking and buckling[57].

Nanoindentation Failure Modes and Observation

In brittle films, nanoindentation failure is simple to observe since most films display buckling and/or blistering when delaminated. During indenter unloading, the delaminated region under the indenter can either remained pinned, leading to a double buckle, or become unpinned, leading to a single buckle also known as a blister. Further increase in load will eventually lead to complete film failure and fragmentation. Figure 13 below shows the three stages of deformation namely surface cracks, delamination and fragmentation. In this case, an optical microscope is usually sufficient to verify delamination has occurred. FIB cross-

sectioning is a useful secondary step used in many studies to observe the interface under the blister[58–60].

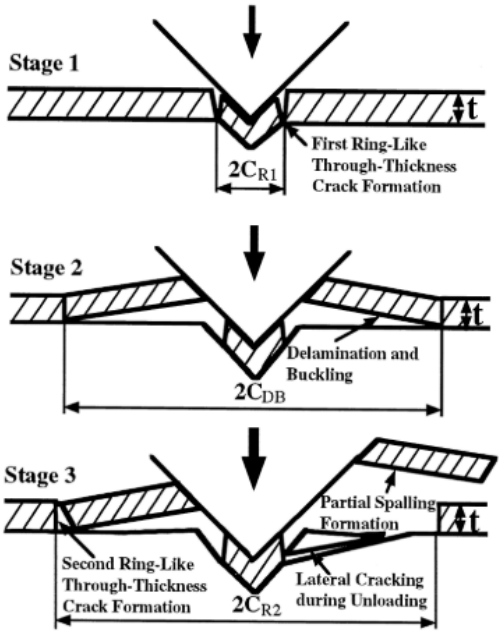


Figure 13: Three stages of deformation in brittle thin films (taken from Li, 1998 [54])

In the case of polymeric materials, delamination cannot be easily seen because polymer films do not display any blistering or cracks and instead show plastic deformation and pile-up. In such systems, double buckling is the expected failure mode due to the lack of residual stresses present in polymer films as compared to metallic or ceramic films. Delamination in polymers, therefore, is mostly inferred from the shape of the load displacement curve, where a deviation indicates delamination, and no detailed visual attempts in observing the cross-sectional delamination has been performed in literature. Several studies[49,52] explain that delamination in polymer thin films can be confirmed by the presence of a crescent like feature at the edge of the indent, as shown in Figure 14. However, because pile-up is a big factor in compliant polymer films, it is often difficult to determine whether such feature is attributed to delamination, pile-up, or a combination of both.

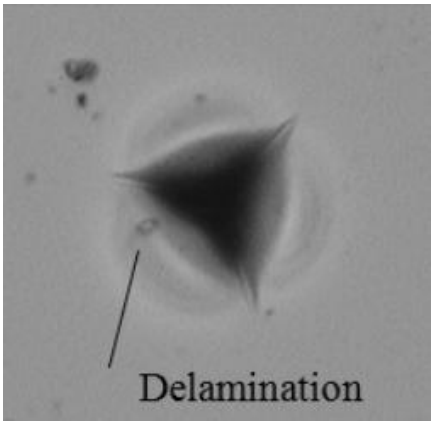


Figure 14: Crescent features attributed to delamination in polymer thin films (taken from Kozuki, 2010 [49])

1.4. Nanoscratch Adhesion Testing

As the nanoindentation test grew in popularity, advances in nanoindentation instrument technology allowed for the incorporation of movement in two dimensions resulting in the nanoscratch test. In this test, forces are applied to the indenter tip in the normal and lateral directions, while the normal and lateral displacements are recorded (Figure 15).

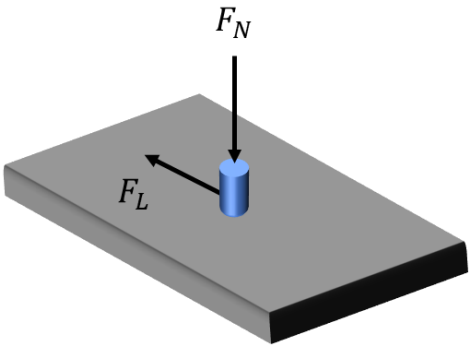


Figure 15: Scratch test setup

The coefficient of friction (μ) in scratch test is calculated as the ratio of the lateral (F_L) and normal forces (F_N):

$$\mu = \frac{F_L}{F_N} \tag{28}$$

A combination of nanoscratch test data and residual scratch images can provide valuable insights into scratch resistance, wear behaviour, film scratch hardness, and film adhesion.

1.4.1. Nanoscratch Model

Early scratch models by Benjamin and Weaver[61] assumed a simple shearing force to be primarily responsible for thin film delamination under the scratch test. However, with the development of the electron microscope, it was revealed that the mechanisms involved in thin film scratch delamination are more complex than initially believed.

This led to the development of the most commonly used scratch model, the Laugier model[62] which uses a Griffith energy balance approach to equate the local stresses to the work of adhesion. The region ahead of the indenter is assumed to reduce its stored elastic energy at the critical load by forming new surfaces (fragmentation or spalling). The model assumes that at the onset of delamination, the region under and ahead of the indenter are still in the elastic region. Plastic yielding is expected at this stage; however, this usually occurs behind the indenter therefore Hertzian contact conditions are still accurate. Additionally, the model assumes that the total work done is solely due to the work of adhesion, and that the work required to deform the surfaces (i.e.: fragmentation work) is negligible. The work required to delaminate the coating, is expressed as:

$$W = \frac{\sigma_{adh}^2}{2E_f} t \qquad (29)$$

Where E_f is the Young's modulus of the film, σ_{adh} is the compressive stress in the coating at failure, and t is the coating thickness. The applied stress is considered to be almost constant throughout the coating thickness and at failure is expressed as:

$$\sigma_{adh} = \frac{2L_c}{\pi d_c^2}\left(\frac{(4+\nu_f)3\pi\mu}{8} - (1-2\nu_f)\right)$$

(30)

Where L_c is the critical load, d_c is the scratch width at failure, μ is the coating coefficient of friction, and ν_f is the coating Poisson ratio. This model is the most widely used model for polymer coatings[42,63,64] and brittle coatings[65–68]. It has been suggested that the assumption of elastic deformation occurring before the critical point may not be applicable for polymers, which display high levels of plastic deformation before failure. Therefore, it has been suggested that the scratch value by Laugier model should only be used an upper bound[64]. Furthermore, the assumption of minimal contribution of fragmentation to the total measured work in brittle films remains unclear.

1.4.2. Influence of Parameters

The critical load at which failure is first observed is regarded as a measure of the thin film adhesion. Critical loads are only semi-quantitative because they are user-defined and have been seen to be influenced by a number of intrinsic and extrinsic scratch parameters summarized in Table 1. Due to the high parameter sensitivity, the scratch test has often been used as a comparative tool to rank the adhesion of different coatings[69].

Extrinsic Parameters	**Intrinsic Parameters**
Coating thickness	Scratch loading rate
Coating hardness	Scratch displacement rate
Substrate hardness	Indenter shape
	Intender tip radius

Table 1: Parameters that affect the critical load during scratch test

The direct influence of these parameters on the critical load has been thoroughly studied in literature[65,70–73] It was found that the scratch loading rate (dL/dt) and displacement rate (dx/dt) do not directly influence the scratch test as long as the ratio between the two remains constant (dL/dx). On the other hand, varying dL/dx significantly influenced the critical load, as seen in Figure 16. The critical load was found to decrease as the dL/dx ratio decreased. No mention on the influence on the calculated delamination energy was given. The authors explain that this behaviour is due to the probability of encountering a defect in the interface increases as dL/dx decreases, leading to a lower value of critical load.

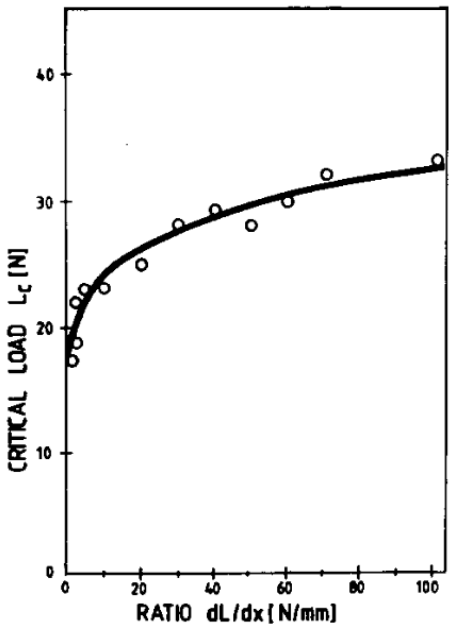


Figure 16: Influence of dL/dx on the critical load (taken from Steinmann, 1987 [70])

It is well-documented that substrate hardness influences the critical load, with a higher substrate hardness leading to an increased critical load[70,71]. This is due to less plastic deformation occurring with harder substrates, and a higher load needed to reach the same level of deformation. Similarly, an increase in coating thickness increases the measured critical load[65,71].

The indenter shape and orientation have been observed to influence the critical load. Different critical loads were observed when using the edge or face forward orientation of a Berkovich tip[74]. Using a larger tip radius has also been seen to increase the observed critical load due to the relationship of the applied average pressure applied by the indenter[70,73]. The difference in critical loads for different tip shapes such as Berkovich and spherical have not been investigated thoroughly in literature however this is expected to affect the critical load as different stress distributions and contact areas are involved[75].

1.4.3. Nanoscratch Failure Modes

During nanoscratching, as the indenter is drawn across the film, compressive stresses are generated in the film that progressively increase with increasing applied normal load. At a sufficiently high stress, the film will begin to fail via a certain failure mechanism that mainly depends on the hardness of both the substrate and the coating. The map described by Bull[76] in Figure 17 shows the influence of the film and substrate properties on the scratch deformation mechanism. In general, for a hard coating on a hard substrate (~H > 5 GPa), interfacial failure (delamination) is observed. The type of delamination can range from buckling, chipping or fragmentation depending on the adhesive strength and the thickness of the coating. This type of failure mechanism is easily observed through optical microscopy or scanning electron microscopy (SEM). Soft coatings (~H < 5 GPa) typically display plastic deformation behaviour regardless of the substrate hardness. If the interfacial shear strength is greater than the coating shear strength, plastic deformation dominates and the film simply piles up around the indenter, completely avoiding any interfacial failure. In this case, the coating removal by the indenter may lead to substrate exposure at sufficiently high loads. On the other hand, if the interfacial shear strength is less than the coating shear strength, cohesive failure mechanisms such as parabolic cracking, fish scaling, followed by delamination can be observed. The cohesive

failure mechanism and damage evolution depends greatly on the polymer's brittle or ductile behaviour[77,78].

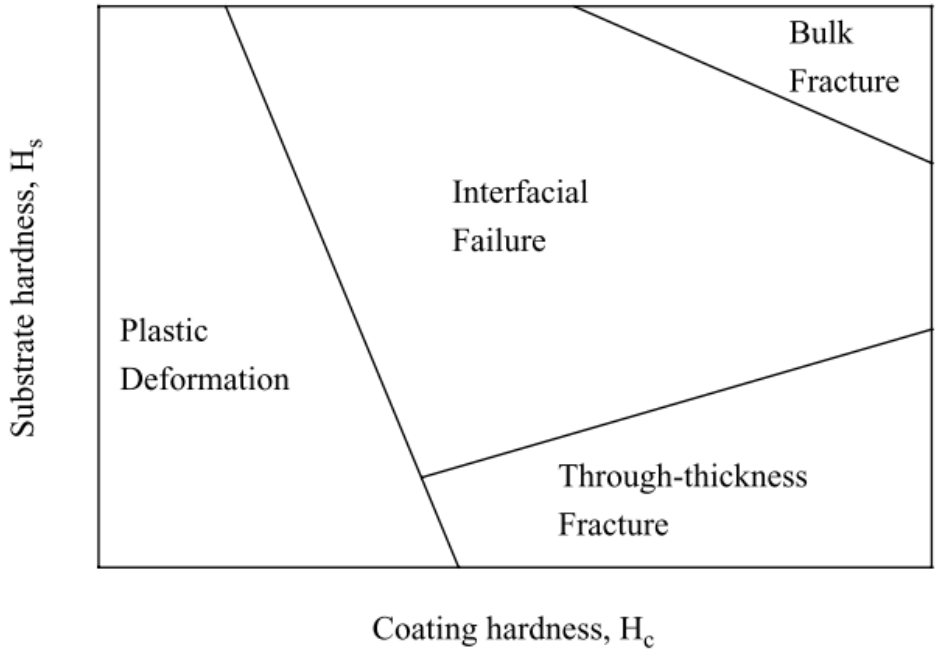


Figure 17: Scratch Deformation Map (taken from Bull, 2006 [76])

The failure condition in scratch tests is user-defined, and it is crucial to select a condition that aligns with the test's objectives. For instance, if the goal is to calculate delamination energy, an adhesive failure mode should be chosen. The failure point chosen can either be assessed qualitatively or quantitatively as shown in Table 2. Quantitative failure assessments are explained further in details in the ASTM standard[79]. Understanding the thin film failure mechanism is important to assign the appropriate failure condition. Additionally, choosing a reproducible failure point assessment method is important to allow comparative studies to be taken, as long as the testing parameters and the failure mechanisms between samples are kept the same. Assessing the failure point is more complex in polymer thin films, and often no clear failure point is reported[42,63].

Qualitative	Quantitative
Cohesive Failure (cohesive chipping, fish scale, parabolic cracking)	Contrast value between scratched and unscratched reaching certain value
Adhesive Failure (adhesive chipping, fragmentation)	Scratch width reaching certain value
Substrate Exposure	Scratch depth reaching certain value
Change in friction coefficient graph	

Table 2: Various Scratch Failure Point Assessment Methods

Overall, the lack of standardization for the nanoscratch test makes it challenging for comparison purposes, ultimately making it only a semi-quantitative test. For the nanoscratch test to output valid and reproducible results for comparative thin film adhesion studies, the following requirements should be met:

1) Well-defined failure mechanism chosen as the critical point
2) Adhesion related failure mode is observed and clearly verified in optical microscopy, SEM or FIB
3) Consistent scratch parameters (dL/dx ratio)

1.5. Introduction to Cohesive Zone Modelling

While many studies discussed so far highlight the importance of combining experimental techniques with finite element modelling to understand thin film mechanical behaviour, an important additional consideration is the ability to simulate crack initiation and interfacial delamination. Cohesive zone modelling (CZM) is particularly well suited for capturing such damage and separation processes. This section therefore reviews the existing

literature employing CZM for modelling cracking and delamination in thin film and coating systems.

Crack modelling is crucial in fracture mechanics for predicting and analysing crack initiation, propagation, and failure in materials. Traditionally, crack modelling approaches have been categorized into two main types: linear elastic fracture mechanics (LEFM) and nonlinear fracture mechanics. LEFM assumes that materials behave elastically up to the point of fracture and uses parameters like stress intensity factors and energy release rates to predict crack growth. Of the LEFM methods, Griffith's fracture theory[94] has been one of the most widely used. However, in many practical applications, materials exhibit significant plasticity or other nonlinear behaviours before fracture occurs. Additionally, the presence of an initial crack is required in LEFM analysis. To address these complexities, nonlinear fracture mechanics approaches, such as the J-integral and the cohesive zone model (CZM), have been developed[95].

Among these techniques, cohesive zone modelling is most commonly used due to its ability to simulate the entire fracture process from crack initiation to propagation[96,97]. In CZM, fracture is considered to occur along the crack tip, with the surfaces resisted by cohesive tractions. Unlike traditional methods that treat fracture as a sudden event, CZM uses a traction-separation law to relate the stresses in the cohesive elements to the separation size of the crack, offering a more accurate representation of the fracture process. Common traction-separation laws include linear, polynomial, or exponential models, with the simplest and most commonly used being the triangular bi-linear shape, which assumes linear-elastic behaviour in the initial phase, as shown in Figure 18.

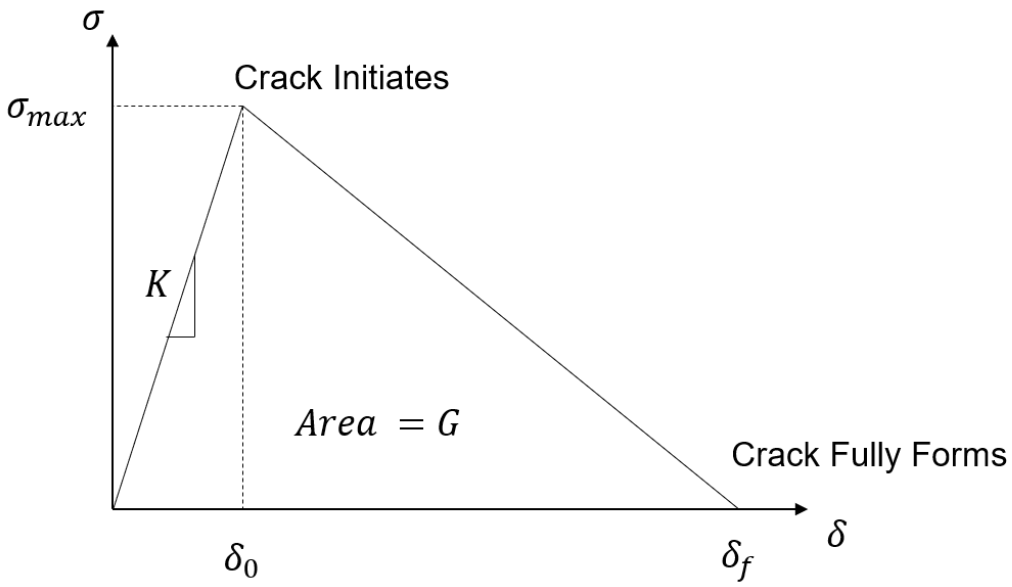


Figure 18: Triangular bi-linear traction separation law

The stresses in the interface increase linearly from zero, reaching a maximum stress value (σ_{max}) at a separation value of δ_0. The slope of the initial portion of the curve represents the elastic stiffness K of the interface. Damage initiation begins when the value of the maximum nominal stress (MAXS) ratio in equation (31) reaches a value of 1:

$$\max\left\{\frac{\langle t_n \rangle}{t_n^0}, \frac{t_s}{t_s^0}, \frac{t_t}{t_t^0}\right\} = 1 \qquad (31)$$

In this equation t_n^0, t_s^0, t_t^0 represent the peak values of the nominal stress normal to the interface, first and second shear directions indicating mode I, II and III failure respectively. For simplicity, the values are assumed to be equal in all three directions. The Macaulay brackets in the normal stress portion indicate that the damage is not initiated in pure compression. This is essential for understanding ABAQUS modelling results.

Following damage initiation, the traction decreases linearly until reaching a final separation of δ_f, where the crack fully opens. The area under the curve is the damage evolution

criteria equal to the interfacial fracture energy, or delamination energy G. Similar to the maximum nominal stress, the damage evolution criterion is satisfied when:

$$\left\{\frac{G_n}{G_n^C}\right\}^\alpha + \left\{\frac{G_s}{G_s^C}\right\}^\alpha + \left\{\frac{G_t}{G_t^C}\right\}^\alpha = 1$$

(32)

Here G_n^C, G_s^C, G_t^C represent the critical fracture energies in the three directions. The power law can be simplified by assuming alpha equal to 1 and assuming the three fracture energy values to be equal in all directions. The extent of damage evolution is represented in ABAQUS by the scalar parameter SDEG, calculated as:

$$SDEG = \frac{\delta(\delta_{max} - \delta_0)}{\delta_{max}(\delta_c - \delta_0)}$$

(33)

SDEG ranges from 0 for undamaged elements to 1 for fully damaged elements. Element deletion can be enabled in ABAQUS to remove fully damaged cohesive elements. The scalar value MAXD, which represents the maximum degradation, is set to 1 by default, enabling element deletion in elements that reach an SDEG value of 1. In mesh controls, the value of MAXD can be reduced to a smaller value (e.g.: 0.9) to allow for less strict deletion conditions.

1.5.1. Cohesive Properties Selection Guidelines

The values of the three parameters: maximum stress σ_{max}, fracture energy G and stiffness K were carefully chosen to ensure the model accurately reflects the material behaviour. The parameter selection guide provided by Dassault (ABAQUS)[98] explains that the fracture energy is the most important parameter that affects the results. Following that, the maximum stress is the next most important, while the stiffness value has the least dependence on the overall results.

The fracture energy (G), can be measured using a wide range of experimental methods including peel tests, nanoindentation and nanoscratching. When the interfacial strength (σ_{max}) is not known, it can be treated as a penalty parameter and calculated from the fracture energy as:

$$\sigma_{max} = \frac{2G}{\delta_f} \tag{34}$$

The value of δ_f is usually set to be some fraction of the cohesive element length ranging from 5-100%, depending on the material properties and model conditions[99,100]. Theoretically, the stiffness of the cohesive layer should be set to an infinite value due to the infinitesimally thin nature of the layer. However, in ABAQUS, this is not numerically feasible. If the stiffness is set too low, the cohesive layer will behave compliantly, negatively affecting the simulation results. Conversely, setting the stiffness too high can cause numerical issues and convergence problems. Ideally, the stiffness should be as high as possible without causing solving errors. In this work and in literature, it has been found that the exact value of the interface stiffness does not impact the cohesive element behaviour, as long as compliant behaviour is avoided[98,101,102].

1.6. Review of Reported Delamination Energies

Table 3 summarizes a range of reported delamination energies for ceramic, metallic and polymer thin films. The analysis method and experimental method used to determine the delamination energies are also summarized.

Film/Substrate	**Delamination Energy (J/m^2)**	**Experimental Method**	**Analysis Method**	**Ref.**
Ceramic Films				
SiN/GaAs	0.7 – 2.59	Nanoindentation	Griffith	80
SiOC/Si	13 - 23	Nanoindentation	Irreversible Work	55
Si_3N_4/BPSG/Si	1.13 – 1.36	Nanoindentation	Hutchinson and Suo	59
SiOCH/SiCN	1.68	Nanoindentation	Marshall and Evans	60
ITO/ glass	32 - 36	Nanoindentation	Irreversible Work	81
MTMS-colloidal silica/glass	11 - 21	Nanoindentation	Irreversible Work	50
MTMS-Ludox/glass	85 - 290	Nanoindentation	Irreversible Work	50
Sol gel/glass	1.5 - 4	Nanoindentation	Thouless	57
Sol gel/glass	1.5 – 2.5	Nanoscratch	Thouless	57
SiOCH/SiCN	0.91	Nanoscratch	Laugier	60
Metallic Films				
Cu/Glass	2 - 4	Nanoindentation	Hutchinson and Suo	82
Cu-Ru/Si	0.57	Nanoindentation	Modified Marshall and Evans	45
W/Si	16 – 20	Micro-wedge Indentation	Marshall and Evans	83

W/Si	6 - 11	Nanoindentation	Marshall and Evans	44
W-Cr(superlayer) /Si	3 - 5			
Cu/Si	0.2 – 2			
Au/glass	0.16	Nanoscratch	Laugier	62
Polymer Films				
PI/Si	200	Nanoindentation	Power Law	49
Functionalized polymer/glass	26 - 95	Nanoindentation	Power Law	52
PET/ITO	24.6	Nanoindentation	Power Law	53
PMMA/epoxy	0.3 - 0.4	Nanoscratch	Laugier	63
PMMA/epoxy	1.2 – 6.6	Nanoscratch	Burnett	63
PVA/Si	0.4*	Nanoscratch	Laugier	42
PVA/PET	8.5*	Nanoscratch	Laugier	42

*Table 3: Summary of delamination energies found in literature for various thin film systems through nanoindentation and nanoscratching. *: calculated from adhesive strength. Range of delamination energies refers to variations due to thickness and/or fabrication conditions.*

1.7. Outline of thesis

This literature review highlighted the importance of interfacial characterization for the performance and longevity of solid-state batteries. Further development of experimental delamination energy assessment methods, such as nanoindentation and nanoscratching is essential to ensure accurate interfacial evaluation.

In Chapter 3, a tungsten thin film on silicon is used as a reference to develop both nanoindentation and nanoscratch techniques. The brittle nature of tungsten makes it an ideal material for method development, as delamination is clearly visible in both tests. Furthermore,

delamination energy values for tungsten on silicon are well documented in the literature, providing a basis for validating the experimentally determined values. Improvements to the analysis method through finite element modelling (FEM) are also introduced. This chapter examines the limitations and sensitivity of both techniques before applying them to more complex materials, such as polymers and battery ceramics, in the following chapters.

In Chapter 4, the mechanical properties and delamination energy of two battery polymer films are studied. Due to polymers' viscoelastic nature, an alternate energy analysis method different to that used in Chapter 3 was required. The accuracy and limitations of this method were further examined using finite element modelling (FEM). FEM was also employed to investigate the influence of material properties on the observed deformation behaviour (plastic deformation vs delamination), with the aim of developing a nanoindentation deformation map, facilitating future failure predictions based on mechanical properties. Finally, the experimental data was compared to FEM and literature values to assess the most appropriate testing method.

In Chapter 5, ceramic LLZO thin films deposited on two different substrates (silicon and NMC) are investigated. The effects of film thickness, substrate and annealing on the film mechanical properties and delamination behaviour were investigated. A charging electrolyte-coated cathode particle undergoing volume contraction was modelled to determine the minimum delamination energy required to prevent delamination for various electrolyte material properties. This allowed for the delamination energy values to be contextualized within the solid-state battery application.

Overall this thesis investigates the delamination behaviour of three classes of materials (polymers, metals and ceramics) and provides a comprehensive overview of the analysis models appropriate for each.

2. METHODS

2.1. Characterization Techniques

2.1.1. Scanning Electron Microscopy (SEM)

Scanning Electron Microscopy (SEM) is a powerful surface characterization technique due to its high magnification and resolution capabilities (Figure 19). In this work, SEM was extensively used to observe the indents and as a complimentary technique to focused-ion beam milling. SEM operates by using electrons instead of light (as in a conventional optical microscope) to form images. Electrons are generated which are accelerated towards the sample. Next, a series of condenser and objective lenses work to focus the beam onto the sample surface. Scan coils are used to control the horizontal and vertical (x-y) position of the beam, allowing the beam to scanned over the surface. Once the electrons reach the sample, three types of signals are generated including: secondary electrons (SE), backscattered electrons

(BSE) and characteristic x-rays which are captured by separate detectors and converted into an image using specialized software.

SE are low-energy electrons generated closest to the surface that give information about the surface of the sample with high resolution. For most imaging applications, this type of imaging mode is used. BSE include elastically scattered electrons that are higher energy compared to SE. These types of electrons are used to distinguish between areas with different elemental compositions, as heavier elements appear brighter due to the higher number of electrons scattered. As the electron beam hits the sample, inner shell electrons are ejected leaving a vacancy. The vacancy is then filled by an outer shell which in turn releases a characteristic x-ray, equal to the energy difference between the two electron shells. The composition of the material can be known from these characteristic x-rays through energy dispersive x-ray spectroscopy detectors (EDS).

Non-conductive samples used in this work (polymers and ceramic films) required a conductive coating in order to avoid charging effects and produce better images. In this work, these samples were coated using a 4 nm thick layer of platinum. Additionally, a low accelerating voltage of 3 kV was needed to image the polymer films as bubbling and degradation was observed at higher kV (5 kV).

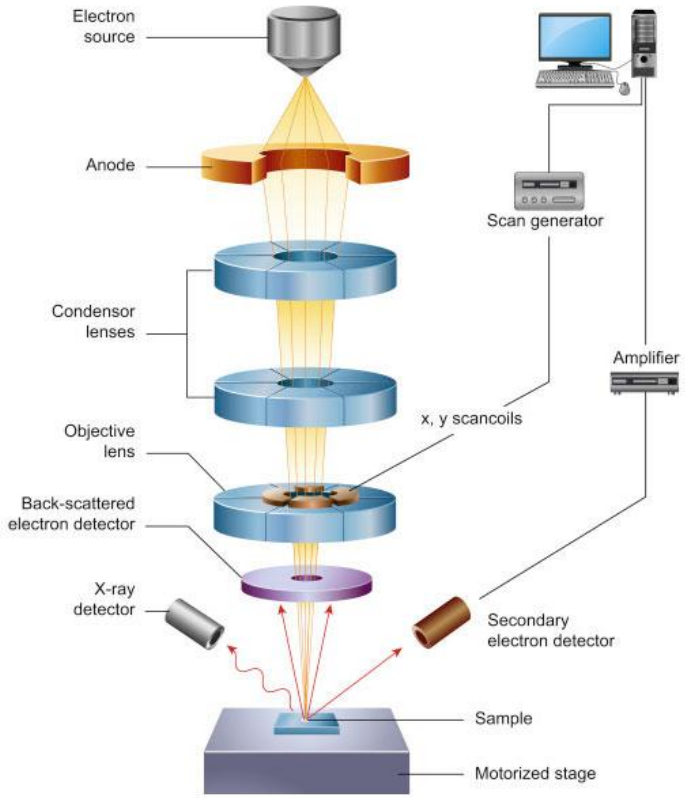


Figure 19: Schematic of SEM setup including the three types of detectors (taken from Nanoscience [84])

2.1.2. Focused Ion Beam (FIB)

Focused Ion Beam (FIB) milling is an important secondary technique employed in this work to observe the interface below the indents and scratches and to measure the thin film thickness. This thesis highlights the importance of FIB for directly observing delamination, which is often overlooked in literature. A combined FIB/SEM setup was used in this work using the Zeiss Auriga, as shown in Figure 20.

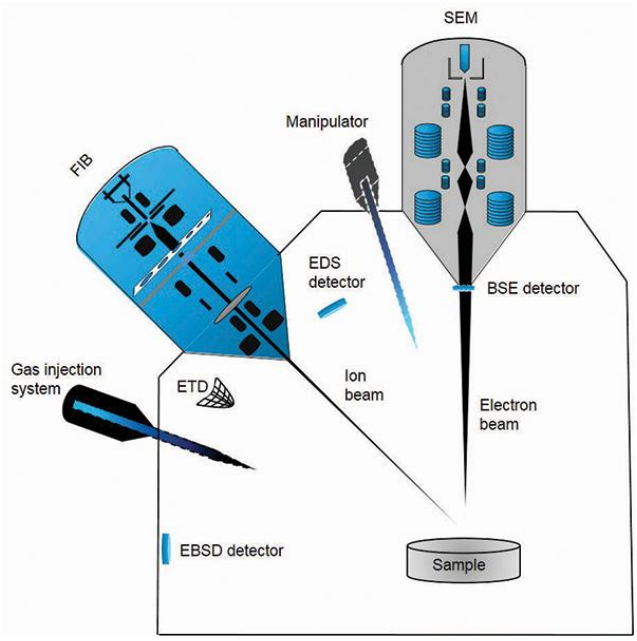


Figure 20: Schematic of a combined SEM/FIB setup (taken from Wolff[85])

To simultaneously use SEM and FIB, the sample is tilted at 54° with respect to the SEM, allowing the sample surface to be perpendicular to the FIB. Instead of using electrons, FIB instead operates using a beam of ions to image and mill the sample. The ions are generated using a liquid metal ion source (LMIS), usually gallium. The positive gallium ions are then accelerated and focused towards the sample to sputter the surface. A gas injection system (GIS) is often included with FIBs to allow in-situ deposition of metal or insulator coatings on the sample. FIB imaging is usually conducted at low currents in order to preserve the sample integrity. The FIB milling process relies on increasing the accelerating current, which enables controlled material removal, allowing for the precise milling of specific geometries. Typical values for imaging and milling currents are 50 pA and 4 nA respectively. Since the sample is tilted with respect to SEM, tilt correction at 36° (angle between electron beam and sample) is necessary to allow for accurate thin film thickness measurements which were analysed in ImageJ software. A FIB milling current of 30kV.4nA was used for all samples, at a depth target of 4–5 µm. GIS was not used in this work as the entire sample surface was pre-coated with platinum.

2.1.3. X-ray Diffraction (XRD)

X-ray diffraction (XRD) is a powerful technique used to analyse a material's crystal structure. In this technique, x-rays are produced by a tungsten filament and filtered through a monochromator to result in x-rays with a single wavelength (monochromatic). The x-rays that reach the sample, interact with the electrons around the atoms, resulting in x-ray scattering. Because the x-rays are scattered in all directions, they can interact with one another leading to both constructive and destructive wave interference. Bragg's law is a fundamental equation in XRD describing the conditions for constructive interference as[86]:

$$n\lambda = 2dsin\theta \tag{35}$$

Where n is an integer, λ is the wavelength of the x-ray, d is the interplanar spacing (distance between two adjacent (hkl) atomic planes), and θ is the angle of incidence. Constructive interference results in a diffraction pattern that is unique to each material. Libraries of known diffraction patterns allow the pattern to be attributed to a specific material. By measuring the diffraction angle θ, the interplanar d spacing can be found through equation (35). The intensity of each diffraction peak is influenced by factors such as the atomic arrangement, the type of atoms, and the crystallographic orientation (texture) of the sample. Analysing peak intensities can provide information on the relative abundance of different phases, preferred orientation, and information about crystal size and residual strain.

2.2. Thin Film Fabrication Techniques

2.2.1. Physical Vapor Deposition (PVD)

Physical vapor deposition (PVD) is a widely used thin film deposition technique carried out in vacuum, which is required to minimize contaminants and to allow precise control

of deposition conditions. Many variations of the PVD process exist including cathodic arc deposition, evaporative deposition, pulsed laser deposition and sputter deposition. The differences between each are attributed to how the material vaporization and deposition are carried out. Sputter deposition involves a sputtering target, sputtering gas (inert gas such as Argon) and a substrate (Figure 21). The sputtering target involves the material that is to be made into the thin film coating. A high voltage is applied between the sputtering target and the substrate, causing ions from the target to be accelerated toward the substrate. The final film thickness is dependent on the sputtering time and material. In this work, this method was used to fabricate the tungsten and LLZO thin films.

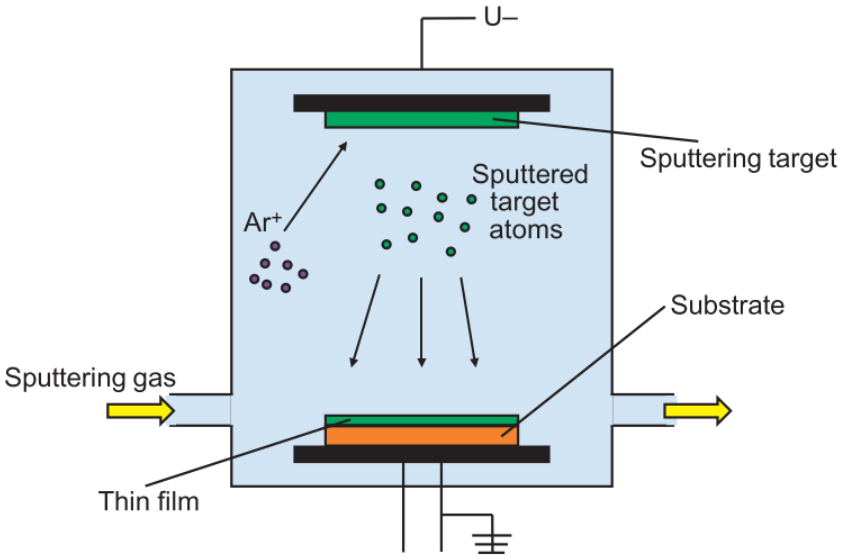


Figure 21: PVD setup (taken from Faraji, 2018 [87])

2.2.2. Solvent Casting

Solvent casting is a widely used method for fabricating polymer films due to its simplicity, versatility, and ability to produce films with uniform thickness and composition. The process involves dissolving a polymer in a suitable solvent to create a homogeneous polymer solution. This solution is then deposited onto a substrate placed into a mold, through either spin coating, dip coating, or drop casting, depending on the desired film thickness and

uniformity. In this work, this method was used to fabricate the polymer (P1 and PEO) thin films.

2.3. Mechanical Testing Techniques

2.3.1. Nanoindentation

Nanoindentation experiments were conducted using a Bruker Premier nanoindenter equipped with a Berkovich diamond tip. The tip area was determined to ensure precise mechanical properties measurements. The area function calibration was performed using fused silica. Since the reduced modulus of fused silica is known (69.6 GPa), the tip contact area can be determined as:

$$A = \frac{\pi}{4}\left[\frac{S}{E_r}\right]^2 \tag{36}$$

100 indents with increasing loads from 100 to 11,000 μN for the low load head, and 1 mN to 1,000 mN for the high load head were performed on the fused silica reference sample with a load profile of 5 second loading, 2 second hold and 5 second unloading as recommended in the Premier manual. The data was then fit to polynomial of the sixth order to obtain the tip area:

$$A = C_0 h_c^2 + C_1 h_c + C_2 h_c^{1/2} + C_3 h_c^{1/4} + C_4 h_c^{1/8} + C_5 h_c^{1/16} \tag{37}$$

Where the coefficient C_0 is fixed and is set to 24.5 for a Berkovich tip.

Both quasi-static (QS) and continuous stiffness measurement (CSM) modes were used depending on the experimental objective. QS indentation was employed for shallow measurements to determine hardness and modulus using the Oliver–Pharr method. In contrast, CSM mode was used primarily for polymeric films to capture depth-dependent mechanical

properties such as storage modulus and hardness throughout the loading cycle. CSM was also used as a supplementary method to estimate thin film thickness based on the depth at which a modulus plateau was observed. Detailed QS and CSM parameters are provided in the experimental setup sections of each chapter.

Two primary challenges were addressed when determining mechanical properties: substrate effects and pile-up. Substrate influence on the measured modulus was assessed by evaluating trends with increasing indentation depth, and applying corrections using the Saha and Nix[33] model, as discussed in Chapter 1. Hardness values corrections were not required, as they are less sensitive to substrate effects as compared to the modulus.

For the polymer films, which exhibited significant pile-up, a correction method proposed by Kese and Bergman[91] (described in Chapter 1) was applied. Pile-up profiles and heights were obtained using Scanning Probe Microscopy (SPM), which is integrated into the nanoindenter system. The same indenter tip was used to scan the surface after indentation, generating topographical maps similar to atomic force microscopy without requiring separate instrumentation or setup.

2.3.2. Nanoscratch

Nanoscratching was conducted using the same setup as nanoindentation, with scratches made under either constant or ramped force. Constant load scratches are useful for determining the sample's coefficient of friction at low loads and provide reliable data on critical load for adhesion testing, though they are time-consuming to perform at multiple loads. Ramped load scratches are quicker, requiring only a single scratch to determine critical load values, and are more commonly used for adhesion testing.

A typical ramped force with tilt correction load profile is given in Figure 22. To correct for sample tilt, a pre-scan scratch is performed at a low load sufficient to capture the tilt of the

scratch path without causing plastic deformation. Following a short stabilization period, the scratch is then executed by ramping the load from zero to the defined peak load.

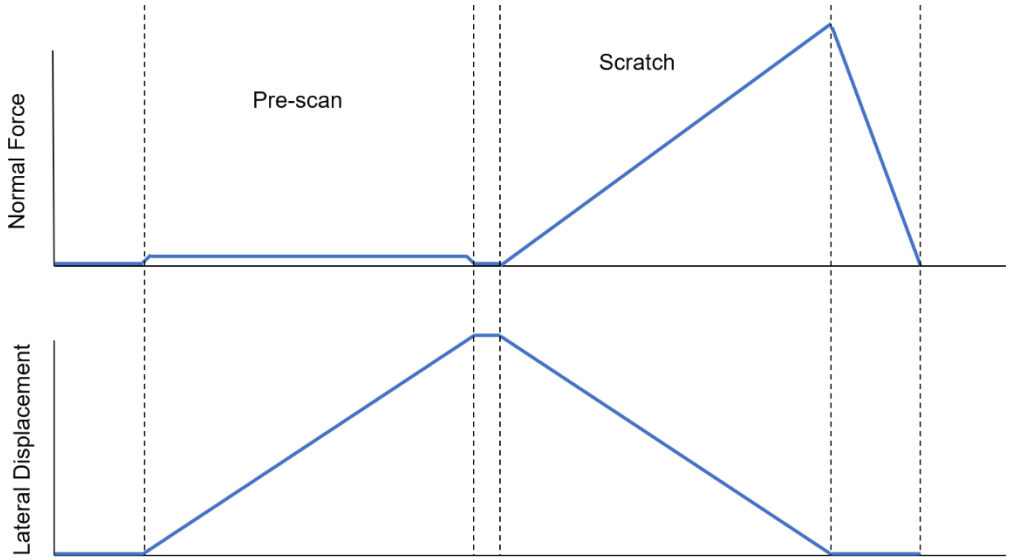


Figure 22: Ramped scratch with tilt correction load function

In the Bruker software, the tilt is corrected by selecting the pre-scan region, calculating the slope, and zeroing this region through linear interpolation. While this method of linear interpolation effectively corrects for surface tilt, it does not account for high surface roughness. Additionally, Bruker's software does not allow the normal displacement values to be re-saved after tilt correction, so in this work, the critical normal displacement at failure was obtained from the software but could not be plotted.

To change the scratch tip orientation, the sign of the lateral displacement was adjusted to alter the direction of the lateral displacement graph. Positive values of lateral displacement resulted in edge forward orientation, while negative lateral displacement resulted in face forward orientation as in Figure 23. The indenter tip is not screwed into the transducer with perfect alignment; therefore, it was found that the scratch orientation was not perfectly perpendicular as in the schematic. However, the tip orientation remained consistent in each test, as the tip was always mounted in a consistent manner.

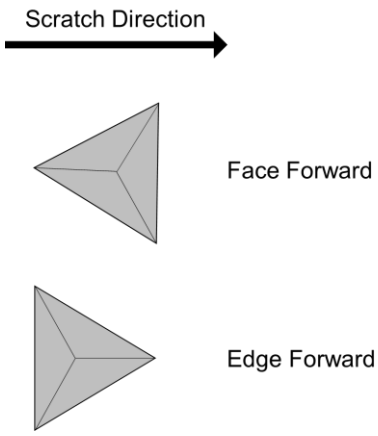


Figure 23: Face forward and edge forward orientations of a Berkovich tip

2.4. Adhesion Testing

Adhesion testing was conducted using the same diamond Berkovich tip as used in nanoindentation and nanoscratch. Although sharper geometries such as cube-corner indenters are known to promote earlier crack initiation and are often used in fracture studies, a Berkovich indenter was selected in this work to ensure stable contact conditions, repeatable measurements across polymers, metals and ceramics, and direct comparability with the majority of published nanoindentation and nanoscratch literature. In addition, the Berkovich geometry provides a representative elastic–plastic stress field suitable for quantitative modulus and hardness extraction and for calibration of the finite element models used in this thesis.

2.4.1. Nanoindentation Adhesion

To evaluate the thin film delamination energy through nanoindentation, the two energy-based methods discussed previously in Chapter 1 were employed. The power curve extrapolation method was used for analysing delamination energy in polymer thin films, while the irreversible work method was applied to tungsten and LLZO thin films. Indents with a 5-2-5 load profile were used. A long hold time was avoided in the adhesion indents as the value

of delaminated area increases during the hold segment, leading to inaccurate delamination energy values.

The power law extrapolation method described by Omiya[48,49] was employed to analyse the polymer thin films. The loading curve was extrapolated either before or after the onset of delamination, which was indicated by a sudden deviation in the loading curve. The effect of extrapolating before or after delamination is discussed in Chapter 4. In both cases, the loading curve was analysed in MATLAB and the data was fit to the following power law relationship:

$$P = ah^b + c \tag{38}$$

Where a, b, c are fitting constants. Next, the difference in areas between the fitted curve and the experimental curve was calculated as the work of delamination (W_d). In the polymer films, the indents did not display clear delamination areas and FIB cross-sectioning was required. The delamination radius was measured in ImageJ software as seen in Figure 24, and the delamination area (A_d) was assumed to be a perfect circle. The delamination energy (G) is then calculated as:

$$G = \frac{W_d}{A_d} \tag{39}$$

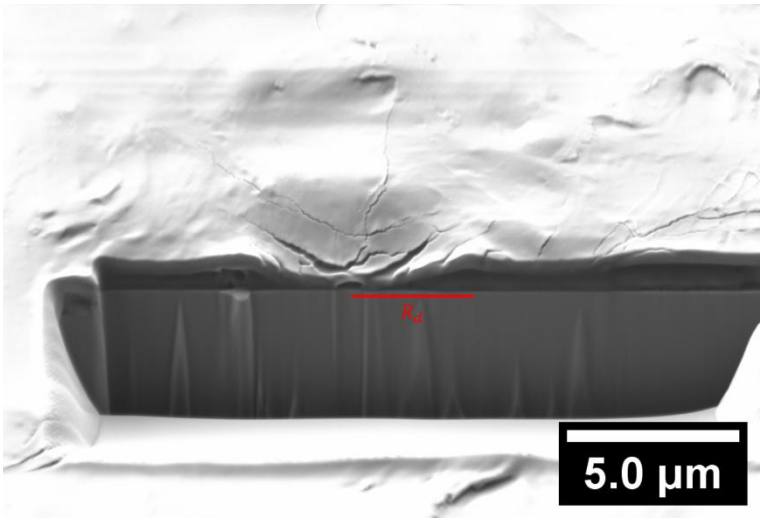


Figure 24: Radius of delamination measurement from FIB (polymer film)

To analyse the brittle films, the method described by Malzbender[50] was used. The irreversible work (area enclosed by the load displacement curve) was calculated in MATLAB and plotted as a function of the maximum applied load. Brittle films undergo three deformation stages, namely plastic deformation (stage I), delamination (stage II) and film fragmentation (stage III). The total irreversible work in each stage is calculated as:

$$Stage\ I: W_{irr} = W_p \tag{40}$$

$$Stage\ II: W_{irr} = W_p + W_d \tag{41}$$

$$Stage\ III: W_{irr} = W_p + W_d + W_f \tag{42}$$

The thick brittle films (>1 µm) tested in this work showed clear delamination areas that were easily calculated from SEM or optical microscopy without the need of FIB as seen in Figure 25. On the other hand, the thin brittle films (< 1 µm) needed FIB cross-sectioning to determine the delamination radius, similar to the polymer films.

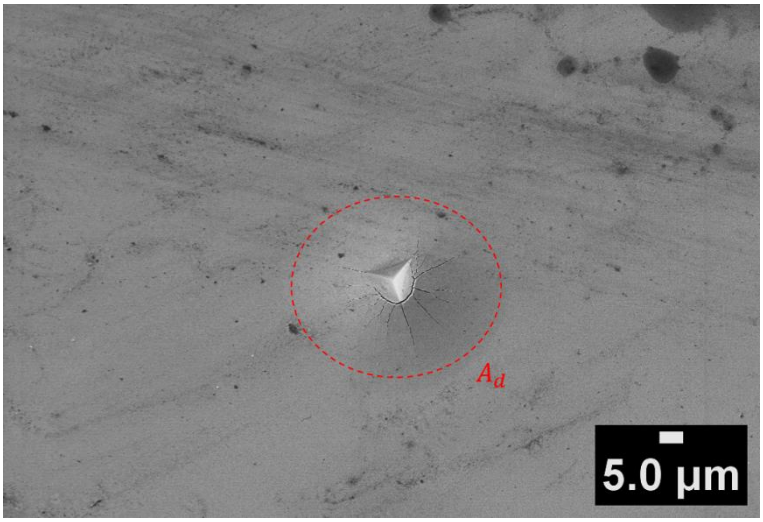


Figure 25: Area of delamination measurement (tungsten film)

In the original work by Malzbender, the plastic work is linearly extrapolated from stage I to stage II to determine the work of delamination. A finite element (FE) nanoindentation model was employed to obtain more accurate values of plastic work, thereby improving the accuracy of the calculated delamination energies. The FEM plastic work corrections were performed on a thin film model with thicknesses corresponding to the experimental films. The film Young's modulus and hardness were either determined from nanoindentation or in the case of tungsten films where significant substrate effects could not be fully corrected for, the values were obtained from literature. The Poisson's ratio for all films was also obtained from literature. The yield strength was initially estimated from the nanoindentation hardness as[32]:

$$\sigma_y = \frac{H}{C} \tag{43}$$

Where C is the constraint factor ranging from 1.5 for materials with low E/σ_y ratios, to 3 for materials with high E/σ_y ratios. The yield strength was then slightly adjusted from the initial estimate to match the FEM irreversible work values in the plastic stage (stage I) with those from the experimental data.

2.4.2. Nanoscratch Adhesion

Nanoscratch adhesion was analysed using the equations described by Laugier[62]:

$$\sigma_{adh} = \frac{2L_c}{\pi d_c^2}\left(\frac{(4+\nu_f)3\pi\mu}{8} - (1-2\nu_f)\right) \quad (44)$$

$$G = \frac{\sigma_{adh}^2}{2E_f}t \quad (45)$$

Here E_f is the Young's modulus of the film, σ_{adh} is the compressive stress in the coating at failure, t is the coating thickness, L_c is the critical load, d_c is the scratch width at failure, μ is the coating coefficient of friction, ν_f is the coating Poisson's ratio.

A clear deviation in friction coefficient, normal displacement and lateral force graphs was observed in the thick brittle films, indicating the critical point. This was assessed alongside the residual scratch image to ensure that the identified critical point corresponded to delamination or fracture. When no clear scratch deviation was observed in the graphs, the critical point was assessed visually. The coefficient of friction for each film was determined from low load scratches (<10 mN) ensuring minimal contribution from material removal or ploughing friction. As explained in Chapter 1, the coefficient of friction is determined as the ratio of the lateral and normal forces during scratching. The scratch width at failure was calculated from the contact depth as follows:

$$d_c = \frac{2h_c}{tan\alpha} \quad (46)$$

Where h_c is the contact depth and α is the effective cone angle. Equation (46) was required to analyse the tungsten films as the scratch width could not be measured visually after fragmentation. The validity of the equation was investigated using a scratch with peak load 30

mN on the 1.9 µm tungsten-silicon film (Figure 26). This peak load is less than the critical load, so no fragmentation took place, and the scratch width at the end of the scratch path was measured through optical microscopy to be 2.24 µm. Using the contact depth from the Bruker software after incorporating tilt correction (428 nm), a scratch width of 2.71 µm was calculated. This demonstrates that equation (46) can accurately determine scratch width from contact depth.

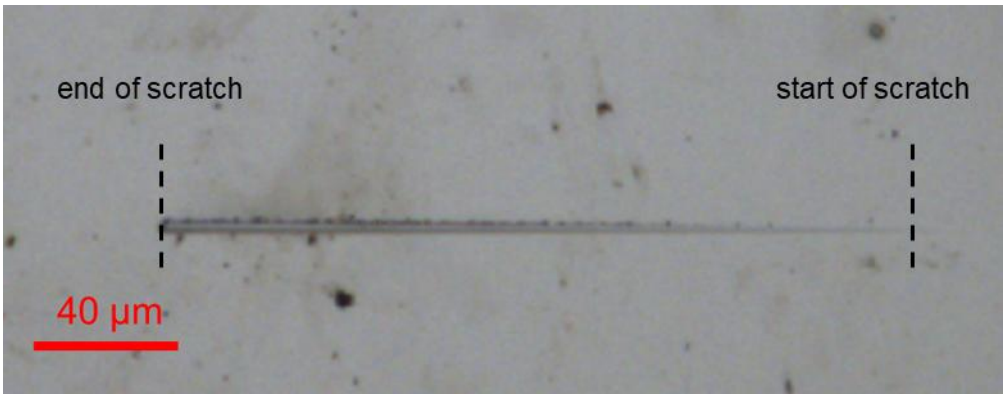


Figure 26: Scratch at 30 mN peak load

2.5. Finite Element Modelling

Nanoindentation and thin film delamination were modelled using ABAQUS. Two types of finite element models were developed: nanoindentation simulations without cohesive zone modelling (CZM) (used in Chapters 3 and 5), and those incorporating CZM to simulate delamination behaviour (used in Chapters 4 and 5).

In Chapter 3, nanoindentation of a tungsten thin film on a silicon substrate was simulated without CZM, as the goal was to extract the irreversible plastic work from Stage I deformation (prior to delamination). This was achieved using a 3D model representing 1/6th of the full geometry, leveraging symmetry around the indentation axis. The mesh design, boundary conditions, and material parameters are detailed in the methods section of Chapter 3.

In Chapter 4, a 2D axisymmetric model incorporating CZM was created. A bilinear traction–separation law, introduced in Chapter 1, was used to describe interfacial damage

evolution under increasing load. Thin film and interface properties were parametrically varied to study their influence on whether plasticity or delamination dominated. Full simulation details are provided in the methods section of Chapter 4.

In Chapter 5**,** a model similar to that used in Chapter 3 was employed to extract the irreversible work for LLZO films. Additionally, a 2D axisymmetric simulation was developed to represent a shrinking cathode particle during battery cycling. The cathode was treated as a central particle coated with a solid electrolyte shell, with a cohesive interface layer in between. This interface was governed by a bilinear traction–separation law, consistent with the cohesive zone approach described in Chapter 4. This model connects the findings of the thesis to practical battery operation by estimating the minimum interfacial toughness required to avoid delamination. Full details of material properties, mesh design, and boundary conditions are provided in the methods section of Chapter 5.

3. METHOD DEVELOPMENT ON TUNGSTEN FILMS

3.1. Aim

The aim of this chapter is to establish the method of quantifying adhesion through nanoindentation and nanoscratching on a tungsten on silicon thin film. This sample was chosen because tungsten undergoes brittle deformation at room temperature which allows for the delamination and failure to be more clearly observed compared to polymers, which undergo plastic deformation. Additionally, tungsten on silicon has been extensively studied in literature with known delamination energy values (G = 5 - 15 J/m^2)[44,83,103]. These values were used as a benchmark to ensure the accuracy of the methodology employed in this thesis. Even though tungsten thin films are not used in solid-state batteries, they are an important aspect in the semiconductor and nuclear fusion industries, making them relevant in the energy storage space. Furthermore, the literature comparing nanoindentation and nanoscratching delamination energies is extremely limited in number[57,60]. Therefore, a comprehensive understanding on the

delamination energy values obtained by both methods is required. Parametric studies have been conducted to further understand the effect on measured delamination energy in both methods. An energy approach was chosen as the route of nanoindentation indent analysis for the films since this could be extended to both brittle and ductile films with some variations to the analysis method. Additionally, finite element modelling has been used to improve on existing nanoindentation delamination analysis.

3.2. Materials and Methods

3.2.1. Thin Film Fabrication

The thin films were fabricated by Matthew Lloyd (Department of Materials). Tungsten was deposited onto silicon substrates using magnetron sputtering in a custom sputtering system equipped with two axially mounted AJA ST20-HV radio frequency (RF) sputtering guns. The substrates were mounted onto a central target block which gave a target-substrate distance of 18 cm. The films were deposited onto (100) orientated p-type doped silicon substrates with thicknesses between 650-700 μm, that were first rinsed with acetone, isopropanol, and deionised water and dried with compress nitrogen. A 51 mm diameter tungsten target with a purity of 99.95% was used with an RF power of 100 W. The substrates were loaded into the sputtering chamber which was evacuated until a base pressure of $1x10^{-4}$ Pa was reached. Deposition was performed for a total of 6978 seconds with an argon working gas pressure of 2.5 Pa. The substrate was not rotated or externally heated during deposition. The deposition resulted in regions with different thicknesses depending on the position of the sample on the wafer.

3.2.2. Nanoindentation Methodology

Nanoindentation experiments were conducted using a Bruker Premier nanoindenter equipped with a Berkovich diamond tip. Quasi-static (QS) indents were employed in this chapter. To determine the elastic modulus and hardness of the tungsten thin films while minimising substrate influence, a grid of 16 shallow indents was performed at peak loads ranging from 1 mN- 10 mN. A load profile consisting of 5 s loading, 2 s hold, and 5 s unloading was used for all measurements. These shallow indents were selected to ensure that the deformation zone remained primarily within the film. Substrate effects on the measured elastic modulus were evaluated by analysing trends in modulus with increasing indentation depth and applying corrections using the modified King expression developed by Saha and Nix[33]. To initiate interfacial delamination and observe fracture behaviour, two additional grids of 16 indents were performed using the same 5 s loading, 2 s hold, and 5 s unloading profile. Peak loads ranged from 50 mN-400 mN (referred to as low load grid) and from 100 mN-1000 mN (referred to as high load grid). These regimes enabled the identification of distinct deformation and failure stages, including plastic deformation, delamination, and film fragmentation,

3.2.3. Nanoscratch Methodology

Nanoscratch testing was performed using the same Bruker Premier nanoindenter and Berkovich diamond tip as used for nanoindentation. All scratches in this chapter were conducted under ramped load conditions. The initial set of scratches was performed with a peak load of 70 mN, a scratch length of 250 μm, and a scratch duration of 30 s. The critical load for failure was identified from a sudden deviation in the friction coefficient signal. Residual scratches were subsequently examined using SEM to confirm the corresponding failure mode and to distinguish between plastic deformation, delamination, and film fragmentation. To investigate the influence of scratch parameters on the measured critical load and calculated

delamination energy, additional scratches were performed over a range of testing conditions. The peak load, scratch length, and scratch time were systematically varied, and the full set of parameters used is summarised in a separate table. This parametric study enabled assessment of the sensitivity of adhesion measurements to scratch conditions and supported direct comparison with nanoindentation based adhesion results.

3.2.4. Silicon Substrate and Tungsten Film Characterization

The surface topography of the silicon wafer prior to coating was characterised using scanning probe microscopy (SPM). SPM measurements were performed using the integrated scanning probe module of the Bruker Premier nanoindenter, using the same diamond tip and instrument configuration as used for nanoindentation and nanoscratch experiments.

Figure 27 shows the SPM images of the silicon wafer. Some impurities and dust were present on the surface that was cleaned off prior to coating. The mean roughness of the silicon wafer was found to be around 1.5 ± 0.2 nm. Figure 28 shows the load-displacement curves, from which an average Young's modulus of 194.16 ± 1.31 GPa and an average hardness of 13.99 ± 1.56 GPa was found.

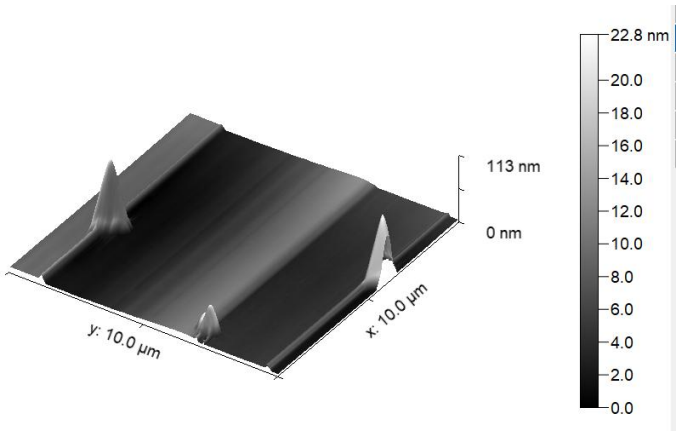


Figure 27: Silicon wafer topography with a measured roughness of 1.5 nm

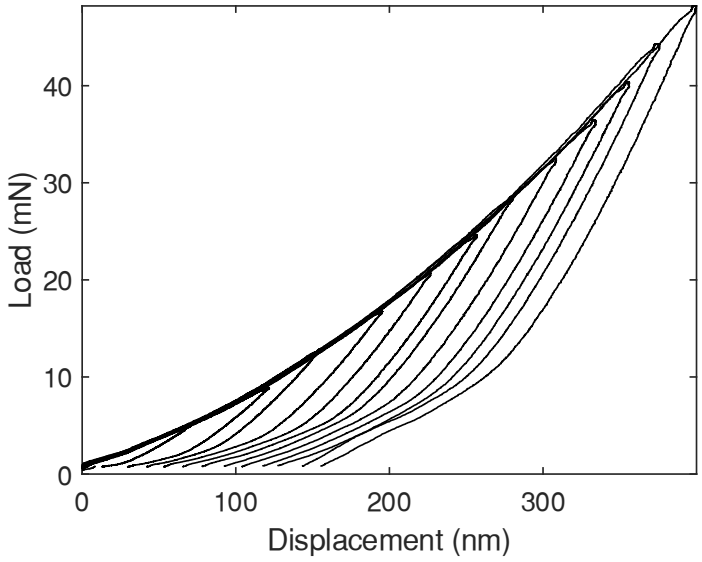


Figure 28: Silicon wafer load displacement curves

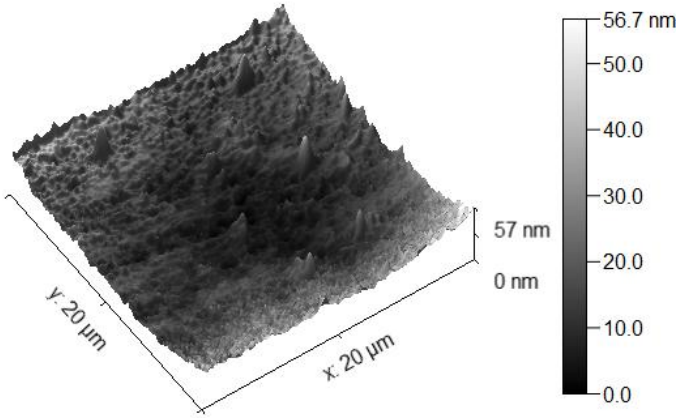


Figure 29: Tungsten film surface topography

SPM images of the tungsten film is shown in Figure 29. The average roughness from 5 SPM images was calculated to be 7 nm. Two samples were cut from the wafer using a diamond scribe in two different areas near the edge of the wafer, and Focused Ion Beam (FIB) cross-section of both is shown in Figure 30. Measurements with tilt corrections (at 36°) revealed the film thicknesses in the two samples to be 1.5 µm and 1.9 µm. No impurities were seen on the surface of the film, and the interface did not contain any irregularities.

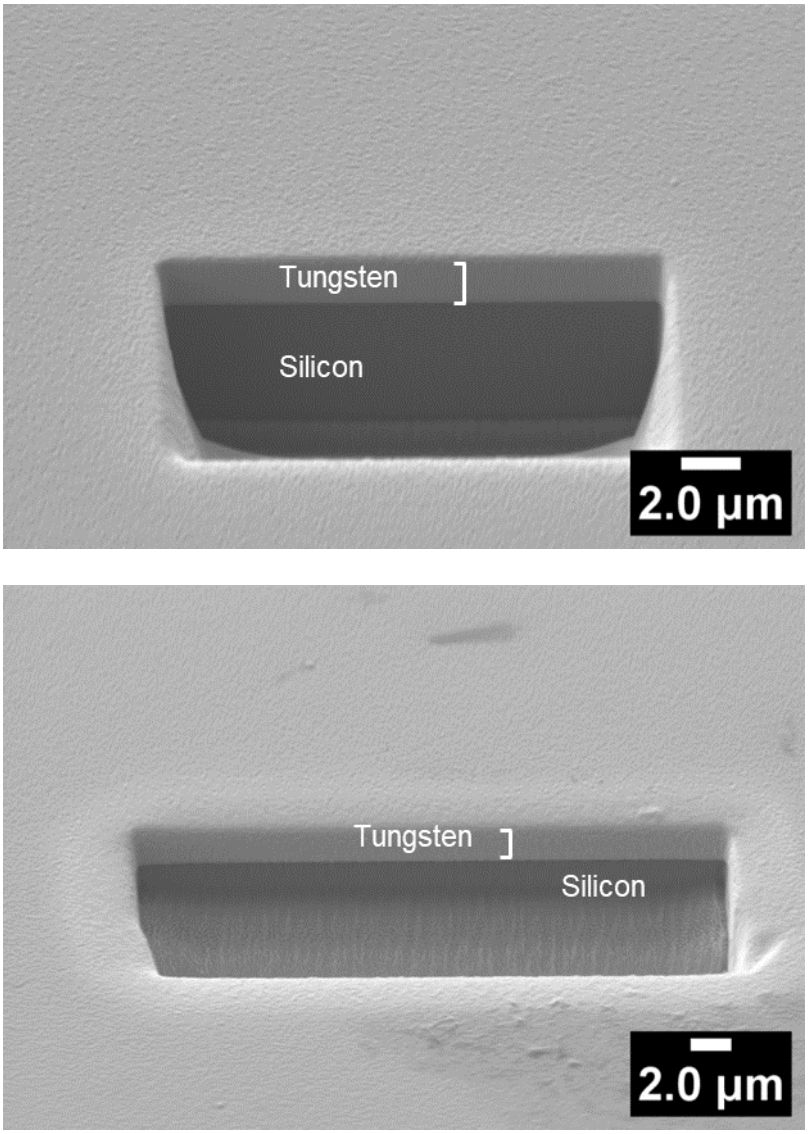


Figure 30: FIB cross-sections of 1.5 µm (top) and 1.9 µm (bottom) films

3.2.5. Finite Element Modelling

ABAQUS was used to model the thin film indentation process. The cohesive behaviour between the film and substrate was not implemented in this model since the aim was to only calculate the irreversible work done by the indenter in stage I (plastic work only). To speed up the computational time, axes of symmetry were implemented and only $1/6^{th}$ of the entire geometry was modelled (Figure 31). Since the model was simulated in displacement control, the outputted force values had to be multiplied by 6 to obtain the force values of the whole model. Linear C3D8R mesh elements were used throughout the model, and the details

of the mesh convergence study is given in Appendix 1. For simplicity and to avoid unnecessary interaction definitions, the thin film system was drawn as one part that was sectioned into a 1.9 µm tungsten layer and a 1 mm thick silicon substrate layer. The material properties used for tungsten and silicon is shown in Table 4. The system was modelled as an elastic-perfectly plastic tungsten on a perfectly elastic silicon substrate. A consistent set of units were used in the model of MPa, µN, and µm. The modulus and yield strength of tungsten were taken from literature for bulk values (E = 410 GPa, σ_y = 750 MPa)[33,83,104]. An estimate of the yield strength was initially obtained from the nanoindentation hardness, however the corresponding load–displacement curves did not align with the experimental data. A yield strength of 750 MPa provided the best agreement with the experimental results (Appendix 2). Tungsten undergoes little to no strain hardening at room temperature due to its BCC structure, therefore this was not implemented in the model[105–107].

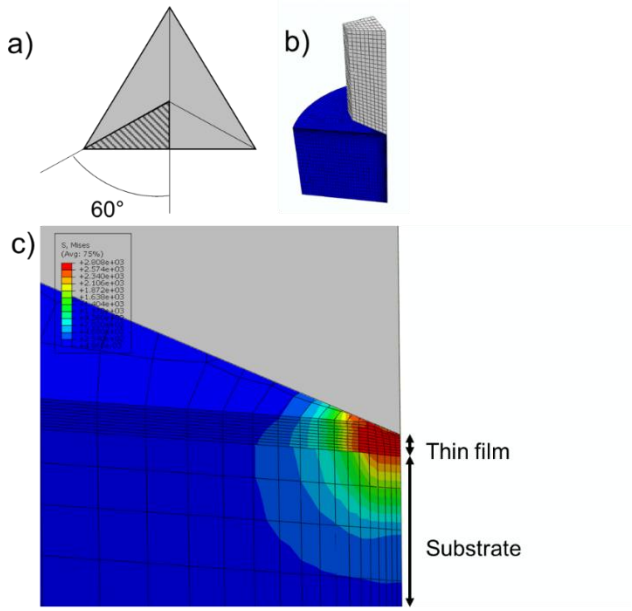


Figure 31: a) The shaded region shows the symmetry axes used. b) and c) show the 3D geometry of model used.

	Young's Modulus (GPa)	**Poisson Ratio**	**Yield Stress (MPa)**
Tungsten	410	0.28	750

Silicon	195	0.3	-

Table 4: FEM Materials Properties

The indenter was modelled as a rigid body, so the diamond mechanical properties did not have to be defined. The interaction between the film and indenter was modelled as hard and frictionless with finite sliding. The boundary conditions used were (in cylindrical coordinates):

1) Indenter:
    - U1 = U2 = UR1 = UR2 = UR3 = 0
    - U3 = displacement (varied from 0.5 – 1.3 μm)
2) Bottom of the substrate
    - U1 = U2 = U3 = UR1 = UR2 = UR3 = 0
3) Sample and indenter in the plane of symmetry
    - U1 = U2 = UR1 = UR2 = UR3 = 0

3.3. Results and Discussion

3.3.1. Hardness and elastic modulus of tungsten thin films

Figure 32 below shows the shallow load displacement curves for the 1.5 μm and 1.9 μm samples. Figure 33 is a plot of the Young's modulus (E) and hardness (H) values as a function of maximum indentation depth. A slight increase in both properties in seen with increasing depths, due to surface effects[108]. Table 5 summarizes the average modulus and hardness values for indents within 10% of the total film thickness (190 nm and 150 nm for the 1.9 μm and 1.5 μm film respectively).

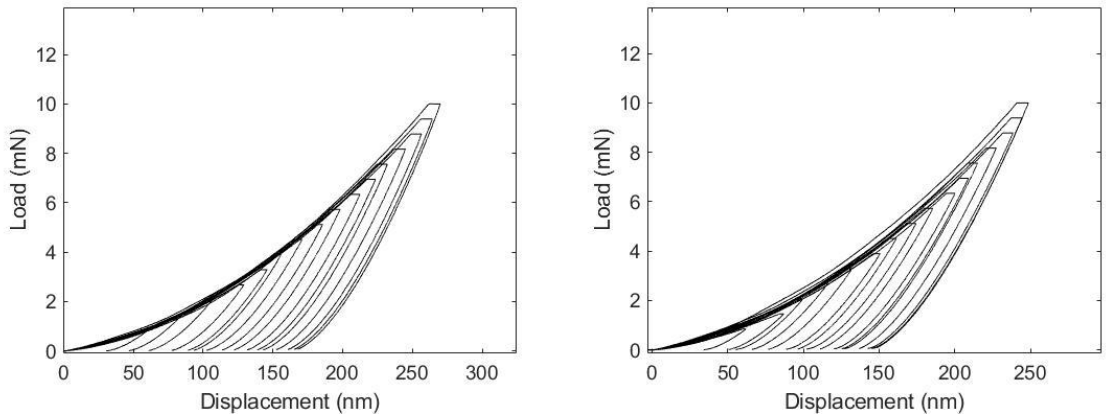


Figure 32: Shallow quasi-static load-displacement curves 1.5 µm (left) and 1.9 µm (right) film

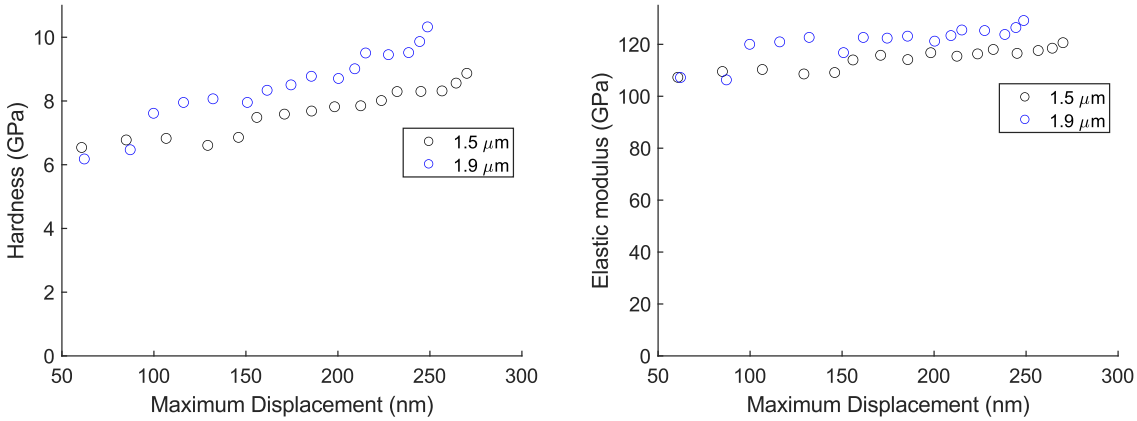


Figure 33: Hardness (left) and elastic modulus (right) as a function of maximum indentation depth

	E (GPa)	**H (GPa)**
1.5 µm	108 ± 2	6.7 ± 0.3
1.9 µm	118 ± 6.1	7.8 ± 0.9

Table 5: Summary of mechanical properties of films

The hardness values obtained from shallow indents are close to that of bulk tungsten (6 GPa)[109] however the Young's modulus is significantly lower than bulk tungsten (410 GPa)[33,83]. This indicates that the hardness is not as affected by the substrate at a given depth as compared to the elastic modulus, and similar observations were reported in literature[34,37]. FEM analysis of thin films by Zak et al.[37] showed that while it is possible to contain the plastic

regime within the film to determine hardness (due to its smaller size), containing the larger elastic regime is difficult even at shallow depths.

To correct for the modulus substrate effects, the modified King expression developed by Saha and Nix[33] was used. The average corrected Young's moduli of the films were found to be 247 GPa and 306 GPa, for the 1.5 µm and 1.9 µm film respectively (Figure 34). The 1.9 µm sample displayed higher values of both uncorrected and corrected modulus compared to the 1.5 µm film due to lower substrate effects occurring for the thicker film at any given depth compared to the thinner film. The corrected modulus for the 1.9 µm film is still below that of bulk tungsten. Similar underestimated tungsten values after applying substrate corrections were found in literature (E = 370 GPa)[83], which could be due to porosity or other fabrication defects.

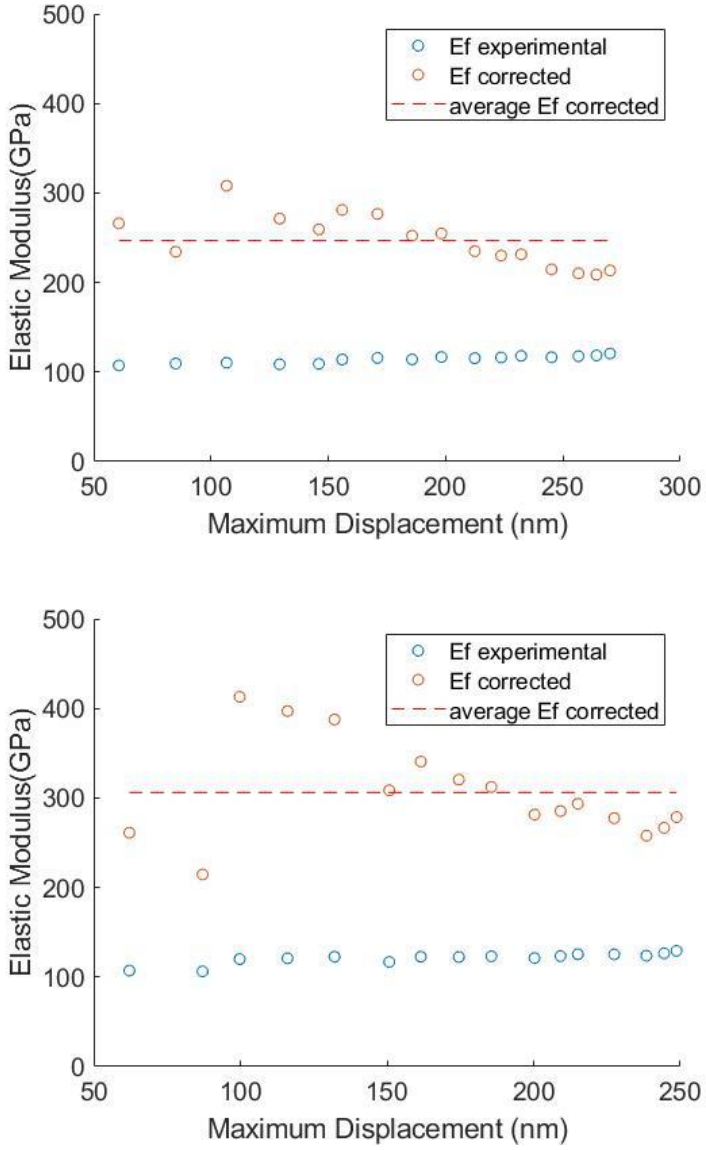


Figure 34: Corrected elastic modulus for 1.5 film (top) and 1.9 film (bottom)

3.3.2. Nanoindentation Adhesion

Indents were carried out on both samples to observe the film delamination using peak loads of 50-400 mN (referred to as low load range) and 100-1,000 mN (referred to as high load range). SEM images at three different peak loads of 73 mN, 370 mN, and 760 mN are shown in Figure 35, showing stages of plastic deformation, blistering (delamination) and fragmentation respectively. The load ranges and maximum indentation depths observed in each stage is summarized in Table 6.

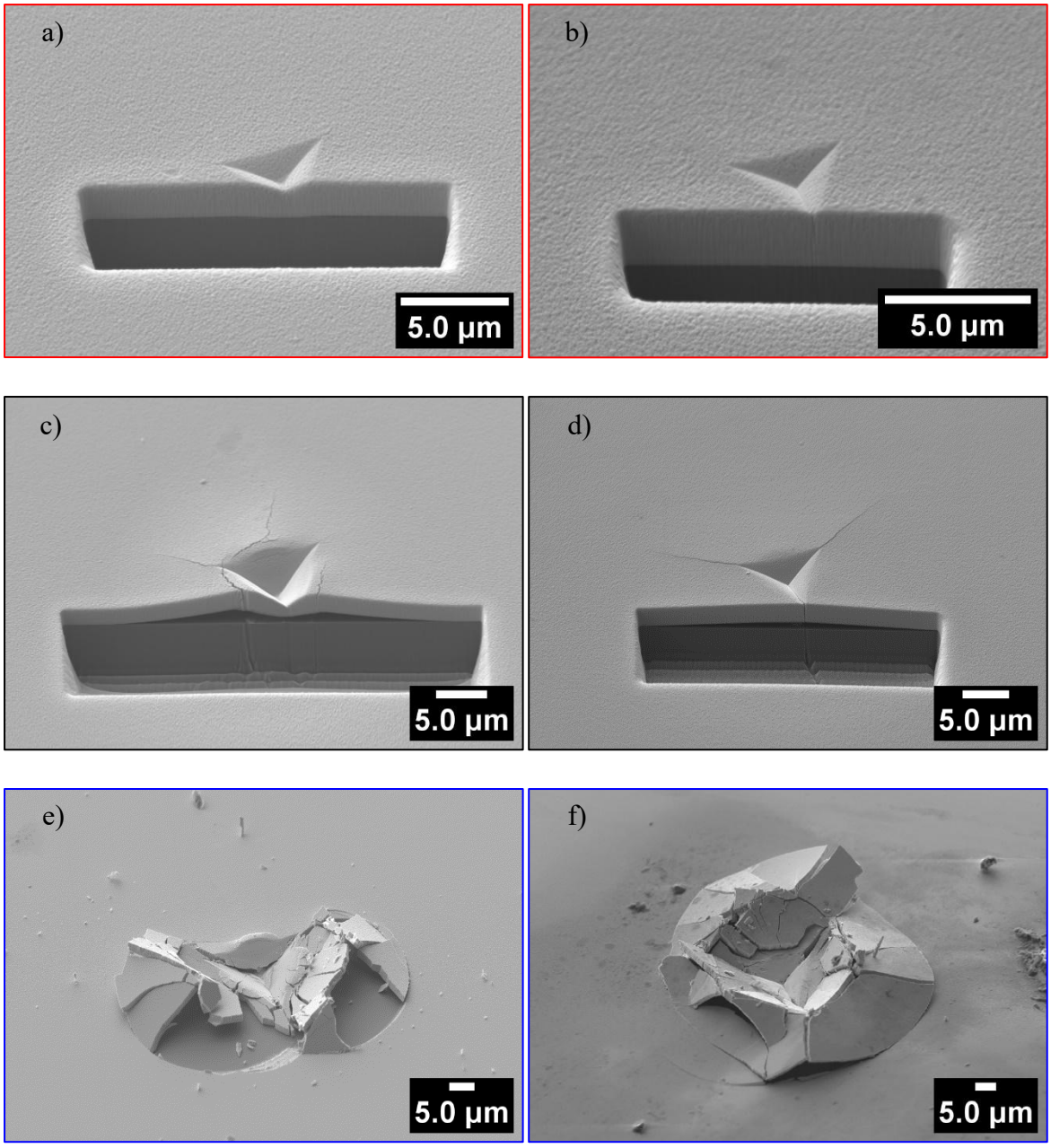


Figure 35: SEM images of three stages of fracture observed in the 1.5 µm film (left) and 1.9 µm film (right) with applied loads of 73 mN (a, b), 370 mN (c, d), 760 mN (e, f)

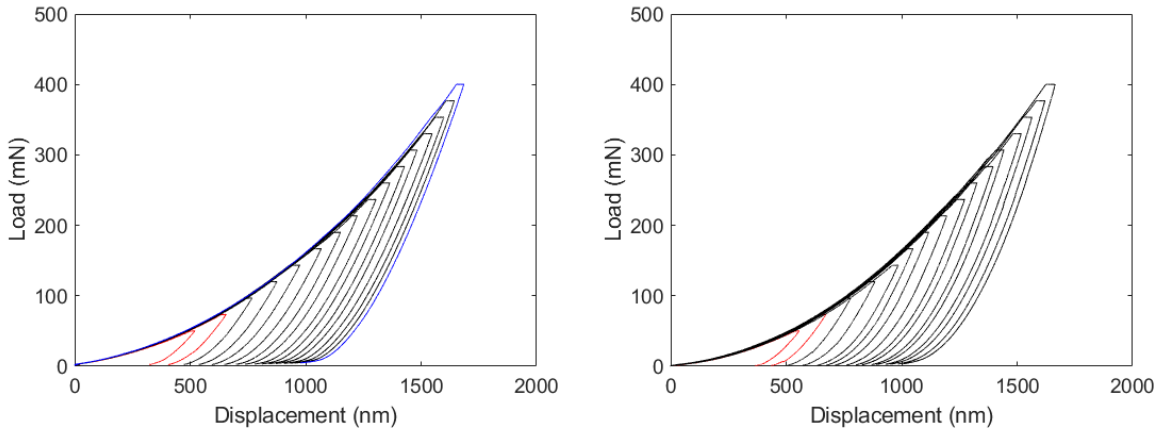


Figure 36: Quasi-static low load displacement curves 1.5 µm (left) and 1.9 µm (right). Red: plastic deformation, black: blistering, and blue: fragmentation

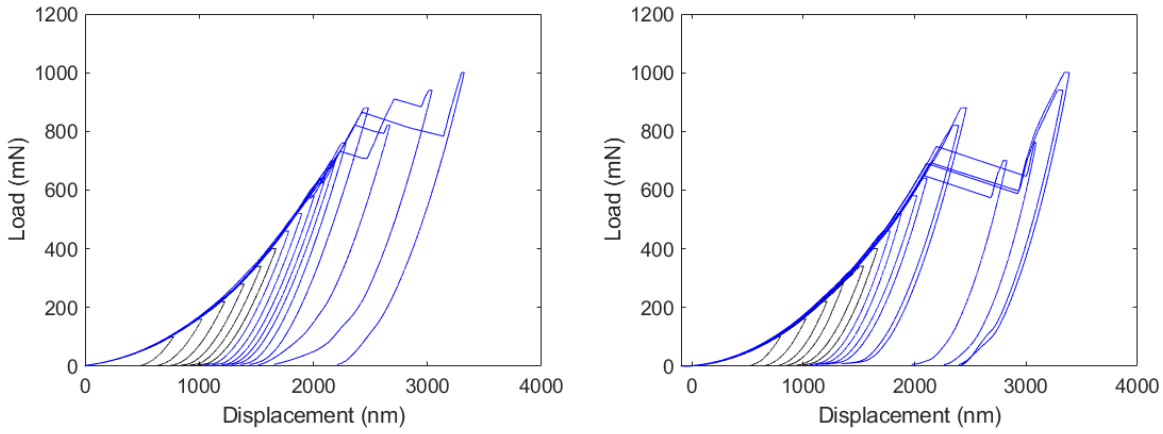


Figure 37: Quasi-static high load displacement curves 1.5 µm (left) and 1.9 µm (right). Black: blistering, and blue: fragmentation

The low load and high load displacement curves are given in Figure 36 and Figure 37. Both samples display no observable slope change in the load displacement curves for the low load regime, and significant steps (blue curves) in the high load curves. SEM and FIB images in Figure 35 highlight three distinct stages of deformation during indentation. Firstly, minimal plastic deformation and surface cracks were observed in the lowest load regime in stage I (Figure 35 a, b). As the loads increased, circular blisters began forming on the surface (stage II). These blisters are indicative of film delamination which are observed subsurface using FIB (Figure 35 c, d). This is formed because double buckling occurs around the indenter as the indenter is driven into the film[59]. Then as the indenter is removed, the portion of the film under

the indenter is no longer pinned and forms a circular raised blister. The radius of the blister was observed to increase as the maximum load increased. This indicates that delamination in this sample is gradual and not an instantaneous event. The absence of curve deviation, despite the occurrence of delamination, has also been reported in literature[57], which was explained by delamination occurring during unloading segment. Additionally, the unpinned geometry of the buckles further supports the occurrence of delamination during unloading[110]. During stage II at higher loads, additional cracks appear, and the radial cracks grew to a critical length while increasing in width. No substrate cracking was observed in this stage, which ensures that the delamination energy is not overestimated. The features visible in the SEM images in the substrate under the indent are an effect of FIB curtaining and not substrate cracking.

The final stage occurs as the blister reaches a critical radius, after which fragmentation occurs in stage III (Figure 35 e, f). FIB and SEM imaging shows that delamination occurs before the occurrence of the large load-displacement steps (observed at large depths in Figure 37). From this observation it can be concluded that these large steps in the loading curve are due to film fragmentation alone. The ratio of the maximum displacement to film thickness (h/t) is also given for each stage in Table 6. From these findings, fragmentation is seen to occur either exactly at (1.5 μm film h/t = 1) or close to the interface (1.9 μm film h/t = 0.9). Meanwhile, blistering is observed at relative depths of 0.4 – 0.5.

	1.5 μm	**1.9 μm**	**Colour Code**
Stage I – plastic deformation and surface cracks	< 73 mN < 700 nm h/t < 0.5	< 73 mN < 700 nm h/t < 0.4	Red
Stage II – blistering	97 mN – 377 mN 750 – 1500 nm	97 – 400 mN 780 – 1600 nm	Black

	0.5 < h/t < 1	0.4 < h/t < 0.8	
Stage III – fragmentation	> 400 mN > 1500 nm h/t > 1	> 460 mN > 1780 nm h/t > 0.9	Blue

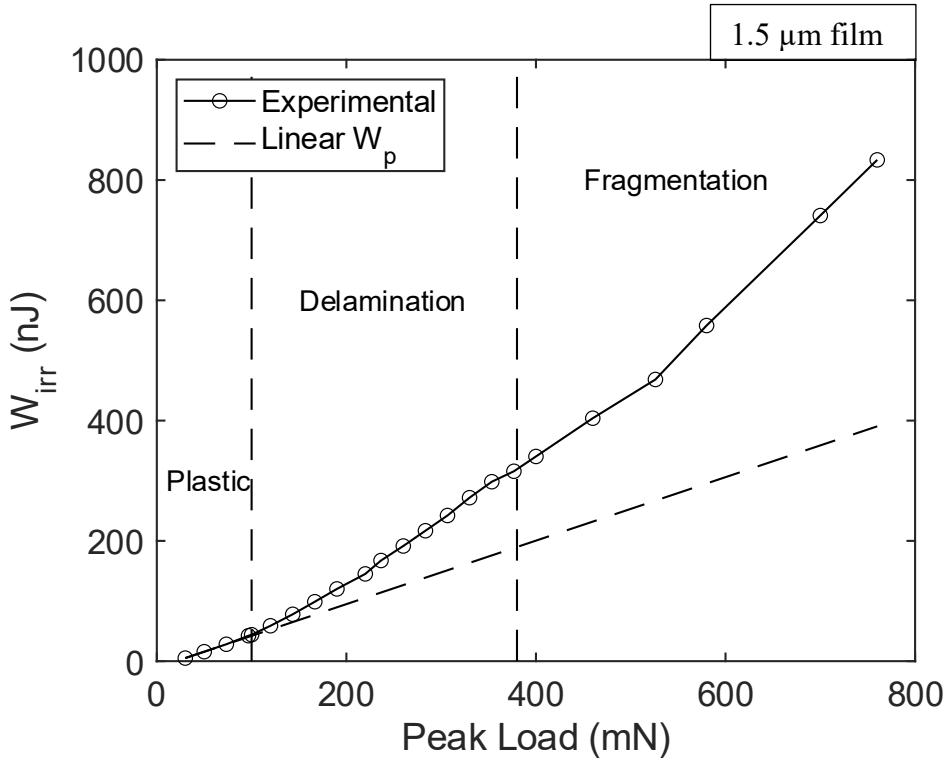
Table 6: Summary of load and maximum displacement ranges for 3 stages of deformation. h/t denotes the ratio of the maximum displacement over the film thickness.

Nanoindentation Adhesion Analysis (Irreversible Work)

Delamination energies were calculated through the energy-based method described by Malzbender[50]. The calculated irreversible work is plotted as a function of the applied load in Figure 38. The main assumption in this analysis method is that there is minimal contribution from other mechanisms such as substrate deformation and plastic deformation due to buckling. From the FIB images of the indents in stage II in Figure 35 (c and d), no substrate cracking has taken place, confirming that substrate deformation has little to no contribution on the work of delamination. The work of delamination is calculated as the difference between the total irreversible work and the linearly extrapolated plastic work (W_p). The area of delamination was obtained by either measuring the radius cross-sectional FIB (and assuming the area to be a perfect circle), or measured directly from SEM. The two methods yielded comparable delamination area values. Therefore, for simplicity, the area measurements obtained from FIB were used in subsequent analyses.

The values of delamination energy calculated are plotted as a function of the applied load in Figure 39 and summarized in Table 7. Only loads within stage II are calculated since the work of delamination is isolated in that stage without the effects of fragmentation. The delamination energy is seen to increase with increasing loads for both samples, agreeing with the previous claim that the delamination process in this material system is not instantaneous but gradual with increasing levels of delamination. Although FIB images have shown that no

substrate cracking has taken place in stage II, the higher delamination energy at higher loads may be due to an increase of substrate effects on the calculated values. This effect is also demonstrated by the higher overall delamination energy values in the thinner 1.5 μm film as compared to the thicker 1.9 μm film, where we expect less substrate effects at a given applied load. Additionally, higher levels of plastic deformation due to buckling is expected at higher loads, leading to higher values of delamination energy.



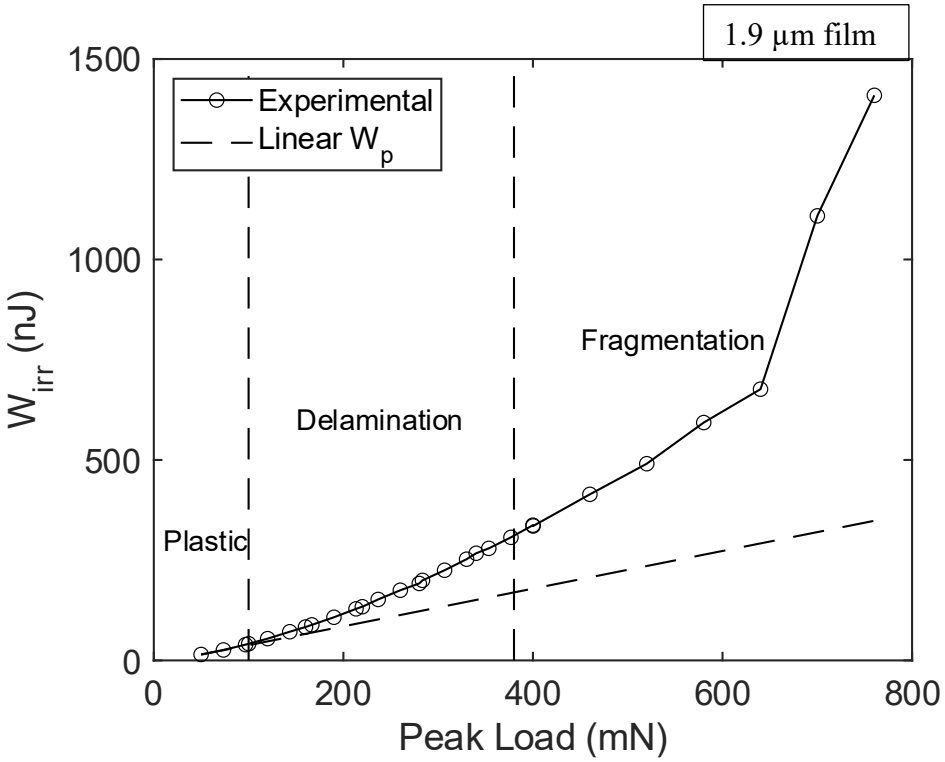


Figure 38: Irreversible work done vs load map for 1.5 µm film (top) and 1.9 µm film (bottom)

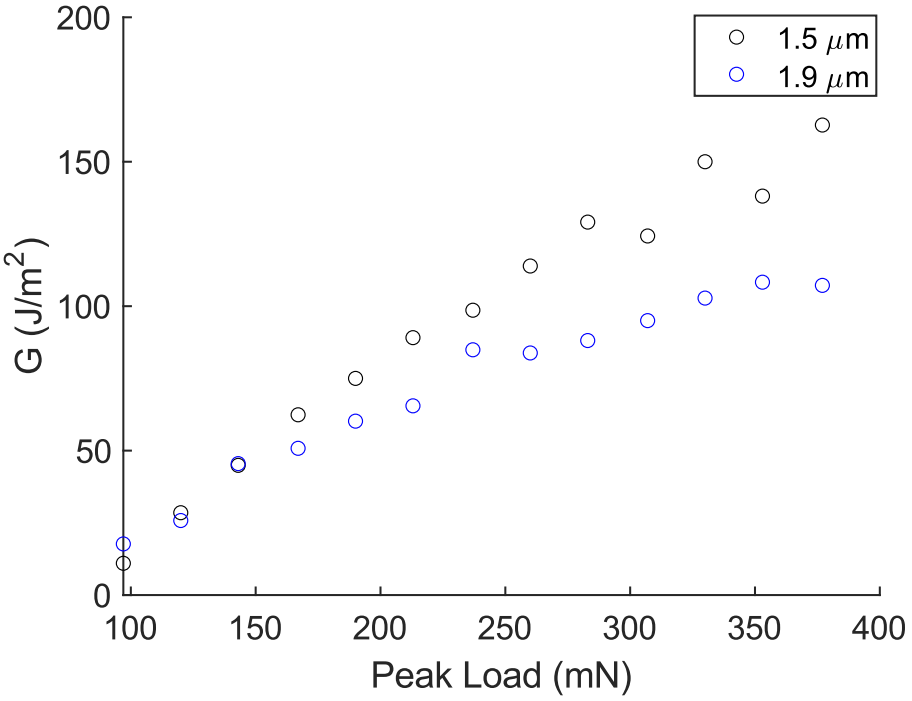


Figure 39: Plot of delamination energy G with increasing load

	1.5 µm	**1.9 µm**
Range of delamination energies	11-162 J/m^2	17-107 J/m^2

Table 7: Summary of range of delamination energies calculated

Influence of loading rate

To study the effect of the loading rate on the delamination energy values, three sets of indents with a peak load of 350 mN were performed with loading rates 52, 104, and 206 mN/s. As seen in Figure 40, no influence of the loading rate was seen on the shape of the load-displacement curves. A small step is seen in the 260 mN/s loading curve (denoted by red arrow) however this is solely due to minor film fracture, as delamination in this sample occurs during unloading. The SEM images of the three indents shown in Figure 41 indicate that all three indents reached a similar level of deformation in the stage II regime. The delamination energy calculated from the three loading rates is summarized in Table 8. Similar delamination energies were calculated for all three loading rates due to the similar load-displacement curve and delamination areas. This suggests that the calculated delamination energy is independent of the applied loading rate.

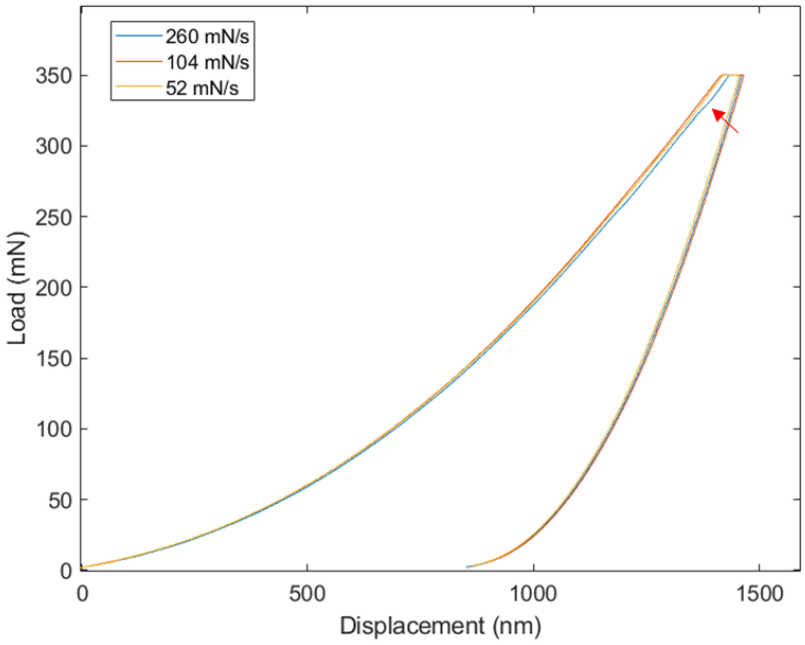


Figure 40: Quasi-static load displacement curve for three different loading rates (260, 104 and 52 mN/s)

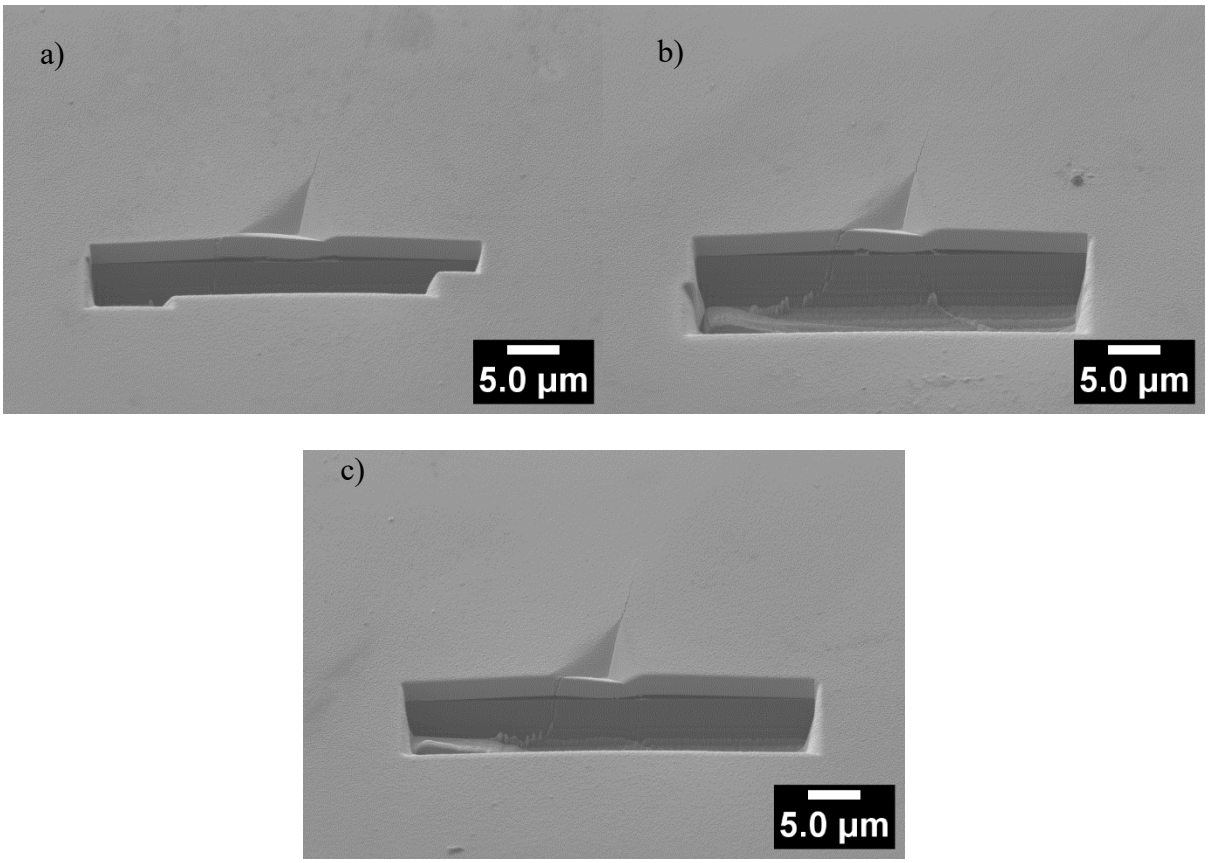


Figure 41: SEM images of indents with three different loading rates of a) 260 mN/s, b) 104 mN/s and c) 52 mN/s

Loading Rate (mN/s)	**Blister Radius (μm)**	W_{irr} **(nJ)**	W_d **(nJ)**	**G** (J/m^2)
260	17	268.7	21.7	23.9
104	17.3	274.7	27.7	29.5
52	17.8	269.8	22.8	23.0

Table 8: Values of delamination energy with different loading rates

FEM Correction

The assumption of linear extrapolated work in the method described in the previous section was investigated using an FEM simulation of the 1.9 μm film. The model only considers the total irreversible work due to plastic dissipation without delamination or fragmentation. A graph of both the FEM and linear extrapolated values of W_p are plotted as a function of the peak load in Figure 42. The simulation appropriately models the plastic dissipation work in the thin film as shown by the agreement of the FEM and experimental W_{irr} value in the low load regime (<97 mN) before any delamination occurs. Appendix 2 presents the load–displacement curves from both experimental and FEM results in the plastic region, demonstrating good agreement.

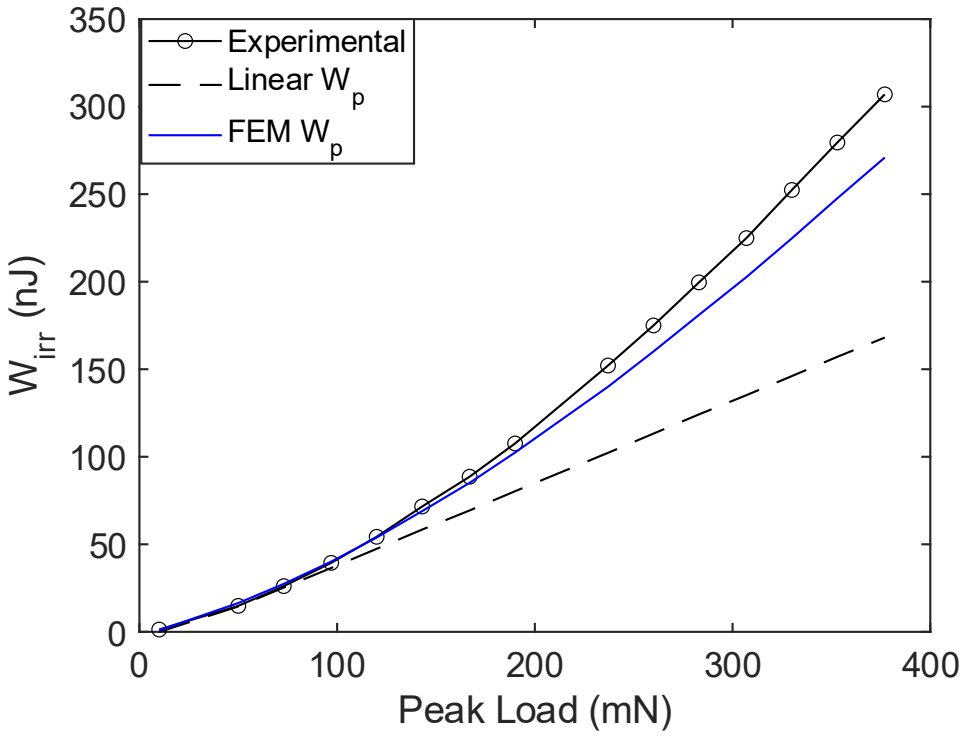


Figure 42: Irreversible work map in the stage II regime with the linearly extrapolated, FEM and experimental curves

The FEM data suggests that the plastic dissipation work does not follow the linear progression proposed by Malzbender and that using a linear extrapolation significantly overestimates the value of the work of delamination. Others reporting this overestimation attribute it to the additional energy dissipation mechanisms that cannot be separated from delamination[57], and to the linear plastic work assumption being incorrect[46]. The model here allows for some of these mechanisms to be captured and provides better predictions of the plastic work, resulting in a smaller range of measured delamination energies (2-29 J/m^2) compared with those calculated with the linear extrapolation (17-107 J/m^2). This reduction in uncertainty in the measured delamination energy provides values that agree well with literature values of tungsten on silicon (5-20 J/m^2)[44,83,103].

3.3.3. Nanoscratch Adhesion

Scratches with ramped force were performed on both samples with the following scratch parameters: peak load = 70 mN, scratch length = 250 µm, and scratch time = 30 seconds in the face forward orientation. SEM images of scratches are given in Figure 43.

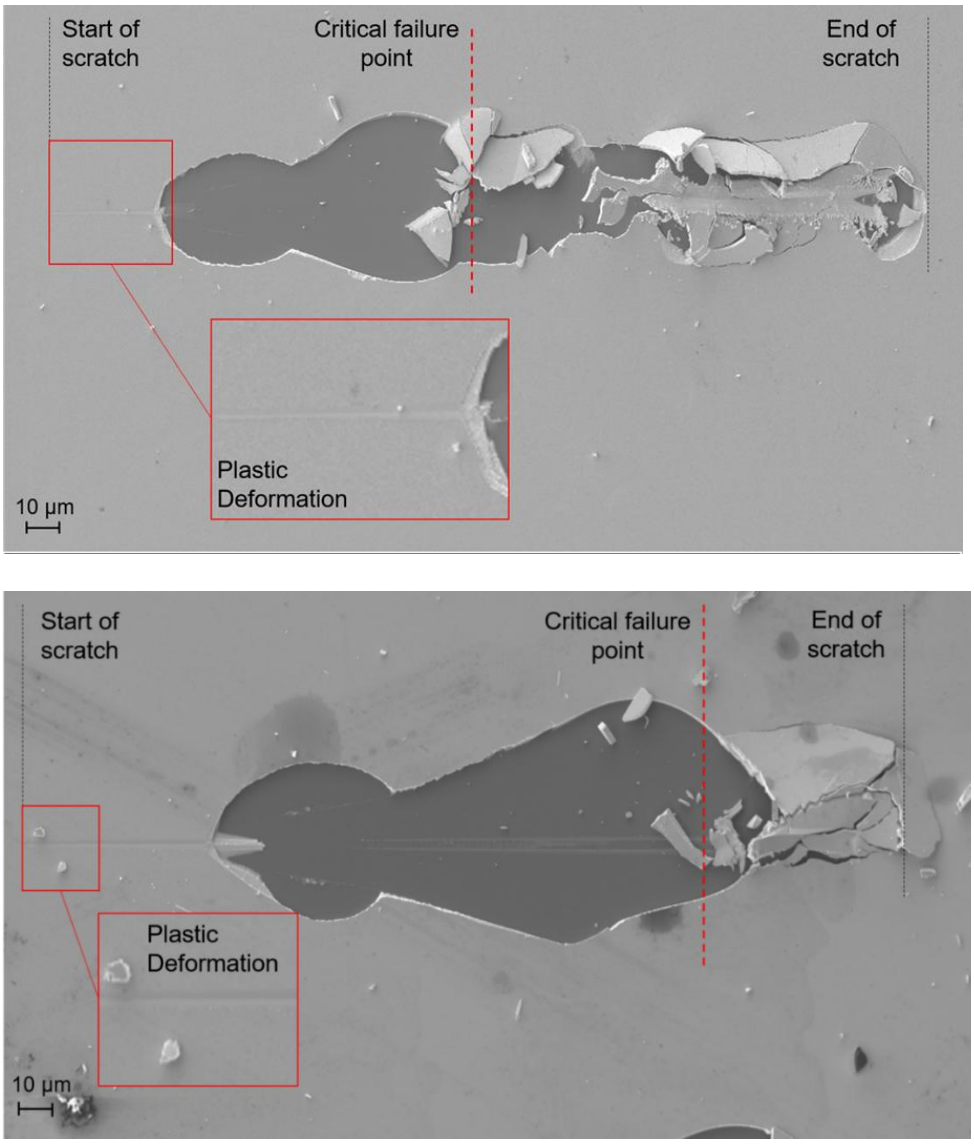


Figure 43: SEM images of scratches on 1.5 µm film (top) and 1.9 µm film (bottom)

In both samples, the scratches first exhibit plastic deformation at low loads, followed by sudden fragmentation as the load increases. The critical point of failure was chosen to be fragmentation in these scratches. It's important to note that as fragmentation occurred in these scratches, the film behind the indenter is also removed at the point of failure as tensile stresses

are concentrated at the rear of the indenter while scratching[67]. This means that the critical point of failure needs to be assessed from the scratch graphs and not from the final SEM image. No buckling or blistering was observed in the scratches before the onset of fragmentation. Fragmentation is expected to be the dominant failure mode for a hard coating on a hard substrate, since the film is too stiff to buckle in response to the applied stresses[111]. This typically occurs when the film thickness exceeds the critical threshold for buckling, which varies depending on the material. In this case, even though the coating is relatively thin, it is still thick enough to resist buckling, leading to fragmentation instead. The sudden transition from plastic deformation to fragmentation indicates that the calculated delamination energy will have a contribution from delamination and film fragmentation combined.

Figure 44 shows the scratch graphs showing the friction coefficient and normal force plotted against scratch time. Failure in a scratch graph is commonly shown as a sudden jump or discontinuity in the scratch graphs, which was observed in both samples. Changes in the friction coefficient during failure occurs because this event disrupt the contact dynamics between the indenter and the surface, leading to sudden variations in the scratch graphs. When delamination or fragmentation happens, sections of the film can chip off, leaving the indenter to interact directly with the underlying substrate, which often has a different friction coefficient than the film. Thus, the fluctuations in friction coefficient reflect a variety of interactions and transitions, making it highly sensitive to the material's failure mechanisms. The 1.5 μm film displayed a lower critical force of 35 mN, while the 1.9 μm film displayed a critical force of 58 mN. This is expected as thicker films need a higher load to fail as higher load is required to reach and delaminate the interface[70–72].

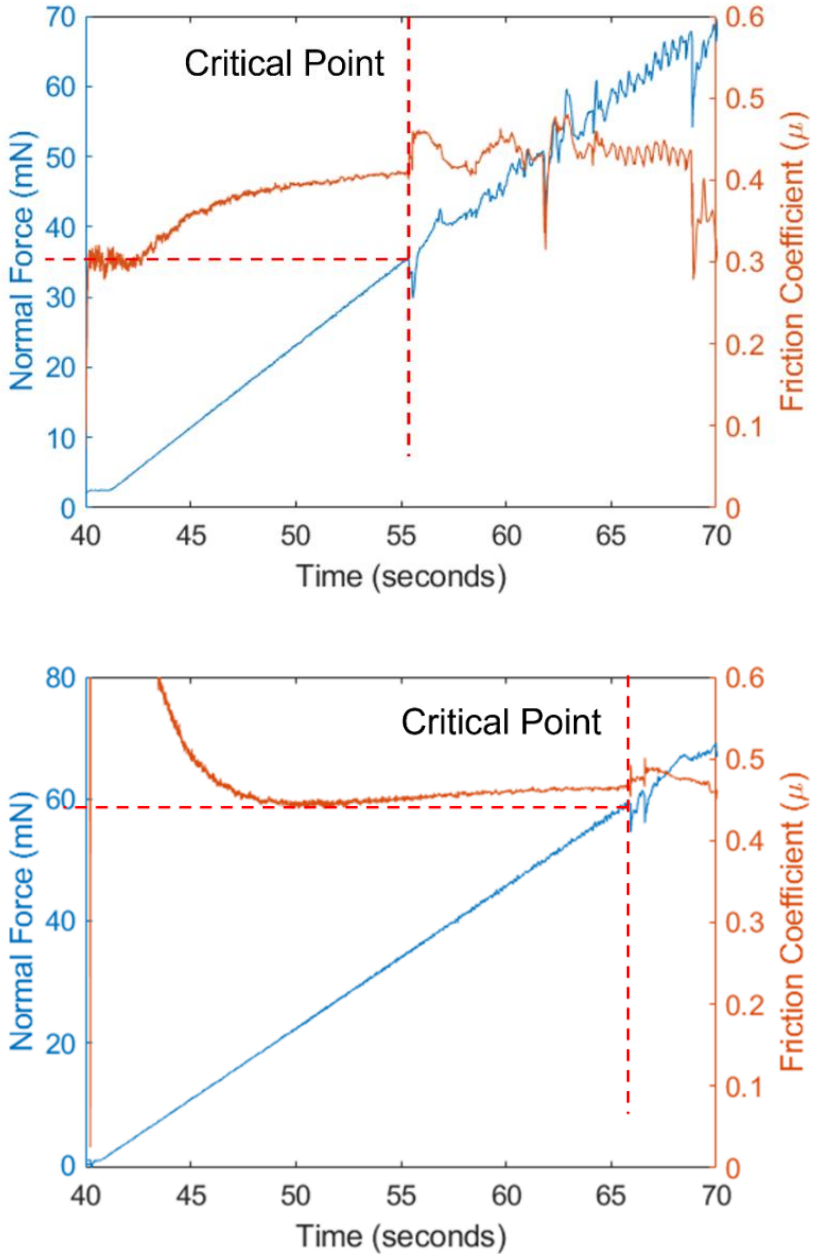


Figure 44: Normal force and friction coefficient graphs for 1.5 μm (top) and 1.9 μm (bottom)

The Laugier model[62] was used to calculate the delamination energy. The critical scratch width was determined from the contact depth as decribed in Chapter 2 (equation (46)). The values for the parameters used along with the calculated adhesion strengths and energies are shown in Table 9 below. The film modulus used for the calculation was based on bulk tungsten values[112].

The thicker (1.9 µm) film produced a lower value of delamination energy due to the higher scratch width despite the higher critical load compared with the thinner film. The film thickness is an intrinsic parameter that affects the results of the scratch tests, so direct comparisons between the delamination energies of the two samples cannot be made.

	P_c (mN)	d_c (µm)	ν_f	μ	E_f (GPa)	σ_a (GPa)	$G_d(J/m^2)$
1.5 µm	35	2.22	0.28	0.3	410	4.8	43
1.9 µm	58	3.42	0.28	0.3	410	3.4	27

Table 9: Properties at point of critical scratch failure

Influence of scratch parameters

To fully capture the effect of scratch parameters on the calculated delamination energy, a parametric study was conducted. The purpose of this section is to show the wide window of delamination energies that the scratch test is able to produce on one sample simply by varying the parameters. Table 10 shows the scratch parameters used along with the calculated adhesion energies tested on the 1.9 µm film. Here, dL/dt is the loading rate, dx/dt is the scratching rate, and dL/dx is the ratio of the two.

Peak Load (mN)	Scratch Length (µm)	Scratch Time (s)	dL/dt	dx/dt	dL/dx	P_c (mN)	hc (nm)	G (J/m^2)
70	250	30	2.33	8.33	0.28	58	610	27
100	180	30	3.33	6.00	0.56	73	717	22
200	250	30	6.67	8.33	0.80	79	751	22
100	100	60	1.67	1.67	1.00	76	720	24
250	200	30	8.33	6.67	1.25	90	810	21
250	100	30	8.33	3.33	2.50	125	980	19

400	100	30	13.33	3.33	4.00	177	1244	15
300	60	10	30.00	6.00	5.00	173	1182	17
500	50	10	50.00	5.00	10.00	118	1003	15
300	20	30	10.00	0.67	15.00	159	1213	13
400	20	30	13.33	0.67	20.00	202	1400	12
600	20	30	20.00	0.67	30.00	237	1494	13
800	20	30	26.67	0.67	40.00	383	1907	12
500	10	5	100.00	2.00	50.00	no failure	-	-

Table 10: Various combinations of scratch parameters tested on 1.9 µm film along with critical load and delamination energy

The critical load is seen to vary significantly in each test between 58 – 383 mN. It is observed that as the ratio dL/dx increases, the critical force observed increases as well, agreeing with previous observations in literature[65,70]. Steinmann et al.[70] explained this trend as a decreased probability of encountering a defect in the interface with increasing dL/dx values, which in turn increases the critical load. No other dependence was found between the critical load and any of the other scratch parameters or other ratios. Calculated delamination energies also had a wide range from 12-27 J/m^2, that increased with lower dL/dx values. At high dL/dx ratios, lower G values were calculated despite the high critical loads, due to the higher contact depth values. The decrease in G with increasing dL/dx can be explained by the reduced contribution of fragmentation work at smaller scratch lengths (dx). Fragmentation tends to overestimate delamination energy, since the total work done by the indenter is a summation of the delamination and fragmentation work, so less fragmentation leads to lower (and more accurate) values of delamination energy. Beyond a dL/dx ratio of 40, no failure was observed due to the extremely low probability of encountering a defect with such high ratios.

Next the influence of the tip orientation was studied, and scratches were performed in the edge forward and face forward orientation. Figure 45 shows the friction coefficient graph for both orientations using the following scratch parameters: peak load = 70 mN, scratch length = 250 μm, scratch time = 30 seconds. Optical images of the scratches using 70 mN, 250 μm and 30 seconds are shown in using the edge forward orientation in Figure 46 and face forward orientation in Figure 47. The face forward orientation led to a higher value of friction coefficient (μ=0.46) as compared to the edge forward orientation (μ=0.20). Conflicting results were found in literature where some studies showed the face forward having a higher coefficient[113], while the opposite was observed in other studies[74]. This discrepancy could be attributed to differences in material properties, surface roughness, and testing conditions.

The friction coefficient is the summation of interfacial and ploughing coefficients[114]. In the face forward orientation, the larger contact area increases the ploughing coefficient, resulting in a higher overall friction coefficient. On the other hand, the edge-forward orientation has a sharper profile, allowing the indenter to cut-through the material more effectively, leading to lower ploughing coefficient. In addition to the ploughing coefficient, FEM studies have also shown that the face forward orientation also increases the interfacial coefficient contribution[113]. These results highlight the critical role of tip geometry in the observed friction behaviour.

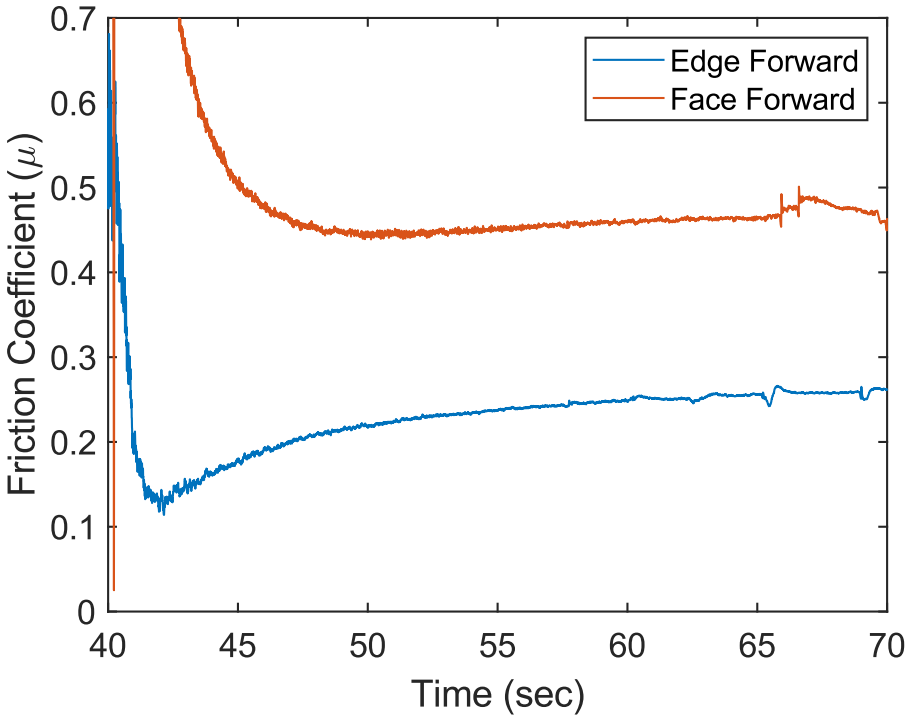


Figure 45: Friction coefficient graphs for the face and edge forward orientation (70mN, 250 µm, 30 seconds)

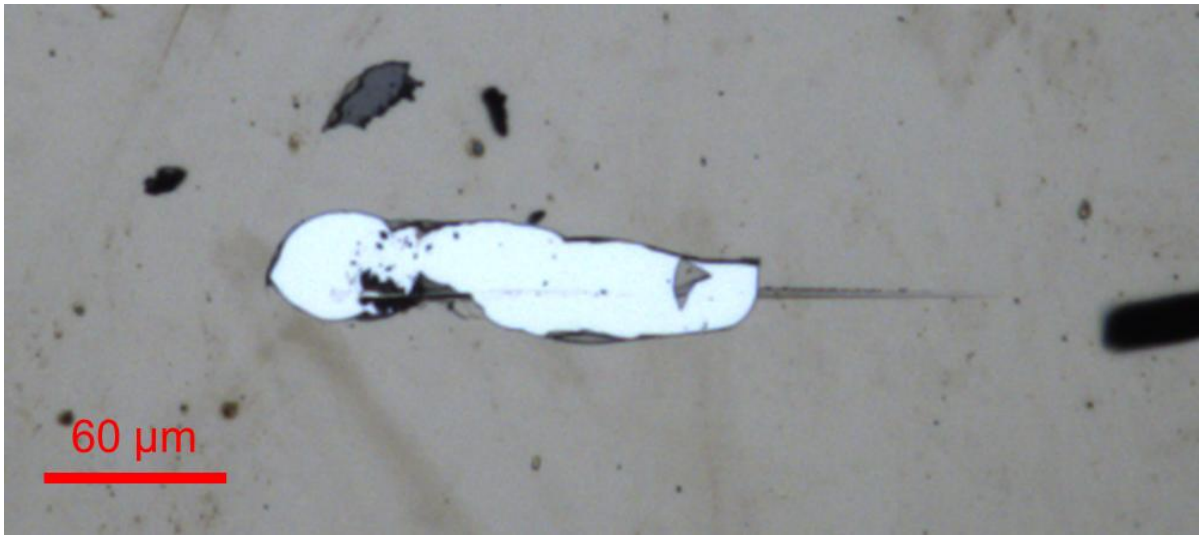


Figure 46: Optical image of edge forward scratch (70 mN, 250 µm, 30 sec)

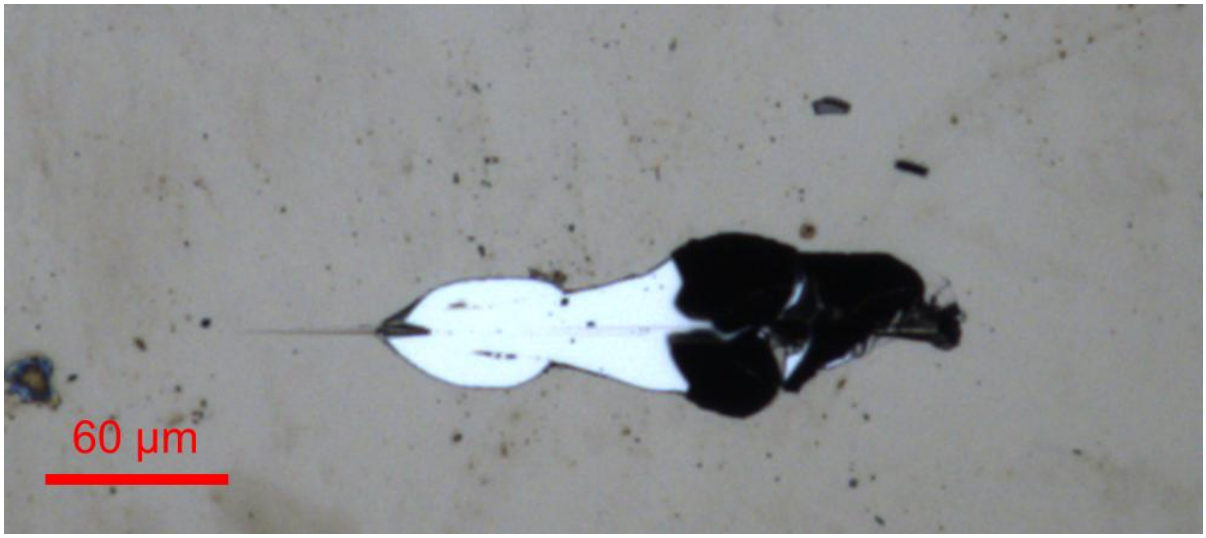


Figure 47: Optical image of face forward scratch (70 mN, 250 µm, 30 sec)

Different sets of scratch parameters were used to further study the effect of orientation on critical load and adhesion energies, with the results summarized in Table 11. From the optical images in in Figure 46 and Figure 47, the face forward orientation resulted in a higher area of fragmentation (6251 μm^2) compared to the edge forward orientation (4246 μm^2). Generally, the edge forward orientation led to higher critical load values and higher delamination energies (25-49 J/m^2) compared to face forward orientation (13-27 J/m^2). Wang [74] explained that lateral crack initiation is more likely in the face forward orientation, which explains the trend of lower critical loads and the optical microscopy images.

Peak Load (mN)	**Scratch Length (µm)**	**Scratch Time (s)**	**dL/dt**	**dx/dt**	**dL/dx**	**P_c (mN)**	**h_c (nm)**	**G (J/m^2)**
Face Forward								
70	250	30	2.33	8.33	0.28	58	610	27
400	100	30	13.33	3.33	4.00	177	1244	15
300	60	10	30.00	6.00	5.00	173	1182	17

600	20	30	20.00	0.67	30.00	237	1494	13
Edge Forward								
70	250	30	2.33	8.33	0.28	40	437	49
400	100	30	13.33	3.33	4.00	197	1099	30
300	60	10	30.00	6.00	5.00	209	1160	27
600	20	30	20.00	0.67	30.00	443	1722	25

Table 11: Effect of scratch tip orientation on critical load and delamination energy

3.4. Comparison and Discussion

Nanoscratch and nanoindentation experiments have been shown to display different deformation mechanics. In nanoindentation, the indent progresses from plastic deformation and surface cracking, to blistering (delamination), and finally fragmentation. In the nanoscratch experiments, the scratch progressed from plastic deformation to sudden fragmentation. The critical loads needed to induce fragmentation in the nanoindentation tests (400 mN and 460 mN for the 1.5 μm and 1.9 μm film, respectively) were much higher than the critical loads for fragmentation seen in the nanoscratch tests (35 mN and 58 mN for 1.5 μm and 1.9 μm film, respectively), which is consistent with literature observations[60]. It is expected that the load needed to induce fragmentation should be higher in nanoindentation since only one force is involved (normal force), meanwhile the presence of two loads (normal and lateral) in nanoscratch, lowers the normal load needed for fragmentation due to the "mode mixity" effect[47]. Furthermore, the h/t ratio at which fragmentation occurred during nanoindentation was found to be 0.9 for the 1.9 μm film. In contrast, during nanoscratch testing, the normal displacement (and subsequently the h/t ratio) at which fragmentation occurred varied depending on the scratch parameters, indicating a less consistent failure threshold. This suggests that nanoindentation offers a more controlled and reproducible method for identifying

the onset of damage based on h/t ratios, whereas scratch-induced failure is more sensitive to test parameters.

Table 12 summarized the values of delamination energies calculated from the nanoindentation method (with and without FEM corrections) and from the nanoscratch test for the 1.9 µm film. Nanoscratch is seen to give higher values of delamination energy as compared to FEM corrected nanoindentation because the work of film fragmentation is included in the delamination energy calculations. The scratch analysis developed by Laugier[62] assumes that the work done by the indenter to fragment the film is small compared to the delamination work, which is not the case for our experiments. Fragmentation is seen to significantly increase the total work during nanoindentation (Figure 38), suggesting that fragmentation will also have a significant contribution to the total work done during nanoscratching. The nanoindentation test with FEM corrections was found to output results agreeing with literature [44,83,103]. Comparable values of G were found using the nanoscratch test with high dL/dx ratios, with the face forward orientation.

Method	**Delamination Energy (J/m^2)**
Nanoindentation	17 – 107
Nanoindentation (FEM Corrected)	2 - 29
Nanoscratch	13 - 49

Table 12: Summary of delamination energy values found for the 1.9 µm film

3.5. Conclusions

This chapter establishes the techniques for quantifying nanoindentation and nanoscratch adhesion on a reference tungsten film. The tungsten thin film mechanical properties were measured through shallow indents. Film hardness properties comparable to bulk tungsten were found due to the plastic zone being contained within the film at these depths.

On the other hand, the Young's modulus had high substrate effects, even below 10% indentation depth, leading to underestimated values (118 GPa). Corrections to the Young's modulus led to values (306 GPa) closer to that of bulk tungsten.

In nanoindentation adhesion testing, three stages of fracture were observed:

- Stage I: plastic deformation and cracking
- Stage II: blister forms and grows with increasing loads until it reaches a critical blister size
- Stage III: past the critical blister size, fragmentation occurs

Conventional linear extrapolation of the plastic dissipated work resulted in a range of delamination energy values of 11-162 J/m^2 and 17-107 J/m^2 from the 1.5 μm and 1.9 μm film, respectively. The 1.5 μm film produced higher delamination energies due to the higher overall substrate effects present. FEM simulations of the 1.9 μm film allowed for the plastic dissipated work to be corrected to give a range of delamination energies of 2-29 J/m^2, which agree more closely agree with literature values. The value of delamination energy through nanoindentation was found to be independent of loading and strain rate.

Different deformation mechanics were observed in nanoscratch tests. The scratch progressed from plastic deformation directly to fragmentation. Tests with a similar set of scratch parameters produced values of adhesive energy for 1.5 μm and 1.9 μm film were found to be 43 J/m^2 and 27 J/m^2 respectively. The critical load for the 1.9 μm film was higher than 1.5 μm, which is expected as critical load increases with thickness, however the critical scratch width led the 1.5 μm sample to have a higher delamination energy. It should be noted that direct comparisons of the delamination energy of two films cannot be made as thin film thickness is a parameter that affects the scratch test. Different scratch parameter combinations were used to show their effect on the values of delamination energy ranging from 13–49 J/m^2. Higher values of dL/dx were found to give higher critical loads and lower delamination energies. The

scratch orientation was found to be an important parameter that significantly altered the delamination energy, with face forward orientation outputting lower delamination energy values as compared to edge forward. Nanoscratch adhesion values comparable to those outputted from nanoindentation and literature were found using high dL/dx ratios and a face forward orientation.

Overall, the high parameter sensitivity, variability in failure mechanisms, and lack of standardized testing protocols in nanoscratch testing make the resulting delamination energy values more difficult to interpret quantitatively. In contrast, nanoindentation provides a more controlled and reproducible approach, independent of strain rate and loading conditions, with values agreeing with those from literature. It allows for a clear identification of damage stages, particularly the formation and growth of blisters prior to fragmentation, which are critical to understanding interfacial failure. Nanoindentation is able to isolate the delamination stage more reliably, making it a more suitable technique for extracting delamination energy. Furthermore, fragmentation observed in nanoindentation occurs at well-defined h/t ratios. This contrasts with the less predictable failure behaviour observed in scratch testing, where fragmentation and delamination are heavily influenced by scratch orientation and test parameters, occurring at inconsistent h/t ratios.

In the context of battery interfaces, nanoindentation more accurately represents the normal stresses caused by cathode particle contraction during cycling. Unlike nanoscratch, which applies dominant shear forces, nanoindentation mimics the out-of-plane loading that drives delamination in solid-state battery interfaces, making it a more relevant technique for evaluating interfacial reliability. This, along with the previously discussed advantages highlights why nanoindentation is the more reliable and suitable method for testing adhesion in battery material interfaces.

4. POLYMER THIN FILMS

4.1. Aim

Polymer thin films are used in various industries including solid-state batteries, electronics, packaging, and medical devices. When subjected to external or internal stresses, weak adhesive strength between the coating and substrate can lead to thin film delamination, affecting both performance and lifetime. Quantifying thin film adhesive properties is challenging due to the ductile nature of polymers. Literature implementing nanoindentation[48,49,52,53,116] and nanoscratch[42,63,64] on polymer thin films are scarce, and the applicability and limitations of these methods have not been thoroughly investigated. Additionally, while predicting scratch deformation mechanics from material properties are well understood through deformation maps[111], there is no equivalent understanding for nanoindentation.

This chapter aims to investigate the different failure mechanics occurring through nanoindentation and nanoscratch in two battery polymer coatings on silicon, polyethylene oxide (PEO) and a novel tri-block copolymer (referred to as P1) and to quantify their delamination energy. Some studies have investigated PEO delamination energy on substrates

such as vanadium oxide[117] (G = 3.2 J/m^2) and polystyrene[118] (G = 4.5 J/m^2). However, the methods used, including peel testing and dual-cantilever beam crack propagation (DCB) test, investigated the behaviour of thick coatings (> 5 μm). No study investigating the adhesive properties of thin PEO coatings (< 2 μm) through nanoindentation or nanoscratching was found in literature. The second battery polymer (P1) investigated in this chapter is a novel polymer with no existing literature investigating its adhesion energy.

The irreversible work method applied in Chapter 3 was suitable for brittle films such as tungsten and LLZO, where plasticity is minimal and energy dissipation beyond elastic recovery is largely due to delamination. However, for polymers, significant energy is also dissipated through viscoelastic and plastic deformation, making this method unsuitable. Therefore, this chapter adopts the energy-based method described by Omiya et al.[48] , which is more appropriate for ductile materials. This methodology is further enhanced here through the use of finite element modelling (FEM) to more accurately capture the underlying mechanics.

4.2. Materials and Methods

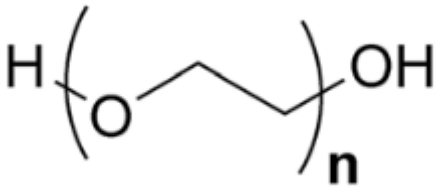
4.2.1. Thin Film Fabrication

All samples used in this chapter were fabricated by Holly Yeo (Department of Chemistry). Polyethylene oxide (PEO) was obtained from Sigma Aldrich with a molecular weight of 10,000 g/mol (Figure 48(a)). The novel triblock copolymer (P1)[119] has three block structure with the sequence ABA where the ‘A’ block represents the hard and ‘B’ represents the soft block (Figure 48(b)). The two A-blocks are shown in red, while the B-block shown in green. The A-block consists of poly(4-vinyl cyclohexene carbonate) (PvCHC) with a glass transition temperature (T_g) of 100 °C. Block B consists of polytrimethylene carbonate (PTMC)

and polycaprolactone (PCL) with a 0.2 TMC:CL molar ratio, and has a T_g of –40 °C. The final polymer structure (P1) has a molar mass of 50,000 g/mol and an A:B ratio content of 0.35:0.65.

The thin films were both prepared on a silicon substrate through solvent casting. The silicon substrate used is an n-type doped (100) silicon wafer with a thickness of 650-700 µm obtained from MEMC Electronic Materials. For both polymers, the polymer was first dissolved in a dichloromethane solvent, then the solution was poured on the silicon substrate which was placed in a Teflon mould and left to evaporate. The films were then dried in a vacuum oven at 60°C for at least 48 hours. The PEO samples were additionally hot pressed after drying using a Carver hot press at 60°C for 20 minutes, at 5,000 psi (34.5 MPa).

a)



b)

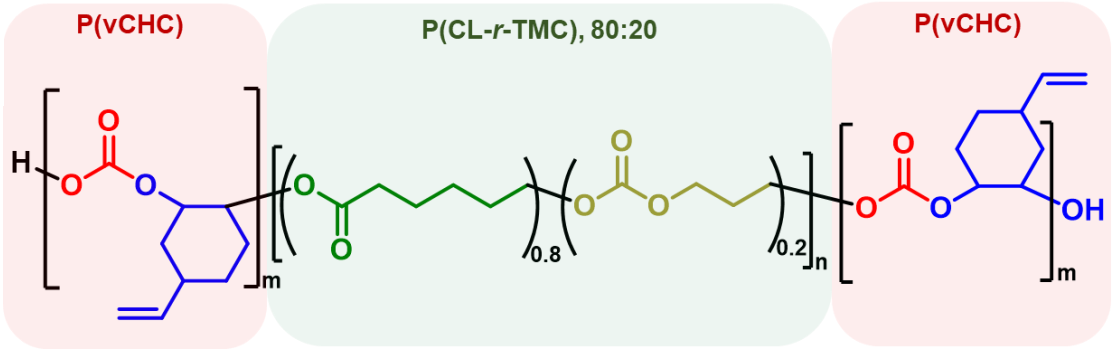


Figure 48: Structure of a) PEO and b) P1 (triblock copolymer)

4.2.2. Nanoindentation Methodology

Nanoindentation experiments were conducted using a Bruker Premier nanoindenter equipped with a Berkovich diamond tip. Continuous stiffness measurement (CSM) mode was used in the thin film characterisation section (Section 4.2.4) to indirectly assess thin film

thickness, where a sudden increase in the measured mechanical properties indicated that the indenter had reached the substrate.

For accurate evaluation of mechanical properties, the inclusion of a hold segment was required to minimise creep effects. Therefore, quasi static (QS) indentation was employed for both mechanical property measurements and nanoindentation based adhesion analysis.

Creep experiments were first performed to determine an appropriate hold time for the polymer thin films to minimise the influence of viscoelastic recovery and thermal drift during the hold segment. For P1–Si, indents were performed with hold times of 10 s, 30 s, 60 s, and 150 s, together with a reference case with no hold time. The peak load was kept constant at 200 μN to ensure that the indenter remained within the film region. For PEO–Si, the same creep procedure was conducted using a peak load of 500 μN for all indents. The creep factor, calculated using the method described by Feng[93], was used to identify an appropriate hold time for both samples, which was subsequently applied in all mechanical property measurements.

Following selection of the appropriate hold time, elastic modulus and hardness measurements were performed on the polymer thin films. QS indentation was used for shallow measurements to determine hardness and modulus using the Oliver–Pharr method. Substrate effects were corrected using the Saha–Nix method, consistent with the approach described in Chapter 3. A grid of 16 indents was performed for each sample with varying peak loads. For P1–Si, peak loads ranged from 100 μN-1,300 μN, while for PEO–Si, peak loads ranged from 500 μN- 2,000 μN. Pile up was visually assessed and quantified using SPM, and corrections were applied using the method proposed by Kese et al.[91].

4.2.3. Nanoscratch Methodology

Nanoscratch testing was performed using the same Bruker Premier nanoindenter and Berkovich diamond tip as used for nanoindentation experiments. Scratches were conducted

under ramped load conditions to determine the critical load for film failure and interfacial delamination.

For P1–Si, ramped load scratches were performed with peak loads ranging from 1,000 μN - 1,600 μN, a scratch duration of 20 s, and a scratch length of 14 μm. The orientation of the Berkovich tip was varied to investigate its influence on the measured critical load and failure behaviour. For PEO–Si, ramped load scratches were performed with peak loads ranging from 400 μN- 900 μN, using the same scratch length and duration as for P1–Si. For these experiments, an edge forward tip orientation was used to promote stable contact conditions and gradual interfacial loading while minimising excessive cutting and material removal. In contrast to brittle tungsten films studied in Chapter 3, polymer coatings exhibit significant viscoelastic deformation and plastic flow, which can lead to severe ploughing and pile up when tested in the face forward orientation.

Film failure was identified through a combination of a sudden change in the normal displacement signal during scratching and post-test SEM of the residual scratch. For polymer films, fracture events were less abrupt than those observed for brittle tungsten coatings, and reliance on friction coefficient data alone was insufficient to reliably detect delamination. Therefore, both scratch graphs and SEM imaging were used to confirm the onset of interfacial failure.

4.2.4. Thin Film Characterization

Film Surface Characterization

Both thin films displayed differences in surface appearance, thickness and mechanical data depending on the area tested. The difference in surface appearance in P1-Si observed by optical microscope in different areas are shown in Figure 49. The coloured areas covered most of the sample, while smaller areas towards the inner edge displayed the grey appearance. The

colourful features observed under the optical microscope are likely due to a residual surface film formed during the fabrication process. These interference effects are not visible in regions with higher film thickness, suggesting they are enhanced in thinner or more uneven areas of the polymer film. Continuous stiffness measurements (CSM) were performed in both areas and the hardness and storage modulus values are shown in Figure 50. For viscoelastic materials such as the polymers tested here, the storage modulus reflects the elastic (recoverable) component of deformation and can be considered an approximation of the elastic modulus under dynamic loading conditions. The sharp deviation in both hardness and modulus indicates the indenter reaching the substrate, from which it can be concluded that the thickness in the coloured areas and the grey areas are around 500 nm and 1400 nm respectively. Additionally, the overall lower hardness and modulus values found in the grey areas compared to the coloured areas indicate lower substrate effects, and therefore higher thickness. In the thin film region, the hardness values remain relatively flat while the modulus increased with increasing displacement. This is expected as the elastic zone (modulus) is much larger than the plastic zone (hardness) and therefore is more susceptible to substrate effects[34,37]. Therefore, for the following thin film mechanical testing section, the thicker grey area was selected for testing to minimize substrate effects.

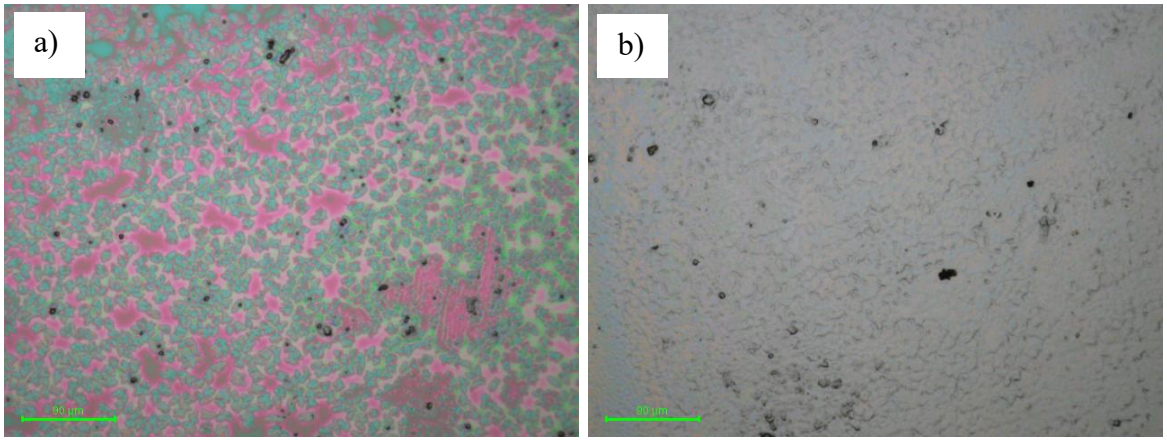


Figure 49: P1-Si a) coloured area (500 nm thickness) and b) grey area (1400 nm thickness)

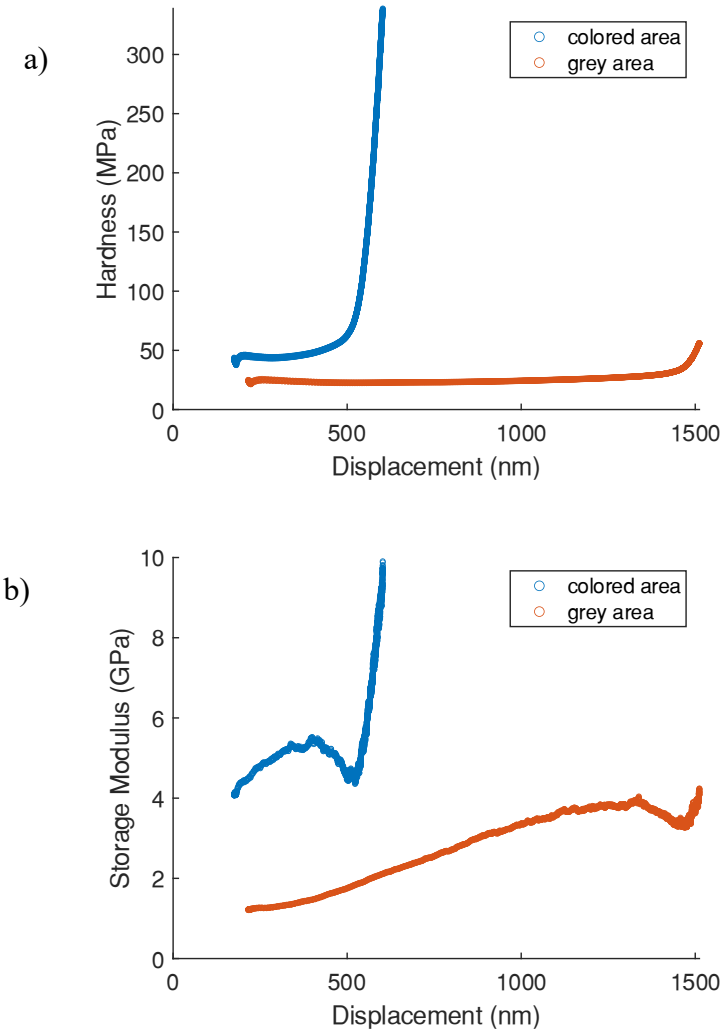


Figure 50: P1-Si a) hardness and b) storage modulus values in the grey and coloured areas

Similar coloured and grey areas were observed in PEO-Si (Figure 51). Overall, the surface in PEO-Si was not smooth and contained many scratches and surface irregularities. Hardness and storage modulus CSM data of the two areas are shown in Figure 52. The sharp deviation indicates that the thickness is 450 nm and 1600 nm in the coloured and grey areas respectively. Similar to P1-Si, the thicker grey area was selected for mechanical properties testing to ensure minimal substrate effects.

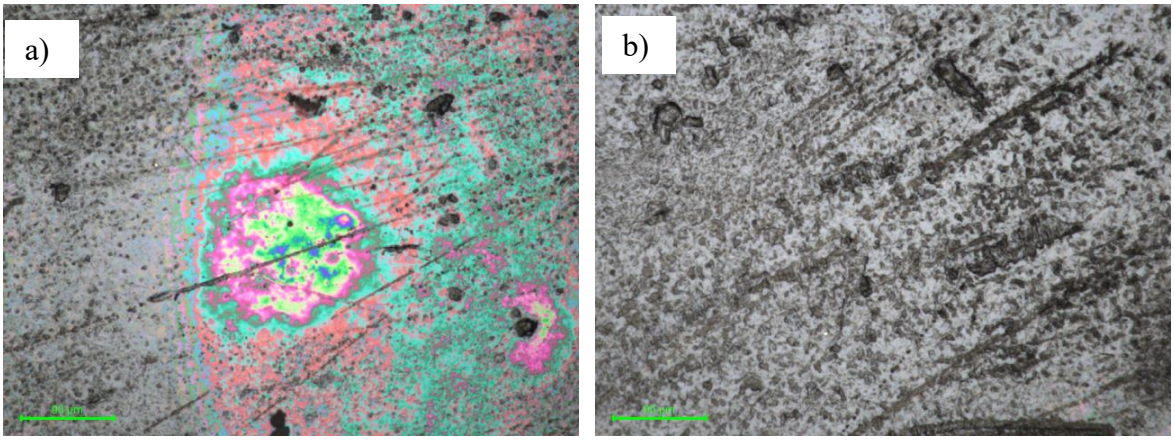


Figure 51: PEO-Si a) coloured area (450 nm thickness) b) grey area (1600 nm thickness)

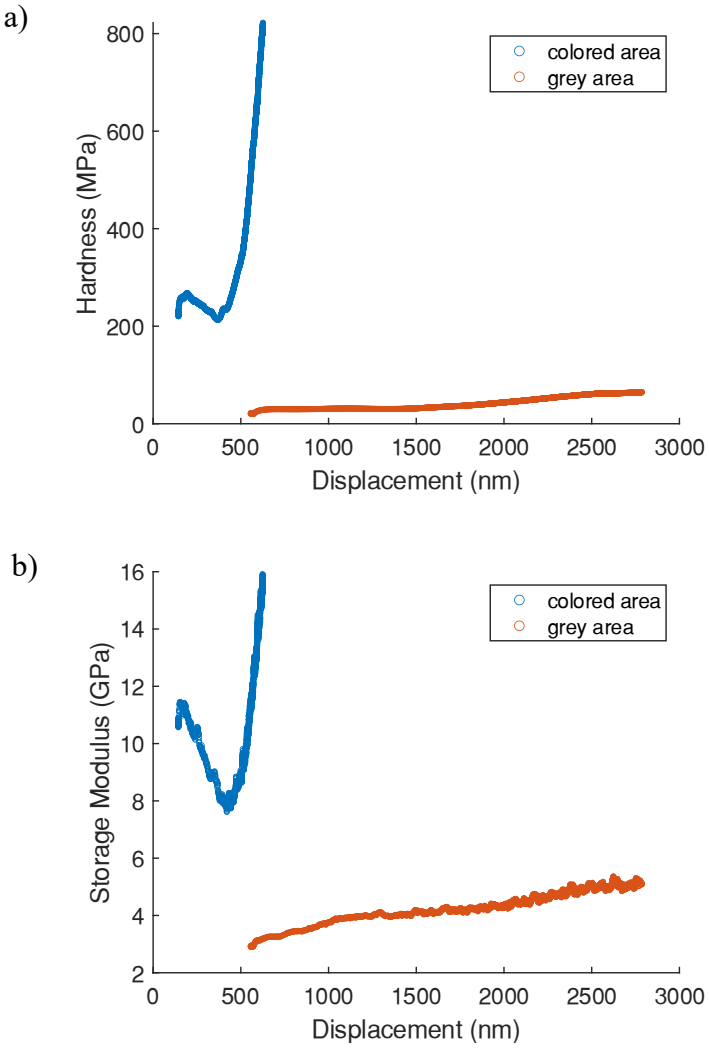


Figure 52: PEO-Si a) hardness and b) storage modulus in grey and coloured areas

Scanning probe microscopy (SPM) images of the grey areas in both samples were taken with the Premier Nanoindenter. The typical small-scale topography of PEO-Si and P1-

Si are shown in Figure 53 and Figure 54 respectively. Five images were taken within the grey areas and an average mean roughness S_a was calculated through the Gwyddion software to be 150 nm in PEO-Si and 68 nm in P1-Si.

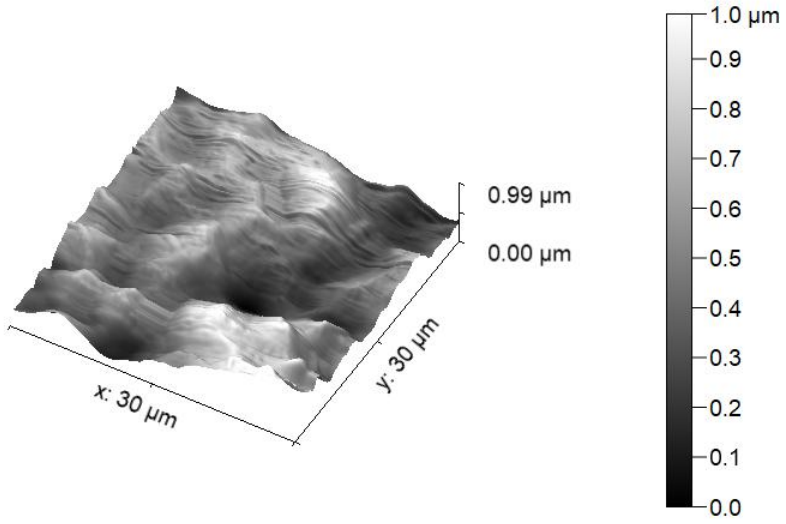


Figure 53: PEO-Si surface roughness

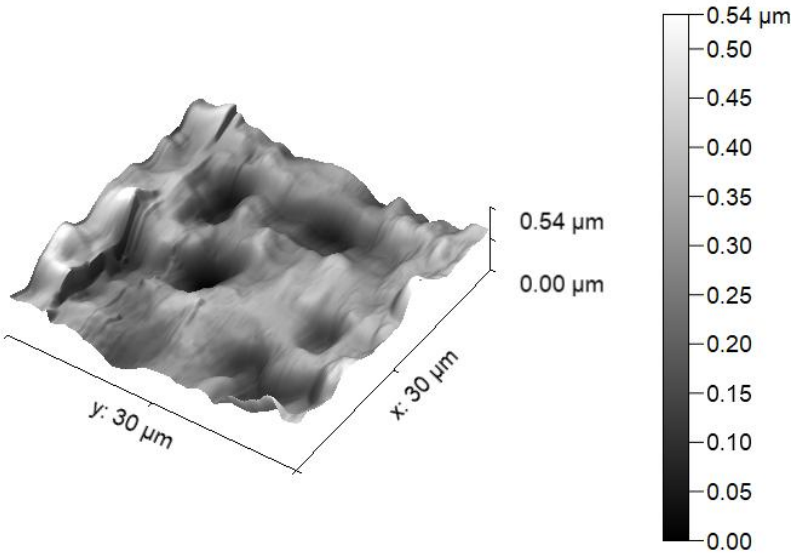


Figure 54: P1-Si surface roughness

FIB Interface cross-section

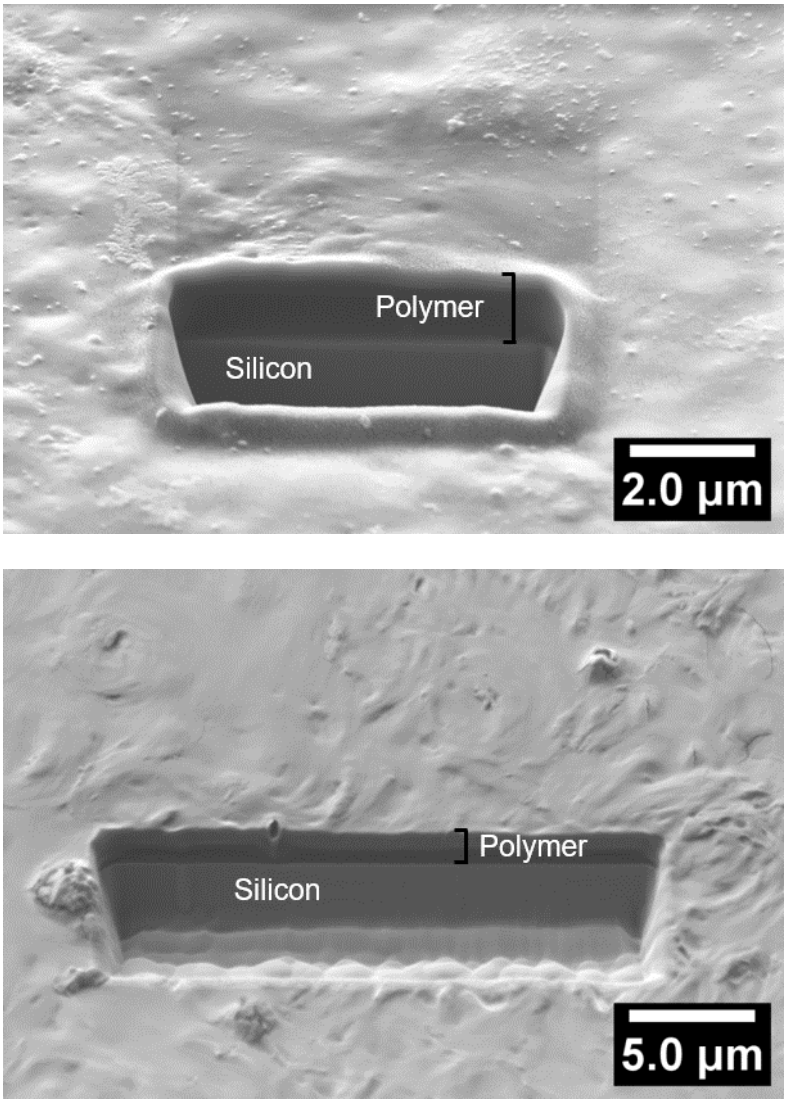


Figure 55: P1-Si (top) and PEO-Si (bottom) FIB cross-section

Focused ion beam (FIB) cross-sectional images of P1-Si and PEO-Si are shown in Figure 55. Tilt correction (at 36°) was turned on to allow for accurate thin film thickness measurements. The thickness of P1-Si was measured to be around 1 µm while PEO-Si thickness was measured to be 1.5 µm, both with slight variations occurring in different areas. The thickness measurements agree with those inferred from the CSM data. In both samples, the polymer appears to have two distinct layers with a lighter top layer and a darker bottom layer. This is due to the low accelerating voltage (5 kV) used for SEM imaging, using higher voltages (e.g. 15 kV) removed the dual contrast in the polymer layer (Figure 56), due to a

higher interaction volume and electron penetration depth. All imaging was conducted using the lower accelerating voltage to avoid damage to the polymer.

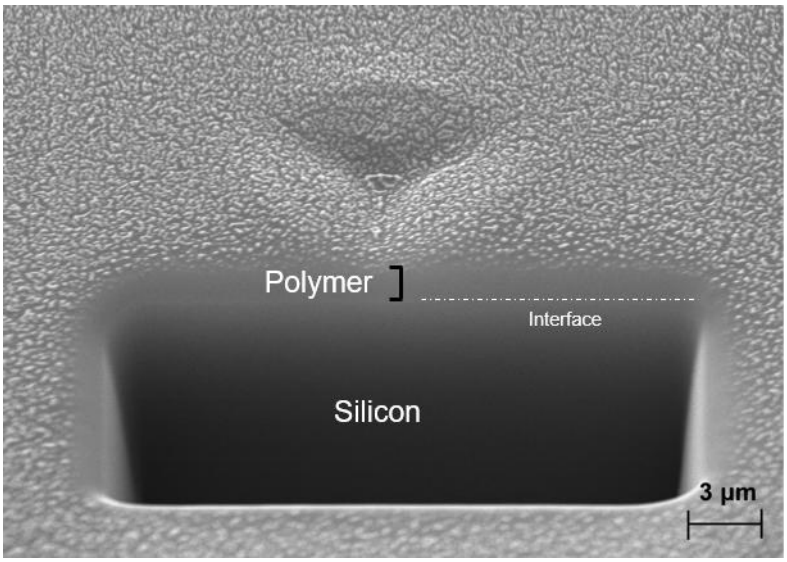


Figure 56: P1-Si using higher accelerating voltage (15 kV)

4.2.5. Finite Element Modelling

An axisymmetric 2D model was developed in ABAQUS to model the thin film delamination. Consistent units were used throughout the model of N, mm and MPa. The system consisted of a thin film (thickness = 1.5 µm for parametric study and 10 µm for power fit energy modelling), a cohesive layer, and a silicon substrate (thickness = 1 mm). An ideal cohesive layer stiffness (K_0) value was found to be 1,000 GPa through trial and error. This value was chosen as it was high enough to eliminate any compliance in the cohesive layer, without being excessively large, which caused convergence issues. The polymer properties, cohesive layer adhesive strength and fracture energy were varied in each model to perform the parametric study, while the silicon substrate properties were kept constant at a Young's modulus of 195 GPa and a Poisson ratio of 0.3, as in Chapter 3. The silicon substrate was considered to be linearly elastic so no plastic properties were defined. The indenter was drawn as a triangle with an angle of 70.3°, resulting in a conical indenter with an infinitely sharp tip. 70.3° was chosen

to allow for the indenter to be equivalent to a Berkovich indenter with the same effective cone angle[32].

The thin film was drawn as one part and sectioned into the polymer, cohesive and substrate layers. A convergence study was conducted on the mesh sizing and it was found that below 0.0004 mm, artificial stress concentrations were formed in the cohesive layer, and the simulation did not converge. Additionally, too large of a mesh size led to modelling inaccuracies. The ideal mesh size was found to be 0.0004 mm in the x-direction and 0.00005 mm in the y-direction near the indenter. Details of the mesh convergence study is given in Appendix 3. An image of the geometry and the mesh near the indenter is shown in Figure 57 with the polymer, cohesive and substrate layers shown in red, yellow and blue, respectively. Far from the expected elastic zone and indenter, a mesh bias was applied to increase the mesh size to save computational time. Mesh elements chosen in the polymer, cohesive layer and substrate were CAX8, COHAX4, and CAX8 respectively. Quadratic elements were necessary in the polymer section to avoid mesh distortion especially in models with low polymer yield strength where excessive distortion was seen using linear elements.

The indenter was modelled as a rigid body and the interaction between the indenter and film was modelled as hard and frictionless with finite sliding. For the boundary conditions, the bottom side of the substrate was fixed in all directions (U1 = U2 = UR3 = 0), the left side of the sample on the axis of symmetry was fixed in x-direction (U1 = UR2 = UR3 = 0). Finally, to perform the indentation, either a displacement boundary condition or a concentrated force was applied on the indenter. It was found that performing the simulation in load or displacement control did not affect the delamination results.

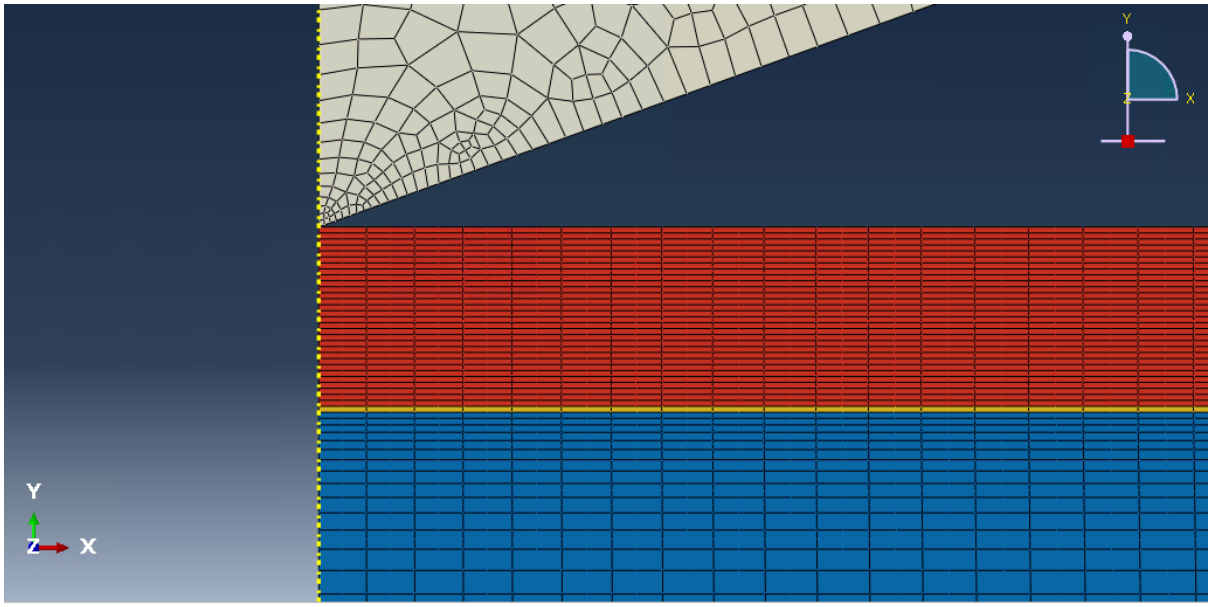


Figure 57: Geometry and mesh in the film (red), cohesive layer (yellow) substrate (blue) and indenter (white)

FEM was performed for the nanoindentation configuration only, and not for nanoscratch testing. This choice was made because nanoindentation provides a well-defined and axisymmetric loading condition, which simplifies the modelling framework and enables reliable numerical convergence. In contrast, nanoscratch testing involves a continuously evolving contact geometry, combined normal and tangential loading, and high parameter sensitivity as observed in Chapter 3, all of which introduce significant additional complexity and uncertainty into the modelling framework. For these reasons, nanoindentation was selected as the preferred configuration for parametric modelling, enabling investigation of the effects of elastic modulus, yield strength, and interfacial cohesive properties on the competition between plastic deformation and delamination, while maintaining a controlled and reproducible loading condition.

4.3. Results and Discussion

4.3.1. Creep, Elastic Modulus and Hardness Measurements

Creep P1-Si

Indents with hold times of 10, 30, 60 and 150 seconds were performed on P1-Si to investigate P1 creep properties. The load was kept constant at 200 μN, to ensure that the indenter is still within the film region. The load displacement curves with the different hold times and with no hold time (0 hold) is shown in Figure 58. The plot of creep displacement during the hold time is shown in Figure 59. High creep displacement rate is displayed in the first few seconds of the hold time which decreases with increasing hold time. Viscoelastic recovery and thermal drift effects during the hold segment were observed in the case of 150 second hold which appear as a decrease in creep displacement. The creep factor described by Feng[93] was calculated for each of the hold times averaged over 4 indents and summarized in Table 13, along with the average elastic modulus and hardness values outputted from the nanoindenter. The creep rate was not calculated for 150 seconds since viscoelastic recovery and thermal drift led to negative creep factors. The effect of creep and thermal drift is minimized when the creep factor is less than 0.1, which is seen using a 60 second hold time. Largest values of modulus and hardness were obtained using no hold time, which is expected as the shape of the unloading curve was steepest, leading to overestimation of properties. Beyond a hold time of 10 seconds, the mechanical properties were seen to remain relatively constant.

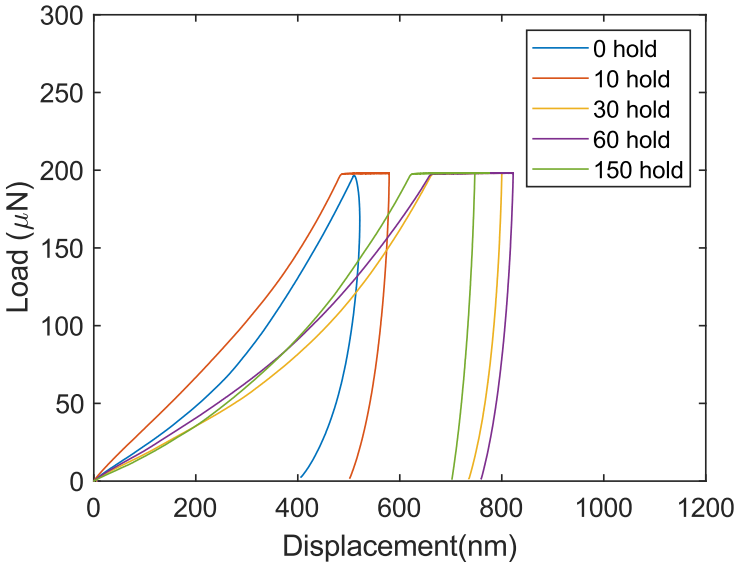


Figure 58: P1-Si Load displacement curve with different hold times

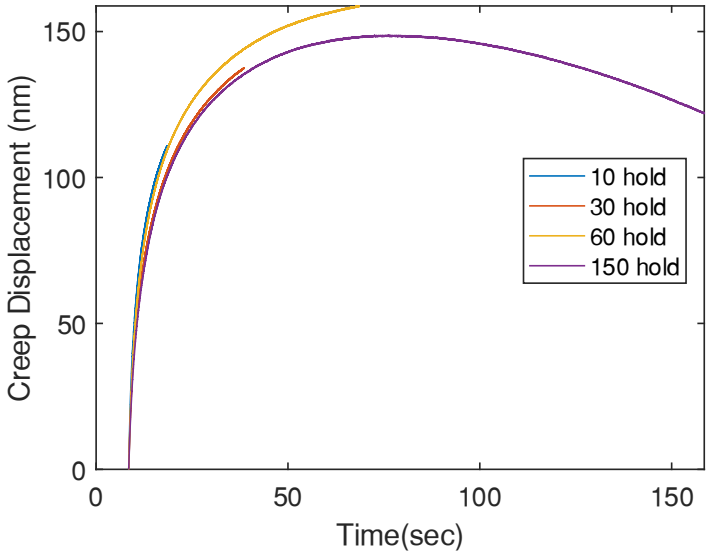


Figure 59: P1-Si Creep displacement for different hold times

Hold Time (seconds)	E (GPa)	H (MPa)	Creep Factor
0	0.62 ± 0.09	15.3 ± 0.002	-
10	0.49 ± 0.1	11.4 ± 3.2	0.29 ± 0.03
30	0.46 ± 0.04	7.6 ± 1.2	0.15 ± 0.02
60	0.59 ± 0.06	8.8 ± 0.09	0.05 ± 0.01

150	0.60 ± 0.05	8.7 ± 0.001	-

Table 13: P1-Si Average elastic modulus, hardness and creep factors for different hold times

Creep PEO-Si

The same creep procedure was conducted on PEO-Si with a peak load of 500 μN for all indents. The load displacement curves and creep displacement graphs are shown in Figure 60 and Figure 61 respectively. Table 14 shows the average elastic modulus, hardness and creep factor for the different hold times. Similar to P1, high modulus and hardness values were observed for the case of no hold time due to the creep bowing of the unloading curve. Out of the four indents tested at 60 seconds hold, one displayed negative creep, therefore the creep factor was not calculated. At 150 second hold, negative creep is also observed. At 30 second hold time, the creep factor is less than 0.1, and no viscoelastic recovery was observed for all indents, therefore this was chosen as the optimal hold time to measure mechanical properties in the next section. Compared to P1, PEO displayed lower levels of viscoelastic creep as indicated by the shape of the creep displacement curves and the lower overall creep factor values.

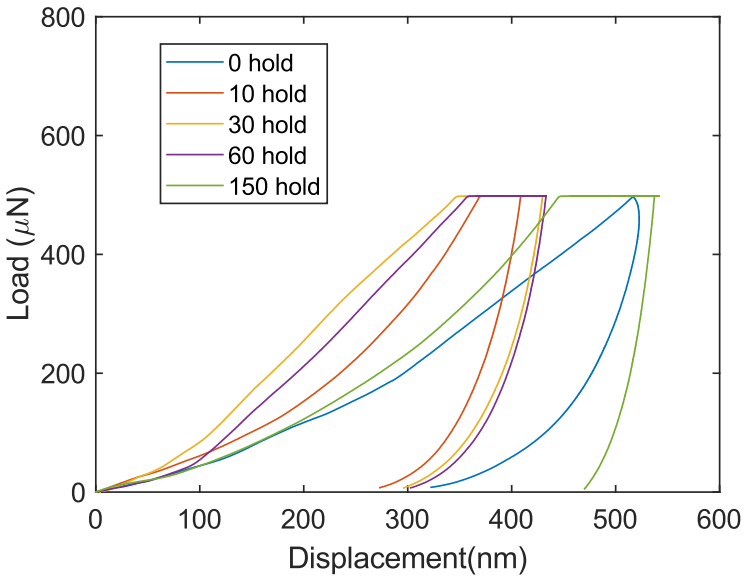


Figure 60: PEO-Si load displacement curve with different hold times

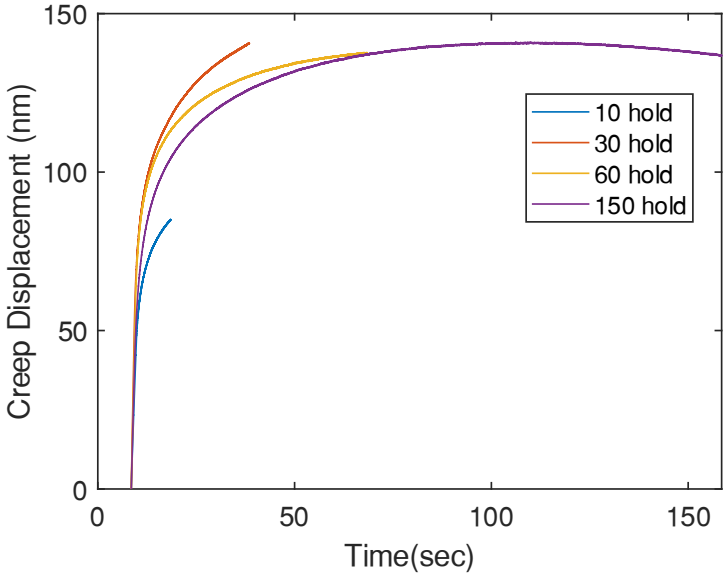


Figure 61: PEO-Si Creep displacement for different hold times

Hold Time (seconds)	E (GPa)	H (MPa)	Creep Factor (%)
0	4.31 ± 0.00	135.2 ± 122.8	-
10	2.65 ± 0.49	78.9 ± 15.4	0.13 ± 0.03
30	3.42 ± 0.74	103 ± 11.5	0.05 ± 0.01
60	4.36 ± 1.18	113.4 ± 46.4	-
150	3.01 ± 1.14	51.8 ± 6.4	-

Table 14: PEO-Si Average elastic modulus, hardness and creep factors for different hold times

Elastic Modulus and Hardness P1-Si

To obtain accurate film-only mechanical properties data, quasi-static indents from 100 µN to 1,300 µN peak load were carried on P1-Si with the appropriate creep hold time of 60 seconds (as determined in the previous section) shown in Figure 62.

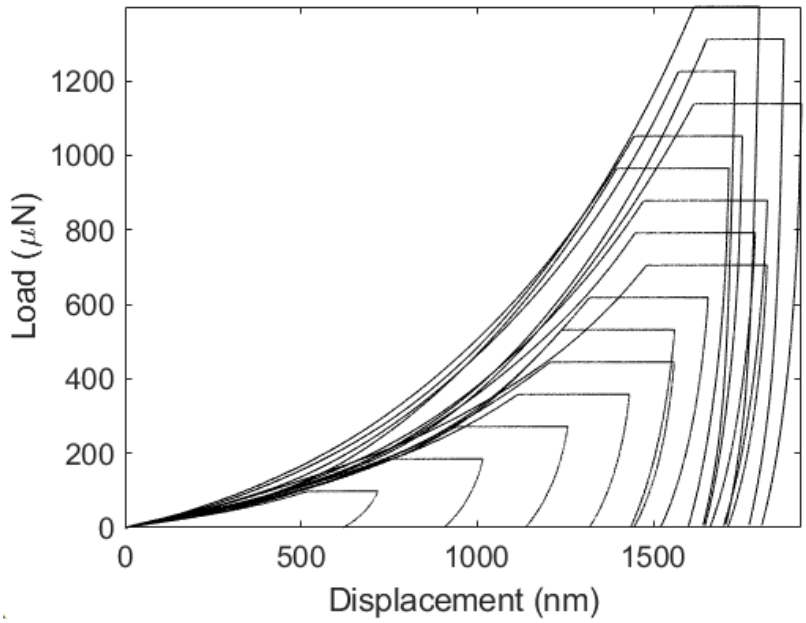


Figure 62: P1-Si quasi-static indents

The results of the elastic modulus and hardness properties are presented in Figure 63. At high indentation depths, high substrate effects were observed that drastically increased the elastic modulus and hardness values measured. Substrate effects are expected when indenting above 10% of the film thickness[33]. However, indenting within 10% (maximum displacement ~ 160 nm) is not possible due to nanoindentation surface effects[108] at such low maximum indentation depths. At depths ranging from 600 – 1500 nm, the hardness values remained relatively constant while modulus increased with increasing depths. The lower influence of substrate effects on hardness is expected since the plastic zone is much smaller than the elastic zone[34,37] and can easily be contained within the film. Using the 11 indents without substrate effect, an average Young's modulus of 0.84 GPa and hardness of 9.11 MPa was found. Tensile tests on bulk P1 performed by Holly Yeo found the modulus of P1 to be 20 MPa, indicating that the nanoindentation properties are overestimate of the tensile elastic modulus. No hardness values of bulk P1 are available for hardness comparison. SPM images of the indent pileup were taken and at high indentation depths a minimal pileup (<10% of indent depth) was observed

(Figure 64) that was mostly overshadowed by the sample roughness, indicating that pileup had minimal to no contribution to the overestimation.

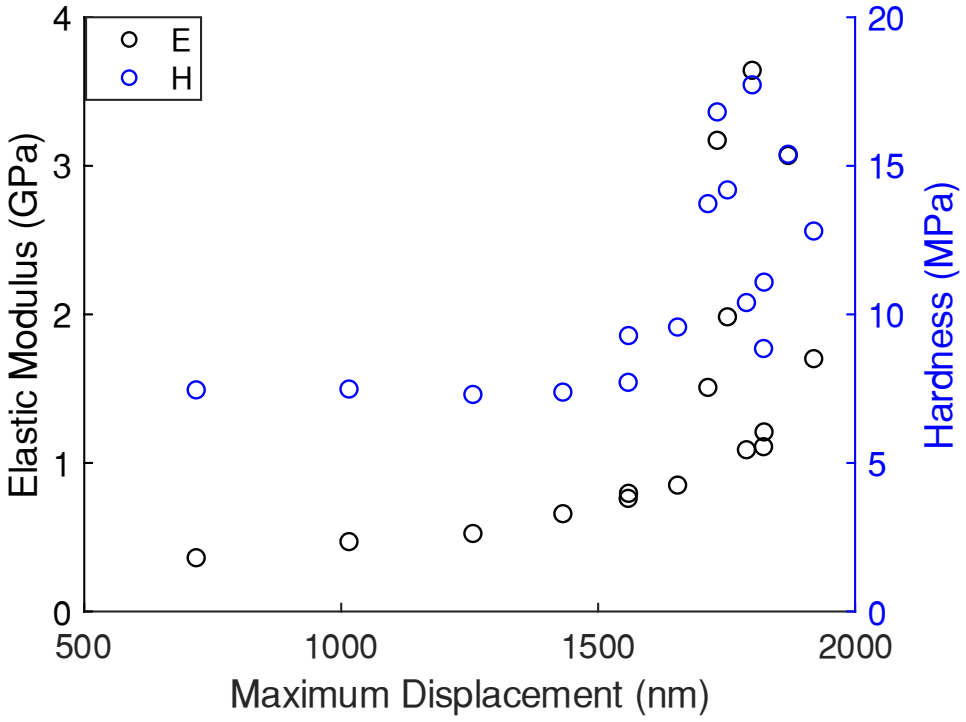


Figure 63: P1-Si elastic modulus and hardness with maximum displacement

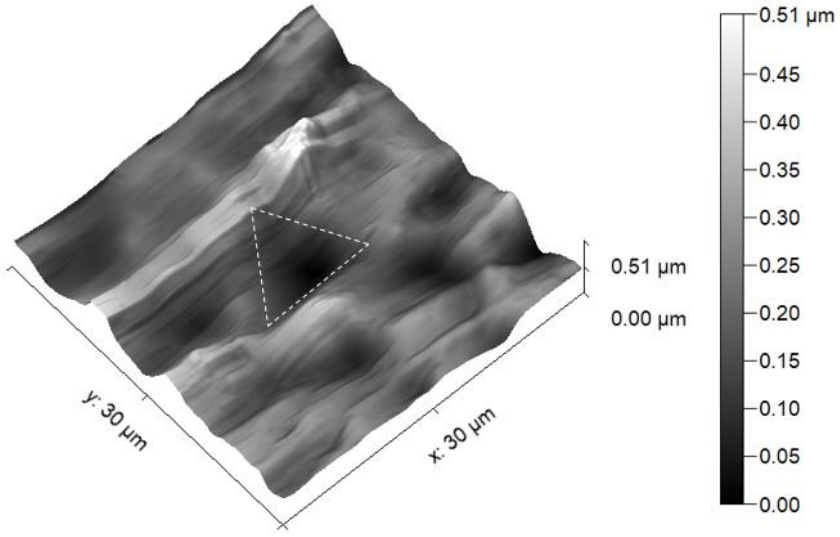


Figure 64: SPM of indent at maximum displacement = 1600 nm

Substrate effect corrections were carried on the modulus through the Saha and Nix method[33], and the results are shown in Figure 65. After corrections, the modulus values

decreased and remained relatively constant, indicating that the substrate effect was the main reason behind the overestimations. The average corrected elastic modulus was found to be 86 MPa which gives much closer results to the tensile test results of 20 MPa. The variations in these two results are likely due to the difference in tensile and compressive behaviour of polymers[121,122]. Furthermore, the method outlined by Saha and Nix provides empirical constants specifically for metals, not for viscoelastic materials, which is expected to lead to some inaccuracies.

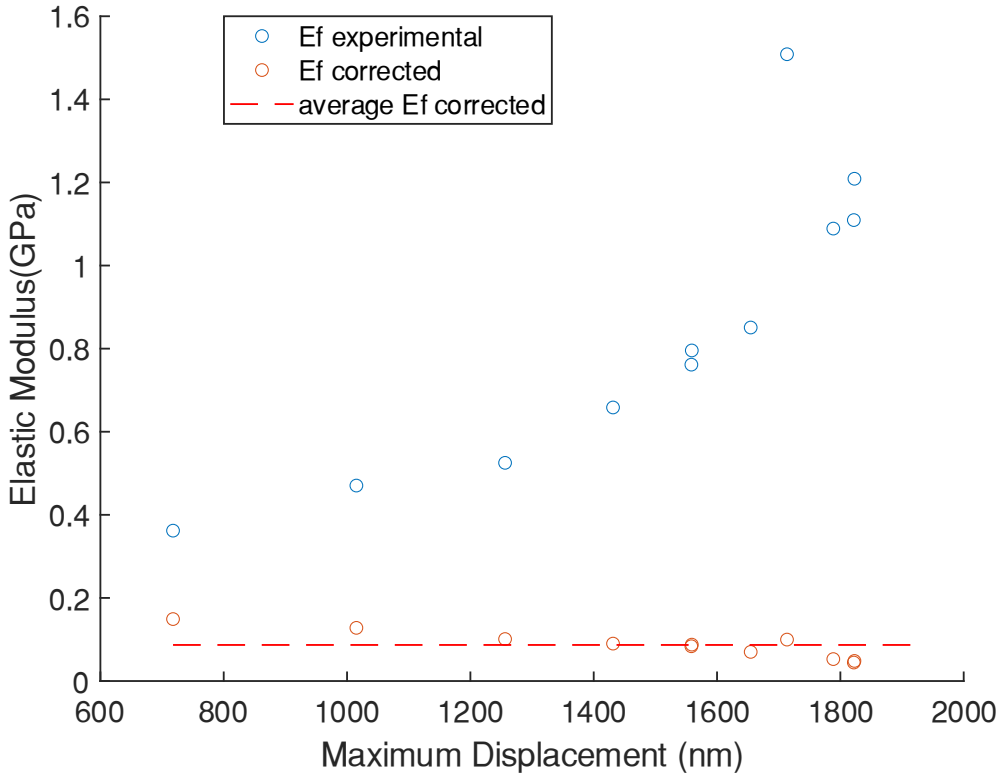


Figure 65: P1-Si substrate effects corrected elastic modulus

Elastic Modulus and Hardness PEO-Si

Using the recommended hold time of 30 seconds for PEO found in the previous section, 16 indents were carried out with the load displacement curves shown in Figure 66. Unlike P1-Si, several curve deviations were observed which indicate that delamination has taken place which will be explored further in the following section. The reduced modulus and

hardness as a function of maximum displacement is given in Figure 67. A large scatter in both the hardness and elastic modulus values are observed. The average elastic modulus was found to be 5.5 GPa and the average hardness equal to 83 MPa. Bulk PEO modulus values vary depending on fabrication process and molecular weight, estimated to range from 30 – 300 MPa[29,123,124]. Literature estimates of PEO with a molecular weight of 10,000 g/mol are extremely limited. The one reference found of spin coated 10,000 g/mol PEO places the modulus at 60 MPa[123]. Even with differences due to processing conditions, the modulus found from nanoindentation is highly overestimated and corrections to the modulus must be made.

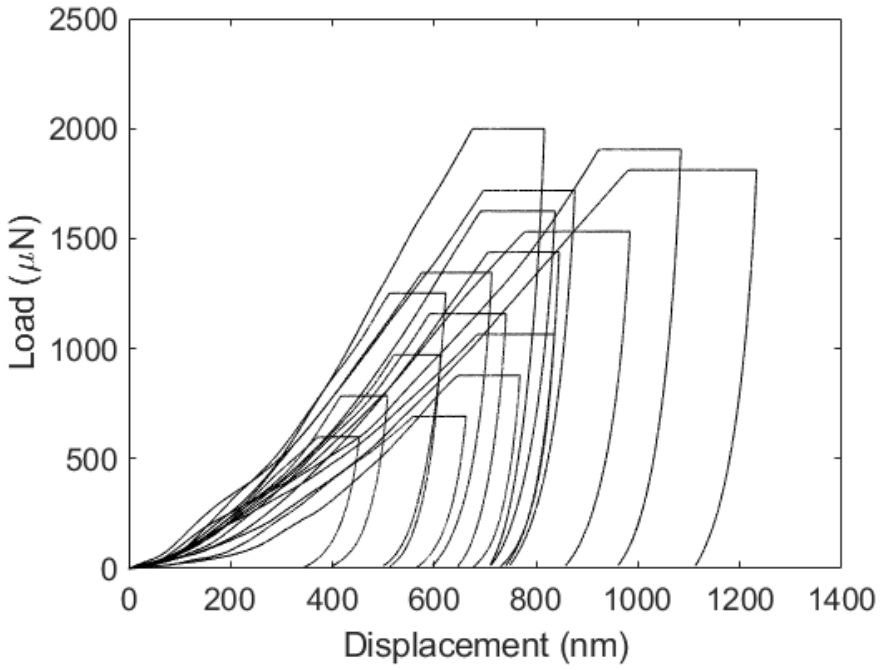


Figure 66: PEO-Si Quasi-static indents

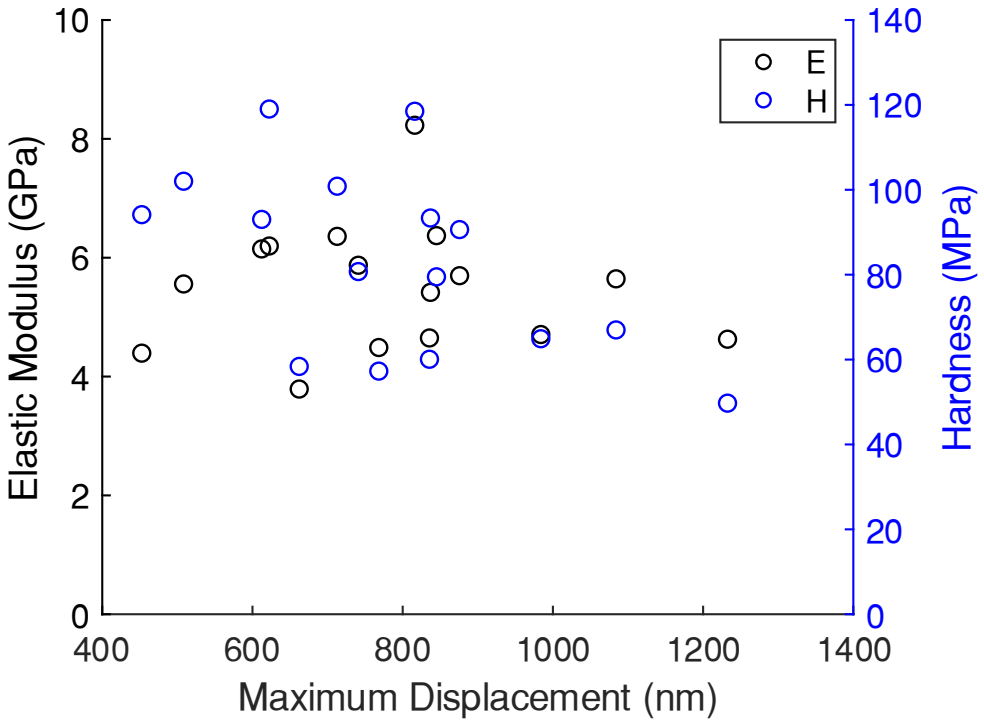


Figure 67: PEO-Si elastic modulus and hardness with maximum displacement

Substrate effect corrections similar to those performed on P1-Si were performed on PEO-Si and the results are presented in Figure 68. An average corrected modulus of 1.59 GPa was found, which is still overestimated compared to the expected PEO range. The scattered mechanical properties seen in Figure 67 suggest that contributions other than the substrate effect are causing the overestimations. In contrast, P1-Si mechanical properties (Figure 63) showed obvious substrate effects with no data scattering. SPM of the indent at 1000 nm maximum displacement is shown in Figure 69, which shows significant amounts of pileup present.

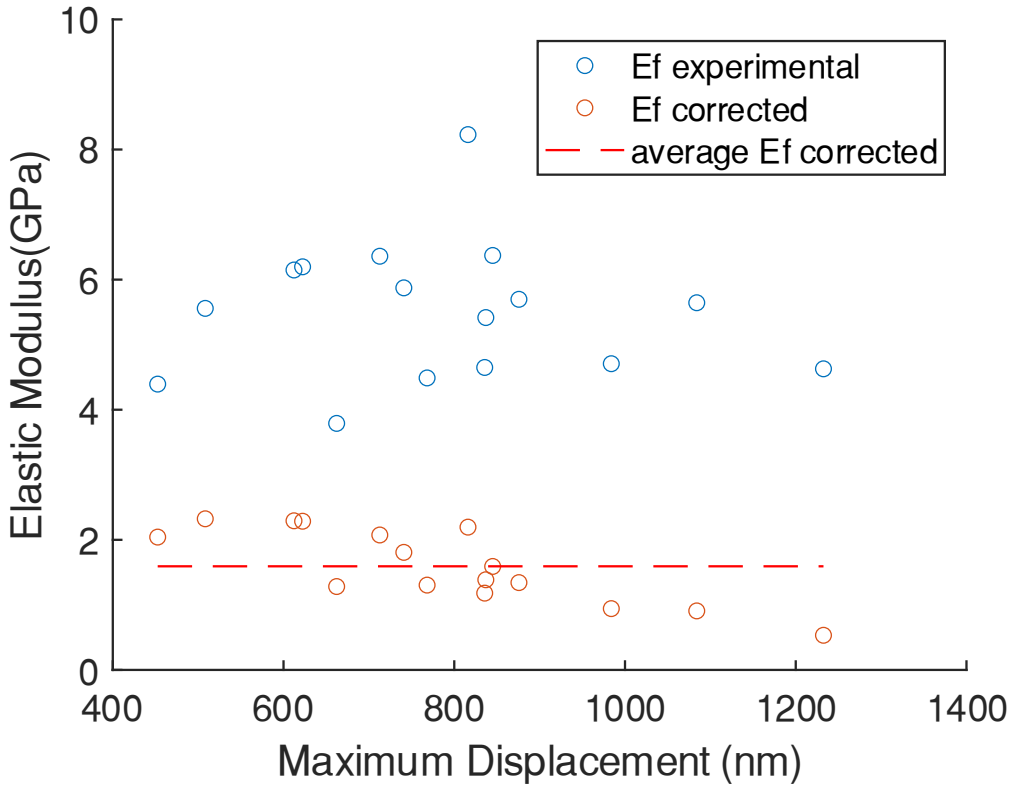


Figure 68: PEO-Si substrate effects corrected elastic modulus

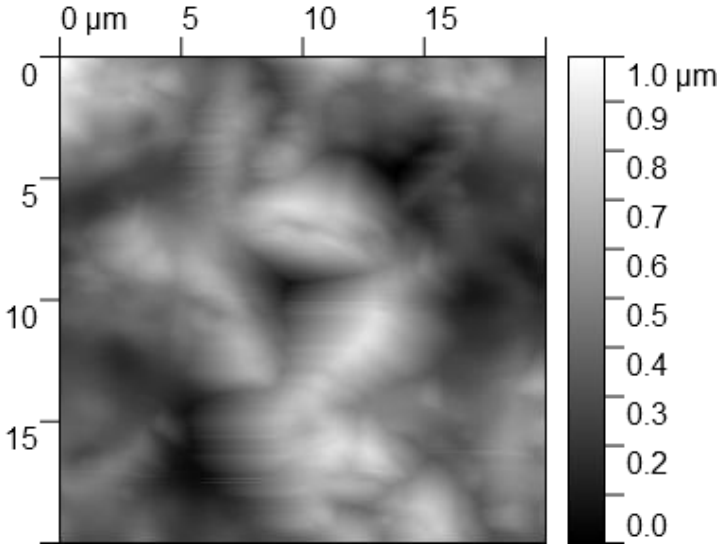


Figure 69: SPM of indent at maximum displacement = 1000 nm

To correct for pileup, the method by Kese et al.[91] described in the methods chapter was used. Indents at constant load of 1500 µN were performed and the results of the Oliver-Pharr contact area (A_{OP}), pileup areas (A_{PU}), nanoindenter elastic modulus (E_{OP}), pileup

corrected elastic modulus (E_{PU}) and finally the elastic modulus corrected for both pileup and substrate (E_{PU+S}) are shown in Table 15. Figure 70 shows the horizontal pileup projection (a_i) measurement from SPM. This horizontal distance is measured from the start of the pile-up near the centre of the indent, to the maximum point of the pileup. The three modulus results are also plotted in Figure 71. The average values for the moduli were E_{OP} = 5.45 GPa, E_{PU} = 3.88 GPa and E_{PU+S} = 0.855 GPa.

A_{OP} (µm²)	A_{PU} (µm²)	E_{OP} (GPa)	E_{PU}(GPa)	E_{PU+S} (GPa)
18.95	16.65	6.33	4.61	1.09
15.65	16.81	6.41	4.44	1.26
26.16	19.67	4.66	3.52	0.62
27.46	23.41	4.49	3.29	0.56
25.06	22.87	4.89	3.54	0.66
18.48	24.52	5.91	3.87	0.94

Table 15: Nanoindenter contact area (A_c') pileup area (A_{PU}), nanoindenter elastic modulus (E'), pileup corrected elastic modulus (E_{PU}) and elastic modulus corrected for both pileup and substrate (E_{PU+S})

The PEO samples used in this study were fabricated with an additional hot-pressing step. Hot pressing PEO composites has been reported to increase the Young's modulus by 5 times as compared to solvent casting[125]. An increase in strength due to hot-pressing has also been reported extensively for other polymers[126–128], owning to a more homogenous and denser microstructure with less voids. Therefore, considering the fabrication conditions used for this sample, the final corrected Young's modulus is within the expected range, with some errors arising from the high surface roughness and irregularities.

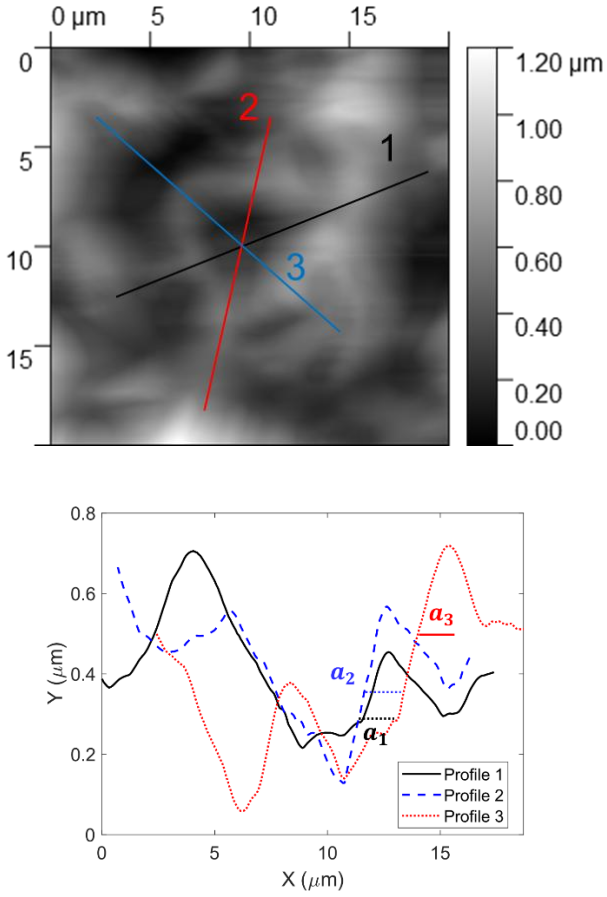


Figure 70: Horizontal pileup projection (a_i) measurement through SPM. The top image shows the indentation site with the three paths used for analysis (profiles 1-3). The bottom image shows the profile plots with a_1,a_2, and a_3 representing the horizontal distance from the centre of the indent to the peak of the pileup

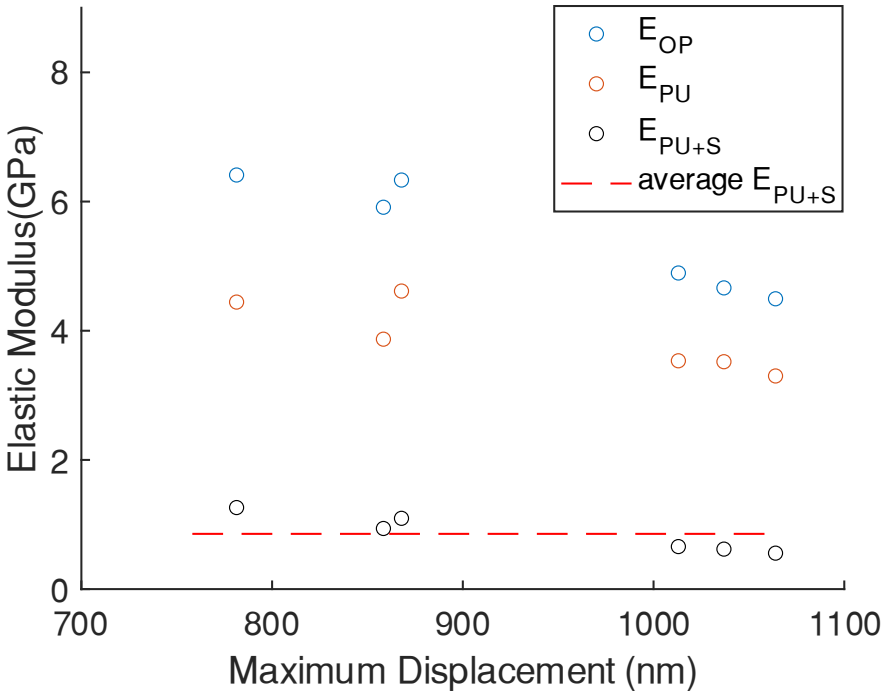


Figure 71: PEO-Si Elastic modulus after pile-up and substrate corrections

4.3.2. Nanoindentation Adhesion

From the quasi-static indents presented in the previous section, no deviations were observed in the P1-Si curves (Figure 62) indicating that no delamination took place. Figure 72 and Figure 73 and shows the FIB cross-sections of the P1-Si indents. No delamination or cohesive failure was observed in both cross-sections. As explained previously, the appearance of the light and dark layers in the polymer region is not due to delamination and is simply an artefact of SEM imaging as seen by comparison to the un-indented interface (Figure 55) and regions far from the indent (Figure 73). Thus, it can be concluded that P1 has simply plastically deformed around the indenter without delamination. No pileup is observed in the SEM images agreeing with the SPM results.

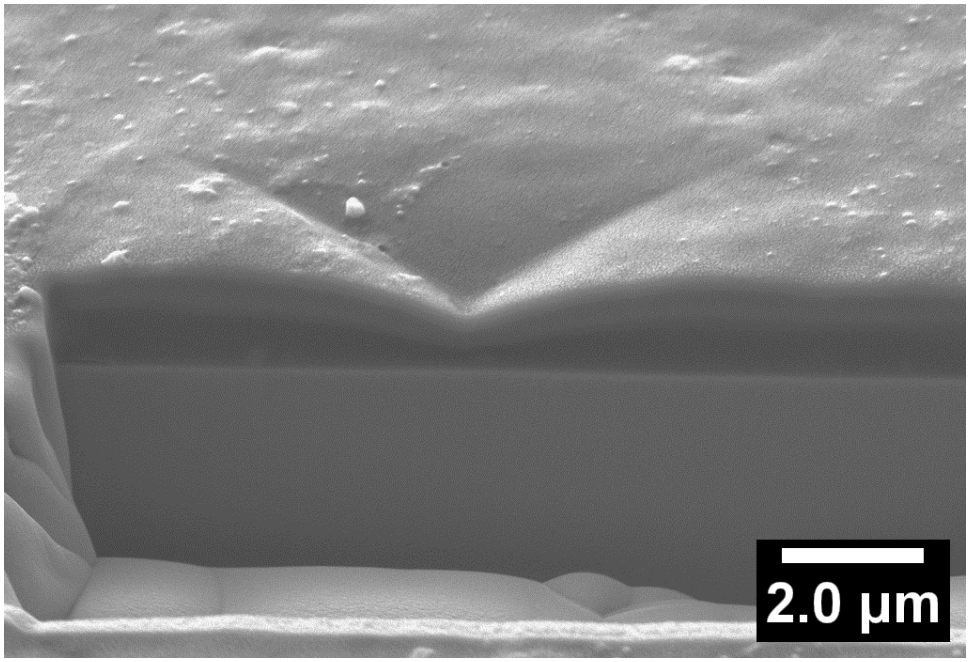


Figure 72: P1-Si indent FIB cross-section (h_{max} = 1136 nm)

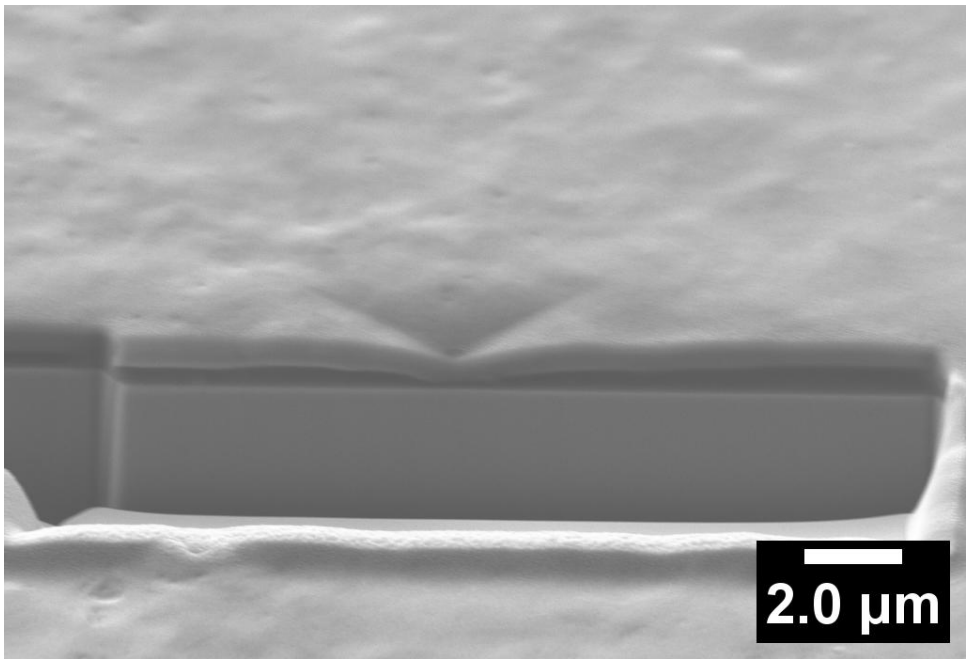


Figure 73: P1-Si indent FIB cross sections (731 nm)

PEO-Si displayed noticeable deviations in the load-displacement curves (Figure 66), with the load at which these deviations occur varying for each indent. This suggests variations in delamination strength and/or film thickness at different indent locations. FIB images of the delaminated indents are shown in Figure 74, Figure 75, and Figure 76 at different maximum

indentation depths. Cohesive failure features are observed in the polymer layer. Along the interface, dark features are seen which suggest delamination. Visually observing delamination in polymers is difficult, as no clear delamination characteristics like blistering are expected. It is possible that delamination occurred during indentation, but due to the film's compliant nature, once the indenter was removed the delaminated film returned to the interface, so no clear gap between the film and substrate is seen. In contrast, the tungsten films tested in the previous chapter had enough rigidity to support the formed blister even after the indenter was removed, leaving a clear delamination gap. Overall, the shape of the load-displacement curves and the presence of features along the interface is sufficient to confirm that delamination occurred.

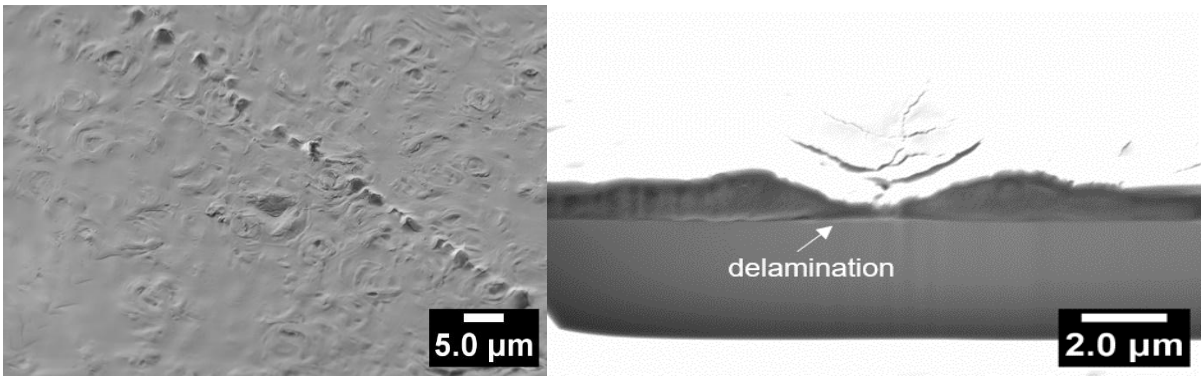


Figure 74: PEO-Si indent FIB cross-section (h_{max} = 944 nm)

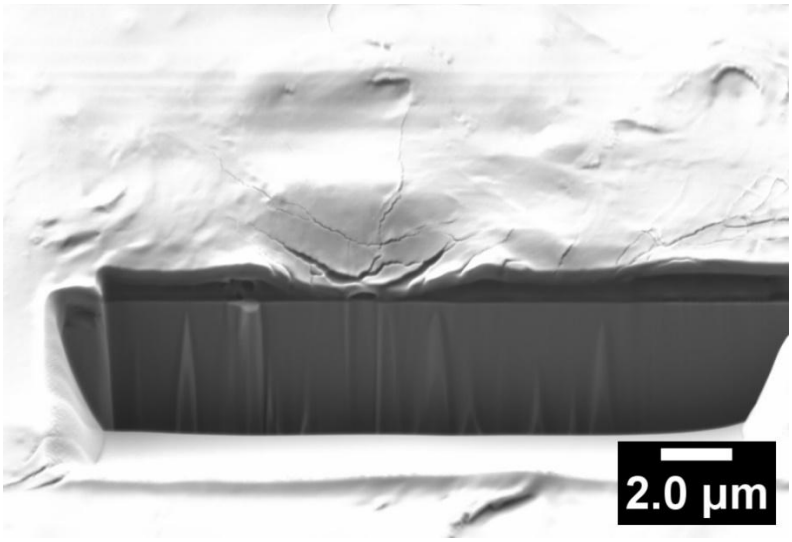


Figure 75: PEO-Si indent FIB cross-section (h_{max} = 1000 nm)

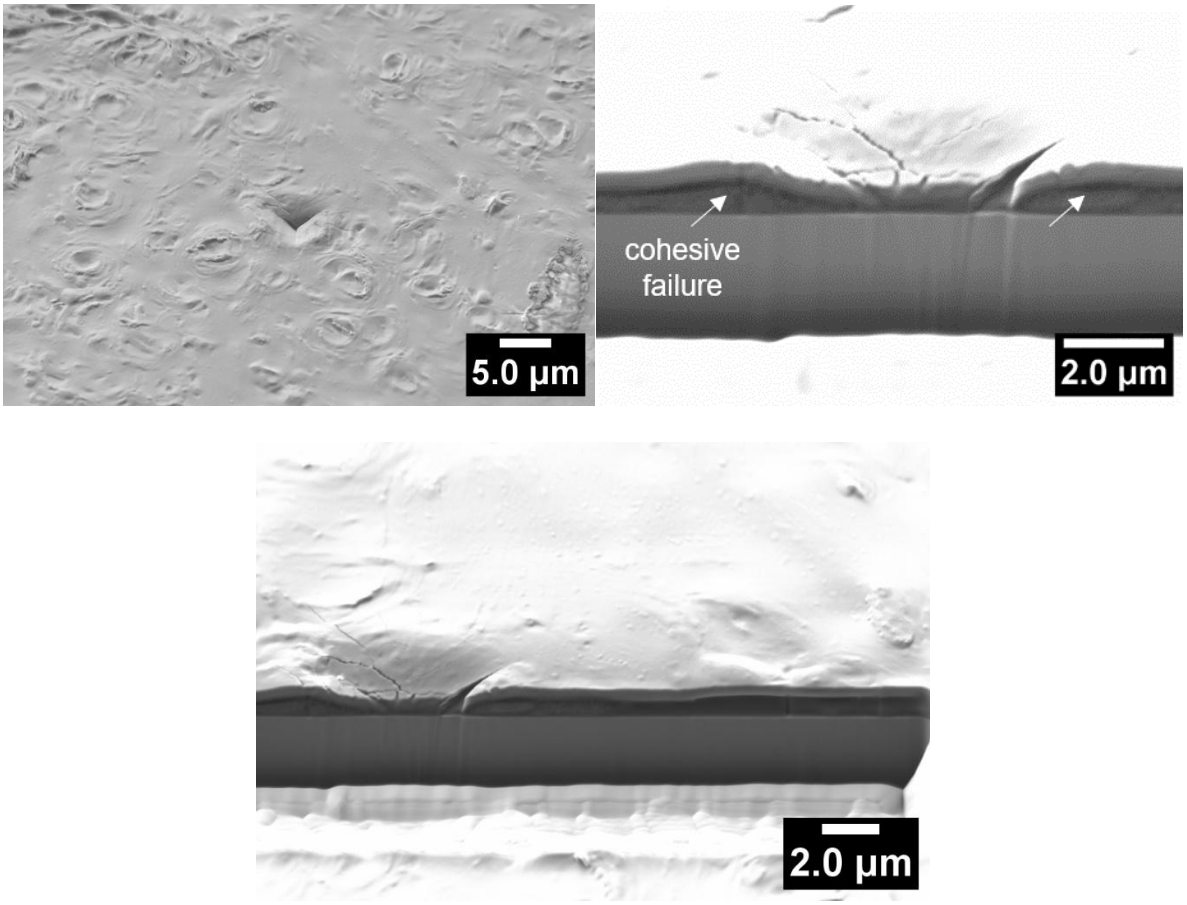


Figure 76: PEO-Si indent FIB cross-section (h_{max} = 1050 nm)

Power Fit FEM investigation

Energy methods in literature for evaluating thin film delamination energy use the portion of the load displacement curve after delamination to fit a power curve backwards to the origin, and the difference in areas is calculated as the work of delamination[48,49,52,53]. Immediate questions arise on the validity of using the data after delamination takes place, as delamination is expected to change the apparent system response. To investigate this, FEM was used to observe the change in thin film stiffness before and after delamination. This was attempted on experimental curves however the experimental noise was too high to observe the stiffness evolution. Figure 77 shows the loading curve and the stiffness for each point in a 10 µm thin film showing a clear delamination point at 5,000 nm displacement.

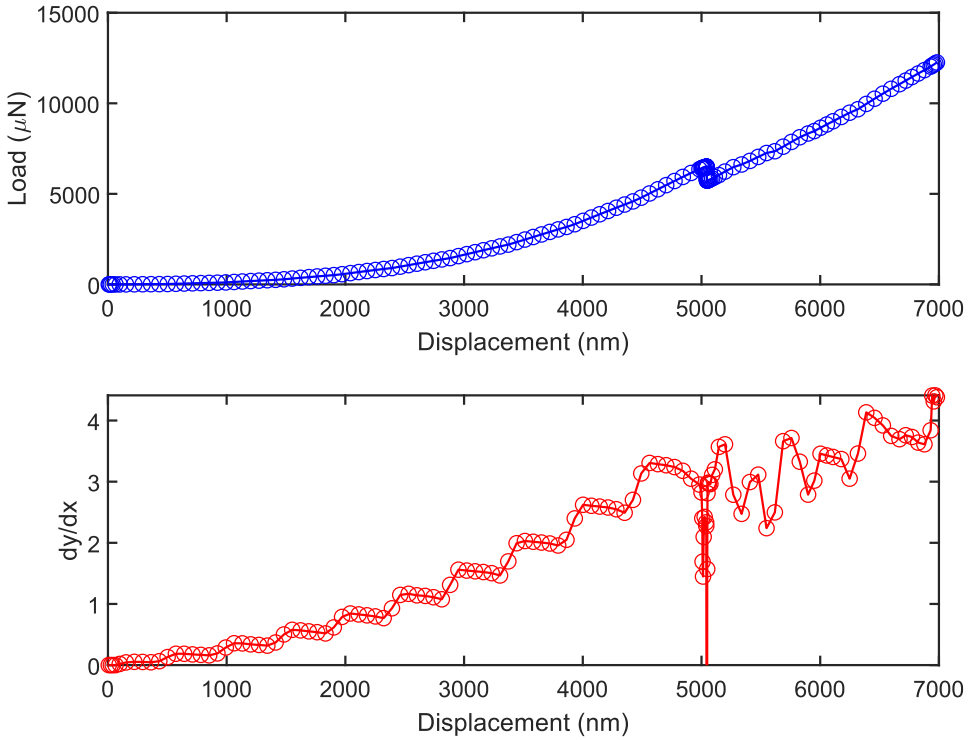


Figure 77: Loading curve (top) and stiffness evolution (bottom) in delaminated thin film (FEM)

A change in system stiffness is observed after delamination takes place. The model was repeated keeping the system properties the same and changing the maximum indentation depth to observe the change in Young's modulus determined through the Oliver-Pharr method, plotted in Figure 78. As the maximum indentation depth increases, the Young's modulus increases due to substrate effects. The thin film in this model had a Young's modulus of 50 MPa. At 10% indentation depth (1 μm), the Oliver-Pharr method outputs a correct value of the film modulus, agreeing with the 10% rule[33]. Further increases in the maximum depth however lead to highly overestimated Young's modulus. At maximum indentation depth of 6 μm after the onset of delamination, the slope of the increase of Young's modulus changes, indicating that delamination is an important event affecting the stiffness of the curve. Therefore, using the experimental data after delamination occurs may not accurately reflect the thin film tested.

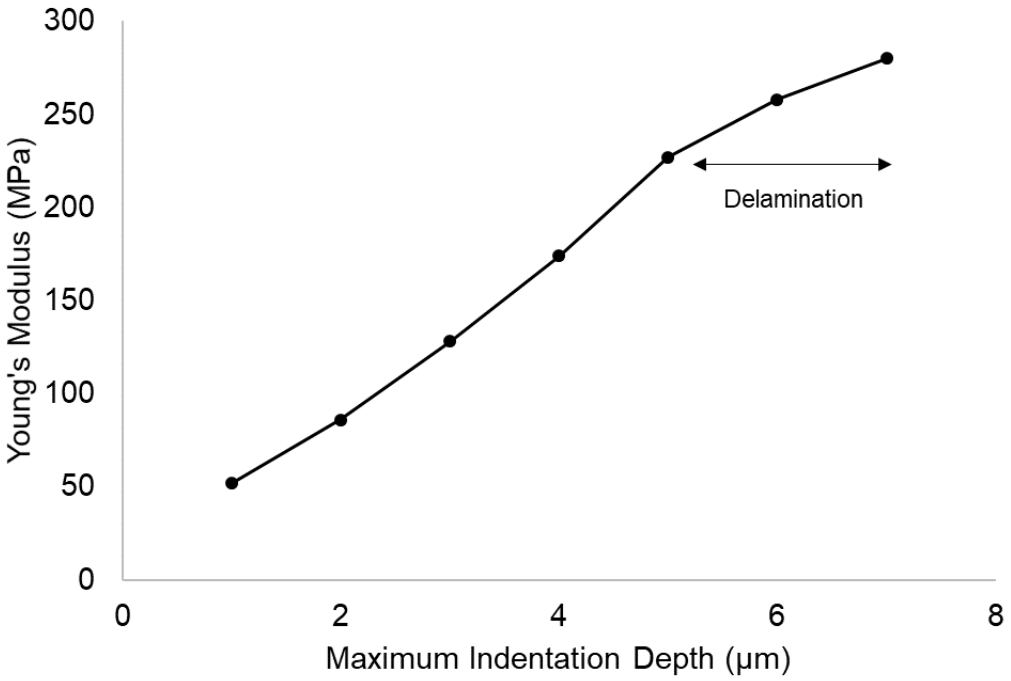


Figure 78: Young's modulus vs maximum indentation depth for a delaminated thin film (FEM)

An alternate way of analysing the load displacement curves is to extrapolate the initial portion of the load displacement curve, since it would be more characteristic of the film and is unaffected by delamination. This method of curve analysis is frequently applied on the fragmentation step to quantify the fracture energy of films[54]. However, in the literature it has not been used to quantify work of delamination in polymers. FEM allows the input a known value of delamination energy (G = 1 J/m^2), followed by curve analysis to quantify the delamination energy to investigate the accuracy of both methods. Figure 79 and Figure 80 show the difference in work of delamination obtained using fitting after and before delamination respectively. Using the radius of delamination as seen in Figure 81, and assuming the area of delamination to be a perfect circle, the delamination energy can be calculated with results summarized in Table 16.

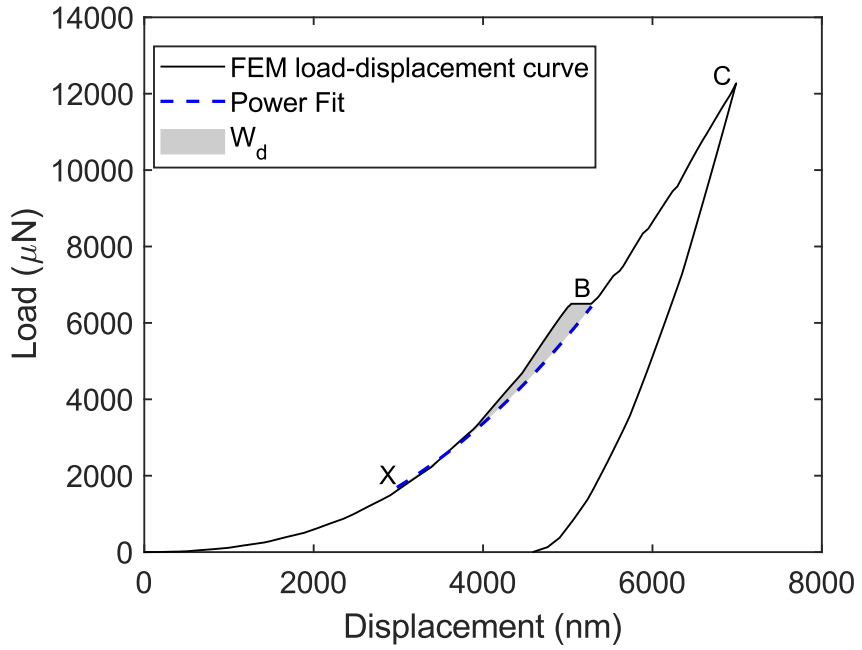


Figure 79: Delamination work using fitting after delamination. The power fit curve is fitted from points B and C and extrapolated backwards to point X. The grey area denotes the calculated work of delamination (difference between curve and power fit line)

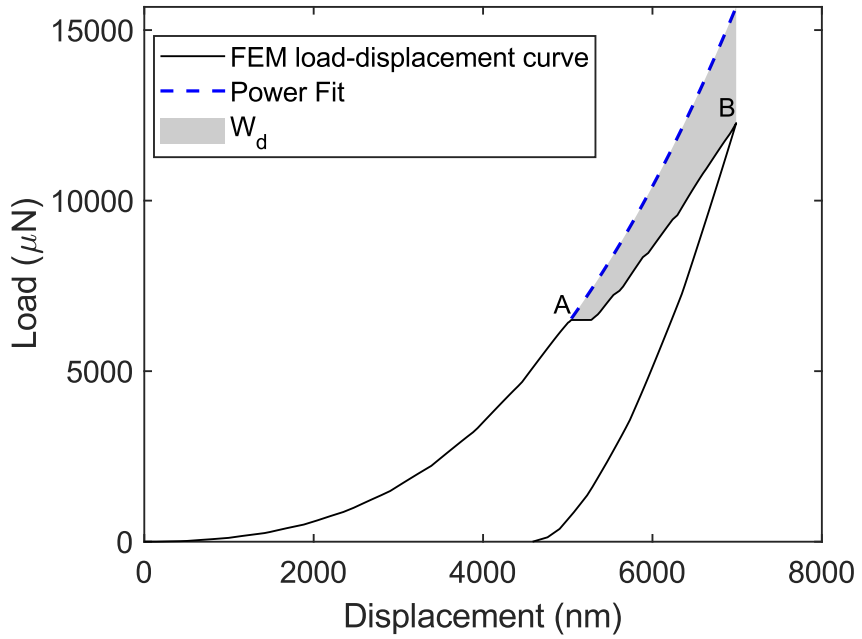


Figure 80: Delamination work using fitting before delamination. The power fit curve is fitted from the origin to point A. The grey area denotes the work of delamination (difference between power fit line and the curve).

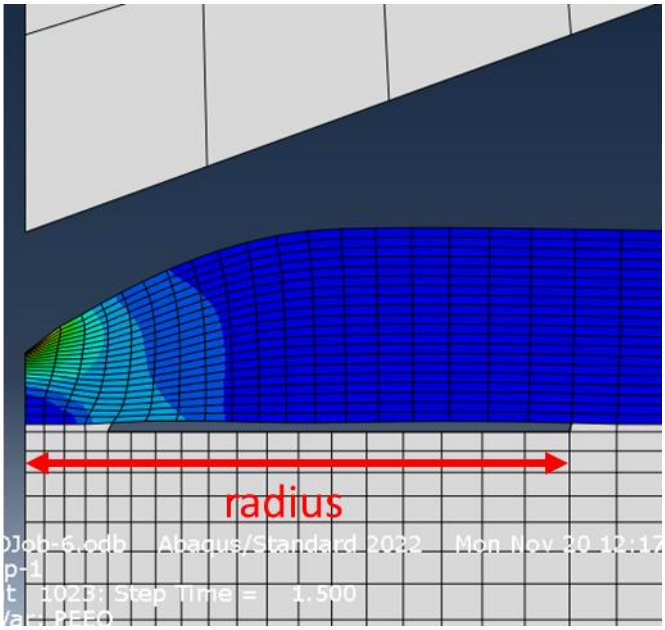


Figure 81: Delamination radius from FEM

		Fitting before delamination		Fitting after delamination	
h_{max} (µm)	**Radius (µm)**	**W_d (nJ)**	**G (J/m^2)**	**W_d (nJ)**	**G (J/m^2)**
6	21.8	0.99	0.66	0.57	0.38
7	28.4	3.26	1.29	0.60	0.24
7.5	30.9	3.57	1.19	0.45	0.15
8	36.3	6.66	1.61	0.39	0.094

Table 16: Calculated values of delamination work and energy using fittings before and after delamination

Fitting the curve before delamination outputs more accurate values of G as compared to fitting after delamination, which significantly underestimates the work of delamination. The variations in the results of fitting before delamination compared to the input value of G may be due to the assumption of the indentation area calculated as a perfect circle. The work of delamination obtained by fitting after delamination does not change significantly with increasing maximum loads, due to the size of the deviation in the curve remaining relatively

similar. Fitting after delamination assumes that delamination is an instantaneous event that only occurs during the curve deviation and ends after the deviation. However, FEM results show the radius of delamination increasing as the maximum indentation increases, suggesting that delamination is a gradual process with increasing levels of delamination with increasing loads. Therefore, it is necessary to analyse the curve from the start of delamination until the end of the loading curve when delamination evolution stops, as demonstrated in fitting before delamination. From these results, we conclude that fitting before delamination provides more accurate values for the delamination energy therefore, this method is used in the following section.

Quantifying PEO-Si Delamination Energy

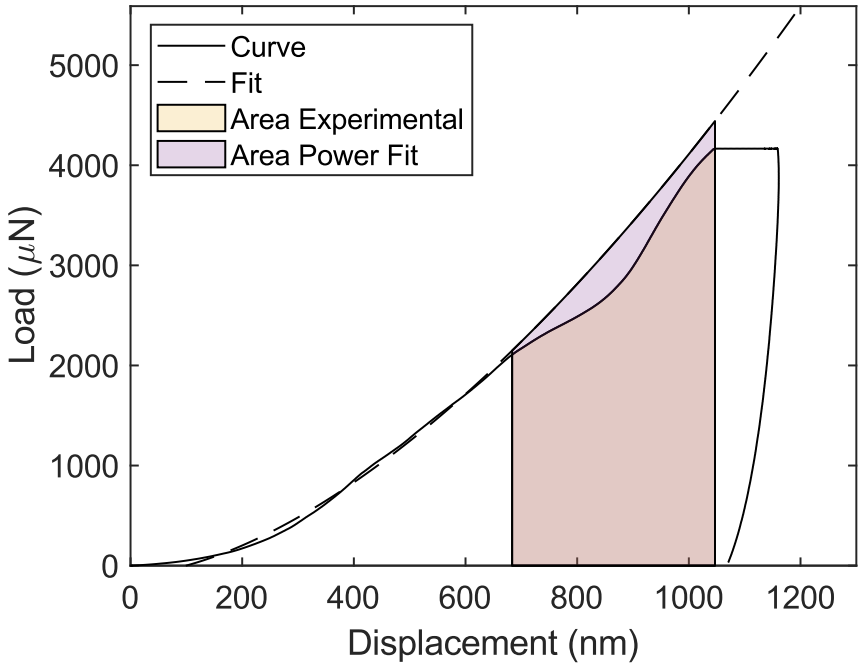


Figure 82: PEO work of delamination at 4166 μN peak load

Figure 82 shows the work of delamination calculation on a PEO-Si indentation curve with a maximum load of 4166 μN. The work of delamination was calculated to be 0.1056 nJ by subtracting the areas under the two curves. Figure 83 shows the indent at 4166 μN peak load

imaged through SPM, revealing elevated regions around the indent. One difficulty faced in measuring the delamination area is differentiating between pileup and delaminated areas. This issue does not arise with brittle films, which display no pileup and clear raised blisters after delamination. Papers evaluating polymer delamination use the total "elevated" area around the indent as the delamination area, with no mention of the pileup area contribution[49,52,53]. Since no thorough explanation of the pileup contribution was found in the literature, the total elevated area around the indent was used in the calculations. The manually drawn delamination area mask shown in Figure 84 was calculated to be 110 μm². The delamination area was also calculated from the SEM image by measuring the delamination radius and by assuming the indentation area to be a perfect circle, resulting in a delamination area of 115 μm². The SPM measurement assumes that the region under the indent is not delaminated (pinned buckle geometry), whereas the SEM measurement assumes an unpinned delamination geometry. Although FIB images did not clearly indicate whether PEO-Si delamination was pinned or unpinned, pinned buckle geometry is expected for compliant polymer films with no film residual stress. Nonetheless, the assumption of a perfect circle delamination area outputs values very close to that from SPM. The delamination energy for the indent at 4166 μN peak load was calculated to be 0.96 J/m^2.

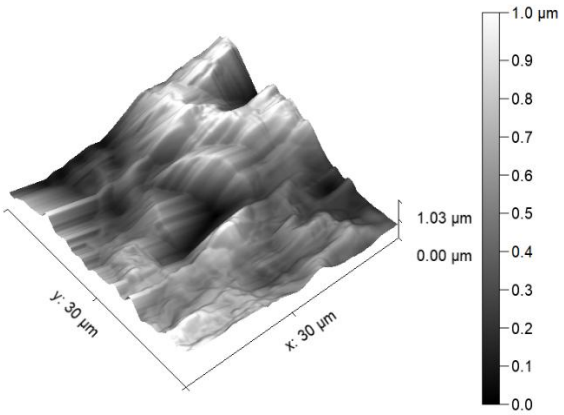


Figure 83: 3D SPM of indent at 4166 μN peak load

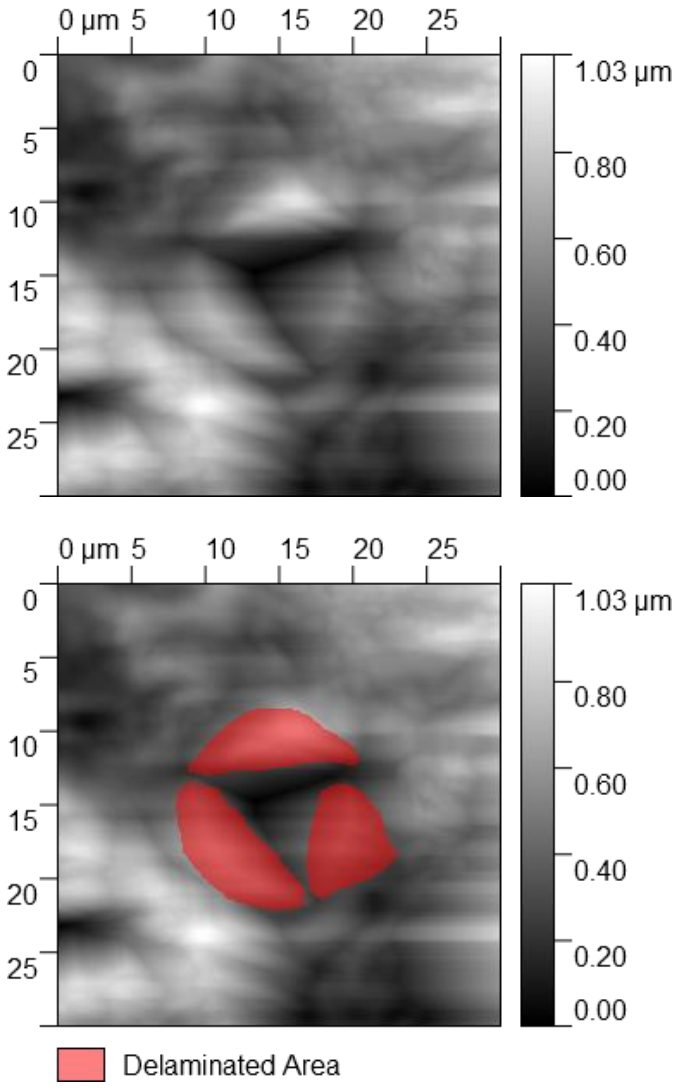


Figure 84: SPM of indent at 4166 µN peak load with delaminated area mask

This process was repeated for several indents with varying peak loads and the results are summarized in Table 17. The delamination areas were measured through the SPM method described earlier. The delamination energy was found to range between 0.92 – 1.72 J/m^2 with no clear dependence on applied load. The average delamination energy value of 1.17 ± 0.34 J/m^2 is realistic and within the expected range for polymers on silicon (1 J/m^2)[129]. The delamination energy is lower than that of PEO on different substrates (3.2 - 4.5 J/m^2)[117,118], however different experimental methods were used in those studies. Additionally, the surface roughness of the silicon wafers used in these experiments is very low (1 nm), and higher

substrate roughness is expected to prevent or delay delamination leading to a larger delamination energy[130,131].

Peak Load (µN)	Work of Delamination (nJ)	Area of delamination (μm^2)	Delamination energy G (J/m^2)
2103	0.0412	44.57	0.92
3478	0.1238	71.87	1.72
3707	0.0901	70.82	1.27
3936	0.0903	95.24	0.95
4166	0.1056	115.41	0.96

Table 17: Delamination energies for PEO-Si

4.3.3. Nanoscratch Adhesion

P1-Si Nanoscratch

5 scratches were performed on P1-Si film with scratch parameters and orientations summarized in Table 18. All scratches were performed in edge forward orientation except scr4 which was performed in face forward orientation. An optical image of the scratches is shown in Figure 85. As expected from the scratch deformation maps[111], plastic deformation was the only observed failure mechanism with no chipping or fragmentation occurring. As the load is increased, the normal displacement of the indenter increases until it finally reaches the film thickness and substrate exposure is observed. Figure 86 shows the FIB cross section of the scratch showing only pileup and substrate exposure. As explained previously, the contrast in the polymer film is due to the low accelerating voltages used in imaging, and is not a feature of delamination, as seen in the FIB interface images in Figure 55. Scr4 displayed a higher level of substrate exposure as compared to scr3 due to the face forward orientation able to plough and remove more of the thin film polymer[132]. Since substrate exposure is the only event

occurring in these scratches, L_c was chosen to be the critical load at which substrate exposure first occurs.

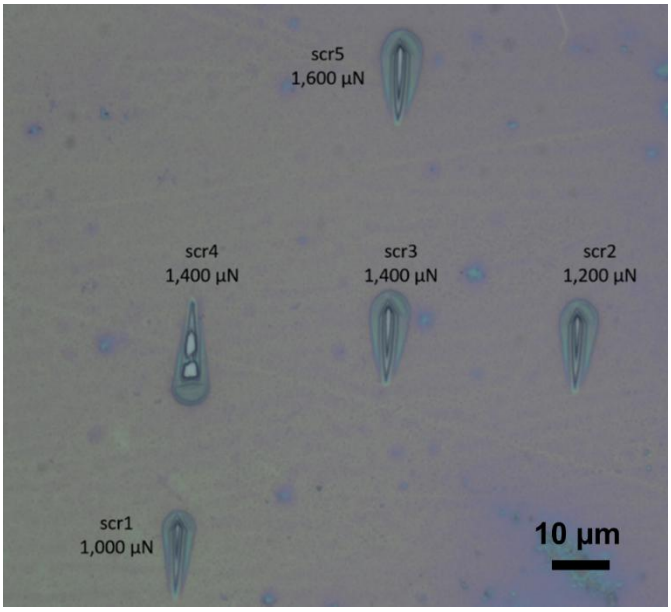


Figure 85: P1-Si film nanoscratch

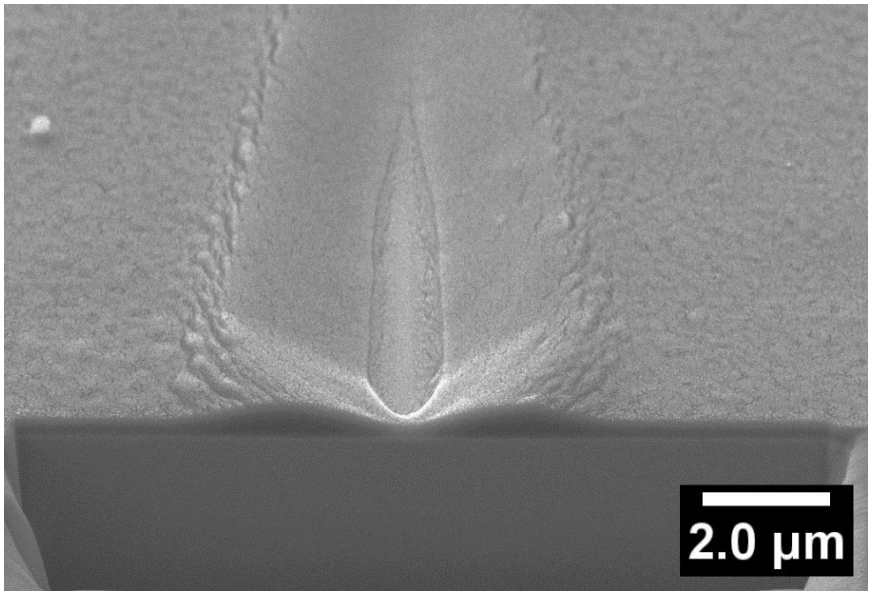


Figure 86: P1-Si FIB cross-section of scratch

	Peak Load (µN)	Scratch time	Scratch length (µm)	h_c (nm)	L_c (µN)	Substrate area exposed %
scr1	1,000	20	14	314	517	1.5 %
scr2	1,200	20	14	308	516	3.1 %
scr3	1,400	20	14	300	520	4.1 %
scr4	1,400	20	14	310	522	11.8 %
scr5	1,600	20	14	332	517	5.2 %

Table 18: P1-Si scratch parameters, critical force and percent substrate area exposed

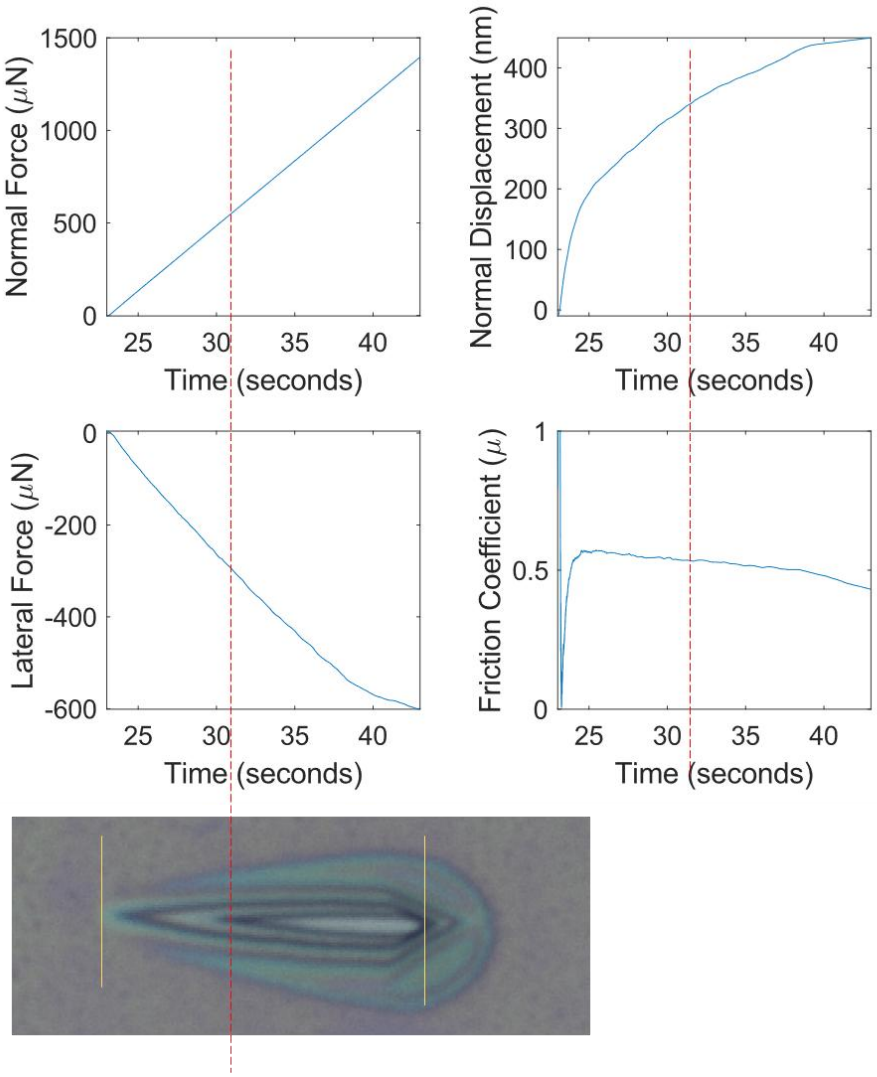


Figure 87: Scr3 scratch graphs (red dotted line denotes start of substrate exposure)

The scratch graphs for scr3 are presented in Figure 87 with the start of substrate exposure marked with the red dotted line. No clear discontinuity in the graphs is observed which is expected as no sudden energy release phenomenon such as fragmentation or chipping occurs. For all the scratch parameters tested, L_c was found to be constant at around 520 μN. The normal displacement at failure for all scratches was also found to be constant at around 310 nm, indicating the film thickness in that region. A decrease in the friction coefficient is seen due to the lower friction coefficient of silicon (μ = 0.07)[133] as compared to P1 (μ~0.5). Typically, material ploughing is associated with an increase in friction coefficient [114], however the absence of friction coefficient increase in the scratch plots suggests that P1 is easily removed by the indenter with minimal ploughing friction. From the FIB image in Figure 86, the thin film thickness is around 280 nm with a few hundred nanometer variation between areas expected. Therefore, it is evident that the failure criteria chosen in this test is dependent on film thickness and film mechanical properties, and not indicative of the adhesive strength of the interface. Due to this, further analysis to extract adhesive strength was not possible. Nonetheless, these results provide a useful indication of P1's scratch resistance behaviour.

PEO-Si Nanoscratch

Scratches were performed on PEO-Si with the scratch parameters summarized in Table 19. At a low peak load of 400 μN (Figure 88), the scratch displayed parabolic cracking followed by fish scaling at the end of the scratch, both of which indicate cohesive failure. Fish scaling is a common deformation behaviour observed in weak, ductile polymers[77,78]. Due to the polymer's ductility, the polymer faces slipping, drawing, followed by substrate compression which leads to the formation of the fish scale feature. At higher peak loads (Figure 89 and Figure 90) material removal is observed. At the onset of material removal, a sudden release in energy occurs due to the drop in resistive forces. Rear pileup is observed in all the

scratches with no side pile-up. SPM images of scratch 4 is shown in Figure 92, confirming little to no side pile-up and high amounts of rear pile-up measuring to a height of 1 μm.

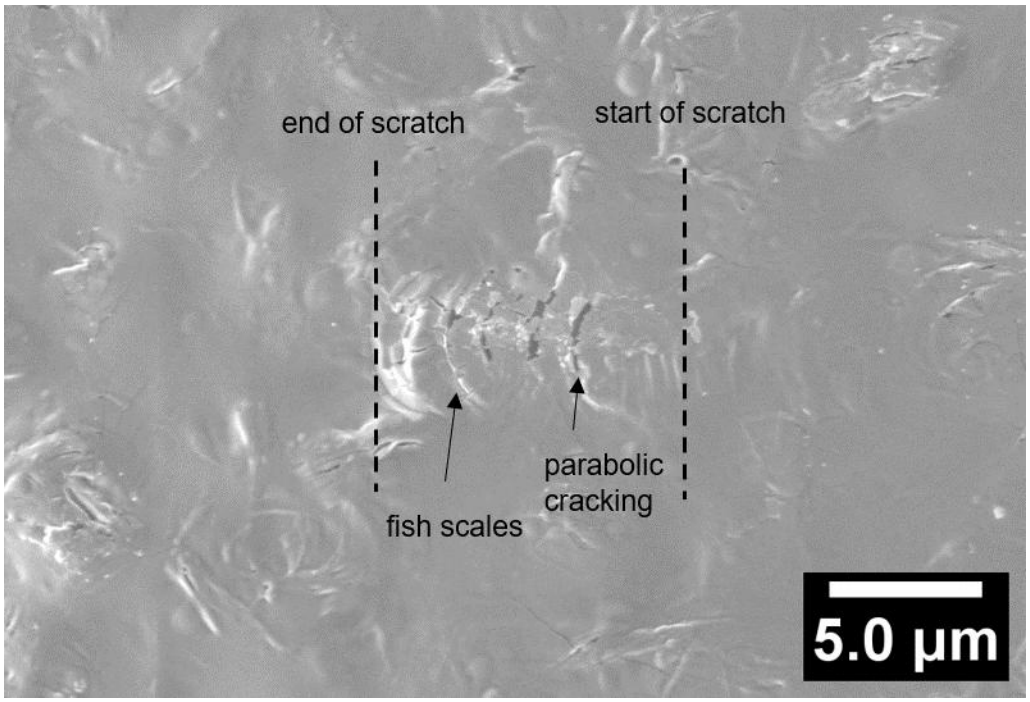


Figure 88: SEM of scratch at 400 μN peak

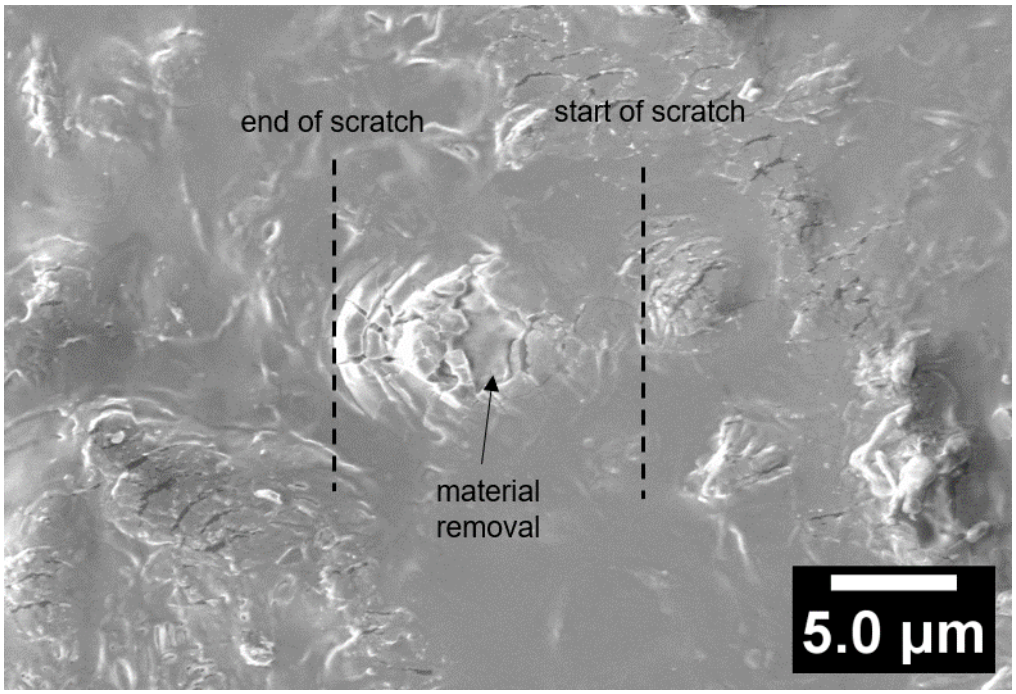


Figure 89: SEM of scratch at 500 μN peak

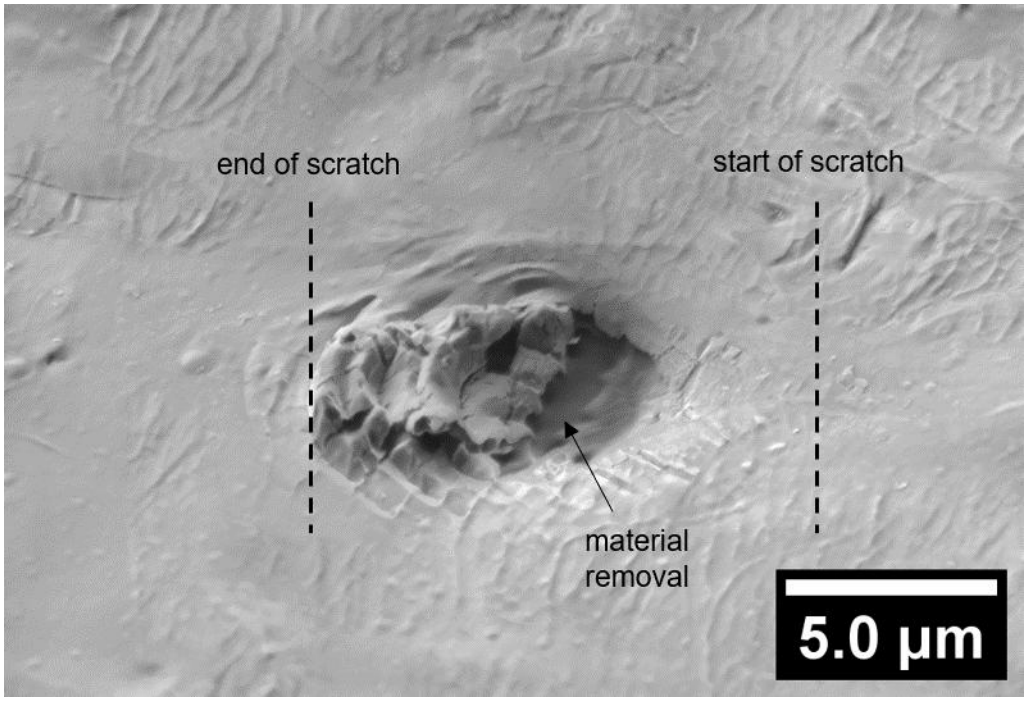


Figure 90: SEM of scratch at 700 µN peak (taken at 54° tilt)

The scratch graphs for scratch 4 are given in Figure 91. The dotted red line in the graph corresponds to the point in the SEM image where material removal was first observed, and a sudden change in the indenter normal displacement graph was observed. Laugier scratch model[62] was applied to determine the delamination energy and the results are summarized in Table 19. The film coefficient of friction needed for the calculations was found from constant low load scratches to be equal to 0.3. The film modulus value used for calculation was 855 MPa, found from nanoindentation after substrate and pileup corrections. The calculated delamination energy is seen to range from 0.42 – 3.48 J/m^2. The variations in delamination energy are expected due to the variations in scratch parameters and the uncertainties in evaluating the critical point from the scratch graphs. Unlike the tungsten results in the previous section, the fracture mechanics occurring during polymer nanoscratching results in a less intense energy release, leading to a less obvious critical point in the scratch graphs. Nonetheless, using a combination of scratch graphs and SEM images to evaluate the critical point results in relatively uniform delamination energies with expected variations from the

parameters. The repeatability of the scratch results was investigated at 900 µN, and the delamination energy was seen to be relatively constant. The average scratch delamination energy from the entire set of scratches was found to be 2.3 ± 0.9 J/m^2.

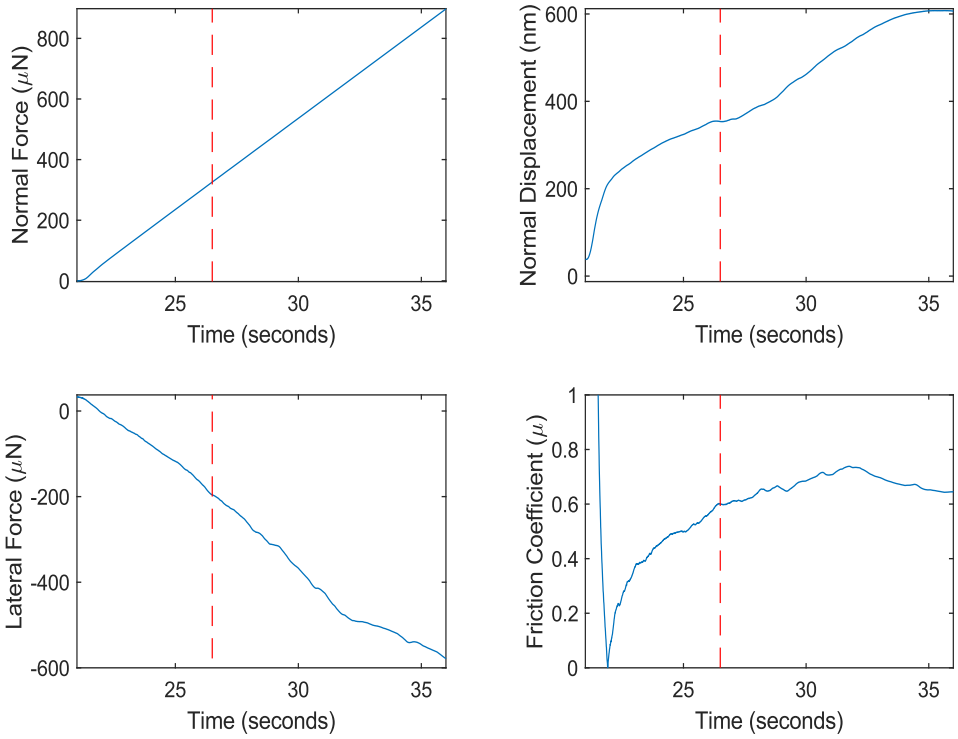


Figure 91: Scratch 4 at 800 µN scratch graphs

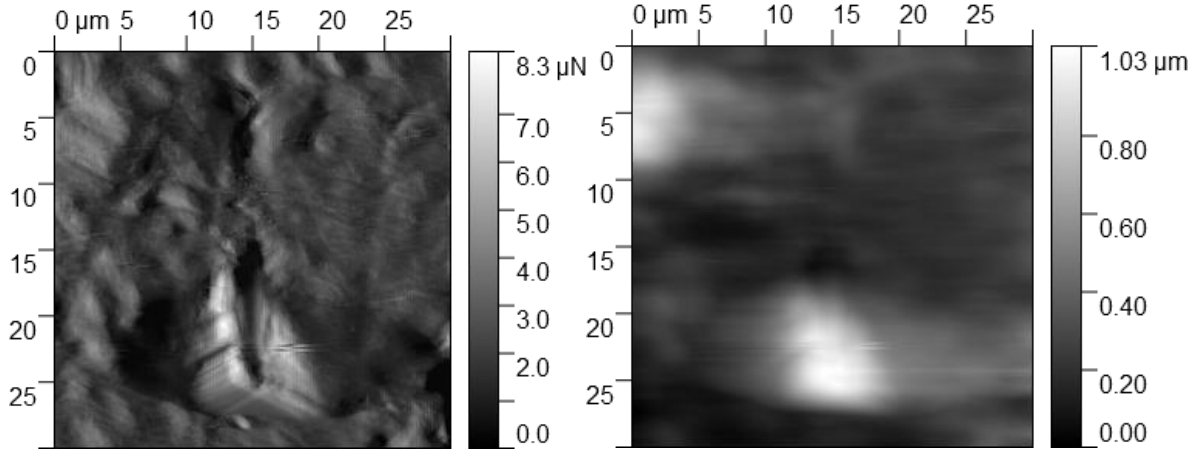


Figure 92: SPM of scratch 4. Force mapping (left) and topography (right)

	Peak Load (μN)	L_c **(μN)**	h_c **(nm)**	σ_a **(MPa)**	$G_d(J/m^2)$
Scr1	500	262	510	22	0.43
Scr2	600	316	376	49	2.01
Scr3	700	381	401	52	2.36
Scr4	800	307	367	50	2.18
Scr5	900	320	354	60	2.74
Scr6	900	341	368	55	2.66
Scr7	900	527	428	63	3.48

Table 19: PEO-Si scratch delamination results for E = 855 MPa

The parameter sensitivity of the film modulus on the calculated delamination energy was investigated by repeating the calculations using the literature range of PEO modulus (E = 60 – 300 MPa [29,123,124]) and the average calculated delamination energies are plotted in Figure 93. The trend follows an inverse relationship as expected from the Laugier equation, with values ranging from G = 32 – 6.5 J/m^2, decreasing as the modulus increases. Overall, using the nanoindentation modulus of 855 MPa resulted in scratch adhesion results (2.3 J/m^2) that agree more closely with that found from nanoindentation adhesion (1.17 J/m^2).

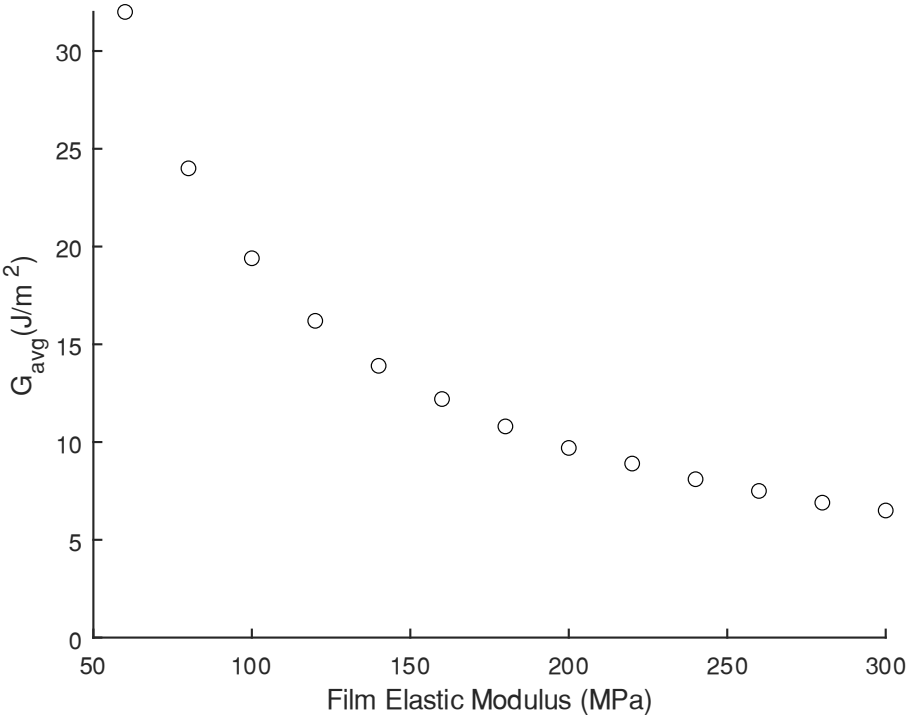


Figure 93: Effect of film elastic modulus on calculated average scratch delamination energy

4.3.4. Nanoindentation FEM Parametric Study

An FEM parametric study was conducted to determine the combination of material properties that would result in either plastic deformation or delamination during nanoindentation. The objective was to create a map of material properties to predict the deformation behaviour of different materials. The map also would provide information on the suitability of the nanoindentation test to quantify delamination energy.

All models were simulated through displacement control and the indenter was moved to a maximum indentation depth equal to 1.4 μm. Full indentation of the thin film (1.5 μm) was attempted but errors arose from direct indentation of the cohesive elements. A series of models were performed for fracture energies (delamination energy G) of 0.5, 1 and 1.2 J/m^2. Fracture energy is converted into interfacial strength (σ_{max}) using the equation (34) described in Chapter 2. Several methods in literature exist for estimating a value of δ_f from the cohesive

zone mesh when σ_{max} is not known[134,135]. However, by assuming $\sigma_{max} \sim \sigma_{adh}$, experimental results can provide a calibrated value of δ_f. From the previous section, the nanoindentation delamination energy for PEO-Si was converted into adhesive strength through the equation[136]:

$$\sigma_{adh} = \sqrt{\frac{G * E_f}{\pi * r_d}} \tag{47}$$

An average value of σ_{adh} = 4 MPa is found which results in a separation value of δ_f = 0.5 µm. This δ_f value is within the reported range for polymer on silicon from other models in literature[101]. Assuming δ_f is constant, σ_{max} values were calculated for G values of 0.5, 1 and 1.2 J/m^2 as 2, 4 and 4.8 MPa respectively.

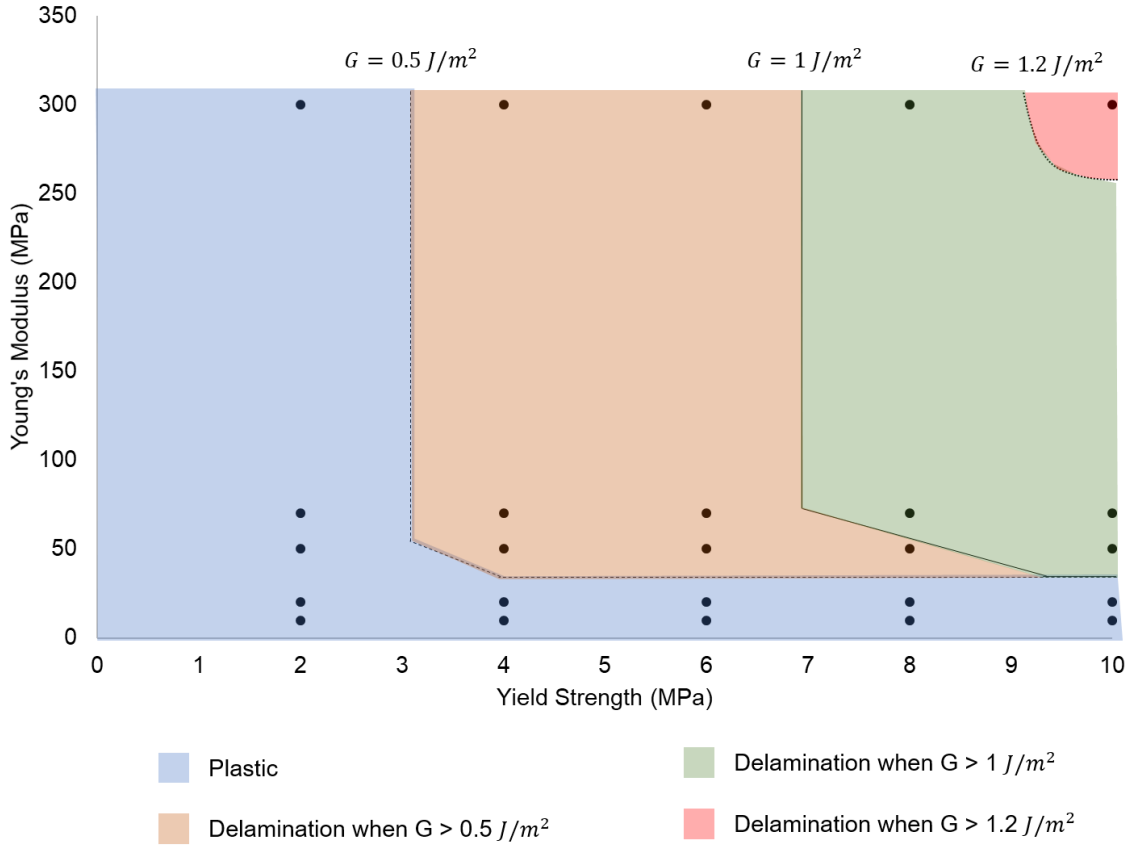


Figure 94: Deformation Map for film thickness = 1.5 µm

Figure 94 shows the transition from plastic deformation to delamination for various polymer properties at the three different fracture energies. For high values of Young's modulus between 60 and 300 MPa, a vertical transition line was observed for G = 0.5 J/m^2 and G = 1 J/m^2 at a yield strength value of 3 and 7 MPa respectively. This transition line occurs at a ratio of adhesive strength to yield strength around 1.75 for both. This ratio is close to that found by Bucci et al.[26] at 1.2, however their study modelling cathode shrinking not nanoindentation and different stress fields and behaviours are expected. For G = 0.5 J/m^2 and G = 1 J/m^2 below a Young's modulus values of around 35 MPa, no delamination was observed even at high yield strength values. For high values of delamination energy at G = 1.2 J/m^2, delamination was only observed at E = 300 MPa and yield = 10 MPa, while the rest of the models only showed plastic deformation. In models displaying delamination, damage consistently initiates around the indenter in the location shown in Figure 95, which is shown as a function of the damage factor SDEG which varies from 0 (undamaged) to 1 (completely damaged). The parametric models were repeated on a film with higher thickness equal to 10 µm and no variations in the map were observed, indicating that the deformation map is independent of film thickness.

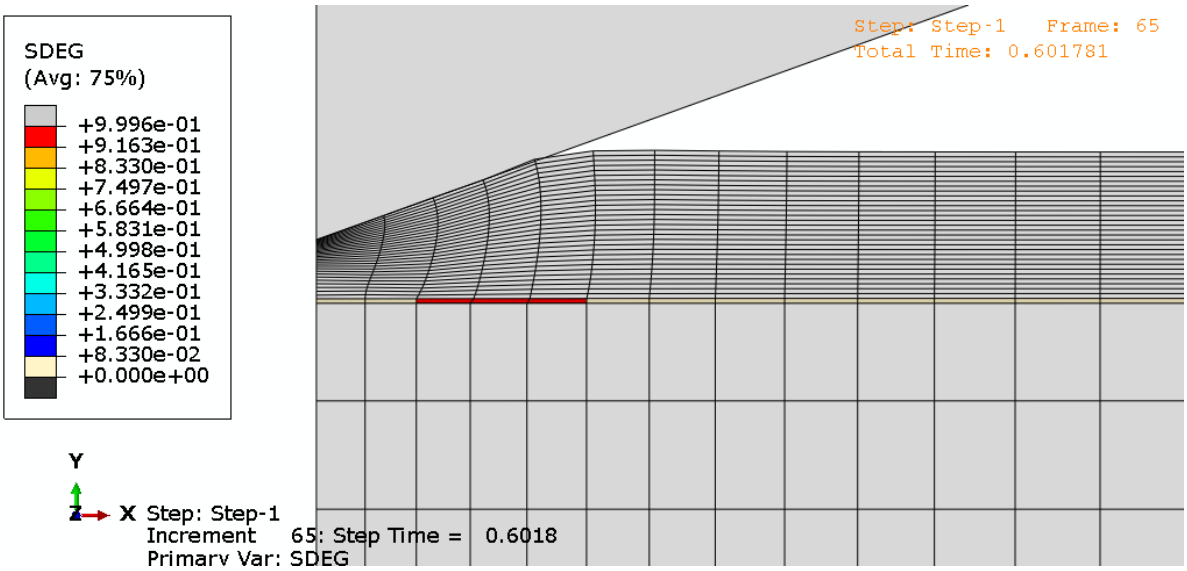


Figure 95: Location of first instance of damage in cohesive layer (red indicating damaged elements i.e.: SDEG > 0)

Effect of Yield Strength

At low yield strengths, plastic deformation was observed to dominate. Polymers with low yield strength are able to prevent stress transfer to the interface through plastic flow, thus avoiding delamination. Figure 96 shows the SDEG damage parameter values as a function of distance away from the indenter (in number of mesh elements) for two models at σ_y = 10 MPa (delaminated) and σ_y = 2 MPa (plastic deformation). The Young's modulus for both models is kept constant at 50 MPa to isolate the effect of the yield strength. For σ_y = 10 MPa, an SDEG value of 1 was reached for a total of 8 elements, beyond which the cohesive elements remain undamaged. Delamination in ABAQUS only occurs in elements that reach an SDEG value of 1 and experience sufficient tensile stresses. This was only observed for elements at the edge of the indentation that resulted in element deletion. On the other hand, the model with σ_y = 2 MPa maintained an SDEG value of 0 throughout the cohesive layer indicating no damage or stress transfer to the interface.

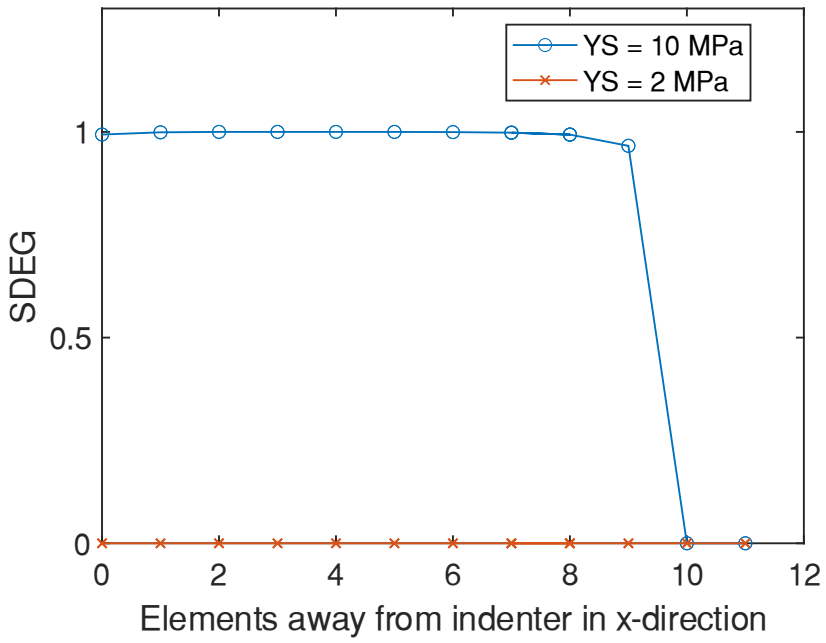


Figure 96: Final SDEG values plotted as a function of distance from the indenter tip in the x-direction, measured after unloading

The equivalent plastic strain (PEEQ) at maximum indentation is shown in Figure 97. The plastic strain is more localized under the tip for σ_y = 10 MPa, meanwhile for σ_y = 2 MPa there is more distribution of the plastic strain in the film. A concentration of plastic strain at the bottom of the film near the interface is observed for σ_y = 2 MPa, indicating that the stress has not been transferred to the interface. A strain concentration was not observed for σ_y = 10 MPa due to the stress being effectively transferred to the interface.

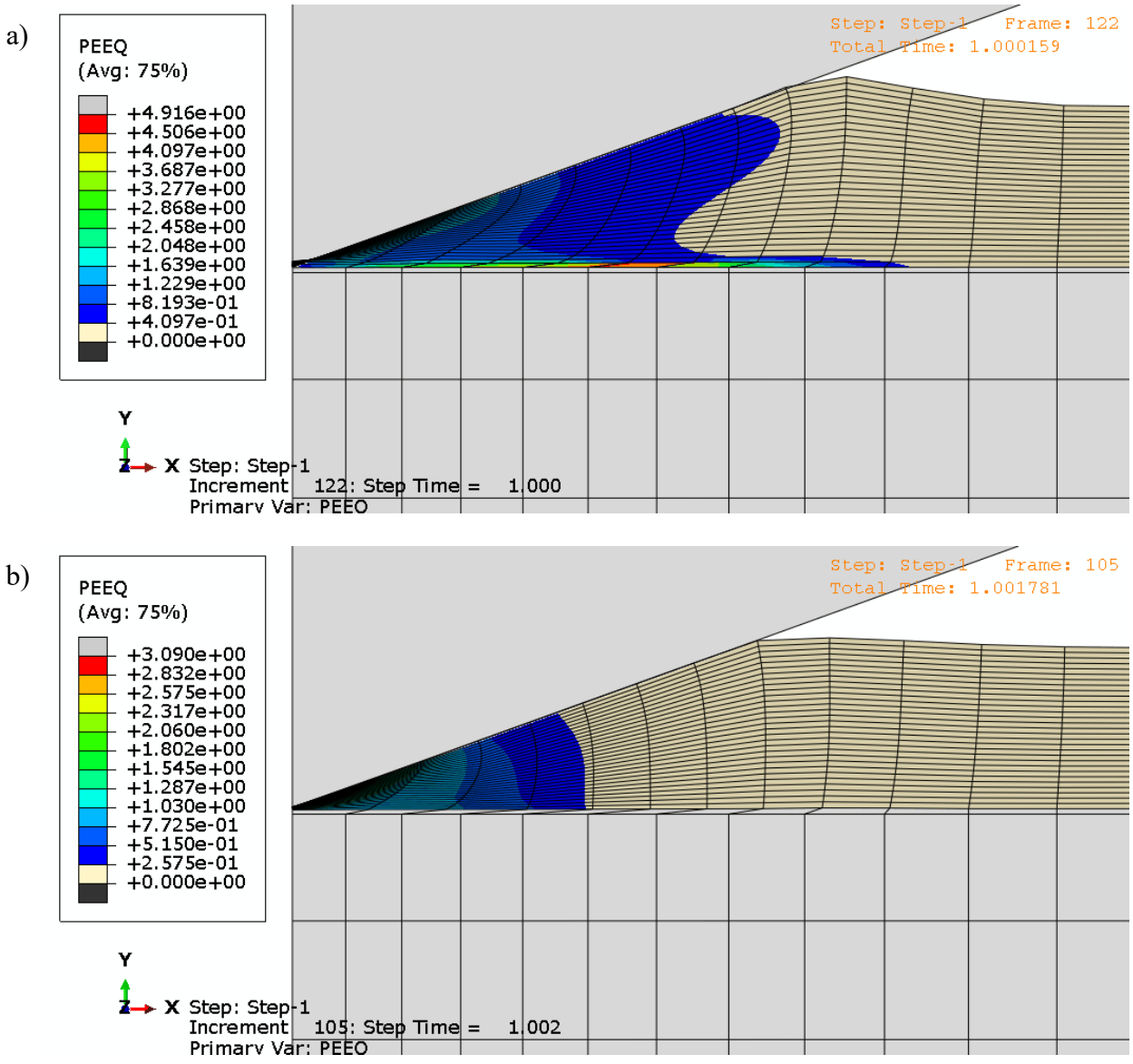


Figure 97: Equivalent plastic strain at maximum indentation for a) σ_y= 2 MPa b) σ_y= 10 MPa

Figure 98 shows the load displacement curves for the two models. After unloading, σ_y = 10 MPa exhibits a larger elastic recovery depth h_e than σ_y = 2 MPa, indicating lower levels of plastic deformation. Since the FEM model was performed under displacement control, greater force was required for indenter penetration in σ_y = 10 MPa due to the delayed onset of yielding as compared to σ_y = 2 MPa. The higher forces involved in σ_y = 10 MPa may have additionally contributed to delamination. Delamination in the σ_y = 10 MPa model takes place during unloading therefore no deviation is seen in the loading curve.

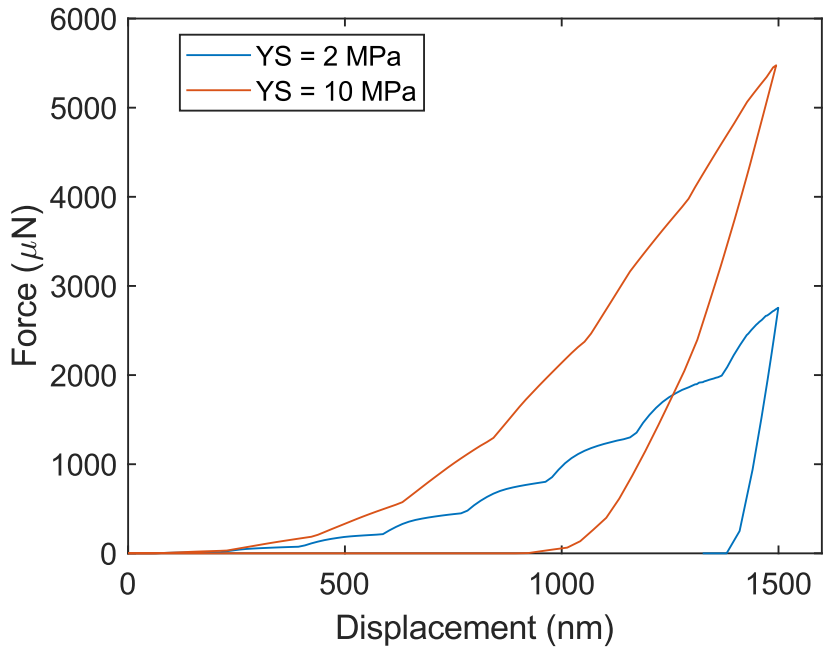


Figure 98: Load displacement curves for models at σ_y= 2 MPa and σ_y= 10 MPa, both at E = 50 MPa

Effect of Young's modulus

For G = 0.5 J/m^2 and 1 J/m^2, the Young's modulus was seen to influence the deformation behaviour below 70 MPa and no delamination was observed for a modulus below 35 MPa. Materials with higher Young's modulus values are stiffer and not easily deformed, leading to the stresses being concentrated at the interface, which initiate delamination. Figure 99 shows the force displacement curves for two models both at σ_y = 10 MPa and modulus

values of E = 300 MPa (delaminated) and E = 20 MPa (plastic deformation). Due to the higher stiffness in the E = 300 MPa model, higher forces were generated to drive the indenter into the film. The difference in the Von Mises stresses in both models is shown in Figure 100, where much higher stresses were generated in E = 300 MPa due to the higher forces involved. Higher levels of plastic deformation are seen in the E = 300 MPa model, which is also reflected in the resulting plastic depth h_p in the load displacement curve.

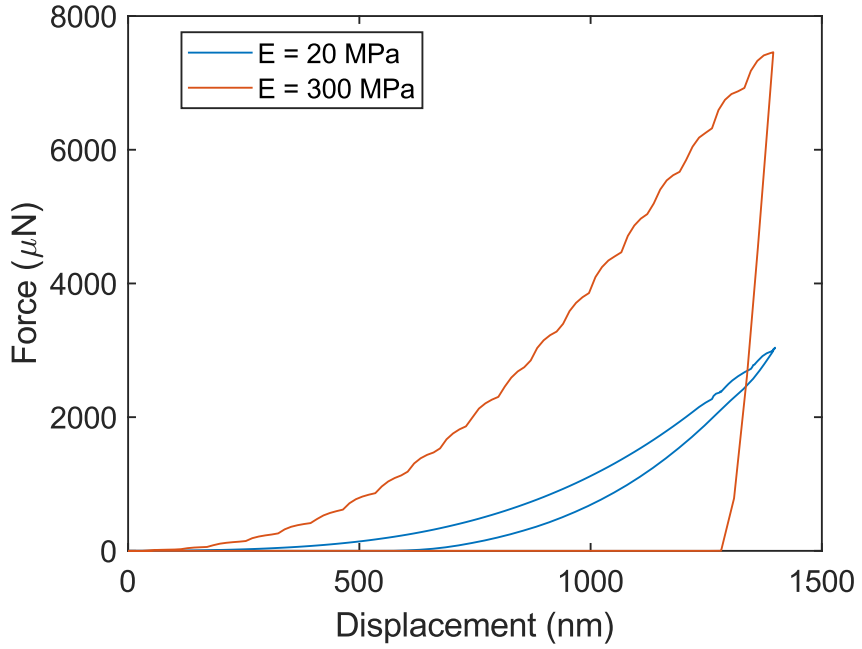


Figure 99: Load displacement curves for models at E = 300 MPa and E = 20 MPa, both at σ_y= 10 MPa

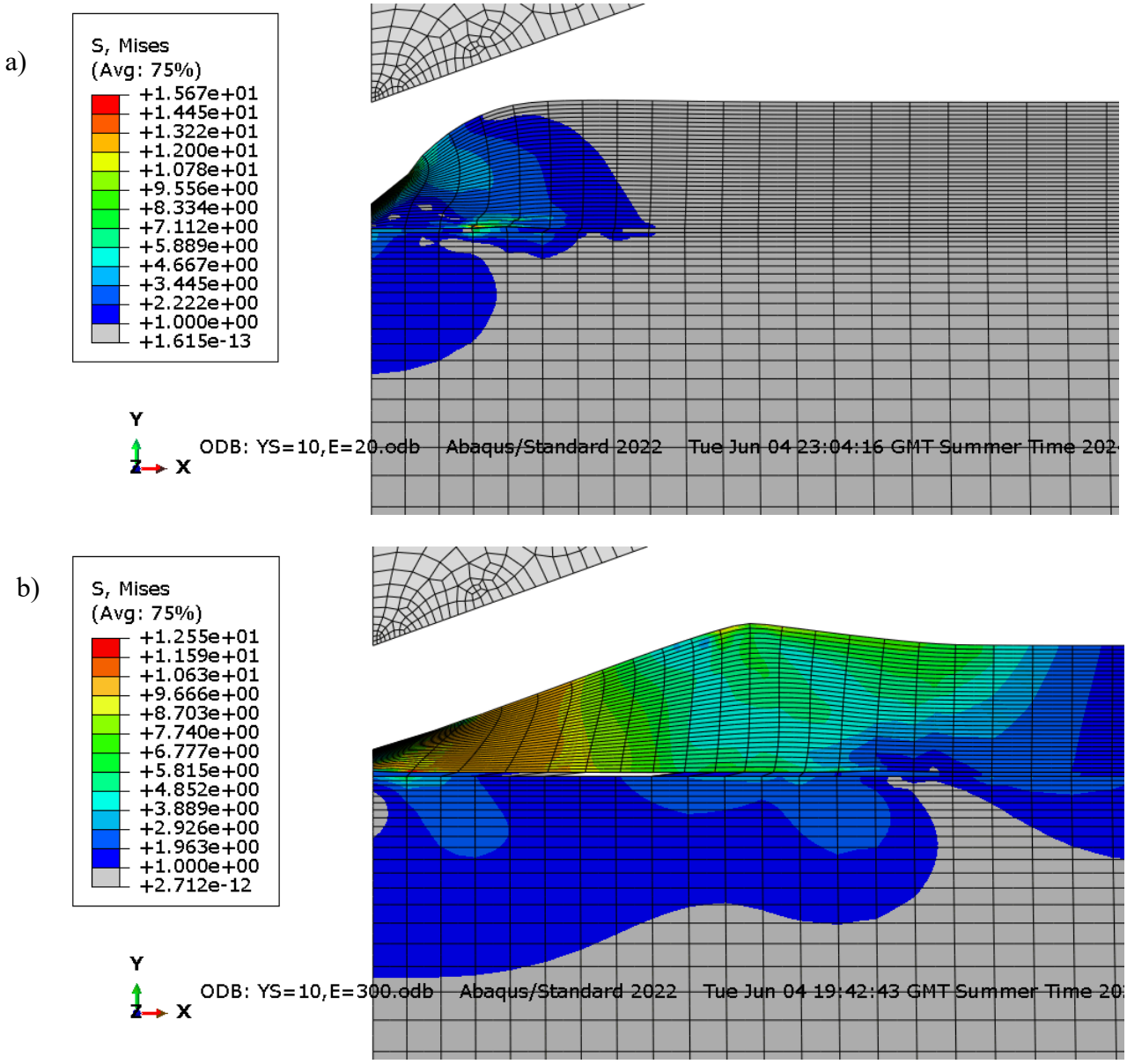


Figure 100: Von mises stresses for models at YS = 10 MPa and modulus at a) E = 20 MPa and b) E = 300 MPa

Figure 101 shows the SDEG values at the interface for both models. Higher number of damaged elements are seen in E = 300 MPa that extend further away from the indenter compared to E = 20 MPa. The cohesive elements in the E = 20 MPa model exhibited SDEG values close to 1, however no element reached fully damaged values.

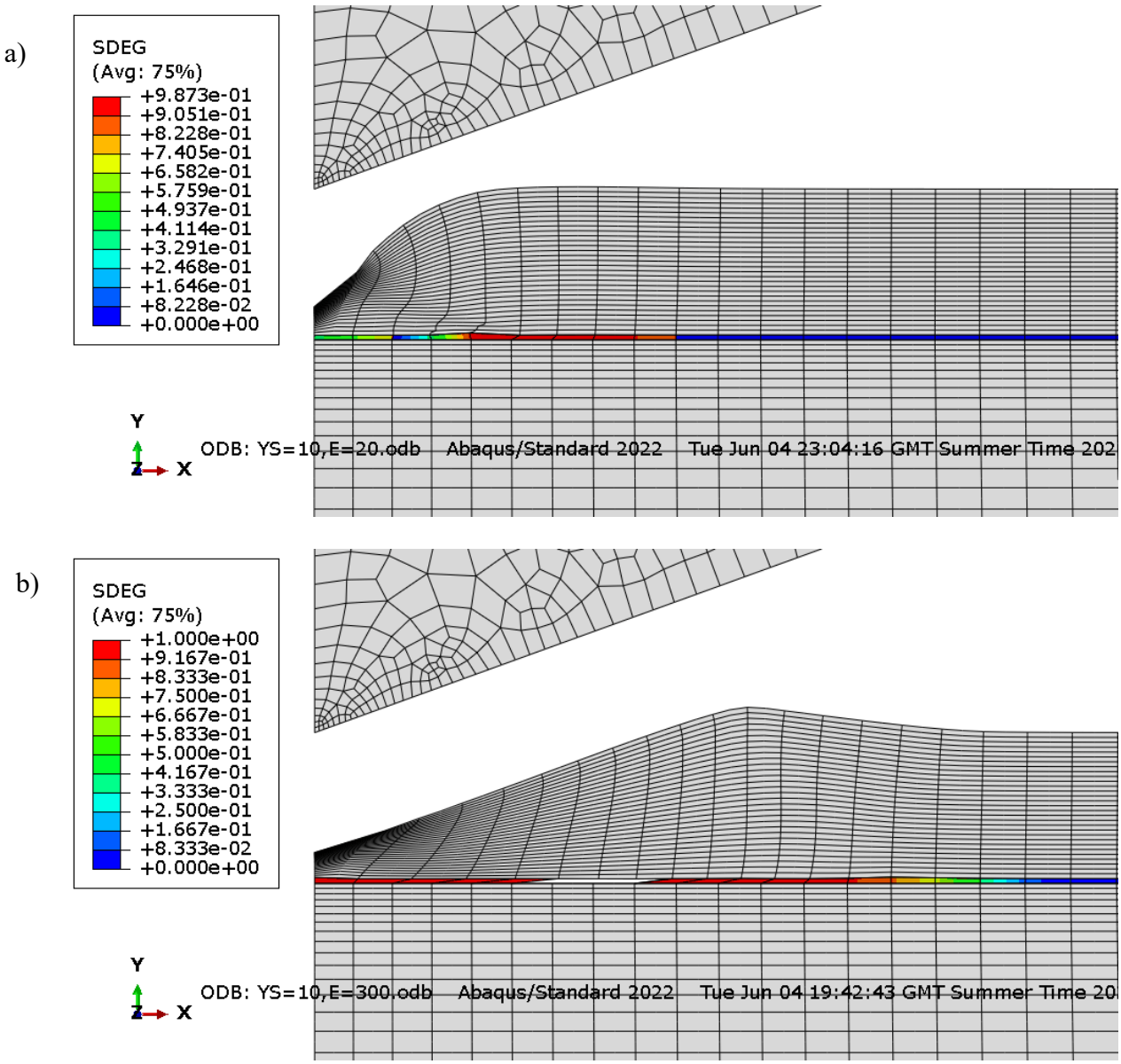


Figure 101: SDEG values at YS = 10 MPa and a) E = 20 MPa and b) E = 300 MPa

Comparison of FEM map and Experimental

In this section, the behaviour of P1 and PEO predicted by the deformation map in Figure 94 is compared with the results of the experiments. The literature range of PEO (60-300 MPa) is above the map transition point (35 MPa), therefore it is expected that in this region there will be no dependence on Young's modulus, and the exact value of PEO Young's modulus will not impact the expected deformation. To estimate PEO's yield strength, the indentation hardness was used which is related to the yield strength though a constraint factor

(C) as in Chapter 2 equation (43). Constraint factors for polymers range from C = 1.5 – 3[137]. A constraint factor of 3 was chosen as a conservative estimate for the yield strength of PEO. The CSM data for PEO in the grey region presented in Figure 52 gives a hardness value of 30 MPa within the film region, leading to a calculated yield strength value of 10 MPa. This is within the expected range of yield strength for PEO with different molecular weights from literature (7 – 8 MPa) [29,124]. In summary, the mechanical properties of P1 and estimates for PEO used to evaluate their behaviour from the FEM deformation map are summarized below as:

- $E_{P1} = 20\ MPa, \sigma_{y,P1} = 2\ MPa$
- $E_{PEO} \approx 60 - 300\ MPa,\ \sigma_{y,PEO} \approx 8 - 10\ MPa$

The deformation map places P1 in the plastic region for all three values of delamination energy tested. Additional FEM models were performed with weaker interfaces and P1 delamination was first observed at G = 0.25 J/m^2 which gives a lower bound for the delamination energy of P1-Si. Meanwhile, PEO is placed in the delamination region at 1 J/m^2 < G < 1.2 J/m^2. This prediction agrees well with the results of the nanoindentation experiments which outputted a delamination energy for PEO-Si at 1.17 J/m^2. The scratch tests resulted in a higher delamination energy (2.3 J/m^2) which FEM suggests is slightly overestimated, likely due to the high parameter sensitivity and semi-quantitative nature of the scratch test.

4.4. Conclusions

This chapter has explored the film-only mechanical properties, nanoindentation adhesion and nanoscratch adhesion behaviour of two thin film polymer systems, P1-Si and PEO-Si. Creep was minimized in both polymers by selecting an appropriate hold time which reduced the creep factor without introducing viscoelastic recovery during indentation. Due to both film's low thickness (~1400 – 1600 nm), indenting within the 10% film thickness range was not possible and high substrate effects were observed for the elastic modulus. The hardness

was found not to be as affected as the modulus by substrate effects, which is expected due to the smaller size of the plastic zone contained within the film. Substrate corrections to the elastic modulus were applied to both systems, with additional pileup corrections applied to the PEO thin film. After applying corrections, the modulus of both films was closer to the expected bulk values.

P1-Si was found to avoid nanoindentation delamination and instead plastically deformed around the indent. Nanoscratch results also supported this observation where the P1-Si scratches simply plastically deformed around the indenter leading to pileup, and no cohesive or interfacial failure was observed. On the other hand, PEO-Si displayed curve deviations in the load displacement curves, indicating delamination. Through FEM, it was found that analysing the curves using the data before delamination gave more accurate results as delamination affects the system's apparent stiffness. Using this method, an average delamination energy of 1.17 J/m^2 was found for PEO-Si. PEO-Si scratches showed high levels of fish scaling, parabolic cracking followed by material removal. Difficulties were encountered in assessing the failure point through the scratch graphs alone as no significant energy release event such as fragmentation was expected. The scratch results were analysed using the literature range of elastic modulus of PEO (E = 60-300 MPa) and a range of average delamination energy of G = 32 – 6.5 J/m^2 was found, with decreasing values of G as E increases. The scratch results were also analysed using the corrected modulus found from nanoindentation (E = 855 MPa), which outputted an average scratch delamination energy of 2.3 J/m^2, agreeing more with the nanoindentation adhesion energy (1.17 J/m^2).

FEM parametric study was carried out to generate a map of the expected nanoindentation deformation behaviour (plastic deformation or delamination) for a range of Young's modulus, yield strength and delamination energy values. It was found that below a Young's modulus of 35 MPa, no delamination was observed. For a given delamination energy

and Young's modulus (above 35 MPa), lower yield strength materials displayed plastic deformation while higher yield strength displayed delamination. The FEM deformation map provides valuable insight into the importance of the film mechanical properties, along with the adhesive properties of the interface in determining whether interfacial failure will occur. The map was found to be in good agreement with the nanoindentation results, placing P1 in the plastic deformation regime for all delamination energies tested. A lower bound of G = 0.25 J/m^2 was found for P1 at which delamination was first observed. PEO-Si was placed in the delamination regime between 1 J/m^2 < G < 1.2 J/m^2 which agrees very well with the experimental nanoindentation delamination value of 1.17 J/m^2 . PEO nanoscratch delamination energy value (2.3 J/m^2) is believed to be slightly overestimated compared to the FEM and nanoindentation results due the nanoscratch test's inherent parameter sensitivity and semi-quantitative nature.

Overall, the nanoindentation test provided more accurate adhesion values that align better with FEM results. Additionally, unlike the nanoscratch test, the nanoindentation test is not sensitive to parameters and does not require precise input of film mechanical properties, making it able to produce more reproducible and quantitative results.

5. LLZO THIN FILMS

5.1. Aim

Measurement of delamination energy between electrolyte-electrode materials is necessary for advancing solid-state battery research. Despite its importance, the delamination behaviour at the LLZO/NMC interface remains poorly understood from an experimental standpoint. One study[24] estimated the delamination energy between LLZO and NMC to be 2 J/m^2, however this value is an estimate with no experimental validation. Thus, obtaining experimentally determined delamination energy values is critical for the development of reliable solid-state batteries. To date, no studies have been identified that directly measure the delamination behaviour of these materials using mechanical testing methods.

The aim of this chapter is to apply the techniques developed in Chapter 3 to battery material thin films. Here we produce LLZO thin films on NMC and investigate the effect of annealing, film thickness, and substrate by XRD, nanoscratch and nanoindentation to find and compare the delamination energies. Finally, the delamination energy values measured for the films in this chapter, along with those from Chapter 4 (polymer thin films), are contextualized into solid-state battery applications using a finite element (FE) model of a charging cathode

particle. The volume contraction is modelled to understand the minimum delamination energy required to avoid delamination for a range of electrolyte mechanical properties.

5.2. Materials and Methods

5.2.1. Thin film fabrication

The thin films tested in this Chapter were provided by Stephen Turrell (Department of Materials). A PVD system integrated into an argon-filled glovebox was used for the deposition of thin films. Two LLZO on silicon films, and two LLZO on NMC on silicon films were fabricated. The first LLZO on silicon film (400 nm film) was fabricated using a MB EVAP (MBraun) PVD system, while the other three films were fabricated using a DST2-TSGB (Nanostructured Coatings Co.) PVD system. Details of the sputtering conditions and durations are given in Appendix 4. Prior to deposition, the silicon substrates were cleaned by sonication in isopropanol and distilled water, then mounted on a glass slide with Kapton tape. The LLZTO ($Li_{6.4}La_3Zr_{1.4}Ta_{0.6}O_{12}$) powder was obtained from MTI Corp. and the NMC powder ($LiNi_{0.83}Mn_{0.06}Co_{0.11}O_2$) was supplied from MSE supplies. The silicon wafers used are similar to those used in the previous chapters.

The films were deposited by RF magnetron sputtering using a circular magnetron source with varying target-to-substrate distances. Sputtering targets were prepared within the glovebox by lightly pressing dried LLZO or NMC powder into a 2” diameter, ~2 mm deep circular copper holder using a glass microscope slide. The base vacuum pressure for the deposition processes was below $5*10^{-5}$ mbar. All samples were stored in the glovebox after fabrication. Annealing of the films was performed in a muffle furnace (MTI KSL-1100X) located inside an argon-filled glovebox. The films were placed on a bed of LLZTO powder within a lidded alumina crucible and annealed at 600°C for 2 hours (10°C/min heating rate).

After annealing, the furnace was turned off and the samples were allowed to cool to room temperature within the furnace. One of the LLZO-NMC films was left unannealed.

5.2.2. Nanoindentation Methodology

Nanoindentation experiments were conducted using a Bruker Premier nanoindenter equipped with a Berkovich diamond tip. Quasi static indentation mode was used to measure mechanical properties and to induce interfacial failure for adhesion analysis. A load profile identical to that used in Chapter 3, consisting of 5 s loading, 2 s hold, and 5 s unloading segments, was employed. Continuous stiffness measurement (CSM) mode was used only for the LLZO–NMC sample to investigate its low measured mechanical properties and to determine whether this behaviour originated from the LLZO film or from the underlying interface. No substrate corrections were applied, as substrate effects were not observed for these samples due to the relatively small elastic modulus mismatch between silicon and LLZO. The maximum peak loads used varied significantly between the four samples tested. Detailed peak load values for each sample and test condition are provided in the corresponding results subsections of this chapter.

5.2.3. Nanoscratch Methodology

Nanoscratch testing was performed using the same Bruker Premier nanoindenter and Berkovich diamond tip as used for nanoindentation. Scratches were conducted under ramped load conditions to determine the critical load for film failure and interfacial delamination.

To ensure a consistent dL/dx ratio, similar to that used in Chapter 3, the same scratch parameters were applied for all samples, with a peak load of 70 mN, a scratch length of 250 μm, and a scratch duration of 30 s. The only exception was the LLZO-Si(400 nm) sample, for which early failure was observed at this load. Therefore, lower scratch parameters were used,

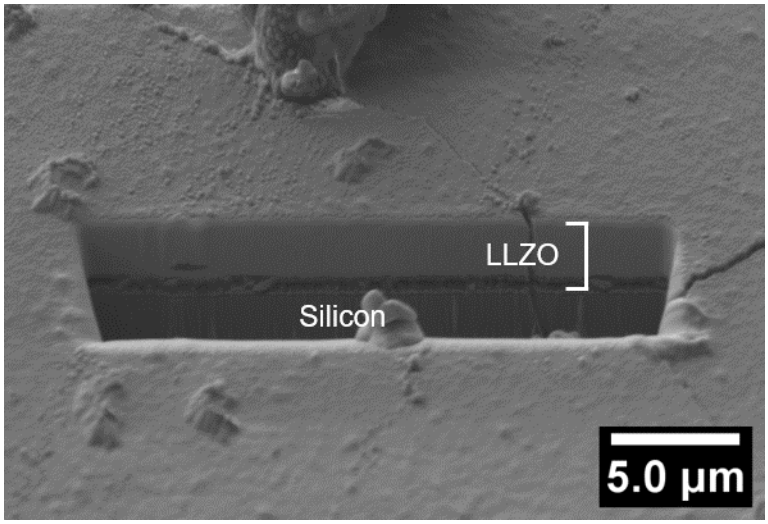
with a peak load of 56 mN, a scratch length of 200 µm, and a scratch duration of 30 s, maintaining a consistent dL/dx ratio with the other samples. The influence of tip orientation is also explored in the results section. Failure was identified using a combination of SEM, optical microscopy, and analysis of the scratch graphs, where a sudden deviation in the scratch graphs was used as an indicator of failure.

5.2.4. Film Characterization

FIB

FIB cross-sectioning was performed to measure the thin film thickness and observe the interface before any indentation or scratching. The two LLZO on silicon wafer samples are shown in Figure 102. The thickness of the sample in Figure 102 (a) is measured to be 2 µm thick (referred to as LLZO-Si(2µm)), while the sample in Figure 102 (b) displayed a thickness of 400 nm (referred to as LLZO-Si(400nm)). Differences in the surface of the two samples and the interface can be seen. LLZO-Si(400nm) displayed raised blisters that covered most of the sample surface. These are due to the thermal expansion mismatch between LLZO and the silicon wafer during annealing and subsequent cooling which generate large amounts of stress at the interface[138]. LLZO-Si(2µm) did not display any blisters due to the rigidity of the thicker film which is able to avoid blistering during annealing and cooling. A thin dark region is observed at the LLZO-Si(2µm) interface, as a result of reactions occurring between the film and the silicon substrate during annealing. A similar feature is expected to be present in the 400 nm film, but due to its reduced thickness, it cannot be as easily seen in the SEM image.

a)



b)

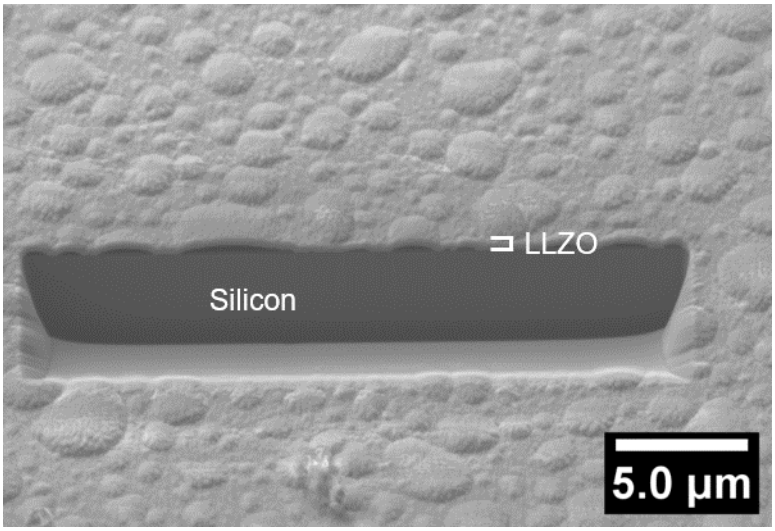
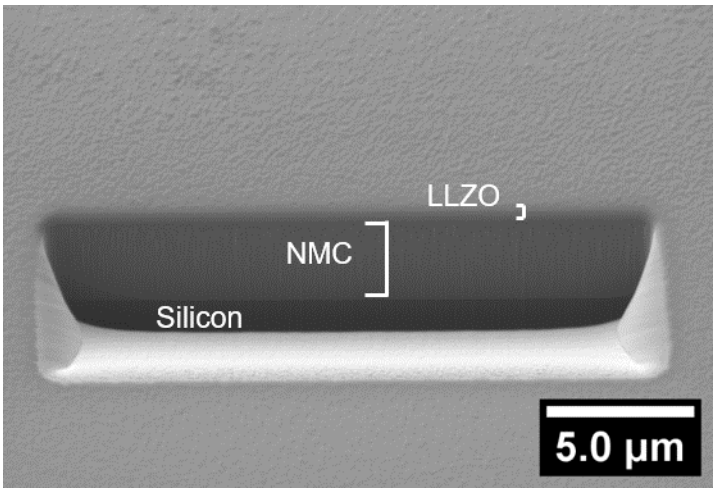


Figure 102: FIB cross-section of a) LLZO-Si(2µm) and b) LLZO-Si(400nm)

Figure 103 shows the cross-sections of the two LLZO on NMC on silicon thin films. Both films were fabricated using the same conditions, with one sample being annealed after sputtering while the other was left unannealed. The annealed sample is referred to as LLZO-NMC while the unannealed sample is referred to as UA-LLZO-NMC. The previous two LLZO on silicon films are both annealed therefore UA-LLZO-NMC represents the only unannealed sample in the batch. The thickness of the LLZO layer in UA-LLZO-NMC was measured to be 500 nm, while the NMC layer was 2.5 µm thick (Figure 103 (a)). The annealed LLZO-NMC sample displayed a higher LLZO thickness of 800 nm, while the NMC layer remained at 2.5 µm (Figure 103 (b)). Blisters similar to those observed in LLZO-Si(400nm) were observed in

the annealed sample due to thermal mismatch and the low film thickness. In both samples, the NMC layer is seen to demonstrate columnar growth.

a)



b)

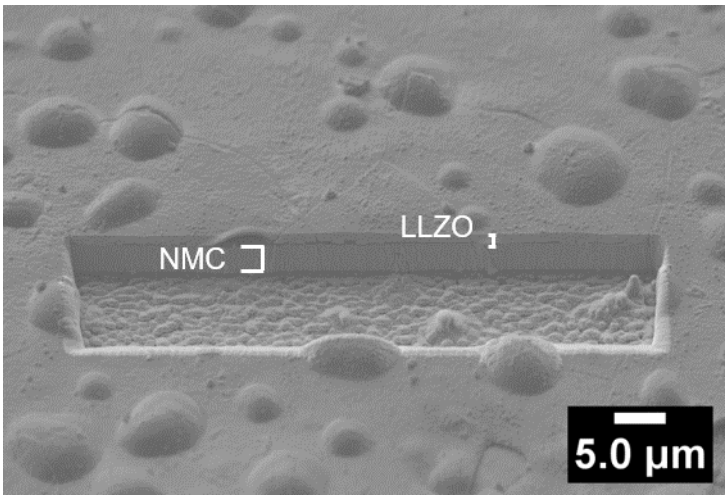


Figure 103: a) UA-LLZO-NMC and b) LLZO-NMC

EDX and XRD

The features seen in the surface of the LLZO-Si(2µm) sample was analysed through EDX in Figure 104, showing that the features are carbon rich, suggesting that these features could be lithium carbonate (Li_2CO_3).

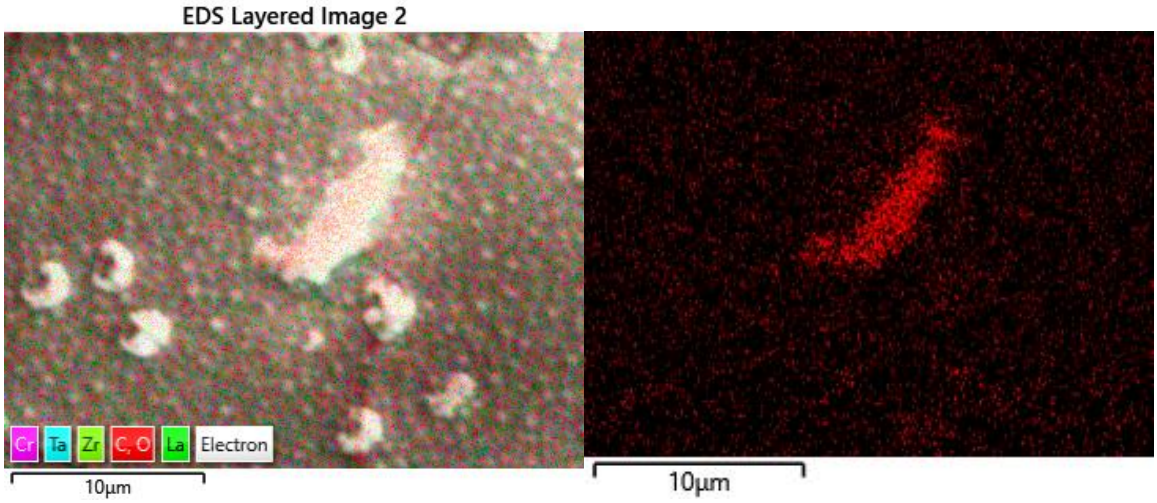


Figure 104: EDX of surface feature in LLZO-Si(2µm)

XRD was performed using the Panalytical Empyrean with a Cu source by Mahmut Erol. The XRD results for the four samples are given in Figure 105, with reference data obtained from ICSD for cubic LLZO (ICSD: 135340), $La_2Zr_2O_7$ (ICSD: 153222), and NMC-811 (ICSD: 33415), for angles 10-60°. A large peak was observed at 69° in all samples (Appendix 5), which is attributed to the (100) silicon wafer[139], so this was not included in the figure. In the LLZO-Si(2µm) sample, the sharp and well-defined peaks indicate a crystalline phase, with a primary peak near 29° and several others near 33°, 47.5°, and 56.4°. These peaks match well with the $La_2Zr_2O_7$ phase, suggesting that LZO is the primary phase. The corresponding Miller indices for each peak is as follows: 29° (222), 33° (400), 47.5° (440), and 56.4° (622). No peaks matching the cubic LLZO structure were found, indicating that the annealing time for this sample was too short, or that there was not enough lithium in the sample. The presence of the cubic LLZO peak is particularly important, as it confirms the formation of the high-conductivity phase desirable for solid-state electrolytes. Its appearance reflects successful crystallization into the functional phase essential for battery performance.

In the thinner LLZO-Si(400nm) sample, most of the LZO peaks are present but their intensities are noticeably reduced as compared to the thicker sample, which is expected due to the reduced film thickness. Additional peaks in this sample are present which match with the

cubic LLTZO phase. Some peak broadening is observed in the pattern, which is due to the small grain size present in this sample. The reduced thickness can indicate that following annealing, compressive residual stresses were generated due to the thermal mismatch between LLZTO and the silicon substrate, possibly contributing to the peak broadening. The LLZO-NMC sample displayed peaks in similar positions as the LLZO-Si samples, but the intensities and shapes of the peaks differ. Specifically, the peak at 45° is intensified in both NMC samples, suggesting that the peak at this position is a combined pattern from both the cubic LLZTO phase and NMC-811. The unannealed UA-LLZO-NMC sample shows broader peaks, particularly near 45°, indicating a very small grain size in this sample. A minor amorphous bump (halo) is observed at low angles, indicating that some fraction of amorphous material is present in this sample. In the three thinner samples, an unknown phase at 54° is detected (denoted by *), expected to be a secondary phase formed during sputtering.

Overall, some expected peaks are missing from the XRD patterns for both the cubic and LZO phase, which is indicative of a preferred overall crystallographic orientation. This is typical for thin films and is influenced by several factors, including the substrate. For instance, more LLZO cubic phase peaks are present on NMC as compared to silicon, as LLZO crystallizes more readily on NMC than on silicon, and the intermediate LZO phase is less likely to form.

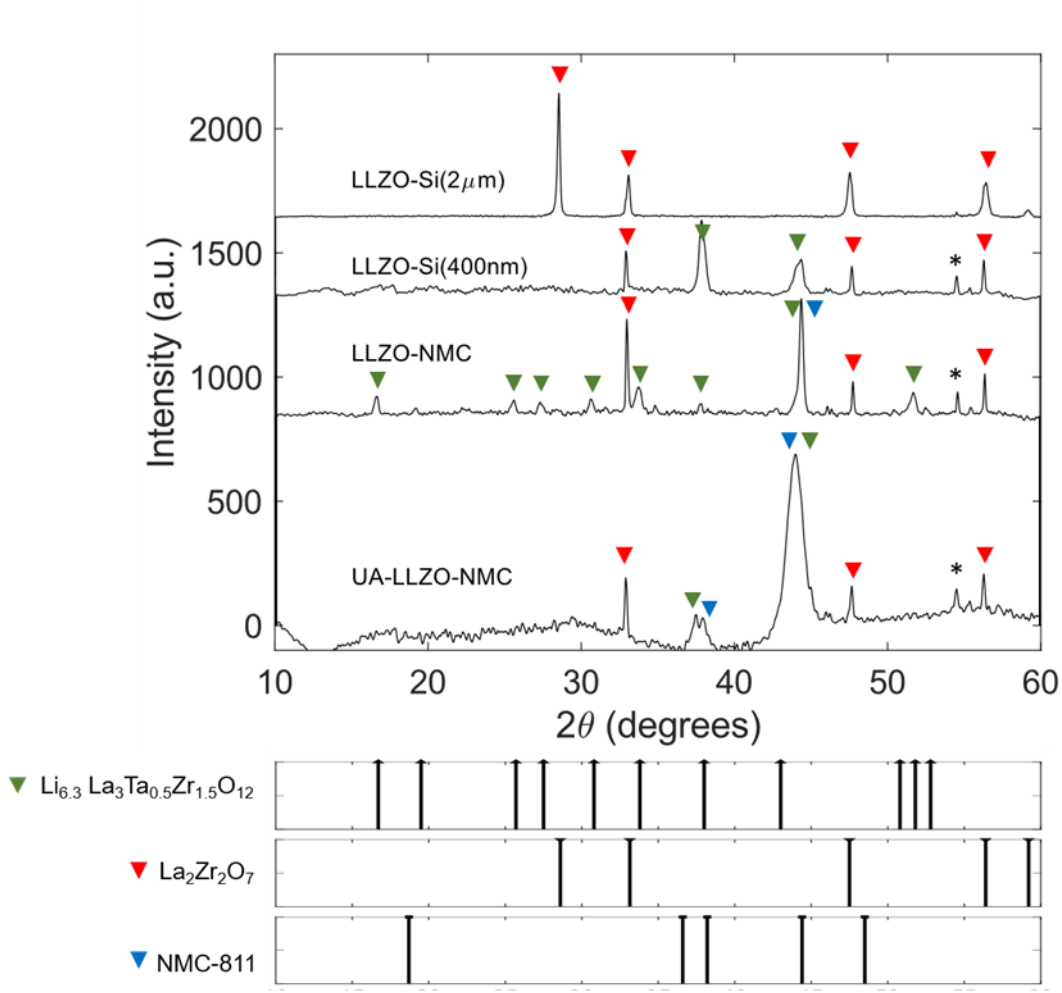


*Figure 105: XRD Patterns of LLZO-Si(2μm), LLZO-Si(400nm), LLZO-NMC, and UA-LLZO-NMC. Reference peaks obtained from ICSD. Green marker: cubic LLTZO, red marker: LZO, blue marker: NMC-811, *: unknown phase*

LLZO Air Sensitivity

Nanoindentation and nanoscratching were performed in air in a Bruker Premier nanoindenter. Each sample was removed from the glovebox and placed directly into the Premier for testing. Overall, no sample was exposed to air for more than 2-3 hours, before being returned to the glovebox where it was stored. To investigate the effect of air exposure on these samples, XRD was performed on a separate set of pristine samples at air exposure intervals of 0, 2, 4, and 8 hours. The results of the LLZO-Si(2μm) sample at various exposure intervals are presented in Figure 106. No significant changes were observed in the diffraction patterns over the measured intervals. The XRD patterns for the remaining three samples, which

also showed no noticeable variation after 0, 2, 4, and 8 hours of air exposure, are provided in Appendix 6.

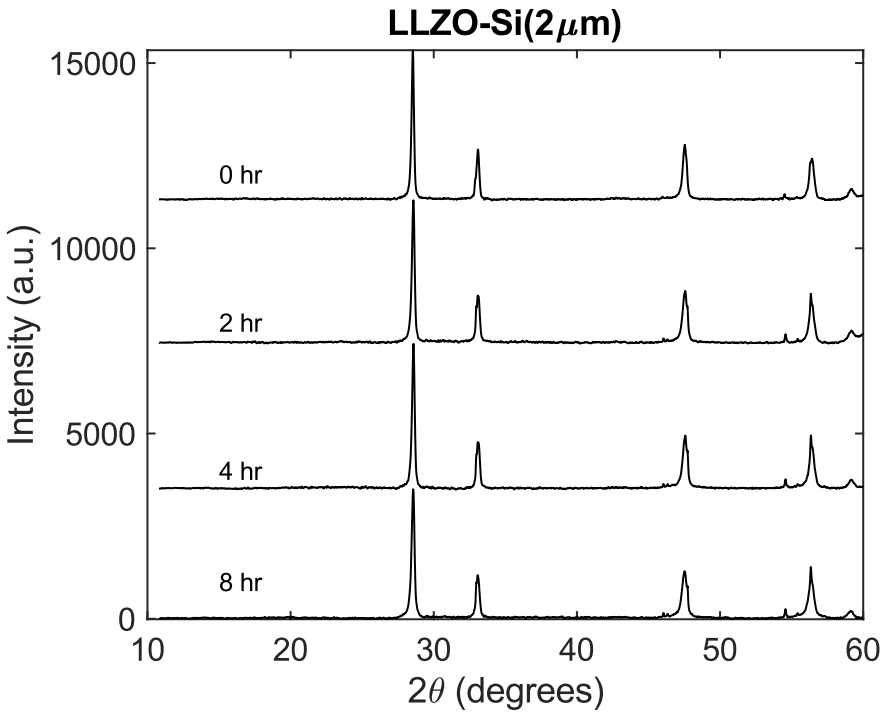


Figure 106: XRD patterns of LLZO-Si(2μm) after 0,2,4, and 8 hours of air exposure

The primary by-products expected to appear after air exposure of LLZO are LiOH and Li_2CO_3[140]. These phases are known to form readily on the surface, even with proper glovebox storage, and are expected to be present in small amounts even at 0-hour air exposure[141]. In the LLZO-Si(2μm) sample, the presence of carbonates was suggested through EDX analysis; however, these phases do not appear distinctly in XRD due to its possible amorphous nature[142], low quantity[143], peak overlap with the primary phases, surface sensitivity of XRD, or measurement conditions. Sharafi et al[140] demonstrated through XPS and Raman spectroscopy that Li_2CO_3 and LiOH form in small quantities on the surface after 24 hours of air exposure, with significant quantities observed only after 120 hours. This indicates that for the time scales used in this work for nanoindentation and nanoscratch testing (< 2–3 hours), significant degradation due to air exposure is not expected. Research within the department has shown that the mechanical properties of bulk LLZTO are not expected to degrade up to 24 hours of

air exposure[144]. Although no peer-reviewed studies have directly investigated the effects of air exposure on the mechanical properties of LLZO, the formation of corrosion by-products within the testing time frame used in this work is expected to be minimal and are unlikely to influence mechanical properties.

5.2.5. Finite Element Modelling

Nanoindentation Model

The details of the model used for extracting the irreversible plastic work during nanoindentation is described previously in Chapter 3. The thin film thickness was adjusted to reflect the films being tested. As the yield strength of LLZO was not known, a convergence study was conducted with different yield strengths, in order for the plastic work to match the experimental results in stage I (plastic region) before delamination takes place. A first estimate of the yield strength was determined from the nanoindentation hardness using a constraint factor of 1.5[32], and iterated to a final yield strength of 5 GPa, agreeing with values reported in the literature[145]. The Young's modulus of the silicon wafer was determined from nanoindentation in Chapter 3.

	Young's Modulus (GPa)	**Yield Strength (GPa)**	**Poisson Ratio**
LLZO	180	5	0.27
Silicon	195	-	0.3

Table 20: Material properties defined in FEM

Cathode Contraction Model

To model the cathode model shrinking in ABAQUS, the particle was simplified to a 2D model as shown in Figure 107. The cathode particle drawn as a circle is depicted in green, with the cohesive layer in grey, and the outer electrolyte shell drawn in red. The particle was drawn as one part and sectioned into three sub-parts, therefore interaction property definitions

between each layer were not needed. The cathode particle radius was set to 5 µm as this is a common NMC particle size[22]. The proportion of active materials in batteries range from 50-60%. Here a loading ratio of 55% is used (corresponding to geometric factor of 1.4[26]), meaning the electrolyte outer radius was calculated to be 7 µm (thickness 2 µm). The cohesive layer was drawn with a 0.1 µm thickness, which ABAQUS overrides due to dealing with cohesive element thickness as a constitutive thickness of 1.

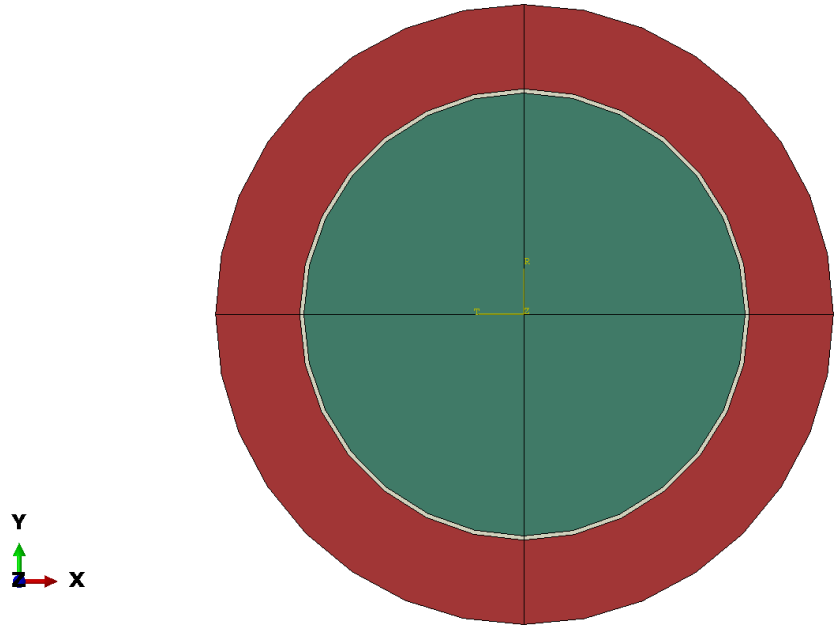


Figure 107: FEM geometry: electrolyte (red), cohesive layer (grey) and cathode (green)

The mesh elements used in the cathode and electrolyte layers were CPS4R, while in the cohesive layer COH2D4 was used. The cathode was modelled as a perfectly elastic NMC particle using literature values of modulus (E = 200 GPa) and Poisson ratio (ν = 0.25)[138]. The mechanical properties of the electrolyte and cohesive layer were varied. The cohesive layer fracture energy was varied from G = 1-30 J/m^2. To determine the corresponding σ_{max} value, the experimental values of G = 1 J/m^2 and σ_{max} = 4 MPa was used, similar to the models used in Chapter 4. Assuming a constant separation at failure, the σ_{max} values corresponding to G = 3, 10, 25, 30 J/m^2 were found to be 12, 40, 100, 120 MPa respectively. The cohesive layer

stiffness was kept constant at 10,000 GPa. As discussed in Chapter 2, this value was chosen to be sufficiently high to prevent artificial compliance, while remaining low enough to avoid numerical convergence issues. Within this acceptable range, the exact stiffness value does not significantly affect the simulation results. It was found that some models resulted in compliant "chewing gum-like" behaviour of the cohesive layer, where the SDEG value reached values very close to 1 (ex: 0.99999). This results in compliant behaviour since the cohesive element does not reach an SDEG value of 1. To avoid this behaviour without changing the cohesive properties, the maximum degradation condition was relaxed from 1 to 0.9. This meant that, instead of the cohesive element being deleted when SDEG = 1, it was removed when SDEG reached 0.9. No compliant behaviour was observed in the models after changing the MAXD value. This also gives more conservative values of failure. To model 5% volumetric change, a 1.69% radial change was needed. Cylindrical coordinates (r: radial, θ : tangential and z: z-axis) were used to define the following boundary conditions:

- Fixing the centre of the cathode $U_R = U_\theta = UR_z = 0$
- Fixing the outer layer of the electrolyte $U_R = U_\theta = UR_z = 0$
- Outer layer of the cathode to simulate shrinking U_R = -0.088 µm. $U_\theta = UR_z = 0$.

5.3. Results and Discussion

5.3.1. Elastic Modulus and Hardness Measurements

Quasi-static indents were carried out on the four samples with varying loads. The applied loads for each sample were chosen to ensure that the maximum depth remains within the film thickness. The elastic modulus and hardness are plotted as a function of the relative displacement (ratio of maximum displacement to film thickness) in Figure 108 and Figure 109 respectively. The average values for each film are summarized in Table 21.

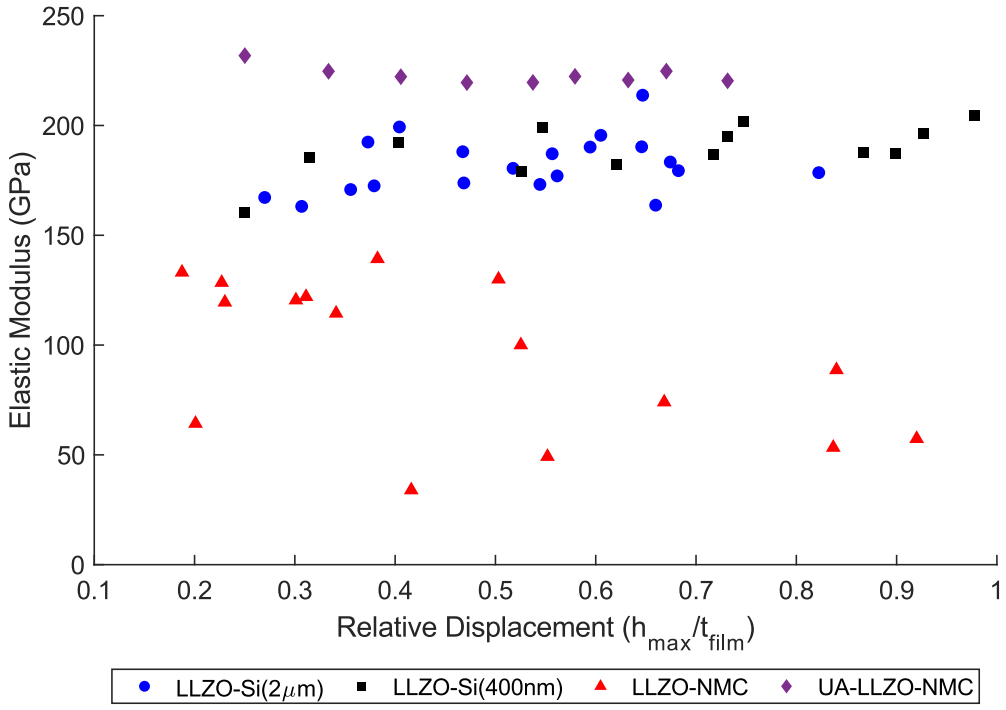


Figure 108: Elastic modulus as a function of relative displacement for LLZO-Si(2μm), LLZO-Si(400nm), LLZO-NMC, UA-LLZO-NMC

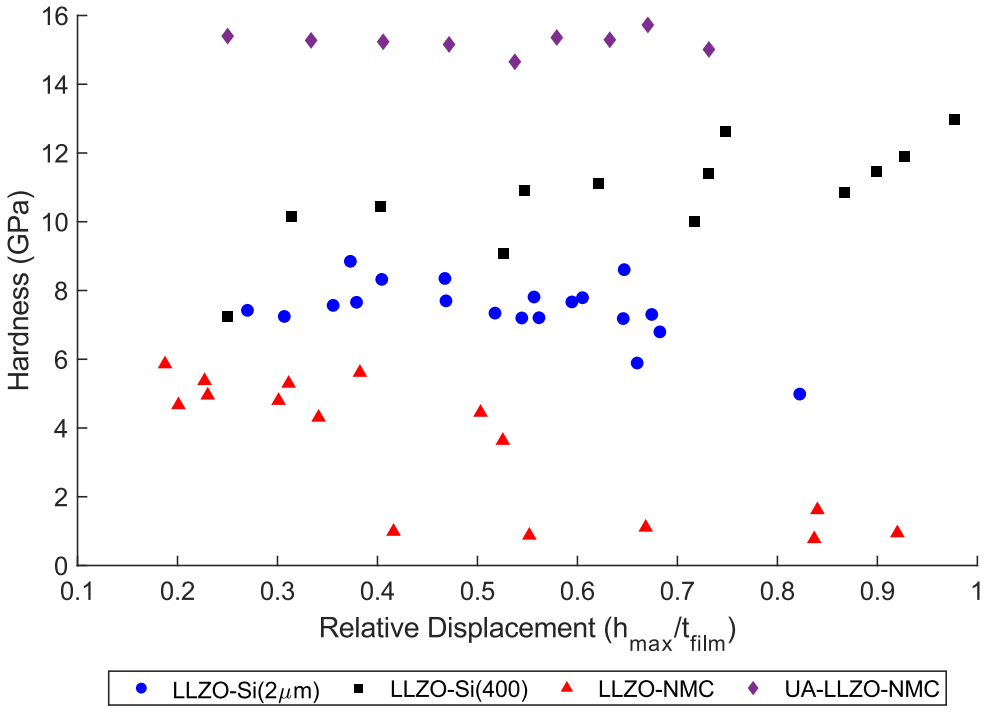


Figure 109: Hardness as a function of relative displacement for LLZO-Si(2μm), LLZO-Si(400nm), LLZO-NMC, UA-LLZO-NMC

	Young's Modulus (GPa)	**Hardness (GPa)**
LLZO-Si(2μm)	181.9 ± 12.8	7.5 ± 0.9
LLZO-Si(400nm)	189.1 ± 11.5	10.8 ± 1.5
LLZO-NMC	95.5 ± 35.1	3.5 ± 1.9
UA-LLZO-NMC	222.9 ± 3.9	15.2 ± 0.3

Table 21: Summary of mechanical properties from quasi-static indents

LLZO-NMC(UA) sample showed the highest elastic modulus and hardness values. Both the LLZO-Si samples showed similar mechanical data with minor variations in the hardness. LLZO-NMC displayed very low mechanical properties from the quasi-static indents. Four CMX indents were carried out on LLZO-NMC to further investigate this effect, and the results of hardness and storage modulus with increasing depths are shown in Figure 110.

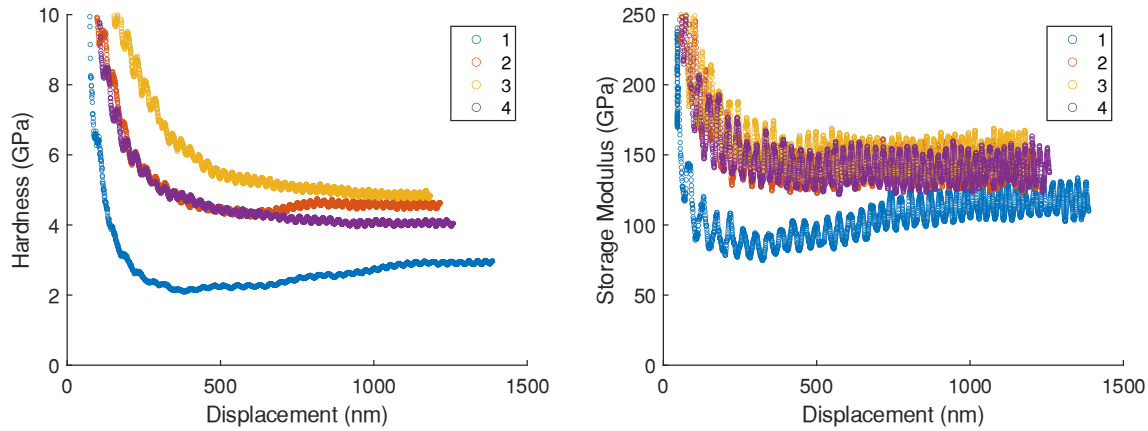


Figure 110: CMX data for LLZO-NMC. Hardness (left) and storage modulus (right) plotted as a function of displacement. The blue curve (curve 1) shows similar mechanical properties to the quasi-static results

Only one of the CMX indents (blue curve) displayed values similar to those from the quasi-static indents, with the other three CMX indents displaying higher mechanical properties. This indicates that there is a large variation in mechanical properties across the sample, likely due to the surface inhomogeneity. Excluding the results from the blue curve, an average hardness of 4–5 GPa and a modulus of 137–150 GPa was found for LLZO. After an indentation depth of 800 nm, the indenter reaches the NMC substrate, which displayed similar mechanical properties to the LLZO layer, with no significant substrate effect observed. The NMC modulus was found to range from E = 150–160 GPa, which is lower than expected for bulk NMC (E=200 GPa)[138].

The film properties from CMX in LLZO-NMC are within the range of literature LLZO values (E = 150-192 GPa)[30,146], however they are lower than that displayed by the other three samples. Co-sintering causes interdiffusion, which is generally understood to increase the interfacial strength[147]. However, it can also lead to secondary phases forming in both the LLZO and NMC layers[143,148,149], which can degrade the film and substrate properties. In contrast, silicon is chemically inert with LLZO under typical annealing conditions[150] (Si degradation begins at 700 °C), meaning that no major interdiffusion occurs. This explains why annealing

decreased the film mechanical properties more in LLZO-NMC compared to the two LLZO-Si films. This trend could also be due to increased lithium content in the film after annealing, which has been shown to decrease both hardness and Young's modulus[151]. The unannealed sample displayed the highest mechanical properties of all samples tested, despite displaying amorphous behaviour as seen from the XRD results. Amorphous ceramics are generally expected to have lower mechanical properties than crystalline structures[152], therefore the observed higher modulus and hardness can be attributed to the lack of secondary phases forming.

Overall, the range of mechanical data found for all samples is within the expected range for LLZO elastic modulus (150-192 GPa)[30,146] and hardness (7.5–9 GPa) [30,153]. No severe substrate effects are seen for any of the samples, which is expected since the silicon wafer (E =195 GPa) and NMC substrate (E=200 GPa)[138] have similar elastic modulus to LLZO.

5.3.2. Nanoindentation Adhesion Experiments

LLZO-Si(2μm)

Indents with a peak load of 100 mN to 400 mN were carried out on LLZO-Si(2μm) and the load displacement curves are given in Figure 111. From 100 to 290 mN, small steps are observed at the end of the load displacement curves at higher loads. At an applied load of 400 mN, a large step in the load displacement curve is seen, indicative of film fragmentation. FIB of the indent at 277 mN peak load is given in Figure 112, displaying clear pinned buckled film delamination. During pinned buckle formation (also referred to as double buckling), the crack length reaches a value larger than the critical buckling length, reducing the overall buckling stress[154,155]. The small steps seen in the load-displacement curves (towards the end of the loading stage just before the hold stage, shown by the red arrow) indicate that the delamination occurs during the loading segment, supported by the observed pinned

geometry[110]. Surface cracks along the corners of the indent are also observed, along with lateral cracking through the film thickness. The presence of these cracks is expected to affect the calculated delamination energy[156,157]. The large step at 400 mN peak load (shown by the blue arrow) can be directly attributed to severe film fragmentation from the SEM image (Figure 113). The fragmentation event reflects the sudden release of stored strain energy in the brittle LLZO film, resulting in a sudden increase in displacement at nearly constant load. The step is much larger than that seen during delamination because fragmentation involves a more abrupt and extensive release of stored energy, leading to a greater displacement jump in the load–displacement curve.

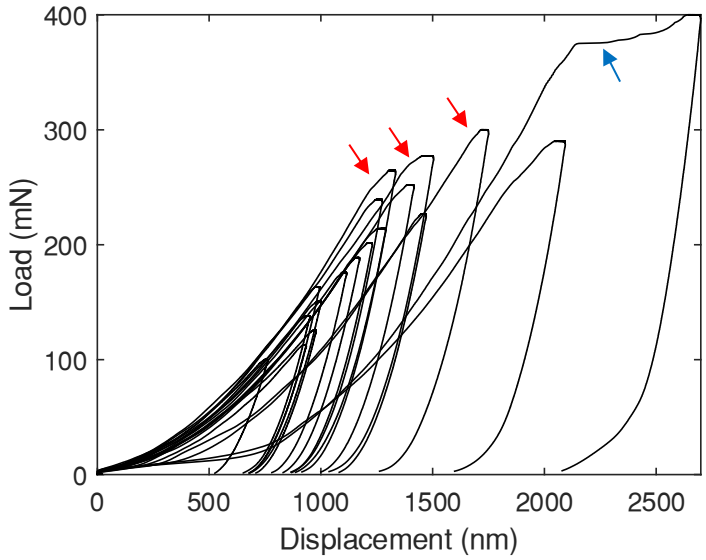


Figure 111: Load displacement curves LLZO-Si(2µm). The red arrow highlights small steps associated with delamination, while the blue arrow marks a larger step indicative of fragmentation.

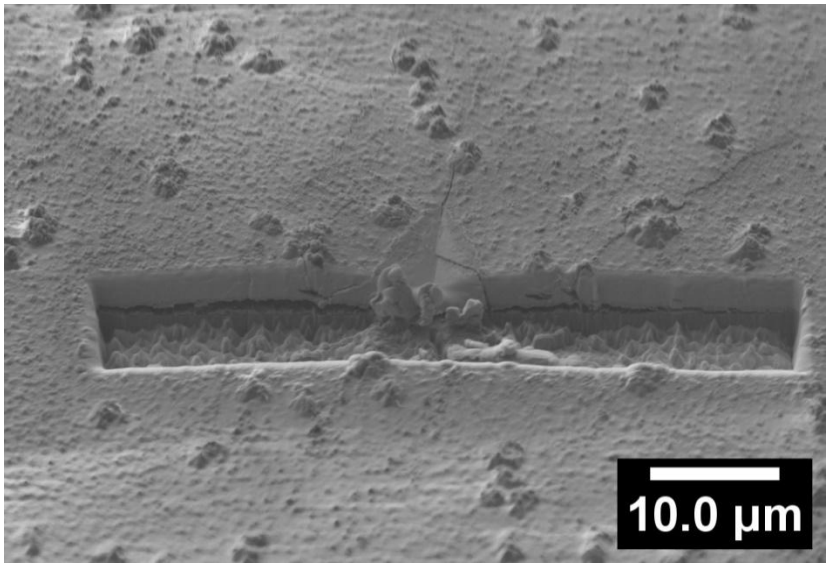


Figure 112: Cross-sectional FIB indent at 277 mN max load (h_{max} = 1500 nm)

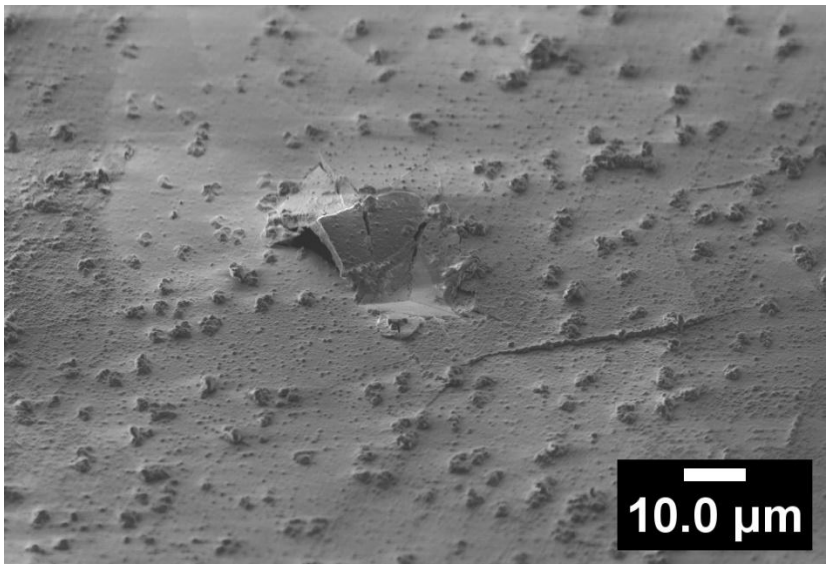


Figure 113: Fragmented indent at 400 mN peak load (h_{max} =2700 nm)

To analyse the work of delamination, the method by Malzbender[50] was used. The irreversible work along with the linearly extrapolated and FEM plastic work are plotted as a function of the applied load in Figure 114. At low loads, the plastic work from FEM agrees closely with the experimental values.

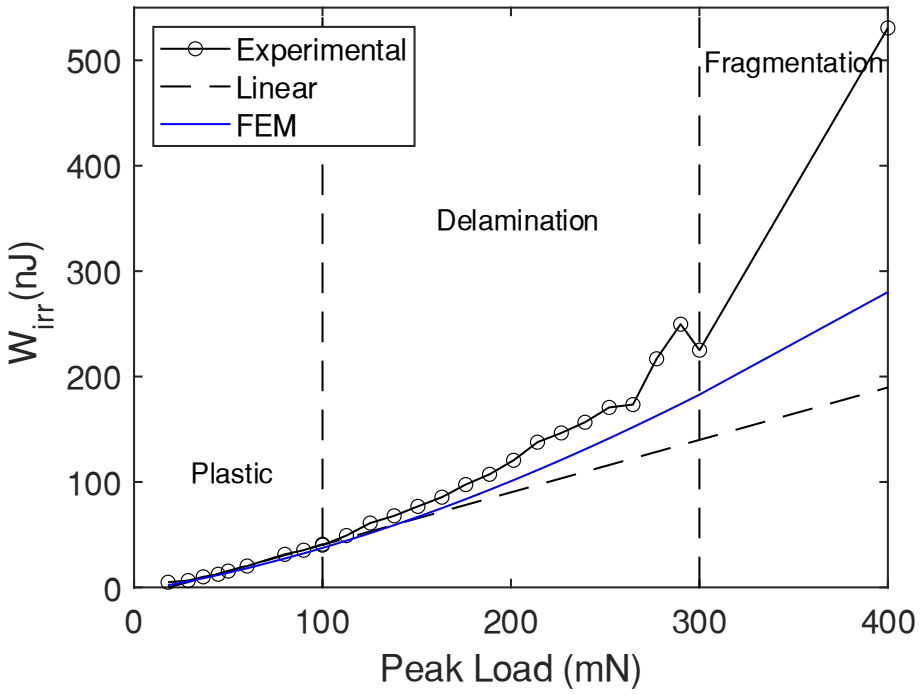


Figure 114: Irreversible work as a function of applied peak load

Optical microscopy was found to be more effective for measuring the delaminated area compared to SEM or FIB. This is because the delaminated areas around the indent exhibited buckling, causing them to rise and create a noticeable optical colour contrast, which made the delaminated regions easier to identify visually. A mask was drawn manually around the delaminated areas in ImageJ and measured (Figure 115).

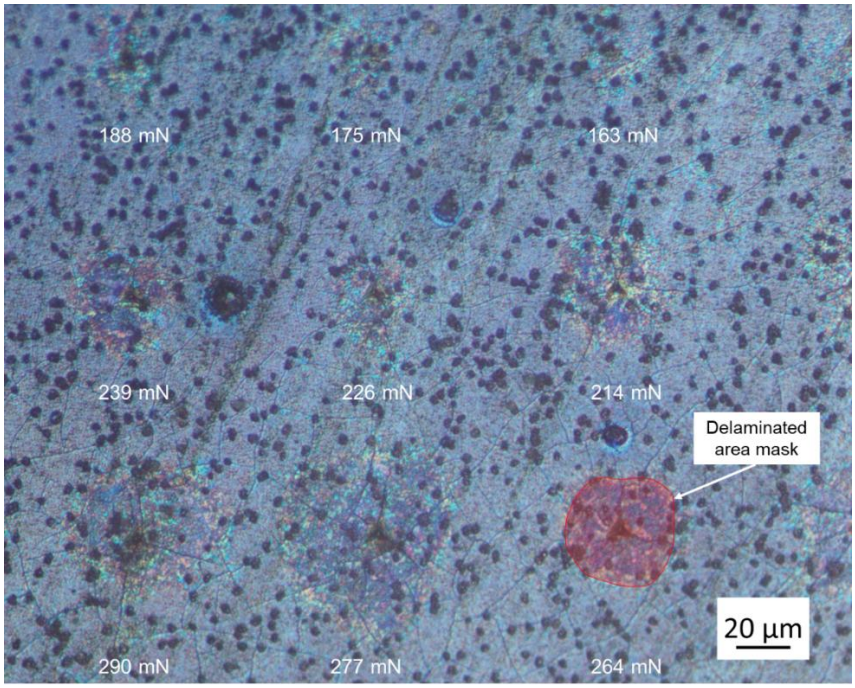


Figure 115: Delamination area measurement from optical microscope

The values of delamination energy calculated using the work of delamination from both linear extrapolation and FEM plastic work are plotted as a function of peak load in Figure 116. Using the linear plastic work, delamination energy values ranging from 23-47 J/m^2 were found. Using the FEM plastic work, a smaller delamination energy range of 15-28 J/m^2 was calculated. The overestimation of plastic work by linear extrapolation was similar to the results found in the tungsten thin films in Chapter 3. No dependence of delamination energy on peak load was observed, indicating that secondary deformation mechanisms effects (film cracking, substrate cracking) are minimized. The average delamination energy from the linear plastic work is G = 31 ± 7 J/m^2, while through FEM an average of G = 21 ± 5 J/m^2 was found.

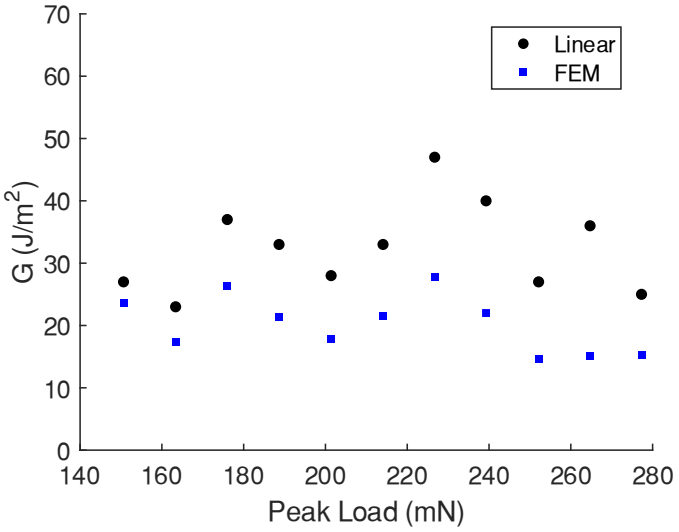


Figure 116: Delamination energy (G) plotted against applied peak load using linear and FEM plastic work

LLZO-Si(400nm)

Indents were carried out with the following load range, 5 – 250 mN (Figure 117) on the LLZO-Si(400nm) film. Similar to the previous sample, small steps are observed at the end of the loading segment (denoted by red arrows in Figure 117), indicating pinned delamination, which was clearly observed through FIB as seen in Figure 118(a). No substrate cracking or deformation can be observed under the indent, ensuring that overestimations would be avoided. No large step in the load displacement curve was observed in films that underwent fragmentation (Figure 118(b)), indicating that fragmentation in thinner films is not a major energy-releasing event compared to thicker films. Compared to the previous thicker sample, the 400 nm film did not display any surface or through-thickness cracking.

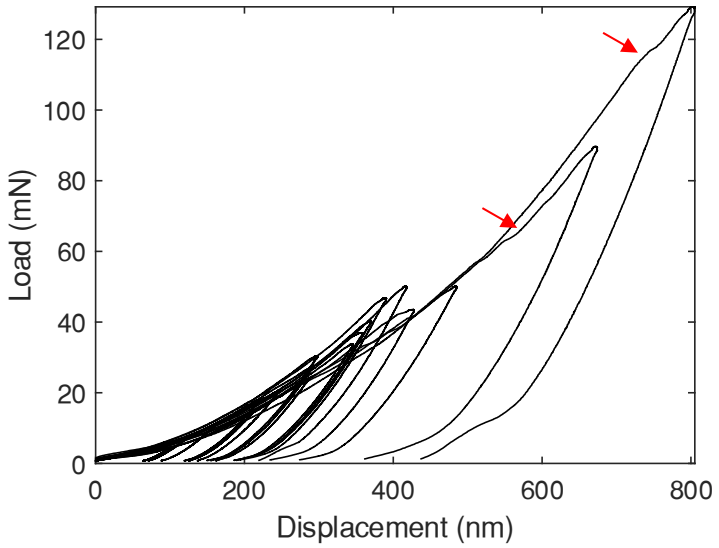


Figure 117: Load displacement curves. The red arrow highlights small steps associated with delamination.

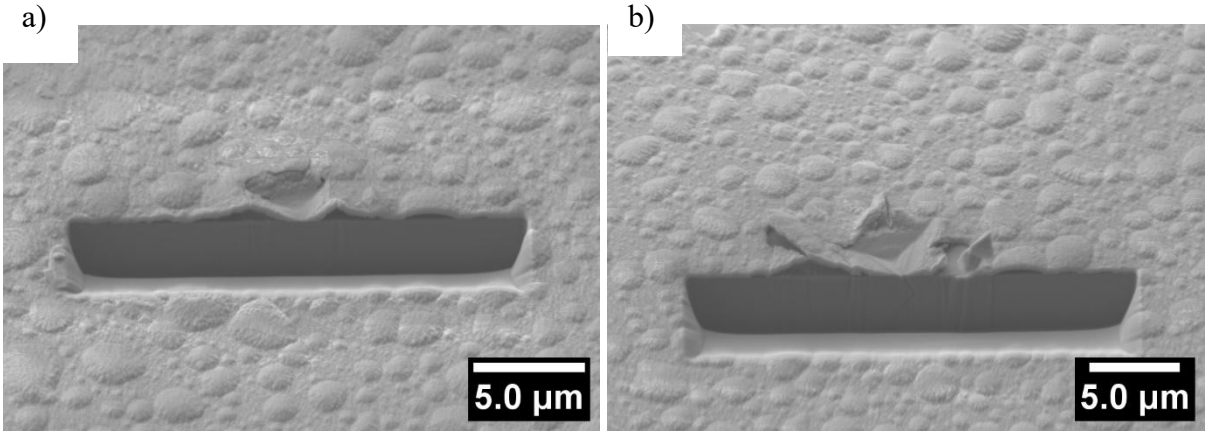


Figure 118: Indent at a) 50 mN (h_{max} = 485 nm) and b) 129 mN (h_{max} = 805 nm)

The irreversible work plot using linear and FEM corrections are plotted in Figure 119. At lower loads (stage I), slight differences are seen in the FEM and experimental values due to the inhomogeneous surface (surface blisters). The delamination areas were observed and measured through optical microscopy as seen in Figure 120. Using the linearly extrapolated plastic work, the delamination energy range was calculated to be 136–284 J/m^2 with an average of 201 ± 57 J/m^2. After implementing FEM corrections, the range was found to be 108–255 J/m^2 with an average of 195 ± 47 J/m^2. The calculated linear and FEM delamination energy with increasing peak loads is shown in Figure 121. It can be seen that in this thin film,

the linear plastic work works well in predicting the plastic work, as no large overestimations are seen except at the highest loads, with both methods outputting a similar average delamination energy value. This indicates that the linear plastic work is only overestimated for thicker films, that undergo more secondary mechanisms that are not accounted for in the linear extrapolation.

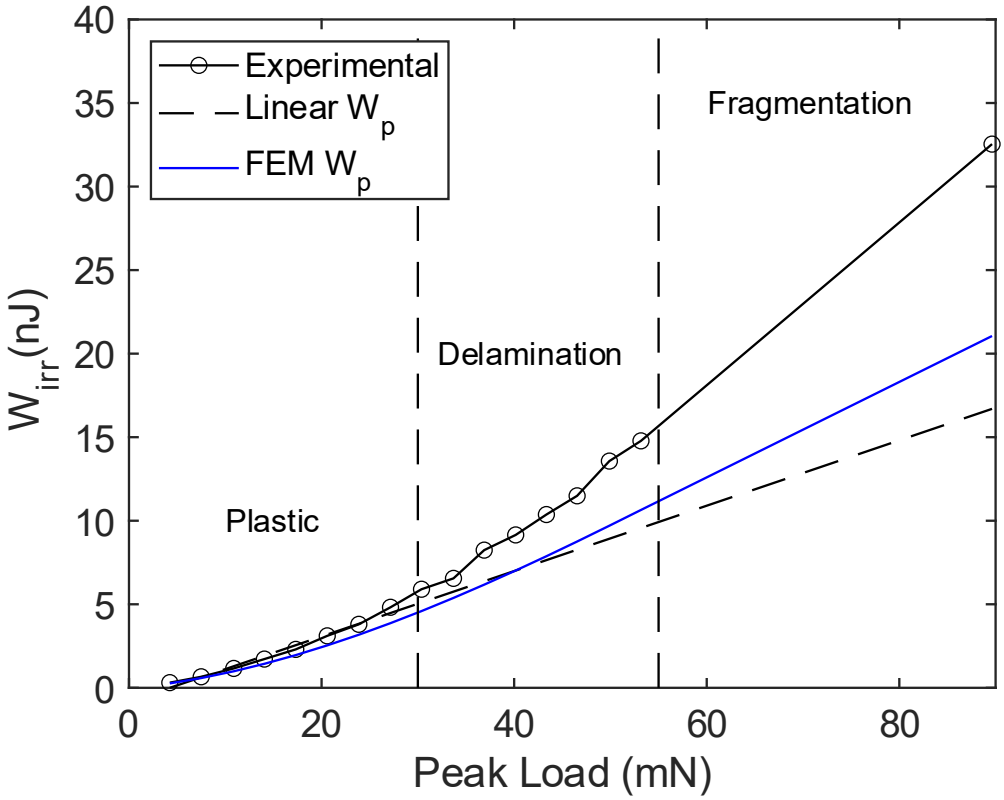


Figure 119: Irreversible work plot for LLZO-Si(400nm)

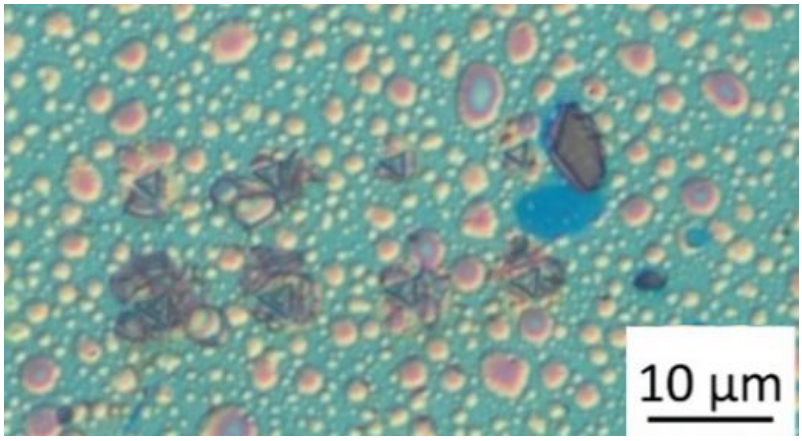


Figure 120: Optical microscope image of indents from 30 - 50 mN showing delaminated areas

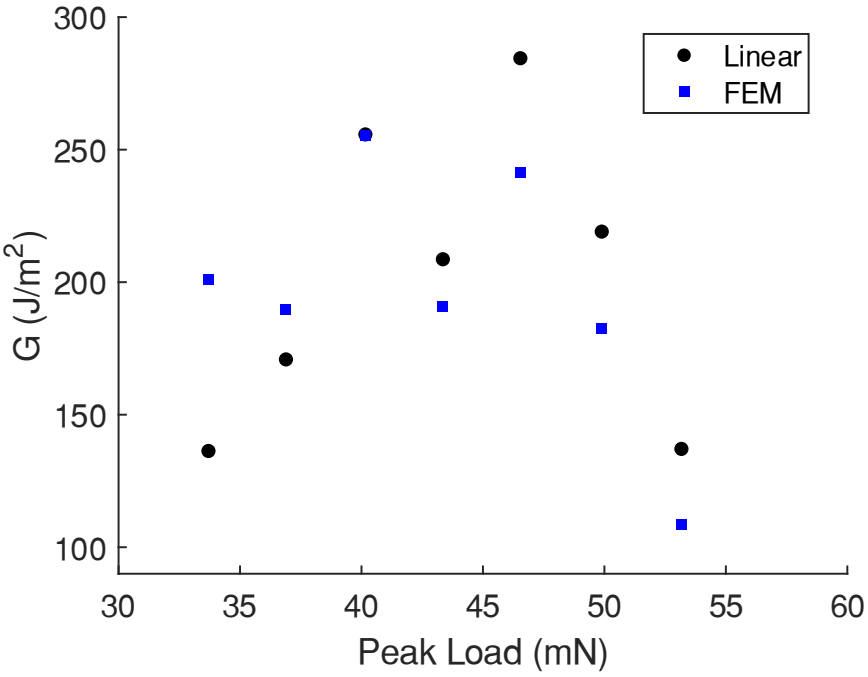


Figure 121: Delamination energy linear and FEM with increasing peak load

LLZO-NMC

Three indent grids were carried out with the following maximum load ranges: grid 1 (1-53 mN), grid 2 (50-300 mN), grid 3 (500-800 mN). The load displacement curves from each grid are shown in Figure 122.

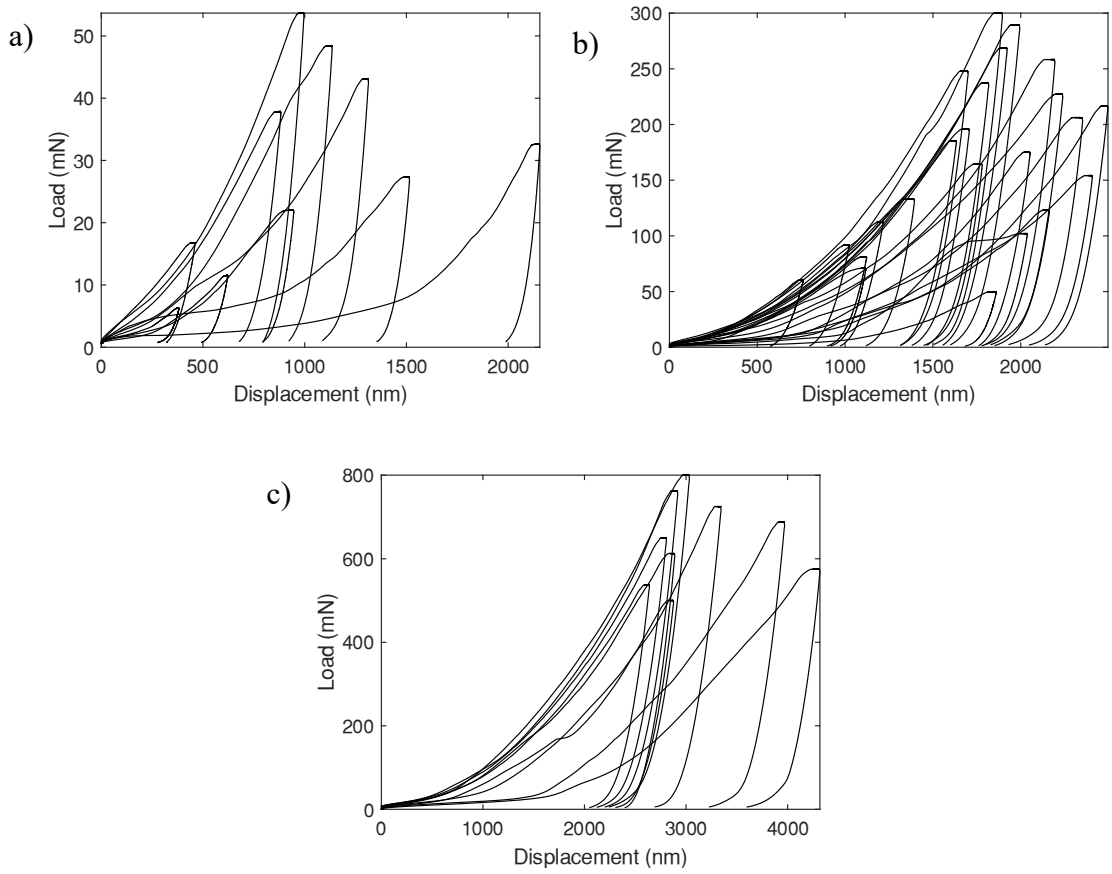


Figure 122: Load displacement curves for a) grid 1 b) grid 2 and c) grid 3

The curves are not uniform due to the large sample inhomogeneity. In grid 1, most of the curves are smooth, with very small curve deviations seen at the end of the curves at higher loads. Figure 123(a) shows the cross-section of the indent at 53 mN, indicating that this is still in the plastic region and no delamination has taken place. At this load, the indenter has reached the NMC substrate, h_{max} > film thickness (800nm). In grid 2 some steps are seen in the higher load curves (for instance, peak load 300 mN). Delamination is confirmed in the FIB cross-section in Figure 123(b) and (c). Excessive substrate cracking and deformation can be seen under the indent in Figure 123(c), which is expected as the indenter displacement is much greater than the film thickness. This indicates that the delamination work will be overestimated at these loads. Unlike the LLZO-Si(400nm) samples, pinned buckling around the indent is not

observed. No significant surface cracks around the corners of the indent are observed in any of the indents.

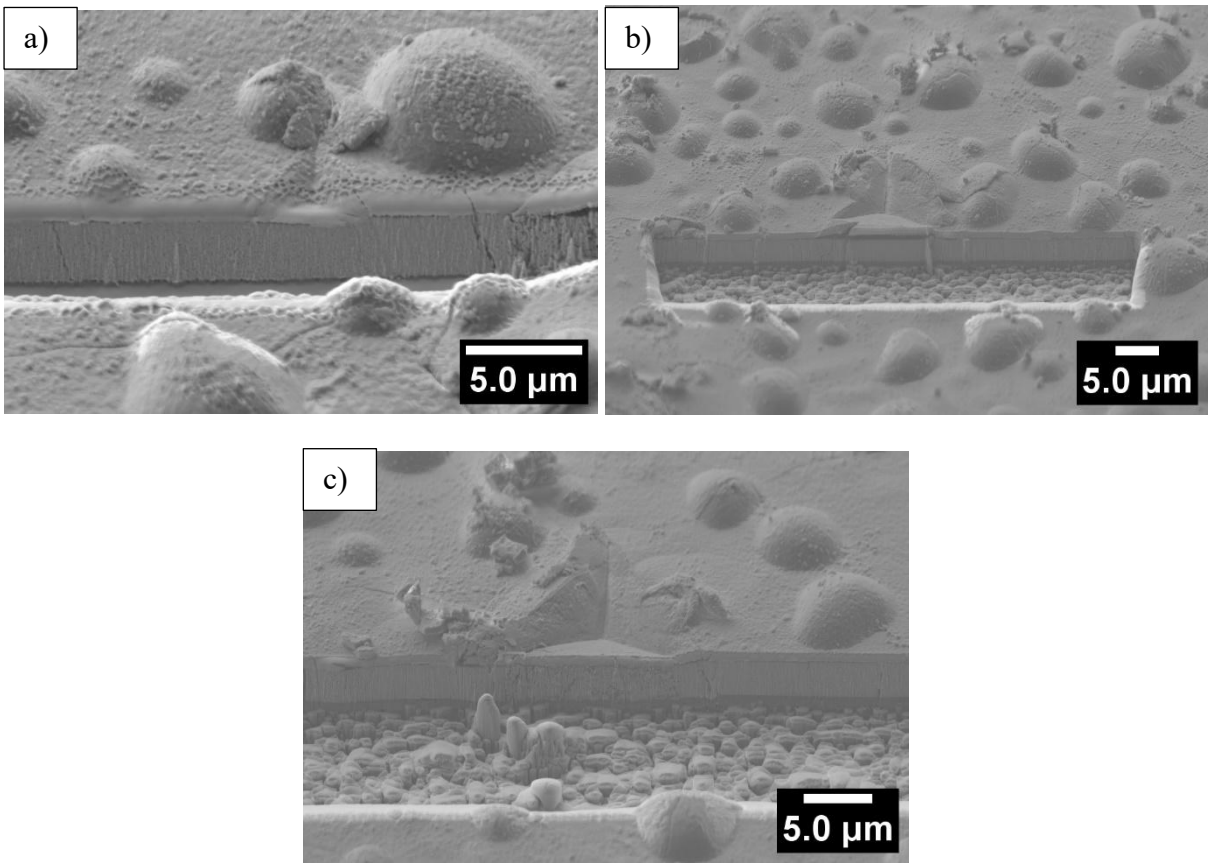


Figure 123: Indent at a) 53 mN maximum load (h_{max} = 996 nm) b) 248 mN peak load (h_{max} = 1700 nm) c) 300 mN maximum load (h_{max} = 1895 nm)

The indents in grid 3 were carried out to showcase the delamination behaviour at the NMC-Si layer. At 500 mN, the NMC layer has been observed to delaminate off the silicon substrate as seen in Figure 124 (denoted by red arrow).

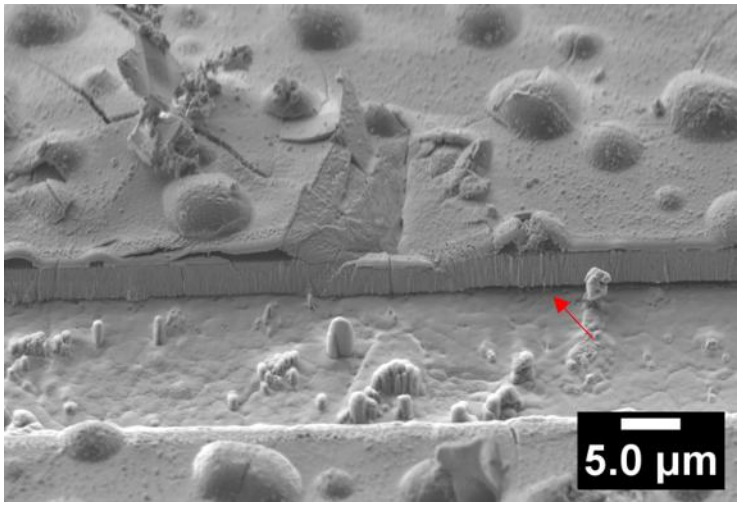


Figure 124: Indent at 500 mN (h_{max} = 2877 nm) showing LLZO film fracture/delamination and NMC delamination off Si

In this film, the onset of LLZO delamination is observed to occur at an indentation depth of 1200 nm, which is greater than the film thickness. This suggests that the delamination analysis model will overestimate the delamination energy due to the large contribution from substrate deformation. The results of LLZO-Si(400nm) showed that the linear extrapolation works well for thinner films, however this is only when the maximum indentation depth is still within the film thickness, which is not the case in this sample. FEM corrections are insufficient to account for the severe substrate deformation occurring, therefore they were not carried out for this sample. The irreversible work for the indents from grid 1 and 2, and grid 3 (up to 600 mN) are plotted in Figure 125. The calculated delamination energy from linear extrapolation ranged from 48 – 184 J/m^2, with an average of 113 ± 36 J/m^2.

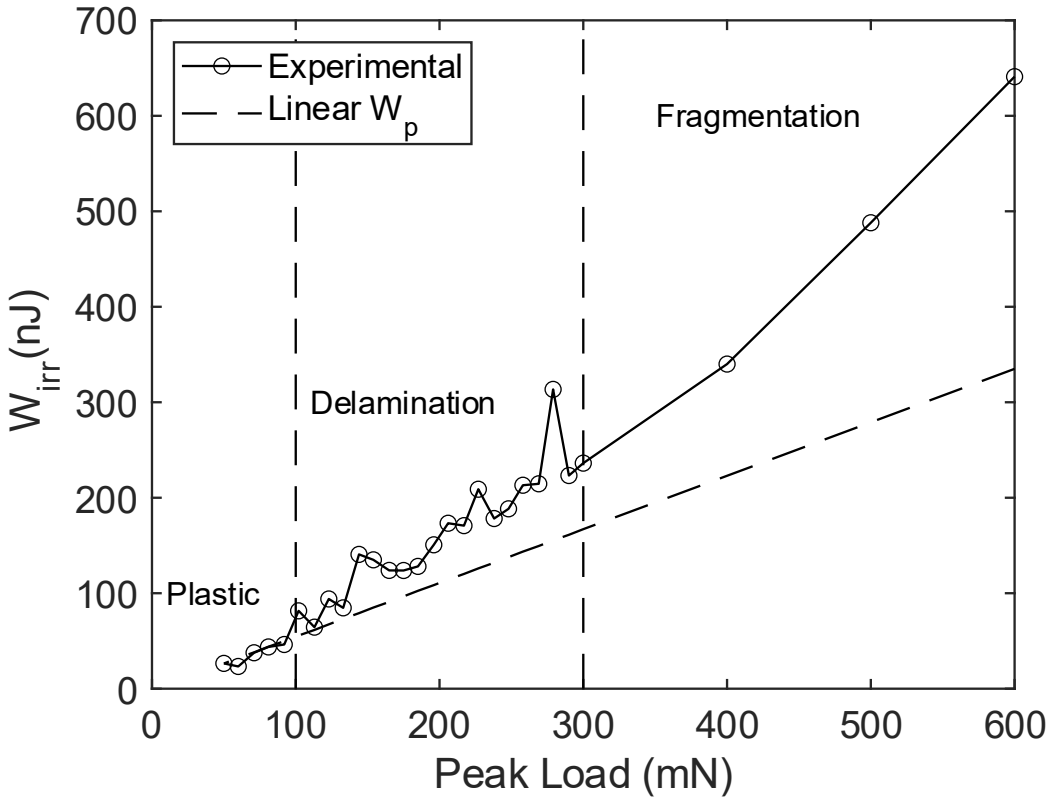


Figure 125: Irreversible work plot LLZO-NMC

UA-LLZO-NMC

Indents were carried out on the UA-LLZO-NMC sample from peak loads 100 – 700 mN with load-displacement curves shown in Figure 126. The curves are smooth and no large steps or deviations are observed. FIB of the indent at peak load 200 mN is shown in Figure 127. At this load, surface cracks around the edges of the indenter have appeared, and no observable delamination or fragmentation occurs. In this indent, the indenter has reached the substrate without leading to any delamination or through thickness cracking.

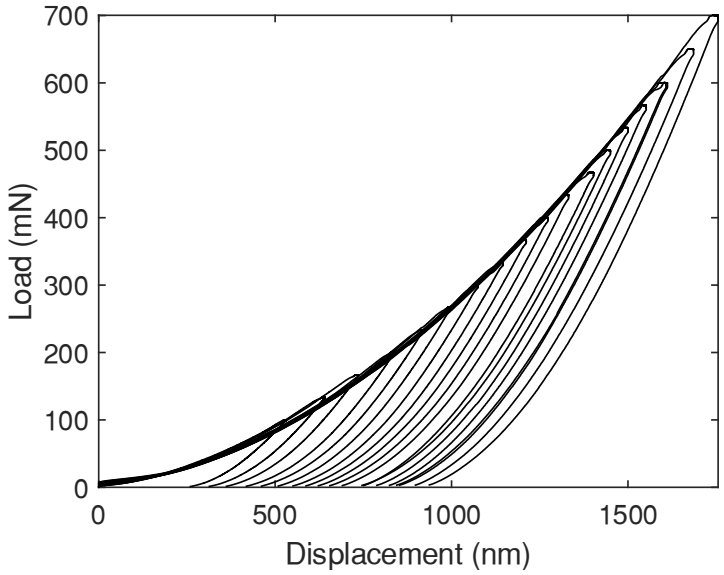


Figure 126: Load displacement curves

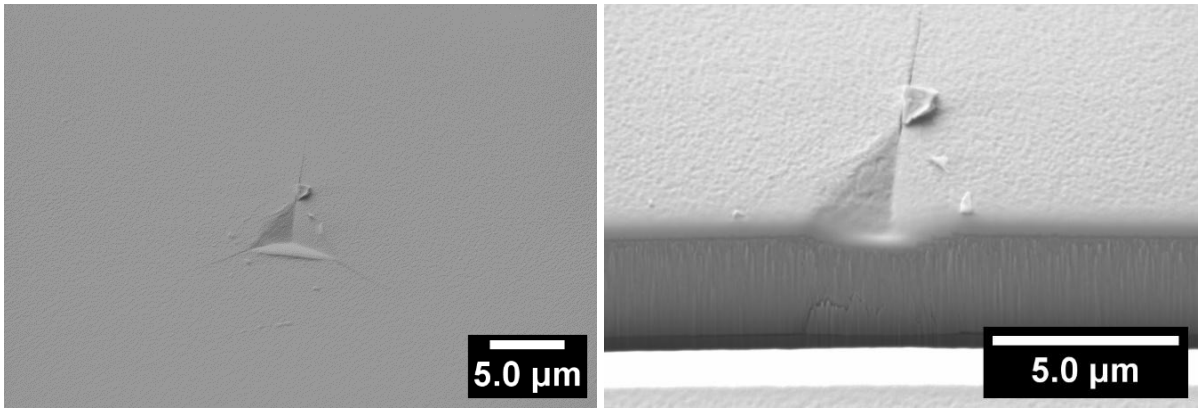


Figure 127: Indent at peak load 200 mN (h_{max} = 800 nm)

At 433 mN, NMC delamination off the silicon substrate (denoted by red arrows) is first observed Figure 128(a), with more severe NMC delamination observed at higher loads (Figure 128(b)). Interestingly, even at these loads, no LLZO film fracture or delamination is observed, which indicates that the UA-LLZO-NMC delamination energy is much higher than that of NMC-Si.

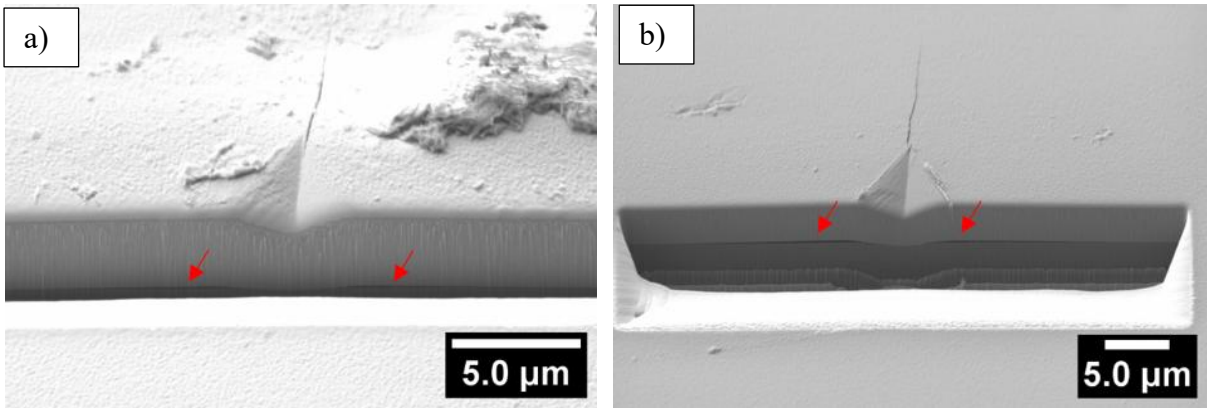


Figure 128: a) start of NMC delamination at 433 mN (h_{max} = 1332 nm) b) indent at 700 mN (h_{max} = 1755 nm)

Nanoindentation Comparison and Discussion

The values of calculated delamination energies using FEM corrections for the two LLZO-Si samples, and linear extrapolation for LLZO-NMC, is plotted against the relative displacement in Figure 129. The critical relative displacement at which delamination begins for the three samples is 0.48, 0.74, and 1.5 for LLZO-Si(2µm), LLZO-Si(400nm), and LLZO-NMC, respectively. LLZO-Si(2µm) produced the most consistent values of delamination energy, with little to no variations with increasing displacement. In contrast, the other two thinner samples, LLZO-Si(400nm) and LLZO-NMC, displayed a dependence on the relative maximum displacement, due to the excessive secondary deformation mechanisms that occurs at higher relative displacements that overestimate the value of G.

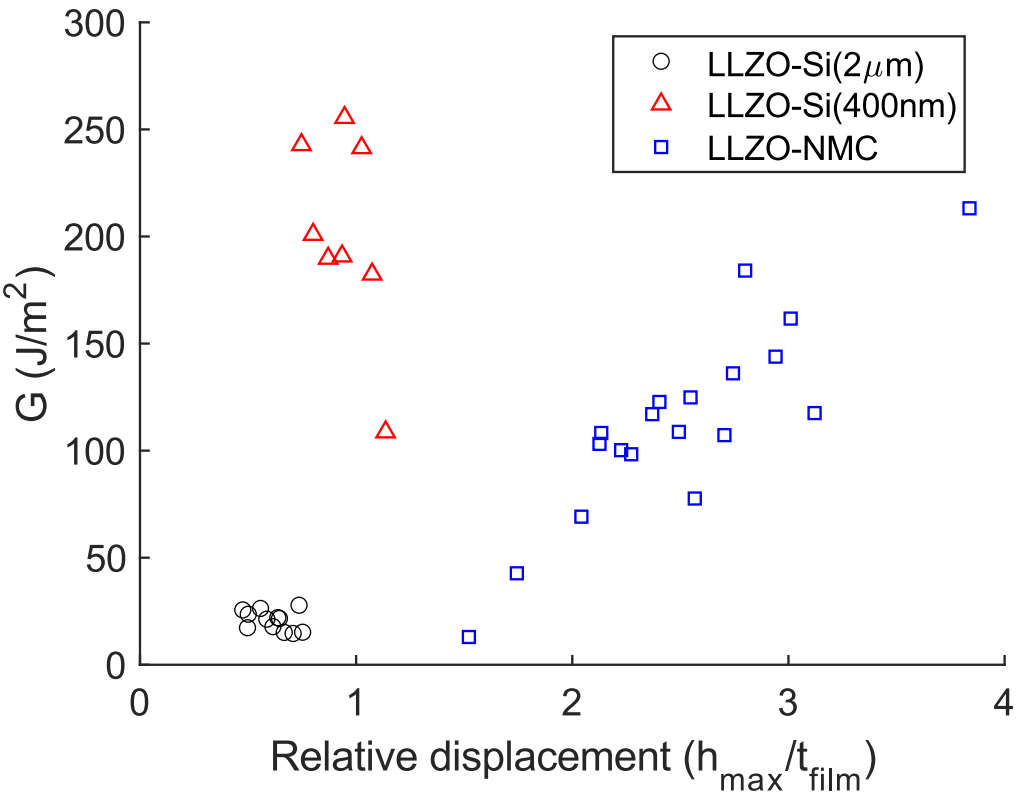


Figure 129: Calculated delamination energy versus relative displacement (FEM corrections used for the two LLZO-Si samples only)

Comparing the two LLZO-Si samples, the thicker 2 µm sample displayed much lower delamination energies as compared to 400nm. A similar decrease in G with increasing thickness has been reported[80], which was attributed to the difference in residual stresses in the two films, despite similar processing conditions. The effect is not fully understood as others have reported the opposite effect[103], while others have reported no change in G with thickness[158]. Fundamentally, the thermodynamic adhesion should be similar in both samples, however nanoindentation adhesion testing is a measure of the experimental adhesion, which is influenced by other conditions[47].

LLZO-NMC displayed the highest critical relative displacement, which may indicate that the delamination energy of this sample was the highest. This is also supported by the FIB cross-section images, where both LLZO-Si films formed very clear buckled delamination

areas, whereas LLZO-NMC did not, possibly due to the stronger interfacial strength in the film. The true quantitative value of LLZO-NMC delamination energy could not be extracted from this sample, due to high substrate effects and the onset of delamination occurring at relative displacement greater than 1. The critical relative displacement is seen to decrease with increasing thicknesses, as seen in the two LLZO-Si samples. Therefore, a thicker LLZO-NMC sample would reduce the critical relative displacement for delamination to a value less than 1, ensuring more accurate measure of delamination energy values. Finally, UA-LLZO-NMC did not display any film delamination or through-thickness cracking, likely due to the amorphous nature of the film and the lower densification. Overall, the effect of annealing on the interface remains uncertain. While annealing is expected to enhance interfacial strength through interdiffusion[147], the results observed here suggest otherwise.

The measured delamination areas are plotted in Figure 130 as a function of relative displacement. The delamination area is seen to decrease as the film thickness decreases (thickness of LLZO-NMC=800 nm). Similar effect of delamination area based on film thickness has been reported elsewhere[158]. These results highlight the impact of film thickness on delamination behaviour, which is particularly relevant for solid-state battery applications. In these systems, minimizing large-scale delamination is crucial for maintaining mechanical and electrochemical stability. These findings suggest that optimizing film thickness can play a vital role in controlling failure modes, which is essential for the reliability of solid-state batteries.

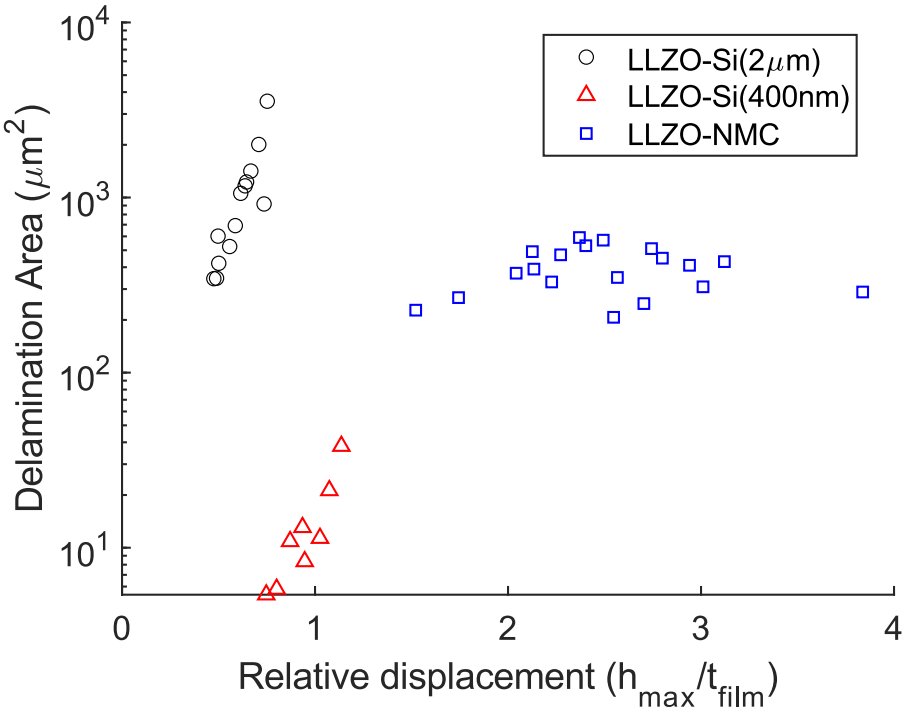


Figure 130: Measured delamination area versus relative displacement

5.3.3. Nanoscratch Adhesion Experiments

LLZO-Si(2μm)

Scratches were performed on LLZO-Si(2μm) using a peak load of 70 mN, scratch length of 250 μm, and scratch time of 30 seconds. The scratch parameters were chosen to ensure a consistent dL/dx ratio as discussed in Chapter 3. Two orientations of face forward and edge forward were investigated. The results of the scratch tests are summarized in Table 22. Figure 131 shows the scratch graph of scr1, which shows a clear deviation at the point of failure. The friction coefficient used in the Laugier calculations were found from low load scratches (μ=0.3), and the Young's modulus of the film used was obtained from nanoindentation experiments.

	h_c (nm)	L_c (mN)	σ_a (GPa)	G (J/m^2)
Edge forward				
Scr1	710	51	2.02	22.92
Scr2	827	57	1.66	15.56
Scr3	952	60	1.32	9.82
Face Forward				
Scr4	850	56.7	1.57	13.79
Scr5	705	46	1.85	19.18
Scr6	786	53	1.71	16.48

Table 22: Results of scratches

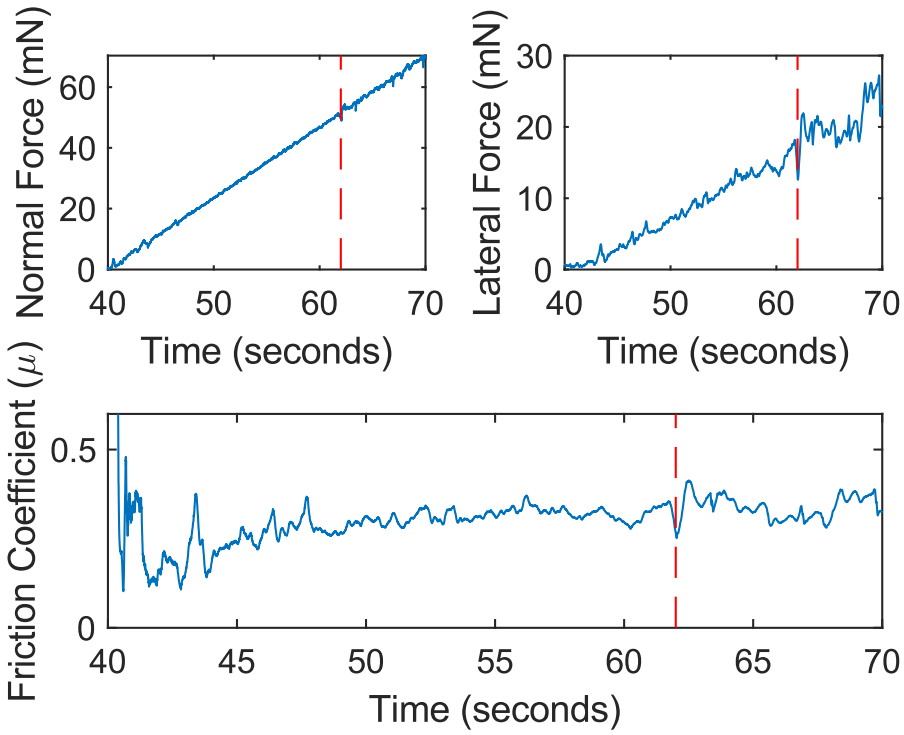


Figure 131: Scratch graphs of scr1 (red dotted line denotes selected point of failure)

The delaminated regions in the films can clearly be seen from optical microscopy images in Figure 132 (scr1), where film buckling is observed at the end of the scratch, verified

by the FIB cross-section in Figure 133. Due to the imperfect tip alignment in the edge-forward orientation, unpinned buckling initially appears on the top side of the scratch, as shown in Figure 132, and later extends to both sides of the scratch at higher loads. Prior to the onset of buckling, minimal plastic deformation and cohesive film chipping are observed on the right side of the scratch. No fragmentation is observed. A large crack is seen on the right side of the blister in Figure 133, however from Figure 132, it can be seen that these surface cracks are present throughout the sample due to the fabrication process and did not result from the scratching experiment.

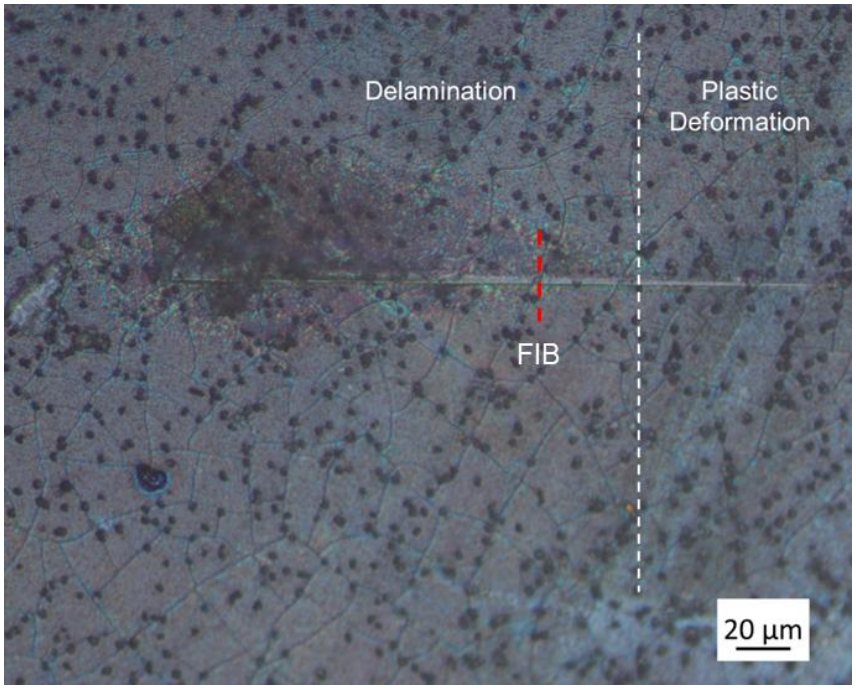


Figure 132: Edge forward orientation scratch (scr2)

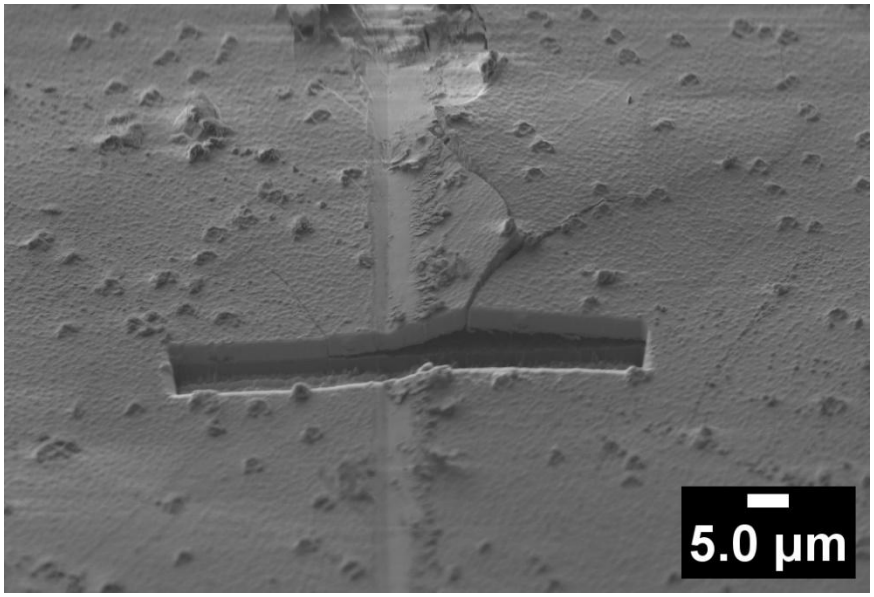


Figure 133: FIB cross-section showing scratch buckling (scr2)

The average edge forward delamination energy is G = 16.1 ± 6.6 J/m^2, meanwhile face forward orientation outputted an average of G = 16.5 ± 2.7 J/m^2. In Chapter 3, it was found that face forward and edge forward orientations recorded different delamination energies. The tungsten films experienced large-scale fragmentation directly after plastic deformation. As a result, the total work done by the indenter involved both delamination and fragmentation, making it difficult to isolate the contributions from each process. The lack of fragmentation in these samples ensures more realistic delamination energies, that are independent of tip orientation.

LLZO-Si(400nm)

Scratches were performed using edge forward orientation with the peak loads 56 mN, scratch length 200 µm, and scratch time 30 seconds, maintaining a consistent dL/dx ratio as the previous sample. It was found that using the parameters 70 mN and 250 µm initiated failure early, therefore the peak load and scratch lengths were lowered. From the SEM images in Figure 134, it can be seen that delamination and small-scale chipping occurs in the early portion of the scratch followed by substrate exposure. The presence of surface blisters likely

contributed to the film chipping more easily. In this sample, pinned buckling takes place, whereas unpinned buckling (blistering) took place in the thicker 2 μm sample. Since the mechanical properties of both films is similar, the mode of buckling (pinned or unpinned), is seen to be dependent on a combination of the film thickness, interfacial strength and film residual stresses.

The scratch graphs in Figure 135 show a discontinuity at 55 seconds (lateral displacement = 100 μm). However, FIB cross-sections in Figure 134 (b) from an earlier portion of the scratch (44 μm, 47 seconds) indicate that delamination started earlier. At 55 seconds, the observed deviations likely result from substrate exposure rather than interfacial failure. No noticeable deviations were seen at 47 seconds, likely because thinner films release less energy at failure compared to thicker ones. Additionally, surface blisters affect the coefficient of friction, complicating the identification of the critical point. This highlights the importance of using both SEM and scratch graphs for accurately determining the critical point, especially in thinner films where sudden failure deviations are less pronounced. The results are summarized in Table 23, and an average delamination energy value of 56.3 ± 8.52 J/m^2 is found.

	h_c (nm)	**L_c (mN)**	**σ_a (GPa)**	**G (J/m^2)**
Scr1	198	13.3	6.84	52.61
Scr2	197	13.0	6.69	50.26
Scr3	184	13.0	7.67	66.04

Table 23: Scratch results for LLZO-Si(400nm)

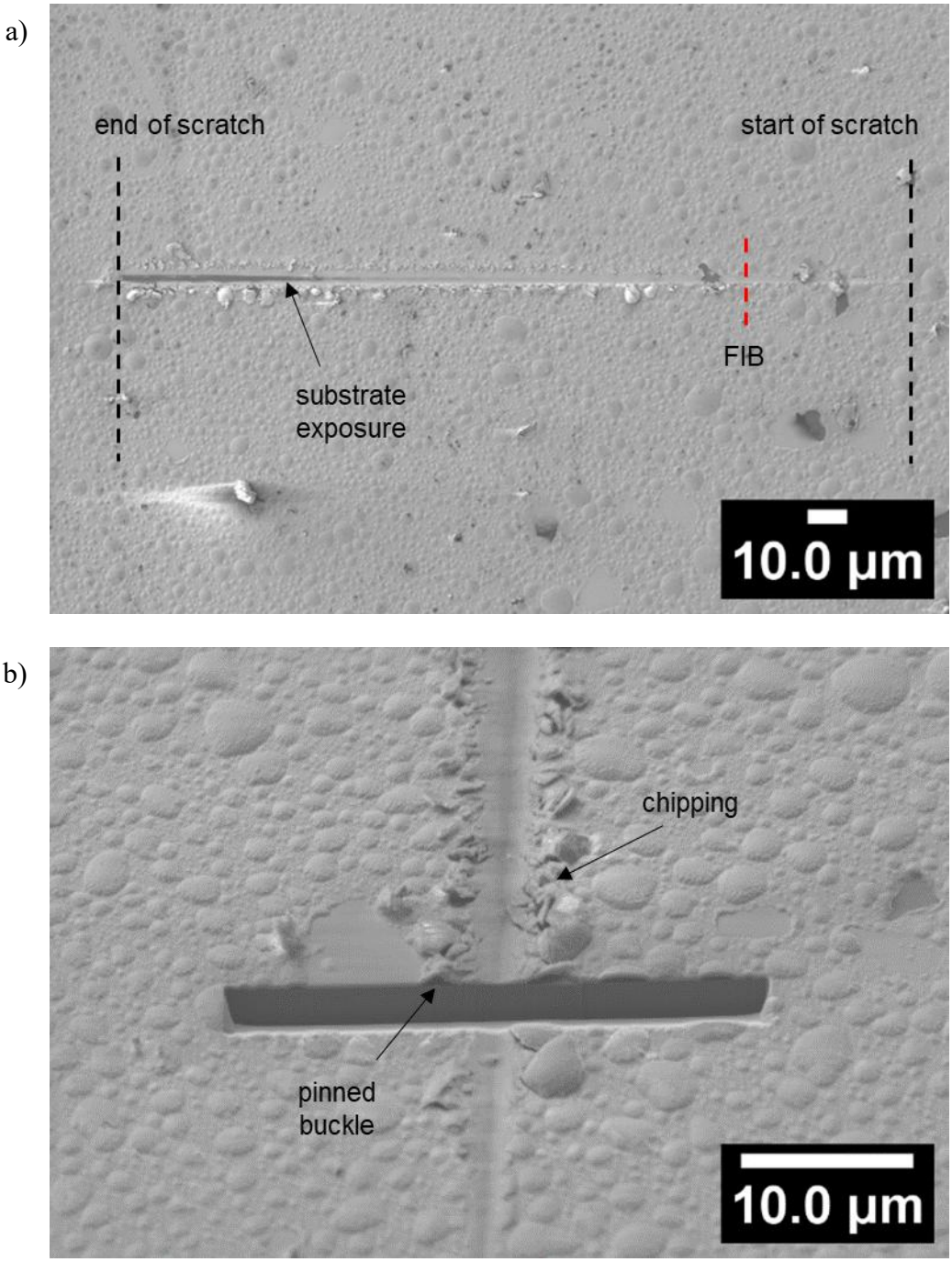


Figure 134: SEM of Scr3 a) full scratch and b) FIB cross-section

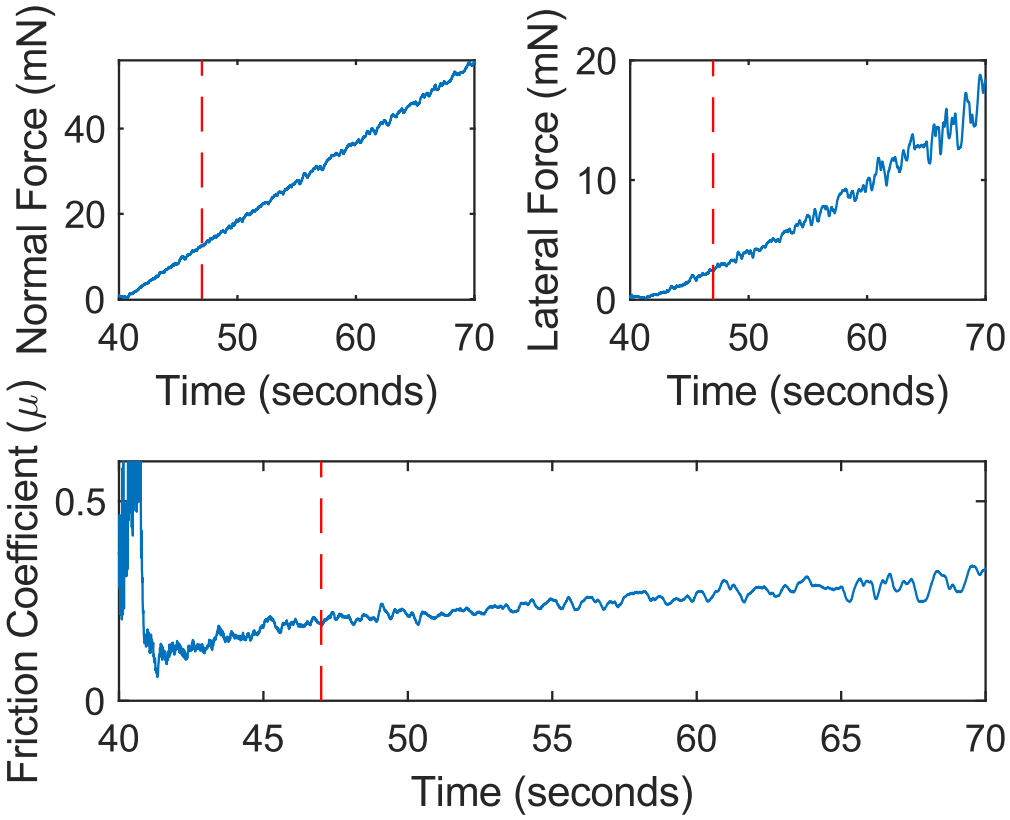


Figure 135: Scr3 scratch graphs (red dotted line denotes selected point of failure)

LLZO-NMC

Scratches were performed with the same orientation and parameters as LLZO-Si(400nm) on LLZO-NMC. The SEM image of the scratch is given in Figure 136 with the FIB cross-section in Figure 137. At the start of the scratch, plastic deformation is observed. As the load increases, film chipping is observed and the NMC layer surface is exposed. From Figure 137, the delaminated areas are not as pronounced as those seen in the LLZO-Si(400nm) sample, and pinned buckling is not observed. This could be either due to the low mechanical properties of the film and substrate, or the high roughness of the substrate which increased the interfacial energy [130,131]. While the roughness of the NMC layer was not directly measured, it can be inferred through the fabrication method used that the surface roughness was significantly higher than the silicon substrate roughness (1.5 nm). The scratch graphs are given in Figure 138 and no clear discontinuity is observed, for reasons similar to those explained for LLZO-

Si(400nm). The scratch parameters including critical load, and critical normal displacement are summarized in Table 24, and an average delamination energy of 2.77 ± 0.53 J/m^2 is found.

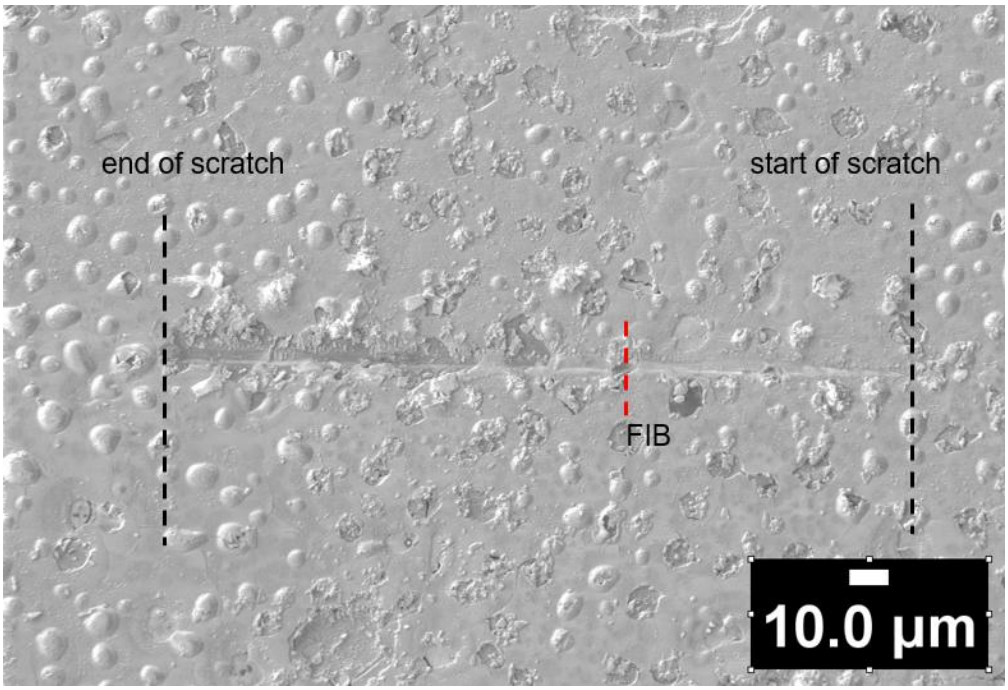


Figure 136: SEM of scr3

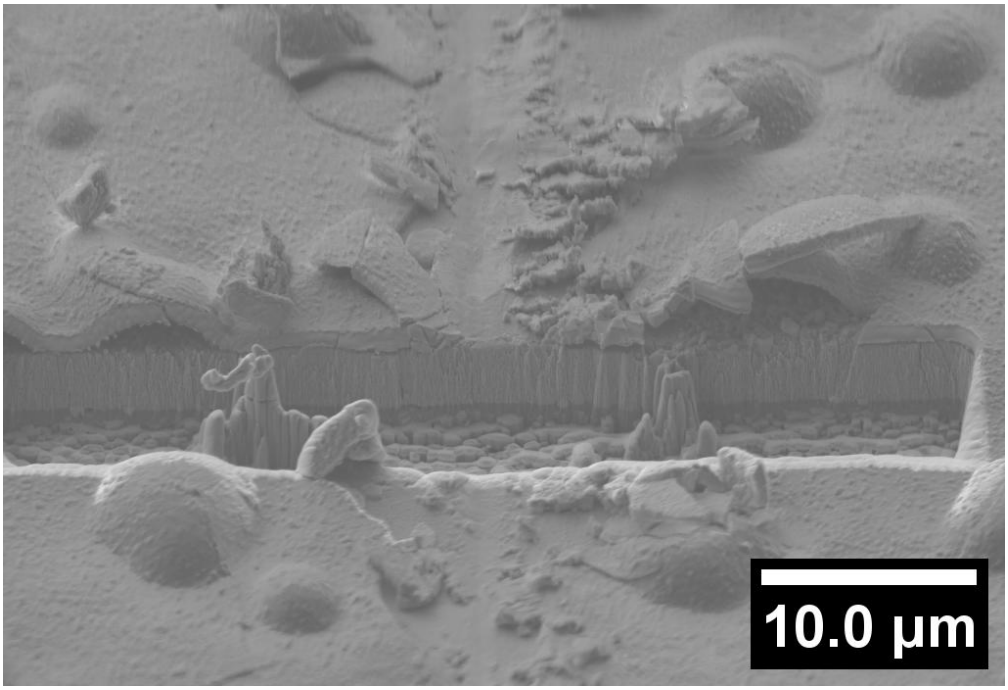


Figure 137: FIB cross-section of scr3

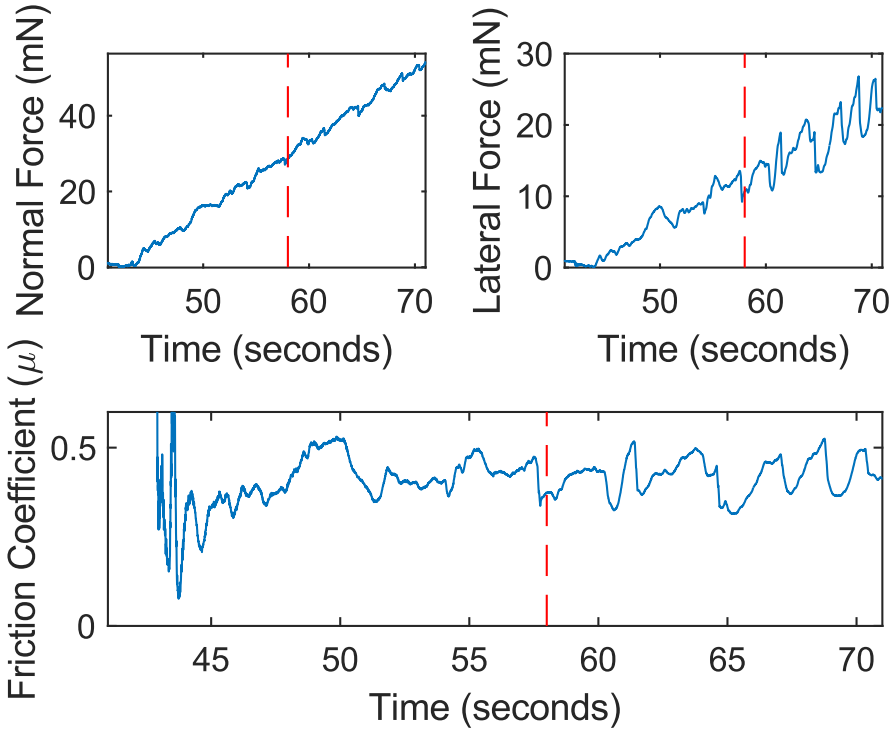


Figure 138: Scratch graphs of scr3 (red dotted line denotes selected point of failure)

	h_c (nm)	L_c (mN)	σ_a (GPa)	G (J/m^2)
Scr1	809	28.8	0.96	2.09
Scr2	484	12.8	1.20	3.20
Scr3	575	18	1.19	3.19
Scr4	473	11	1.10	2.60

Table 24: Scratch Delamination Energy Parameters

UA-LLZO-NMC

Scratches with 70 mN, 250 µm and 30 second scratch time, similar to LLZO-Si(2µm) were performed. The SEM and FIB cross section are shown in Figure 139. Overall, no delamination, film cracking, fragmentation or chipping is observed, indicating that the film cohesive strength along with the interfacial strength are both strong. Along the scratch path, some parabolic cracking can be observed, due to the plastically deformed film being bent back onto the scratch path and compressed by the indenter[111]. From the scratch graphs in Figure 140,

a sudden change in friction coefficient and lateral force is observed at 50 seconds, however no cohesive or adhesive failure is visible in the SEM images (Figure 139). This highlights the importance of post scratch observation in addition to the scratch graphs to evaluate the scratch behaviour accurately.

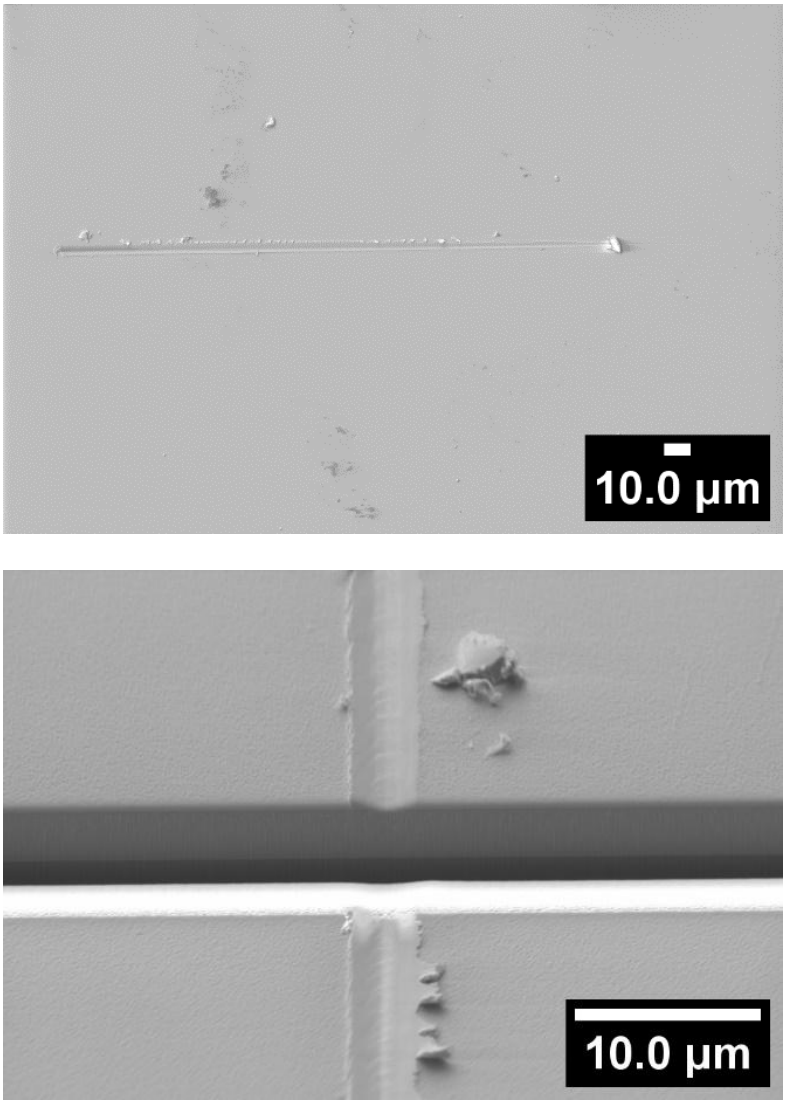


Figure 139: SEM of 70 mN, 250 µm scratch

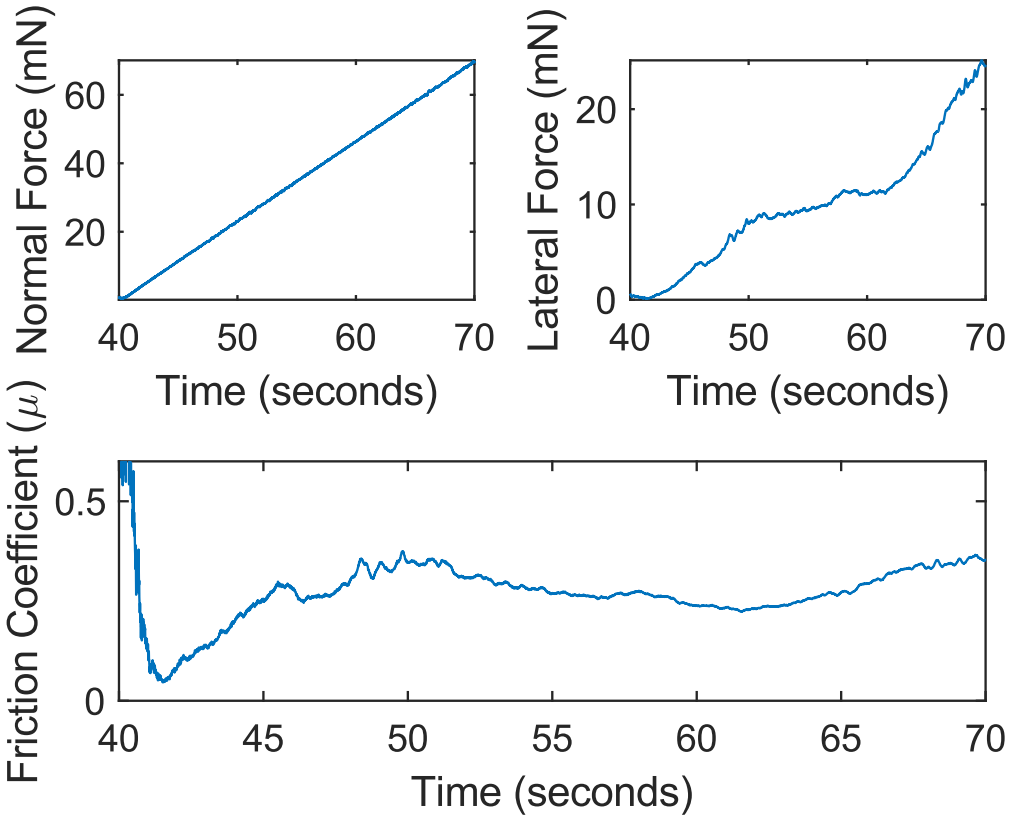


Figure 140: Scratch graphs of 70 mN, 250 μm

Nanoscratch Comparison and Discussion

The results of the nanoscratch experiment are summarized in Table 25, along with the observed interfacial fracture modes and selection of the critical point. The nanoscratch test is semi-quantitative with dependence on extrinsic properties such as film thickness and film hardness. Thicker films are expected to increase the critical load due to the higher forces needed to penetrate the film[71], which was observed in these results. To remove the influence of film thickness, the critical load was divided by the film thickness and plotted in Figure 141 along with the delamination energy, against the film to substrate Young's modulus ratio (to investigate the effect of film substrate modulus mismatch). The modulus of NMC was obtained from the CMX experiments presented earlier (E = 160 GPa), and the modulus of the silicon wafer was determined previously in Chapter 3 from indentation experiments (E = 195 GPa). The critical load/film thickness followed a similar trend to that reported by Zhou et al[120].

LLZO-NMC sample displayed the lowest critical load/film thickness value and lowest delamination energy. These results indicate that the larger the modulus mismatch between the film and substrate, the earlier the thin film delamination occurs. The critical point for LLZO-NMC was chosen to be chipping since no other failure mechanism was observed. There is some debate on whether chipping can truly be considered as a measure of the interfacial properties[111], as chipping can be either adhesive or cohesive in nature. Generally, chipping associated with interfacial failure occurs in front of the crack tip[159,160]. In LLZO-NMC the chipping is mainly seen to occur on the sides of the indenter, indicating that the chipping mode in these samples is likely cohesive. Generally, the delamination energy for chipping is expected to be lower than the delamination energy for buckling, as observed in these results. During chipping, the failure involves the localized detachment of the coating, where cohesive and in some cases adhesive strengths are both compromised, resulting in smaller areas of failure with lower energy requirements. Buckling, on the other hand, usually involves a larger delaminated area and is driven by compressive stresses, requiring more energy to initiate and propagate, hence higher delamination energy is typically needed for buckling. Additionally, from the failure mode maps generated by Bull[111], chipping is expected for coatings and substrates with higher hardness than those experiencing buckling. However, from the nanoindentation results, both LLZO and NMC in the LLZO-NMC sample showed lower hardness than the other LLZO films and the silicon substrate. This discrepancy further supports that the observed chipping may be cohesive, explaining the low values delamination energy in LLZO-NMC.

Overall, the samples exhibited different fracture modes, making direct quantitative comparisons between them challenging, as the criteria for selecting the critical point varied between samples[76], especially in the case of LLZO-NMC which did not exhibit any buckling.

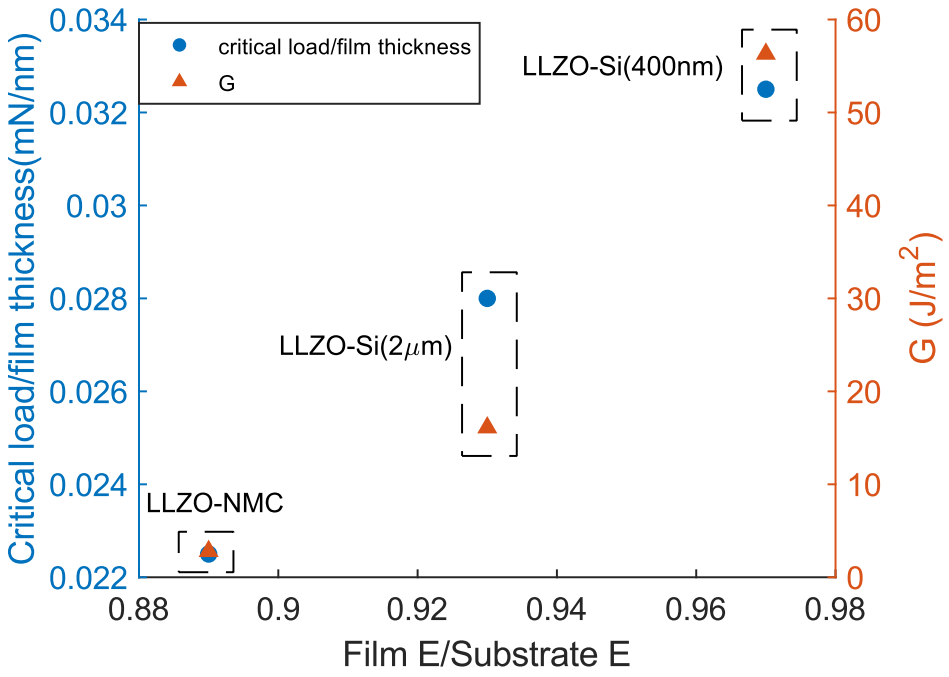


Figure 141: Effect of film to substrate modulus on critical load (normalized with film thickness) and scratch delamination energy

	Observed interfacial fracture mode	**Selection of critical point**	**Average critical load (mN)**	**Average G (J/m^2)**
LLZO-Si(2µm)	Large-scale unpinned buckling	Start of buckling	56	16.1
LLZO-Si(400nm)	Small-scale chipping and pinned buckling	Start of buckling	13	56.3
LLZO-NMC	Medium-scale chipping	Start of chipping	18	2.8
UA-LLZO-NMC	No failure	-	-	-

Table 25: Summary of scratch delamination energies along with the observed interfacial fracture mode

5.3.4. Comparison of nanoindentation and nanoscratch results

A summary of the nanoindentation and nanoscratch results are given in Table 26. For LLZO-Si(2μm), the delamination energy results from nanoindentation and nanoscratching were found to be in good agreement. Typically, nanoscratching of brittle films may overestimate the delamination energy due to the high contribution of fragmentation as seen in Chapter 3 with the tungsten films. Additionally, the tungsten films tested previously displayed a high dependence on the scratch tip orientation. However, the scratch parameters in the LLZO-Si(2μm) sample were chosen to induce delamination before the onset of fragmentation. Due to this, the scratch results agreed with nanoindentation results and were found to be independent of tip orientation.

In contrast, the thinner LLZO-Si(400nm) sample showed a large discrepancy between the two tests, where nanoindentation measured much higher values. This is likely due to the large relative displacements in the delaminated indents, which result in a significant contribution of substrate deformation to the total delamination work. On the other hand, the nanoscratch analysis method by Laugier[62] (stress-based analysis method) is not as highly dependent on the condition of minimal substrate effects, therefore the values are lower. The main condition in the Laugier analysis is that the indenter remains within the film thickness, which is satisfied in the tests. This is further supported by the observations that the critical relative displacement at which delamination begins in LLZO-Si(400nm) is higher in nanoindentation (0.75) compared to nanoscratch (0.50). This indicates that at the onset of delamination, the effect of the substrate is higher in the nanoindentation analysis compared to the nanoscratch analysis. It remains unclear whether using a different set of scratch parameters with different dL/dx ratios would yield results more consistent with those from nanoindentation. As demonstrated in Chapter 3, a wide range of delamination energy values can be obtained simply by adjusting the dL/dx ratio. Overall, a similar trend was observed in

both tests, where higher delamination energy values were found for LLZO-Si(400nm) compared to LLZO-Si(2µm).

In the UA-LLZO-NMC sample, neither test indicated interfacial failure between LLZO and NMC, potentially an effect of the amorphous phases present in the material. The unannealed sample displayed more ductile behaviour and has better adhesion which could be due to the lack of grain boundaries and residual stresses in the amorphous regions. In contrast, the annealed sample (LLZO-NMC) failed in a brittle manner because crystallization introduces residual stresses, thermal mismatch, and grain boundaries that lead to crack initiation, delamination, and fragmentation during testing.

A large discrepancy in the delamination energy values is seen between the two tests for the LLZO-NMC sample, with the nanoscratch test measuring a very low delamination energy. In both tests, interfacial delamination in LLZO-NMC could not be clearly assessed. In nanoscratch, film chipping dominated due to the presence of the blisters. Similarly, in nanoindentation, film fragmentation was more clearly seen than delamination. Even though this sample and LLZO-Si(400nm) are on similar thickness scales, the behaviour at the interface from nanoindentation and nanoscratching differed greatly. The nanoindentation analysis is expected to be highly overestimated due to the large relative displacement values (1.5 - 3) involved. Meanwhile in nanoscratch it is likely that the failure mode seen was solely attributed to cohesive chipping, hence the low values of delamination energy.

	Nanoindentation G (J/m^2)	**Nanoscratch G (J/m^2)**
LLZO-Si(2µm)	15 – 28*	16
LLZO-Si(400nm)	108 – 255*	56
LLZO-NMC	48 - 184	2.8
UA-LLZO-NMC	No failure	No failure

*Table 26: Summary of delamination energies from nanoindentation and nanoscratching. * indicate that FEM corrections were carried out*

5.3.5. Cathode Volume Change Modelling

In solid-state battery operation, delamination can occur during charging as the cathode particle experiences volume contraction. To better understand this process, an ABAQUS model was employed to determine the minimum required delamination energy at the electrolyte-electrode interface to avoid delamination during cathode contraction, for a wide range of electrolyte mechanical properties. This modelling approach allows for delamination energy targets to be set based on the electrolyte material, that can improve the reliability of the battery during cycling. This also allows for the measured delamination energies from nanoindentation and nanoscratching to be put into the solid-state battery operation context. A 5% volume change was modelled as this is within the typical range of volume change for NMC[24,161,162].

Figure 142 shows the required delamination energy to avoid delamination for a range of electrolyte yield strength and Young's modulus values. The material properties were chosen to include the range of the materials experimentally tested, including P1 and PEO from Chapter 4, and LLZO electrolytes tested in this chapter. The black squares on the graph show the expected region for ceramic materials, while the blue circles show the range of material properties for polymers. The red crosses show material properties used in the FEM model, however, do not represent any real-life material behaviour. Each data point on the figure (circles, squares, and plus signs) represents a finite element simulation that was run using different material property combinations.

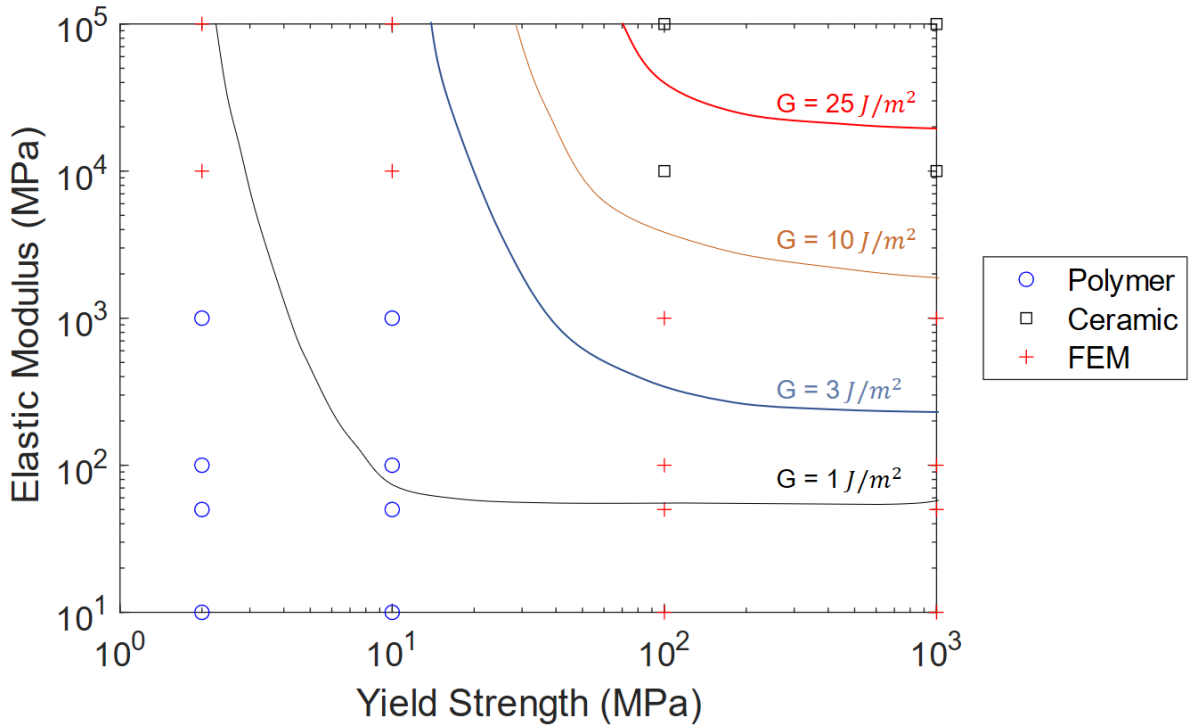


Figure 142: Delamination energy targets needed to avoid delamination at 5% volume change for different values of electrolyte elastic modulus and yield strength. Each data point shown corresponds to an individual FEM simulation where the elastic modulus and yield strength were varied.

The results show that for the polymer region, delamination is avoided even at low delamination energy values of 1 J/m^2. The low yield strength and modulus allows plastic flow to dominate, avoiding stress transfer to the interface. These results agree with the those from Chapter 4 nanoindentation delamination modelling, and literature[24,26]. More brittle materials such as ceramics are seen to require a higher delamination energy to avoid delamination. Finally, at G = 30 J/m^2, all material properties tested avoided delamination.

These results allow for the creation of a target minimum delamination energy value for 5% volume change applications, roughly G = 1 J/m^2 for polymers and G = 10-30 J/m^2 for ceramics. Additionally, the model highlights the critical role of both the electrolyte's mechanical properties and the interfacial fracture energy in predicting the system's ability to avoid delamination during cathode contraction. This highlights the need for optimizing not

only the fracture toughness at the interface but also the intrinsic properties of the electrolyte to ensure mechanical stability during battery cycling. The exact values of LLZO-NMC delamination energy could not be extracted from the nanoindentation and nanoscratch tests, however based on a comparison to the LLZO-Si(400nm) film, it is estimated to be greater than 30 J/m^2. This places both LLZO-NMC and UA-LLZO-NMC in a range that is likely to avoid delamination, as indicated in Figure 142.

5.4. Conclusions

This chapter has investigated the mechanical properties and delamination energy of LLZO thin films on silicon and NMC substrates through nanoindentation and nanoscratch. It was found that sputtering LLZO on NMC resulted in more cubic LLZO formation as compared to silicon substrates. The mechanical properties of the LLZO films were consistent with values reported in the literature. However, in the case of LLZO-NMC, lower mechanical properties were observed. This reduction is likely due to either the formation of secondary phases between LLZO and NMC during the co-sintering process or potential lithium diffusion across the interface, which could weaken the film structure and its mechanical integrity.

Through nanoindentation, all films except UA-LLZO-NMC, displayed deviations in the loading portion of the load-displacement curve, which is indicative of pinned buckles forming during loading. This was observed in LLZO-Si(2μm) which formed large, pinned buckles, and in LLZO-Si(400nm) where smaller pinned buckles were observed. In the thicker 2 μm film, a large variation in linearly extrapolated and FEM plastic work was found (similar to the 1.9 μm tungsten films in Chapter 3), where the linear extrapolation led to overestimated G values. In the thinner film however, the linear and FEM plastic work values were found to be in good agreement. This indicates that the linear plastic work extrapolation assumption works well for thinner films. In LLZO-NMC, interfacial failure was seen at displacements

much greater than the film thickness. This complicated the nanoindentation analysis as high substrate effects were included in the results. A thicker LLZO-NMC film is expected to reduce the critical relative displacement at which delamination first occurs, which would allow for more accurate values. Additionally, separating delamination and film fracture proved challenging. This overlap complicated the assessment of the true delamination energy and makes it harder to analyse the mechanical behaviour of the interface in isolation. The critical relative displacement where delamination was first observed was highest for the LLZO-NMC (at 2.36), then LLZO-Si(400nm) (at 0.75) then finally LLZO-Si(2μm) (at 0.49). The critical relative displacement can give a qualitative ranking of the delamination energies of the interfaces, with LLZO-NMC being the strongest and LLZO-Si(2μm) being the weakest. Through the irreversible work method, nanoindentation delamination energy ranges of G = 15 – 28 J/m^2 for LLZO-Si(2μm), G = 108 – 255 J/m^2 were found for LLZO-Si(400nm), and G = 48 – 184 J/m^2 for LLZO-NMC. The delamination area was seen to decrease with decreasing film thickness.

Through nanoscratch, the two LLZO-Si films displayed buckling, with the thicker 2 μm film displaying large, unpinned buckles (blisters), while the thinner 400nm film displayed pinned buckling. The LLZO-NMC film on the other hand, did not display any buckling. Therefore, the critical point selection differed between the silicon and NMC substrate films. Nanoscratching underestimated the delamination energy in the LLZO-NMC film, as the only observed failure mode in this sample was chipping, leading to very low nanoscratch values (G = 2.8 J/m^2), which is likely a representation of the cohesive chipping strength and not interfacial chipping. The nanoindentation and nanoscratch results of the two LLZO-Si films were in good agreement. In LLZO-Si(2μm), delamination before the onset of fragmentation could be achieved, which led to nanoscratch G values that were similar to the nanoindentation results, and independent of scratch tip orientation. This is in contrast to the tungsten films in

Chapter 3, where delamination without fragmentation could not be isolated, leading to a dependence on the scratch tip orientation.

No interfacial failure was observed during nanoscratch or nanoindentation testing of the unannealed UA-LLZO-NMC sample. XRD analysis suggested the presence of amorphous phases in the sample. The reduction in crystallinity minimizes grain boundaries, which are typical sites for crack nucleation and propagation. Additionally, the absence of residual stresses from annealing contributed to greater resistance to interfacial failure and surface cracking under mechanical loading. The exact influence of annealing on the interface remains unclear, as it should increase interdiffusion at the interface, which would lead to a higher delamination energy. However, the opposite effect was observed in these results. It remains unclear whether annealing at more optimized conditions would improve the interfacial strength.

FE models of an electrolyte coated cathode particle with 5% volume contraction was conducted to understand the minimum delamination energy needed to avoid delamination, for a range of different electrolyte properties. It was found that more compliant electrolytes required a lower delamination energy of 1 J/m^2, meanwhile stiffer electrolytes (such as ceramics) required higher energies to avoid delamination, up to 30 J/m^2. The results show that based on the preliminary results of LLZO-NMC and UA-LLZO-NMC, they are both believed to be above the minimum delamination energy threshold.

6. CONCLUSIONS

In Chapter 3, nanoindentation and nanoscratch adhesion testing methodology was developed on a reference tungsten silicon thin film. Three stages of fracture were observed: I- plastic deformation and surface cracks, II- delamination and blistering and finally, III- film fragmentation. The irreversible work done was used to calculate the work of delamination. Conventional linear plastic work extrapolation was found to greatly overestimate the work of delamination leading to a large range of values that increase with increase applied load (17-107 J/m^2). FEM corrections were employed which resulted in a smaller range of delamination energies (2-29 J/m^2) which agree well with literature values of tungsten on silicon. In the nanoscratch test, the film was found to progress from plastic deformation directly to fragmentation., meaning that the work of fragmentation was included into the overall work done calculation. The values of G were found to be heavily influenced by scratch parameters, and a range of 13 – 49 J/m^2 was found through changing the parameters. The scratch tip orientation was also found to influence the delamination energies, with face forward resulting in lower values. Comparable values between nanoindentation and nanoscratch were found using high dL/dx ratios and a face forward orientation. Isolating the delamination event was

possible through nanoindentation but not through nanoscratching. Additionally, the lack of standardized parameter selection guide for nanoscratching made the results difficult to interpret. Meanwhile, the nanoindentation delamination energy results were comparable to literature and not parameter sensitive.

In Chapter 2, two polymer electrolytes PEO and a novel tri-block copolymer (P1) on silicon were tested. A different nanoindentation adhesion analysis method from the one developed in Chapter 3 was required due to delamination occurring during the loading phase of the curve, as well as observed deviations in the curve indicative of delamination. Through FEM, it was found that the conventional literature method of fitting the loading curve after delamination resulted in less accurate values compared to fitting the data before delamination. This is because delamination alters the apparent stiffness of the system, making post-delamination data unreliable for accurately reflecting the material's properties. Through nanoindentation, P1 was found to avoid delamination through pile-up and plastic deformation, and no deviations in the loading curve were observed. Meanwhile, PEO displayed curve deviations and delamination was observed through FIB. By fitting the curve (before delamination), an average delamination energy of 1.17 J/m^2 was found. Through nanoscratching, P1 scratches displayed pile-up and substrate exposure only. Meanwhile, PEO showed fish scaling, and parabolic cracking followed by material removal. Through nanoscratch, a delamination energy of 2.3 $J/m^2$was found for PEO. FEM was conducted to create a failure map to understand the influence of film yield strength and Young's modulus on the nanoindentation failure mechanism (plastic deformation or delamination). Lower yield strength and Young's modulus were found to avoid delamination through plastic deformation, as early onset of yielding and lower stiffness allowed the stress to be transferred away from the interface. The map placed PEO in the delamination region for G between 1 – 1.2 J/m^2, agreeing with the nanoindentation results. Through FEM a lower bound of 0.25 J/m^2 was

found for P1. Similar to the results of Chapter 3, overall nanoindentation was found to provide more consistent and reproducible results.

In Chapter 5, LLZO films on silicon and NMC substrates were tested. Through nanoindentation testing, the thicker LLZO-Si(2μm) film displayed large, pinned buckle delamination, while in the thinner film LLZO-Si(400nm), smaller pinned buckles were observed. Through the irreversible work method, delamination energy values of G = 108 – 255 J/m^2 were found for LLZO-Si(400nm) and G = 15 – 28 J/m^2 for LLZO-Si(2μm). FEM corrections to the plastic work resulted in lower delamination energies for LLZO-Si(2μm) as compared to the linear extrapolation, similar to the results in Chapter 3. In the thinner film however, the assumption of linear plastic work extrapolation was found to agree well with the results of FEM, indicating that the linear assumption works well for thinner films. LLZO-NMC displayed delamination, at relative displacements (h_{max}/t_{film}) > 1, meaning that the high degree of substrate deformation led to overestimated values of G = 48 – 184 J/m^2. A qualitative ranking of the films based on the critical relative displacement at which delamination first occurred was deduced as follows (from strongest to weakest): UA-LLZO-NMC (no failure), LLZO-NMC (2.36), LLZO-Si (400nm) (0.75), and LLZO-Si (2μm) (0.49).

Through nanoscratch, different failure criteria were observed for each sample as the LLZO-Si films displayed buckling meanwhile LLZO-NMC displayed chipping only. A G value of 16 J/m^2 was found for LLZO-Si(2μm) which is in good agreement with the results of nanoindentation. As compared to the tungsten films in Chapter 3, delamination before the onset of fragmentation could be isolated in nanoscratch, which explains the consistent results between the two tests that were independent of scratch tip orientation. For LLZO-Si(400nm), a G value of 56 J/m^2 was found which is lower than nanoindentation, possibly due to nanoscratch parameter sensitivity, or some overestimations in the nanoindentation analysis due to high h_{max}/t_{film} values. Low values of nanoscratch delamination energy were found for LLZO-

NMC (G = 2.8 J/m^2). This is due to the failure point being defined as start of chipping, which indicates that the calculated value is representative of cohesive chipping rather than delamination. This interpretation is further supported by the observation that chipping in LLZO-NMC occurred along the sides of the scratch, rather than ahead of the indenter, where interfacial chipping is typically seen. Overall, the results of nanoindentation have shown that LLZO-NMC has a greater adhesion energy than LLZO-Si, however more work needs to be done on a thicker LLZO-NMC sample which would display clearer interfacial failure mechanisms during scratching and fail at lower h_{max}/t_{film} ratios in nanoindentation. UA-LLZO-NMC did not exhibit any interfacial failure during nanoscratching, which is likely attributed to the presence of amorphous phases, as indicated by XRD results. The absence of residual stresses and grain boundaries possibly prevented crack initiation and propagation, which typically occur along grain boundaries in crystalline materials. Annealing should increase the interfacial strength due to interdiffusion, however the opposite effect was observed in these results. More work needs to be done into finding optimal annealing conditions to improve interfacial diffusion.

Based on the cathode volume contraction FE models, it was concluded that a target delamination energy of 1 J/m^2 is required for polymers and 10-30 J/m^2 for ceramics to prevent delamination under a 5% volume change. For LLZO-NMC and UA-LLZO-NMC, preliminary results presented in this thesis suggest that their delamination energies exceed the minimum threshold required to prevent failure.

7. REFERENCES

1. *2022 UK Greenhouse Gas Emissions, Final Figures*. https://assets.publishing.service.gov.uk/media/65c0d15863a23d0013c821e9/2022-final-greenhouse-gas-emissions-statistical-release.pdf (2022).
2. Tyers, R., Hutton, G., Walker, A. & Stewart, I. *Electric Vehicles and Infrastructure*. (2024).
3. Janek, J. & Zeier, W. G. A solid future for battery development. *Nat Energy* **1**, 1–4 (2016).
4. Zhang, H., Yang, Y., Ren, D., Wang, L. & He, X. Graphite as anode materials: Fundamental mechanism, recent progress and advances. *Energy Storage Mater* **36**, 147–170 (2021).
5. Xu, W. *et al.* Lithium metal anodes for rechargeable batteries. *Energy Environ Sci* **7**, 513–537 (2014).

6. Miyazaki, R. High-Capacity Anode Materials for All-Solid-State Lithium Batteries. *Front Energy Res* **8**, 1–6 (2020).

7. Xue, Z., He, D. & Xie, X. Poly(ethylene oxide)-based electrolytes for lithium-ion batteries. *J Mater Chem A Mater* **3**, 19218–19253 (2015).

8. Devaux, D. *et al.* Optimization of Block Copolymer Electrolytes for Lithium Metal Batteries. *Chemistry of Materials* **27**, 4682–4692 (2015).

9. Bouchet, R. *et al.* Charge transport in nanostructured PS-PEO-PS triblock copolymer electrolytes. *Macromolecules* **47**, 2659–2665 (2014).

10. Cao, X. H. *et al.* Simultaneous Improvement of Ionic Conductivity and Mechanical Strength in Block Copolymer Electrolytes with Double Conductive Nanophases. *Macromol Rapid Commun* **41**, 1–6 (2020).

11. Wu, F. *et al.* Polymer electrolytes and interfaces toward solid-state batteries: Recent advances and prospects. *Energy Storage Mater* **33**, 26–54 (2020).

12. Li, Y., Han, J. T., Wang, C. A., Xie, H. & Goodenough, J. B. Optimizing Li+ conductivity in a garnet framework. *J Mater Chem* **22**, 15357–15361 (2012).

13. Kataoka, K. Oxide single crystals with high lithium-ion conductivity as solid electrolytes for all-solid-state lithium secondary battery applications. *Journal of the Ceramic Society of Japan* **128**, 7–18 (2020).

14. Lim, Y.-J., An, Y.-H. & Jo, N.-J. Polystyrene-Al2O3 composite solid polymer electrolyte for lithium secondary battery. *Nanoscale Res Lett* **7**, 3–8 (2012).

15. Shim, J., Kim, D. G., Kim, H. J., Lee, J. H. & Lee, J. C. Polymer composite electrolytes having core-shell silica fillers with anion-trapping boron moiety in the shell layer for all-solid-state lithium-ion batteries. *ACS Appl Mater Interfaces* **7**, 7690–7701 (2015).

16. Li, J. *et al.* A promising composite solid electrolyte incorporating LLZO into PEO/PVDF matrix for all-solid-state lithium-ion batteries. *Ionics (Kiel)* **26**, 1101–1108 (2020).

17. Zheng, J., Tang, M. & Hu, Y. Y. Lithium Ion Pathway within Li7La3Zr2O12-Polyethylene Oxide Composite Electrolytes. *Angewandte Chemie - International Edition* **55**, 12538–12542 (2016).

18. Zhang, X. *et al.* Li6.4La3Zr1.4Ta0.6O12 Reinforced Polystyrene-Poly(ethylene oxide)-Poly(propylene oxide)-Poly(ethylene oxide)-Polystyrene pentablock copolymer-based composite solid electrolytes for solid-state lithium metal batteries. *J Power Sources* **542**, 231797 (2022).

19. Liu, W. *et al.* Enhancing ionic conductivity in composite polymer electrolytes with well-aligned ceramic nanowires. *Nat Energy* **2**, 1–7 (2017).

20. Zagórski, J. *et al.* Garnet-Polymer Composite Electrolytes: New Insights on Local Li-Ion Dynamics and Electrodeposition Stability with Li Metal Anodes. *ACS Appl Energy Mater* **2**, 1734–1746 (2019).

21. Hao, F. & Mukherjee, P. P. Mesoscale Analysis of the Electrolyte-Electrode Interface in All-Solid-State Li-Ion Batteries. *J Electrochem Soc* **165**, A1857–A1864 (2018).

22. Wang, D. *et al.* Mitigating the Interfacial Degradation in Cathodes for High-Performance Oxide-Based Solid-State Lithium Batteries. *ACS Appl Mater Interfaces* **11**, 4954–4961 (2019).

23. Koerver, R. *et al.* Capacity Fade in Solid-State Batteries: Interphase Formation and Chemomechanical Processes in Nickel-Rich Layered Oxide Cathodes and Lithium Thiophosphate Solid Electrolytes. *Chemistry of Materials* **29**, 5574–5582 (2017).

24. Barai, P. *et al.* Investigation of Delamination-Induced Performance Decay at the Cathode/LLZO Interface. *Chemistry of Materials* **33**, 5527–5541 (2021).

25. Bucci, G., Swamy, T., Chiang, Y. M. & Carter, W. C. Modeling of internal mechanical failure of all-solid-state batteries during electrochemical cycling, and implications for battery design. *J Mater Chem A Mater* **5**, 19422–19430 (2017).

26. Bucci, G., Talamini, B., Renuka Balakrishna, A., Chiang, Y. M. & Carter, W. C. Mechanical instability of electrode-electrolyte interfaces in solid-state batteries. *Phys Rev Mater* **2**, 1–11 (2018).

27. Oliver, W. C. & Pharr, G. M. An improved technique for determining hardness and elastic modulus using load and displacement sensing indentation experiments. *J Mater Res* **7**, 1564–1583 (1992).

28. Aspinall, J., Armstrong, D. E. J. & Pasta, M. EBSD-coupled indentation: nanoscale mechanics of lithium metal. *Mater Today Energy* **30**, 101183 (2022).

29. Hua, L. Enhanced physical properties of PEO /GRAPHENE composites. *J Phys Conf Ser* **1798**, (2021).

30. Ni, J. E., Case, E. D., Sakamoto, J. S., Rangasamy, E. & Wolfenstine, J. B. Room temperature elastic moduli and Vickers hardness of hot-pressed LLZO cubic garnet. *J Mater Sci* **47**, 7978–7985 (2012).

31. Herbert, E. G., Tenhaeff, W. E., Dudney, N. J. & Pharr, G. M. Mechanical characterization of LiPON films using nanoindentation. *Thin Solid Films* **520**, 413–418 (2011).

32. Fischer-Cripps, A. & Nicholson, D. *Nanoindentation. Mechanical Engineering Series*. *Applied Mechanics Reviews* vol. 57 (2004).

33. Saha, R. & Nix, W. D. Effects of the substrate on the determination of thin film mechanical properties by nanoindentation. *Acta Mater* **50**, 23–38 (2002).

34. Bull, S. J. Microstructure and indentation response of TiN coatings: The effect of measurement method. *Thin Solid Films* **688**, 137452 (2019).

35. Tsui, T. Y. & Pharr, G. M. Substrate effects on nanoindentation mechanical property measurement of soft films on hard substrates. *J Mater Res* **14**, 292–301 (1999).

36. Geng, K., Yang, F., Druffel, T. & Grulke, E. A. Nanoindentation behavior of ultrathin polymeric films. *Polymer (Guildf)* **46**, 11768–11772 (2005).

37. Zak, S., Trost, C. O. W., Kreiml, P. & Cordill, M. J. Accurate measurement of thin film mechanical properties using nanoindentation. *J Mater Res* **37**, 1373–1389 (2022).

38. Jönsson, B. & Hogmark, S. Hardness measurements of thin films. *Thin Solid Films* **114**, 257–269 (1984).

39. Korsunsky, A. M., McGurk, M. R., Bull, S. J. & Page, T. F. On the hardness of coated systems. *Surf Coat Technol* **99**, 171–183 (1998).

40. King, R. B. Elastic analysis of some punch problems for a layered medium. *Int J Solids Struct* **23**, 1657–1664 (1987).

41. Doerner, M. F. & Nix, W. D. A method for interpreting the data from depth-sensing indentation instruments. *J Mater Res* **1**, 601–609 (1986).

42. Humood, M. *et al.* Nanoindentation and nanoscratch of sub-micron polymer nanocomposite films on compliant substrate. *Thin Solid Films* **736**, (2021).

43. Marshall, D. B. & Evans, A. G. Measurement of adherence of residually stressed thin films by indentation. I. Mechanics of interface delamination. *J Appl Phys* **56**, 2632–2638 (1984).

44. Kriese, M. D., Gerberich, W. W. & Moody, N. R. Quantitative adhesion measures of multilayer films: Part II. Indentation of W/Cu, W/W, Cr/W. *J Mater Res* **14**, 3019–3026 (1999).

45. Zhou, Q. *et al.* Adhesion energy and related plastic deformation mechanism of Cu/Ru nanostructured multilayer film. *J Alloys Compd* **772**, 823–827 (2019).

46. Albrecht, J. *et al.* Thin film adhesion measurement by nanoindentation: Review of methodologies and validation by means of finite element simulations. *2019 IEEE 21st Electronics Packaging Technology Conference, EPTC 2019* 417–420 (2019) doi:10.1109/EPTC47984.2019.9026575.

47. Volinsky, A. A., Moody, N. R. & Gerberich, W. W. Interfacial toughness measurements for thin films on substrates. *Acta Mater* **50**, 441–466 (2002).

48. Omiya, M., Kishimoto, K. & Nakano, T. Evaluation of the interfacial strength of layered structures by indentation method. *Journal of Applied Mechanics, Transactions ASME* **75**, 0310061–0310066 (2008).

49. KOZUKI, K. & KISHIMOTO, K. Film Thickness Dependency of Interfacial Strength Evaluation for Thin Film Coating Structure by Nanoindentation Method. *Journal of Solid Mechanics and Materials Engineering* **4**, 771–780 (2010).

50. Malzbender, J. U. & With, G. De. Energy dissipation , fracture toughness and the indentation load **.** displacement curve of coated materials. *Surf Coat Technol* **135**, 60–68 (2000).

51. Li, W. & Siegmund, T. An analysis of the indentation test to determine the interface toughness in a weakly bonded thin film coating - Substrate system. *Acta Mater* **52**, 2989–2999 (2004).

52. INOUE, K. *et al.* Evaluation of interfacial strength of multilayer thin films polymer by nanoindentation technique. *Mechanical Engineering Journal* **6**, 18-00326-18–00326 (2019).

53. Omiya, M., Kozuki, K., Kishimoto, K. & Inoue, H. Nano-Indentation approach to interfacial strength evaluation. *The Abstracts of ATEM : International Conference on Advanced Technology in Experimental Mechanics : Asian Conference on Experimental Mechanics* **2007.6**, _OS5-1-4-1-_OS5-1-4-6 (2007).

54. Li, X. & Bhushan, B. Measurement of fracture toughness of ultra-thin amorphous carbon films. *Thin Solid Films* **315**, 214–221 (1998).

55. M. Takeda, N. Matoba, M. O. and M. S. Evaluation of Adhesion Between UV-cured SiOC Film and Si Substrate by Nanoindentation Method. *Materials Research* **1193**, 2–7 (2009).

56. Chen, J. & Bull, S. J. Indentation fracture and toughness assessment for thin optical coatings on glass. *J Phys D Appl Phys* **40**, 5401–5417 (2007).

57. Den Toonder, J., Malzbender, J., De With, G. & Balkenende, R. Fracture toughness and adhesion energy of sol-gel coatings on glass. *J Mater Res* **17**, 224–233 (2002).

58. Volinsky, A. A., Vella, J. B. & Gerberich, W. W. Fracture toughness, adhesion and mechanical properties of low-K dielectric thin films measured by nanoindentation. *Thin Solid Films* **429**, 201–210 (2003).

59. Kleinbichler, A. *et al.* New Insights into Nanoindentation-Based Adhesion Testing. *Jom* **69**, 2237–2245 (2017).

60. Chang, S. Y., Tsai, H. C., Chang, J. Y., Lin, S. J. & Chang, Y. S. Analyses of interface adhesion between porous SiOCH low-k film and SiCN layers by nanoindentation and nanoscratch tests. *Thin Solid Films* **516**, 5334–5338 (2008).

61. Benjamin, P. & Weaver, C. Measurement of adhesion of thin films. *Proc R Soc Lond A Math Phys Sci* **254**, 163–176 (1960).

62. Laugier, M. T. An energy approach to the adhesion of coatings using the scratch test. *Thin Solid Films* **117**, 243–249 (1984).

63. Mallikarjunachari, G. & Ghosh, P. Analysis of strength and response of polymer nano thin film interfaces applying nanoindentation and nanoscratch techniques. *Polymer (Guildf)* **90**, 53–66 (2016).

64. Boddaert, X. *et al.* Organic ultrathin film adhesion on compliant substrate using scratch test technique. *Thin Solid Films* **528**, 194–198 (2013).

65. Deyneka-Dupriez, N. *et al.* Interfacial adhesion and friction of pyrolytic carbon thin films on silicon substrates. *J Mater Res* **23**, 2749–2756 (2008).

66. Lee, J., Polychronopoulou, K., Cloud, A. N., Abelson, J. R. & Polycarpou, A. A. Shear strength measurements of hafnium diboride thin solid films. *Wear* **318**, 168–176 (2014).

67. He, A. & Huang, H. Nanoscratch characteristics and interfacial adhesion energy of SiN/GaAs film/substrate bilayer systems. *International Journal of Surface Science and Engineering* **7**, 382–396 (2013).

68. Liu, Z., Sun, J., Wu, J. Da, Wang, P. N. & Shen, W. Determination of adhesion energy of cnx thin film on silicon from micro-scratch testing. *Tribology Transactions* **47**, 130–137 (2004).

69. Weaver, C. Adhesion of thin films. in *J Vac Sci Technol* vol. 12 18–25 (1974).

70. Steinmann, P. A., Tardy, Y. & Hintermann, H. E. Adhesion testing by the scratch test method: The influence of intrinsic and extrinsic parameters on the critical load. *Thin Solid Films* **154**, 333–349 (1987).

71. Wirasate, S. & Boerio, F. J. Effect of Adhesion , Film Thickness , and Substrate Hardness on the Scratch Behavior of Poly (carbonate) Films. *Journal of Adhesion* **8464**, 509–528 (2005).

72. Burnett, P. J. & Rickerby, D. S. The Scratch Adhesion Test: An Elastic-Plastic Indentation Analysis. *Thin Solid Films* **157**, 233–254 (1988).

73. Beake, B. D., Ogwu, A. A. & Wagner, T. Influence of experimental factors and film thickness on the measured critical load in the nanoscratch test. *Materials Science and Engineering: A* **423**, 70–73 (2006).

74. Wang, W. *et al.* Experimental and numerical investigation on the effect of scratch direction on material removal and friction characteristic in BK7 scratching. *Materials* **13**, (2020).

75. Liu, M. & Yan, F. Comparison of Microscratch Responses of Metals Between Berkovich and Rockwell C Indenters Under Progressive Normal Force. *Tribol Lett* **69**, 1–16 (2021).

76. Bull, S. J. & Berasetegui, E. G. An overview of the potential of quantitative coating adhesion measurement by scratch testing. *Tribol Int* **39**, 99–114 (2006).

77. Jiang, H., Browning, R. & Sue, H. J. Understanding of scratch-induced damage mechanisms in polymers. *Polymer (Guildf)* **50**, 4056–4065 (2009).

78. Barr, C. J., Wang, L., Coffey, J. K. & Daver, F. Influence of surface texturing on scratch/mar visibility for polymeric materials: a review. *J Mater Sci* **52**, 1221–1234 (2017).

79. *D7027 − 20 Standard Test Method for Evaluation of Scratch Resistance of Polymeric Coatings and Plastics Using an Instrumented Scratch Machine*. (2020) doi:10.1520/D7027-20.2.

80. Lu, M. & Huang, H. Determination of the energy release rate in the interfacial delamination of silicon nitride film on gallium arsenide substrate via nanoindentation. *J Mater Res* **29**, 801–810 (2014).

81. Chen, J. & Bull, S. J. Assessment of the toughness of thin coatings using nanoindentation under displacement control. *Thin Solid Films* **494**, 1–7 (2006).

82. Lassnig, A. *et al.* Microstructural Effects on the Interfacial Adhesion of Nanometer-Thick Cu Films on Glass Substrates: Implications for Microelectronic Devices. *ACS Appl Nano Mater* **4**, 61–70 (2021).

83. De Boer, M. P. & Gerberich, W. W. Microwedge indentation of the thin film fine line - II. Experiment. *Acta Mater* **44**, 3177–3187 (1996).

84. Nanoscience. Scanning Electron Microscopy. https://www.nanoscience.com/techniques/scanning-electron-microscopy/.

85. Wolff, A. Focused ion beams: An overview of the technology and its capabilities. *Wiley Analytical Science Magazine* https://analyticalscience.wiley.com/content/article-do/focused-ion-beams-overview-technology-and-its-capabilities.

86. Cullity, B. D., & Stock, S. R. *Elements of X-Ray Diffraction*. (Prentice-Hall, 2001).

87. Faraji, G., Kim, H. S. & Kashi, H. T. Introduction. *Severe Plastic Deformation* 1–17 (2018) doi:10.1016/b978-0-12-813518-1.00020-5.

88. Hertz, H. On the Contact of Elastic Solids. *Miscellaneous papers (Journal fur die reine und angewandte Mathematik)* **92**, 146–162 (1881).

89. Doerner, M. F. & Nix, W. D. A method for interpreting the data from depth-sensing indentation instruments. *J Mater Res* **1**, 601–609 (1986).

90. Bolshakov, A. & Pharr, G. M. Influences of pileup on the measurement of mechanical properties by load and depth sensing indentation techniques. *J Mater Res* **13**, 1049–1058 (1998).

91. Kese, K. O., Li, Z. C. & Bergman, B. Method to account for true contact area in soda-lime glass during nanoindentation with the Berkovich tip. *Materials Science and Engineering: A* **404**, 1–8 (2005).

92. Chudoba, T. & Richter, F. Investigation of creep behaviour under load during indentation experiments and its influence on hardness and modulus results. *Surf Coat Technol* **148**, 191–198 (2001).

93. Feng, G. & Ngan, A. H. W. Effects of creep and thermal drift on modulus measurement using depth-sensing indentation. *J Mater Res* **17**, 660–668 (2002).

94. Griffith, A. A. The phenomena of rapture and flow in soilds. *Philos. Trans. R. Soc. London* vol. 221 163–198 Preprint at http://mbarkey.eng.ua.edu/courses/AEM644/Griffith1921fracture.pdf (1920).

95. Barenblatt, G. I. The Mathematical Theory of Equilibrium Cracks in Brittle Fracture. in 55–129 (1962). doi:10.1016/S0065-2156(08)70121-2.

96. Elices, M., Guinea, G. V., Gómez, J. & Planas, J. The cohesive zone model: Advantages, limitations and challenges. *Eng Fract Mech* **69**, 137–163 (2001).

97. Hallett, S. R. & Harper, P. W. *Modelling Delamination with Cohesive Interface Elements*. *Numerical Modelling of Failure in Advanced Composite Materials* (Elsevier Ltd., 2015). doi:10.1016/B978-0-08-100332-9.00002-5.

98. Dassault Systemes Simulia Corp. *Selecting Material Parameters in Abaqus for Cohesive Elements Defined in Terms of Traction-Separation*.

99. Diehl, T. On using a penalty-based cohesive-zone finite element approach, Part II: Inelastic peeling of an epoxy-bonded aluminum strip. *Int J Adhes Adhes* **28**, 256–265 (2008).

100. Diehl, T. On using a penalty-based cohesive-zone finite element approach, Part I: Elastic solution benchmarks. *Int J Adhes Adhes* **28**, 237–255 (2008).

101. Zhang, S. *et al.* Directly Probing the Fracture Behavior of Ultrathin Polymeric Films. *ACS Polymers Au* **1**, 16–29 (2021).

102. Song, K., Dávila, C. G. & Rose, C. A. Guidelines and Parameter Selection for the Simulation of Progressive Delamination. 1–15 (2018).

103. De Boer, M. P., Kriese, M. & Gerberich, W. W. Investigation of a new fracture mechanics specimen for thin film adhesion measurement. *J Mater Res* **12**, 2673–2685 (1997).

104. Lakshmi Prasad, B. S. & Raja Annamalai, A. Effect of Rhenium addition on tungsten heavy alloys processed through spark plasma sintering. *Ain Shams Engineering Journal* **12**, 2957–2963 (2021).

105. Zhu, C. C. *et al.* The dynamical mechanical properties of tungsten under compression at working temperature range of divertors. *Journal of Nuclear Materials* **469**, 120–124 (2016).

106. Ren, C. *et al.* Methods for improving ductility of tungsten - A review. *Int J Refract Metals Hard Mater* **75**, 170–183 (2018).

107. Armstrong, R. W., Elban, W. L. & Walley, S. M. Nano-Indentation Hardness and Strain Hardening of Silicon, Sodium Chloride and Tungsten Crystals. *Exp Mech* **62**, 359–364 (2022).

108. Zhang, T. Y. & Xu, W. H. Surface effects on nanoindentation. *J Mater Res* **17**, 1715–1720 (2002).

109. Xiao, X. *et al.* High temperature nano-indentation of tungsten: Modelling and experimental validation. *Materials Science and Engineering: A* **743**, 106–113 (2019).

110. Gerberich, W. W. & Cordill, M. J. Physics of adhesion. *Reports on Progress in Physics* **69**, 2157–2203 (2006).

111. Bull, S. J. Failure mode maps in the thin film scratch adhesion test. *Tribol Int* **30**, 491–498 (1997).

112. Hertzberg, R. *Deformation and Fracture Mechanics of Engineering Materials*. (Hoboken, New Jersey : John Wiley & Sons, Inc., 2013).

113. Chamani, H. R. & Ayatollahi, M. R. The effect of Berkovich tip orientations on friction coefficient in nanoscratch testing of metals. *Tribol Int* **103**, 25–36 (2016).

114. Beake, B. D., Harris, A. J. & Liskiewicz, T. W. Review of recent progress in nanoscratch testing. *Tribology - Materials, Surfaces and Interfaces* **7**, 87–96 (2013).

115. Gent, A. N. & Hamed, G. R. Peel Mechanics for an Elastic-Plastic Adherend. *Rubber Chemistry and Technology* **52**, 1057–1071 (1979).

116. Mallikarjunachari, G. & Ghosh, P. Nanomechanical study of polymer-polymer thin film interface under applied service conditions. *J Appl Polym Sci* **133**, 1–13 (2016).

117. Su, X., Zhang, T., Liang, X., Gao, H. & Sheldon, B. W. Employing nanoscale surface morphologies to improve interfacial adhesion between solid electrolytes and Li ion battery cathodes. *Acta Mater* **98**, 175–181 (2015).

118. Cole, P. J., Cook, R. F. & Macosko, C. W. Adhesion between immiscible polymers correlated with interfacial entanglements. *Macromolecules* **36**, 2808–2815 (2003).

119. Yeo, H. *et al.* Alternatives to fluorinated binders: recyclable copolyester/carbonate electrolytes for high-capacity solid composite cathodes. *Chem Sci* **15**, 2371–2379 (2024).

120. Zhou, B., Randall, N. & Prorok, B. Correlation between adhesion strength and thin film/substrate mechanical properties using the nano-scratch technique. *Materials Research Society Symposium Proceedings* **1297**, 11–16 (2011).

121. Inoue, N., Yonezu, A., Watanabe, Y., Yamamura, H. & Xu, B. Prediction of asymmetric yield strengths of polymeric materials at tension and compression using spherical indentation. *Journal of Engineering Materials and Technology, Transactions of the ASME* **139**, 1–11 (2017).

122. Ward, I. M. & Sweeney, J. *Mechanical Properties of Solid Polymers*. (Wiley, 2012). doi:10.1002/9781119967125.

123. Jee, A. Y., Lee, H., Lee, Y. & Lee, M. Determination of the elastic modulus of poly(ethylene oxide) using a photoisomerizing dye. *Chem Phys* **422**, 246–250 (2013).

124. Qin, W., Yang, Q., He, Y., Zhang, L. & Hu, H. Finite elastic-viscoplastic deformation behaviour of PEO-based solid polymer electrolyte: Experimental investigation and constitutive modelling. *Mechanics of Materials* **185**, 104773 (2023).

125. Zhao, L. *et al.* Hot-Pressing Enhances Mechanical Strength of PEO Solid Polymer Electrolyte for All-Solid-State Sodium Metal Batteries. *Small Methods* **2301579**, 1–9 (2024).

126. Younesi, M. & Bahrololoom, M. E. Effect of temperature and pressure of hot pressing on the mechanical properties of PP-HA bio-composites. *Mater Des* **30**, 3482–3488 (2009).

127. Tharazi, I. *et al.* Optimization of Hot Press Parameters on Tensile Strength for Unidirectional Long Kenaf Fiber Reinforced Polylactic-Acid Composite. *Procedia Eng* **184**, 478–485 (2017).

128. Kiran, G., Suman, K., Rao, N. & Rao, R. A study on the influence of hot press forming process parameters on mechanical properties of green composites using Taguchi experimental design. *International Journal of Engineering, Science and Technology* **3**, 253–263 (2011).

129. Smith, J. W. *et al.* Measurement of the fracture toughness of polymer-non-polymer interfaces. *J Mater Sci* **28**, 4234–4244 (1993).

130. Deng, S. *et al.* Coarse-Grained Molecular Dynamics Simulations of Nanoscale Roughness Effects on Oil Film Delamination. *Tribol Lett* **72**, 1–12 (2024).

131. Balint, D. S. & Hutchinson, J. W. Mode II edge delamination of compressed thin films. *Journal of Applied Mechanics, Transactions ASME* **68**, 725–730 (2001).

132. Jardret, V. D. & Oliver, W. C. Viscoelastic behavior of polymer films during scratch test: A quantitative analysis. *Materials Research Society Symposium - Proceedings* **594**, 251–256 (2000).

133. Beake, B. D., Liskiewicz, T. W. & Smith, J. F. Deformation of Si(100) in spherical contacts - Comparison of nano-fretting and nano-scratch tests with nano-indentation. *Surf Coat Technol* **206**, 1921–1926 (2011).

134. Diehl, T. On using a penalty-based cohesive-zone finite element approach, Part I: Elastic solution benchmarks. *Int J Adhes Adhes* **28**, 237–255 (2008).

135. Diehl, T. On using a penalty-based cohesive-zone finite element approach, Part II: Inelastic peeling of an epoxy-bonded aluminum strip. *Int J Adhes Adhes* **28**, 256–265 (2008).

136. Anderson, T. L. *Fracture Mechanics : Fundamentals and Applications, Fourth Edition*. vol. Fourth edi (CRC Press, Boca Raton, 2017).

137. Koch, T. & Seidler, S. Correlations between indentation hardness and yield stress in thermoplastic polymers. *Strain* **45**, 26–33 (2009).

138. Cheng, E. J. *et al.* Mechanical and physical properties of LiNi0.33Mn0.33Co0.33O2 (NMC). *J Eur Ceram Soc* **37**, 3213–3217 (2017).

139. Chi, T. T. K., Le, N. T., Hien, B. T. T., Trung, D. Q. & Liem, N. Q. Preparation of SERS Substrates for the Detection of Organic Molecules at Low Concentration. *Communications in Physics* **26**, 261 (2017).

140. Sharafi, A. *et al.* Impact of air exposure and surface chemistry on Li-Li7La3Zr2O12 interfacial resistance. *J Mater Chem A Mater* **5**, 13475–13487 (2017).

141. Sastre, J., Chen, X., Aribia, A., Tiwari, A. N. & Romanyuk, Y. E. Fast Charge Transfer across the Li7La3Zr2O12Solid Electrolyte/LiCoO2Cathode Interface Enabled by an Interphase-Engineered All-Thin-Film Architecture. *ACS Appl Mater Interfaces* **12**, 36196–36207 (2020).

142. Ebrahiminia, M., Hooper, J. B. & Bedrov, D. Structural, mechanical, and dynamical properties of amorphous Li 2 CO 3 from molecular dynamics simulations. *Crystals (Basel)* **8**, (2018).

143. Kim, Y., Waluyo, I., Hunt, A. & Yildiz, B. Avoiding CO2 Improves Thermal Stability at the Interface of Li7La3Zr2O12 Electrolyte with Layered Oxide Cathodes. *Adv Energy Mater* **12**, (2022).

144. Scales, R. J. *et al.* Effect of environment on nanoindentation induced cracking in Ta-doped Li7La3Zr2O12 garnet. *Ijnrd* **2**, 54–59 (2019).

145. McConohy, G. *et al.* Mechanical regulation of lithium intrusion probability in garnet solid electrolytes. *Nat Energy* **8**, 241–250 (2023).

146. Deng, Z., Wang, Z., Chu, I.-H., Luo, J. & Ong, S. P. Elastic Properties of Alkali Superionic Conductor Electrolytes from First Principles Calculations. *J Electrochem Soc* **163**, A67–A74 (2016).

147. Daelemans, L., Kizildag, N., Van Paepegem, W., D'hooge, D. R. & De Clerck, K. Interdiffusing core-shell nanofiber interleaved composites for excellent Mode I and Mode II delamination resistance. *Compos Sci Technol* **175**, 143–150 (2019).

148. Kim, A., Woo, S., Kang, M., Park, H. & Kang, B. Research Progresses of Garnet-Type Solid Electrolytes for Developing All-Solid-State Li Batteries. *Front Chem* **8**, 1–13 (2020).

149. Neelanarayanan, S. & Ramesha, K. Applied Interfaces advances at the cathode – electrolyte interface for. 868–895 (2024) doi:10.1039/d4lf00099d.

150. Kudryashov, D., Gudovskikh, A., Uvarov, A. & Nikitina, E. Investigation of silicon wafers thermal degradation by photoluminescence decay measurements. *AIP Conf Proc* **2012**, (2018).

151. Wang, X. *et al.* Quantifying Electrochemical Reactions and Properties of Amorphous Silicon in a Conventional Lithium-Ion Battery Configuration. *Chemistry of Materials* **29**, 5831–5840 (2017).

152. Hojo, J. *Materials Chemistry of Ceramics*. *Materials Chemistry of Ceramics* (2019). doi:10.1007/978-981-13-9935-0.

153. Yan, G. *et al.* An investigation on strength distribution, subcritical crack growth and lifetime of the lithium-ion conductor Li7La3Zr2O12. *J Mater Sci* **54**, 5671–5681 (2019).

154. Liu, D. *et al.* Characterization of the Interfacial Toughness in a Novel 'gaN-on-Diamond' Material for High-Power RF Devices. *ACS Appl Electron Mater* **1**, 354–369 (2019).

155. Volinsky, A. A., Bahr, D. F., Kriese, M. D., Moody, N. R. & Gerberich, W. Nanoindentation methods in interfacial fracture toughness.pdf. *Comprehensive Structural Integrity* 5232 (2003).

156. Kriese, M. D., Gerberich, W. W. & Moody, N. R. Quantitative adhesion measures of multilayer films: Part I. Indentation mechanics. *J Mater Res* **14**, 3007–3018 (1999).

157. Thouless, M. D., Hutchinson, J. W. & Liniger, E. G. Plane-strain, buckling-driven delamination of thin films: Model experiments and mode-II fracture. *Acta Metallurgica Et Materialia* **40**, 2639–2649 (1992).

158. Bernoulli, D. *et al.* Cohesive and adhesive failure of hard and brittle films on ductile metallic substrates: A film thickness size effect analysis of the model system hydrogenated diamond-like carbon (a-C:H) on Ti substrates. *Acta Mater* **83**, 29–36 (2015).

159. Malzbender, J. & De With, G. A model to determine the interfacial fracture toughness for chipped coatings. *Surf Coat Technol* **154**, 21–26 (2002).

160. Botero, C. A., Cabezas, L., Sarin, V. K., Llanes, L. & Jiménez-Piqué, E. Nanoscratch Testing of 3Al2O3·2SiO2 EBCs: Assessment of Induced Damage and Estimation of Adhesion Strength. *Ceramics* **6**, 664–677 (2023).

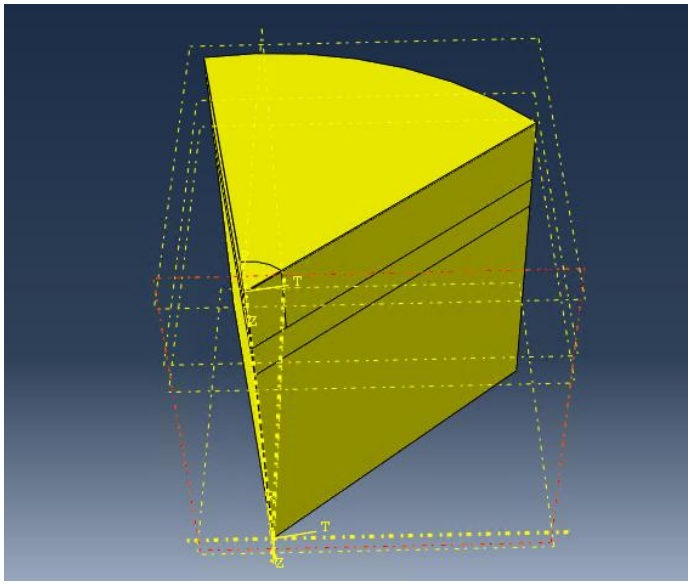
161. Nanda, J. & Augustyn, V. *Transition Metal Oxides for Electrochemical Energy Storage*. *Transition Metal Oxides for Electrochemical Energy Storage* (2022). doi:10.1002/9783527817252.

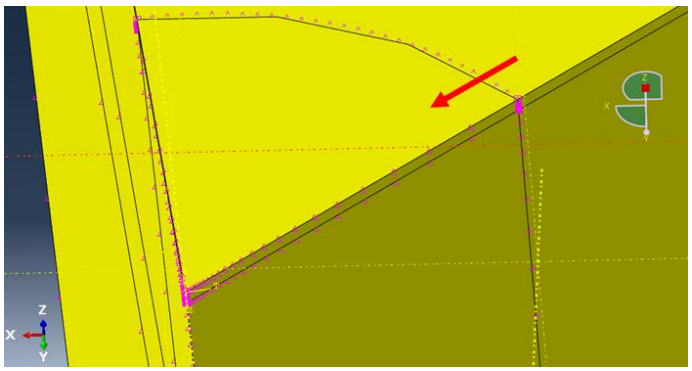
162. Shishvan, S. S., Fleck, N. A., McMeeking, R. M. & Deshpande, V. S. Cracking and associated volumetric expansion of NMC811 secondary particles. *J Power Sources* **588**, 233745 (2023).

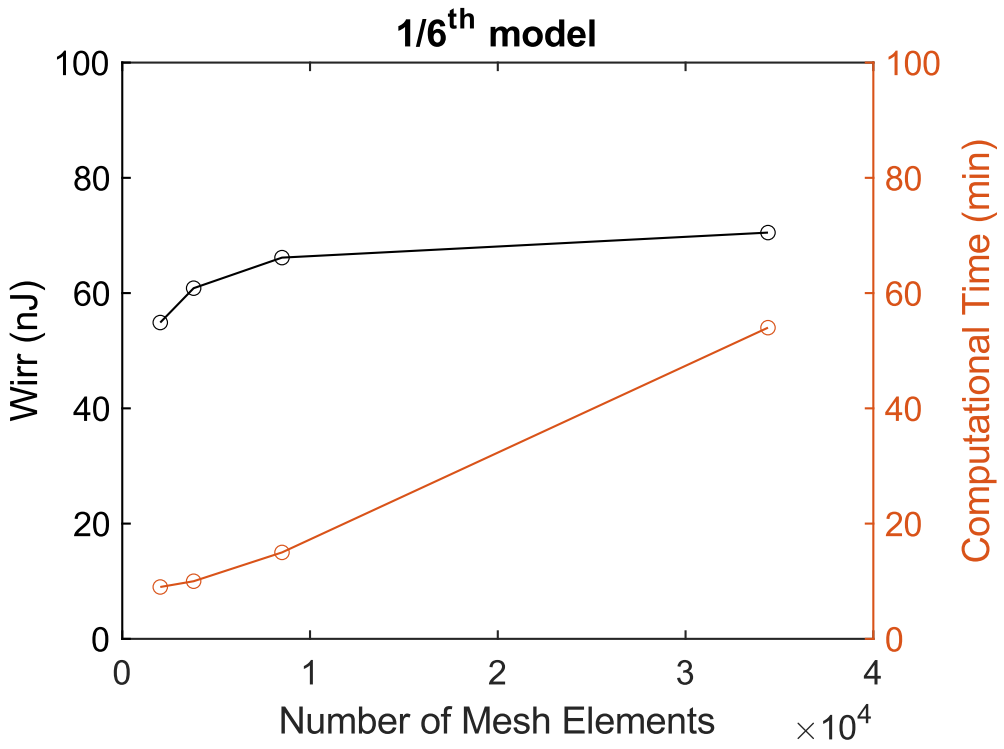
APPENDIX

Appendix 1: Mesh Convergence (1/6th model)

The number of mesh elements in the film regions shown (under the indenter) was varied for convergence.

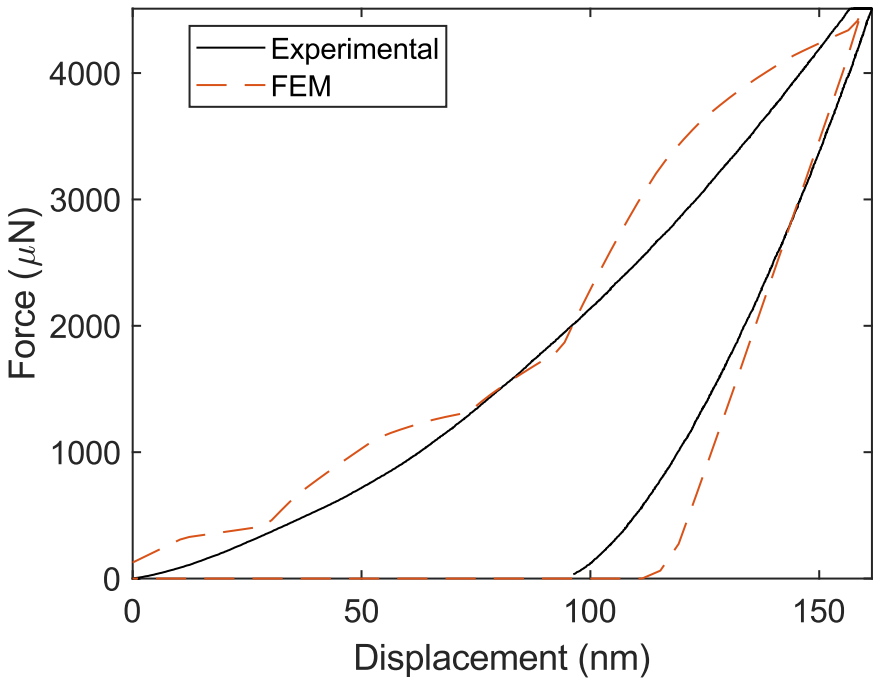






$1x10^4$ mesh elements was selected as optimal mesh size for modelling.

Appendix 2: Load-displacement curve (FEM vs Experimental) tungsten on silicon



The deviations in the FEM curve are due to the mesh. The irreversible work (area under the curve) was also found to be in good agreement.

Appendix 3: Mesh Convergence (Cohesive model)

Mesh Elements in Film	S, Mises (MPa)	Delamination (yes/no)	Computational Time (min)
2,680	2.0778	No	7
10,050	6.2095	Yes	8
50,250	7.9615	Yes	11
100,500	7.3815	Yes	118

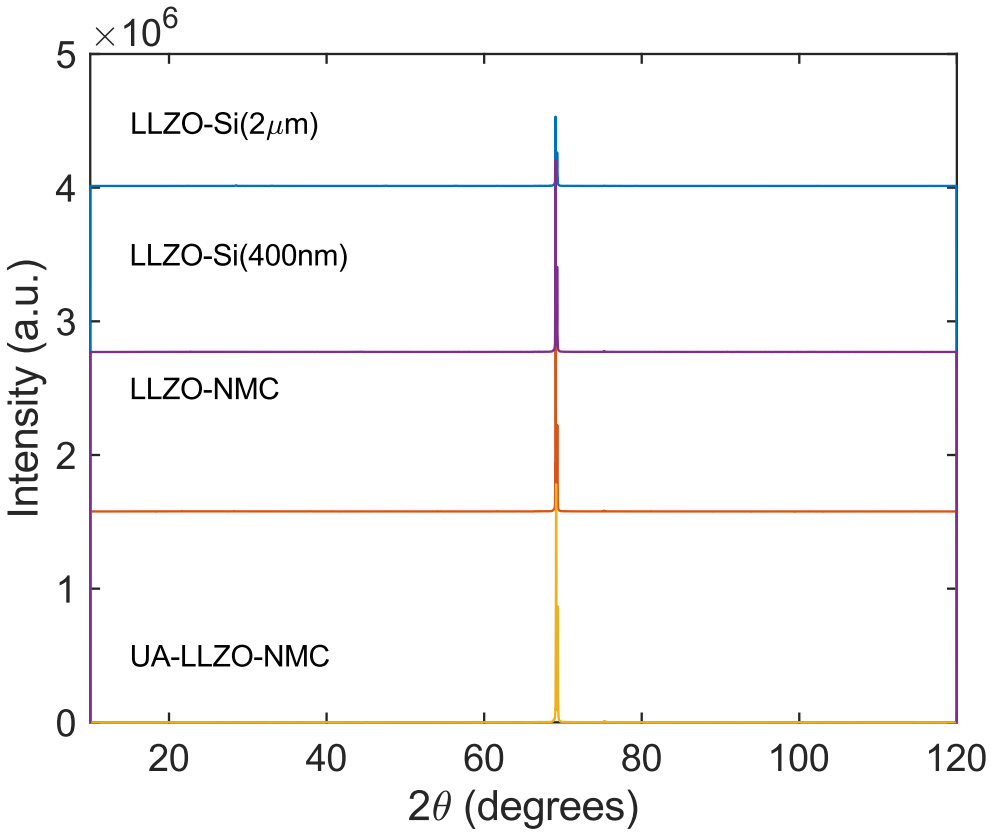
The Von mises stress measured from the bottom layer of the film (under the indenter). 50,250 was chosen as optimal mesh size for modelling.

Appendix 4: LLZO Films Sputtering Conditions

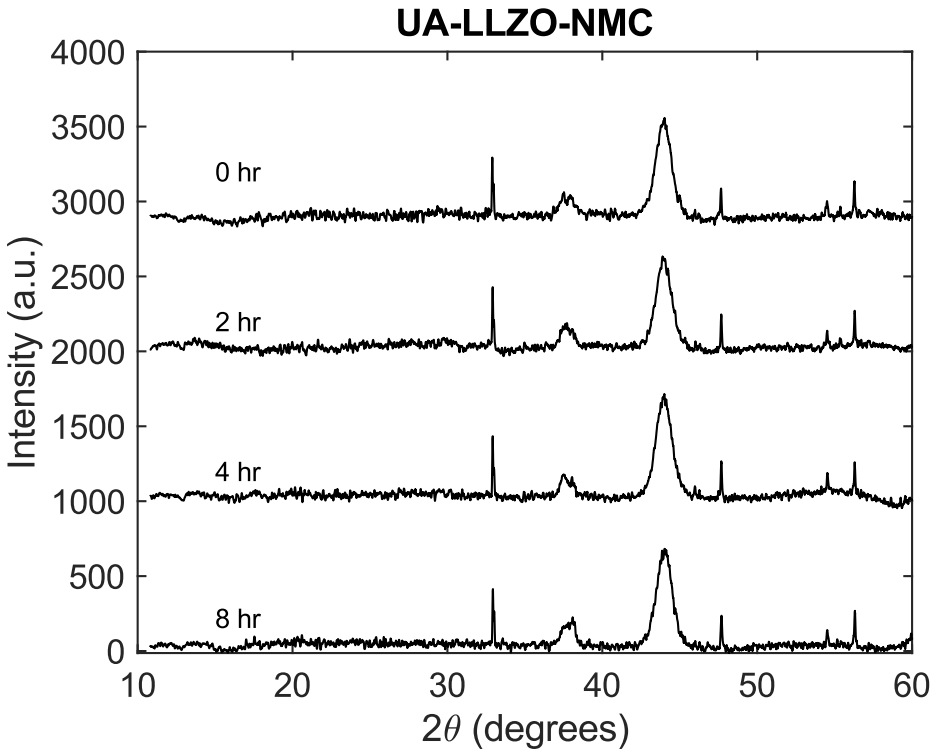
	LLZO-Si(400nm)	LLZO-Si(2µm)	LLZO-NMC	
			LLZO	NMC
PVD System	MB EVAP (MBraun)	DST2-TSGB (Nano-Structured Coatings Co.)	DST2-TSGB (Nano-Structured Coatings Co.)	DST2-TSGB (Nano-Structured Coatings Co.)
Target Material	LLZTO	LLZTO	LLZTO	NMC-811

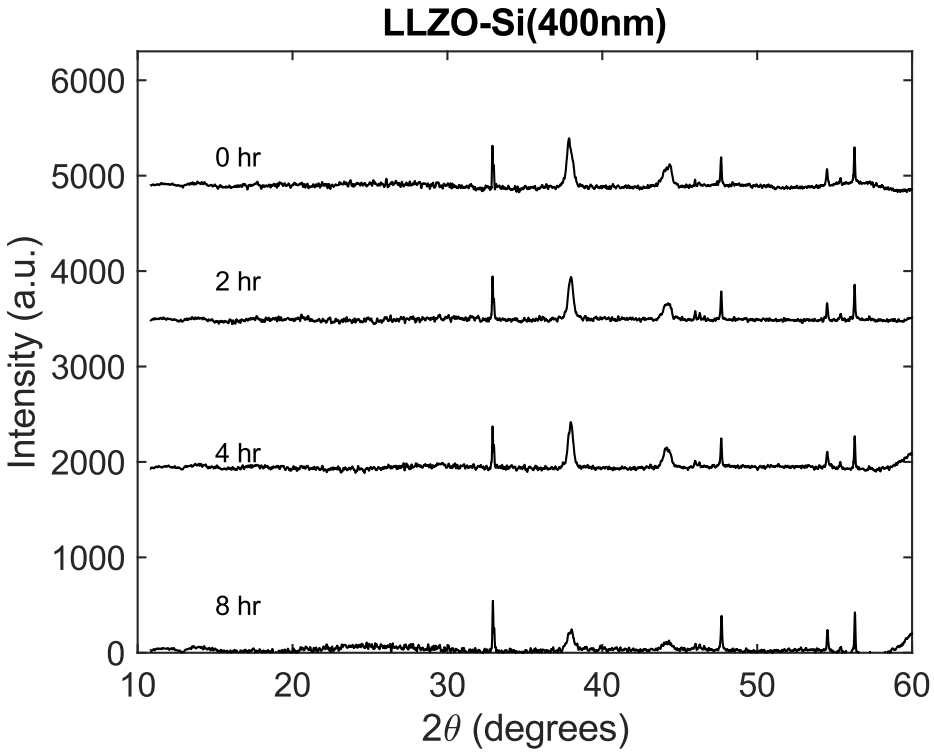
Target to substrate distance (cm)	12	3	3	3
Argon flow rate (sccm)	20	9	19	14
Process pressure (mbar)	$1*10^{-2}$	$7*10^{-3}$	$3*10^{-3}$	$3*10^{-3}$
RF power (W)	50	50	50	50
Deposition duration (h)	18	4	0.75	8

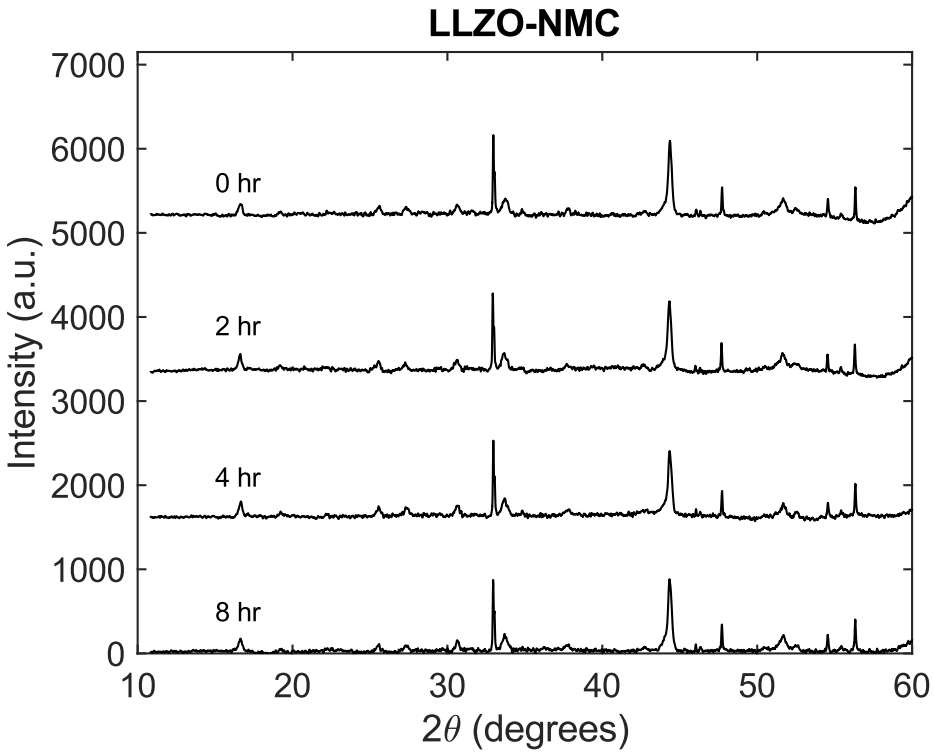
Appendix 5: XRD results with silicon substrate



Appendix 6: XRD Air exposure






LLZO-NMC
Intensity (a.u.)
2θ (degrees)
0 hr
2 hr
4 hr
8 hr
0
1000
2000
3000
4000
5000
6000
7000
10
20
30
40
50
60